.

Solid-state NMR studies on precursor derived Si-B-C-N and B-C-N ceramics

Von der Fakultät Chemie der Universität Stuttgart
zur Erlangung der Würde eines
Doktors der Naturwissenschaften (Dr. rer. nat.)
genehmigte Abhandlung

vorgelegt von

Otgontuul Tsetsgee
aus Ulan Bator, Mongolei

Hauptberichter:	Prof. Dr. Klaus Müller
Mitberichter:	Priv.-Doz. Dr. Günter Majer
Mitprüfer und Prüfungsvorsitzender:	Prof. Dr. Helmut Bertagnolli
Tag der mündlichen Prüfung:	16 Juni 2009

Institut für Physikalische Chemie der Universität Stuttgart

April 2009

Solid-state NMR studies on precursor derived Si-B-C-N and B-C-N ceramics

Dissertation for the degree of

Doctor of Natural Sciences

submitted to the

Faculty of Chemistry, University of Stuttgart

presented by

Otgontuul Tsetsgee

from Ulan Bator, Mongolia

accepted on the recommendation of

Prof. Dr. Klaus Müller, examiner

Priv.-Doz. Dr. Günter Majer, co-examiner

Prof. Dr. Helmut Bertagnolli, co-examiner

Institute of Physical Chemistry, University of Stuttgart

April, 2009

to my mother, Tsetsgee Yarimpil

Acknowledgement

First, I would like to express my sincere and deepest gratitude to my supervisor Prof. Dr. Klaus Müller for introducing me in a very interesting research field. I am extremely grateful for his patience and knowledge, valuable advice and discussions, and support throughout my research work.

I would like to thank Priv.-Doz. Dr. Günter Majer for his role as co-examiner and for writing second advisory opinion. I also would like to thank Prof. Dr. Helmut Bertagnolli for taking the chair in the examination board.

I would like to thank the Graduiertenkolleg "*Modern Methods of Magnetic Resonance in Material Science*" for providing the fellowship and Deutsche Forschungsgemeinschaft for financial support of this project. I also thank the Mongolian Academy of Science for providing an opportunity to study in Germany.

It is my pleasure to thank all people working in IPC. My special thanks go to Mrs. Inge Blankenship for her secretarial help and kindness. I also thank Dr. Dieter Leicht for his help in administrative procedures. I would also like to thank Mr. Walter Ottmüller and Mr. Jochen Graf for mechanical workshop support, Mr. Jürgen Hußke for help in electronics and Dr. Stefan Jagiella for computer help.

I want to thank my former and present colleagues at the University of Stuttgart for creating a friendly and cooperative working atmosphere; Dr. Gokulakrishnan Srinivasan, Dr. Jorge Garibay and Dr. Xiorang Yang for helping me at the beginning of my PhD study, Dr. Kamalakannan Kailasam, M.Sc. Poonkodi Balasibramaniyan, M.Sc. Christiane Heuber, M.Sc. Lida Grassemzadeh and M.Sc. Tahira Yasmin for their support, comments and suggestions, and Dr. Fabrizia Poli for her valuable discussions and comments improved my thesis. I also would like to thank my friend Laura Valiente for her encouragement.

Finally, I wish to express my warmest gratitude to my dear family, to my mother,

brothers and sisters for their love and emotional support, and to my husband Enkhjargal and son Borkhuu for all of support and love throughout this time.

Contents

Chapter 1

Introduction

The subject of ceramics covers a wide range of materials. It is basically distinguished between traditional and advanced ceramics. Up to 1950s the most important of these were the traditional ceramics, which are derived from naturally occurring raw materials and which include clay-based products such as tablewares, sanitarywares as well as structural claywares like bricks and pipes. This group also includes cements, glasses and refractories. Advanced ceramics are also known as engineering ceramics whereas the phrases *special, fine* and *technical* have been used in connection with these materials [1, 2]. Chemically, ceramics are inorganic nonmetallic compounds, whose formation is due to the action of heat [3].

Among the ceramics, two different classes can be recognized, namely oxide and non-oxide materials. Oxide ceramics frequently include silicate structures, which are relatively low melting materials. In the last two decades, also non-oxide ceramics containing the elements Si, C, B and N are suitable candidates for high temperature applications, because of their chemical and mechanical high temperature stability [4–6]. Materials such as Si_3N_4, SiC, BN and Si_3N_4/SiC composites are conventionally prepared by the powder technology [7, 8]. Densification of powders is commonly performed by sintering under high temperatures to overcome the low self-diffusion

coefficients of such covalently bonded ceramic materials [9]. This method of preparation usually requires sinter additives [10, 11], which by the formation of oxide-based secondary phases increases the atomic mobility and reduces the thermal, chemical and mechanical high temperature stability.

An alternative approach that recently has attracted wide attention is the use of precursor polymers, which offers a number of advantages as compared to the classical powder technology. Novel ceramic materials with high temperature stability and good oxidation resistance can be obtained from molecular units (precursors) without sintering additives [12–19]. Since such precursor-derived materials do not contain grain boundaries, their mechanical properties at higher temperatures are better than those obtained by conventional methods. These polymer-derived ceramics have a homogeneous chemical distribution on an atomic scale and controllable microstructures and properties. Moreover, silicon nitride- and silicon carbide- based composites (Si-C-N ceramics) exhibit exceptional material properties (as expressed by the creep and corrosion resistance, high tensile strength and hardness), and possess a great potential for high temperature applications. However, independent of the specific precursors, the thermal stability of Si-C-N ternary ceramics is limited to 1480 °C due to the reaction of Si_3N_4 with free carbon to form N_2 [20–22].

More recently, it has been demonstrated that the addition of boron to Si-C-N materials increases their thermal stability and the temperature of crystallization. Some Si-B-C-N materials remain amorphous up to 1700 °C and do not decompose significantly up to 2000 °C [23–26]. The first report on Si-B-C-N materials was published by Takamizawa and coworkers [27, 28]. During the last two decades numerous Si-B-C-N ceramics with different compositions were synthesized and characterized with respect to the basic structure, crosslinking mechanism and ceramic conversion behavior by solid-state NMR [29–32], IR [33, 34], XRD [33, 35–37], TEM [38, 39] and XPS [29, 40]. Precursors for Si-B-C-N ceramics are

generally divided into two groups: (i) those based on borazine and its derivates as the boron-nitride source, and (ii) those without borazine units in the polymeric network. The first borazine-based Si-B-C-N polymers where published by Nöth in 1961 [41], long before their potential as preceramics was recognized. In 1990, Seyferth *et al.* [42] reported on the first polymeric Si-B-C-N precursors, obtained by dehydrocoupling of borane dimethylsulfide, $BH_3{\cdot}SMe_2$, and cyclotri(methylsilazane), $(SiMeH\text{-}NH)_3$. In this context, the work of Riedel *et al.* [25, 31, 43, 44], Jansen *et al.* [45–51], and Aldinger *et al.* [36, 37, 52–54] should be mentioned, who independently reported synthesis of quaternary Si-B-C-N ceramics from structurally different single-source precursors. In spite of the numerous recent publications about new Si-B-C-N ceramics [55–60], the effect of boron on the reactions during thermolysis is not clearly understood. It has been speculated that the presence of boron might retard the diffusion of other atoms and hinder the formation of crystalline ceramics. Therefore, the understanding of the transformation process of precursor polymers into amorphous Si-B-C-N ceramics is important for further development of ceramics with better material properties.

Boron-containing polysilazanes, carbon-containing polyborosilazanes and silylated borazine derivates have shown to be excellent precursor polymers for the transformation to the quaternary system Si-B-C-N. In general, these polymers consist of Si-N skeletons, which are more or less crosslinked via B, B-N, B-C or borazine units. In the present contribution, boron-modified polysilazanes and polysilylcarbodiimides, which are crosslinked by C-B-C, carrying different substituents bonded to silicon and nitrogen centers, are studied. The polymer-to-ceramic conversion involves several amorphous intermediate steps which rules out common techniques for structural characterization, such as X-ray diffraction, etc. In this work, we used solid-state NMR spectroscopy, which has been found to be particularly powerful to extract the structural features of amorphous

ceramic intermediates. NMR spectroscopy probes the molecular environment (short-range order) around selected nuclei, whose magnetic properties strongly depend on the local electronic environment and the dipolar interactions with nuclei in the next neighborhood. Furthermore, NMR spectroscopy is particularly attractive for ternary and quaternary oxide free ceramics, as they possess several NMR active nuclei such as ^{13}C, ^{29}Si and ^{11}B, which can be studied directly without further isotopic enrichment.

In the present contribution, multinuclear solid-state NMR spectroscopy which was used to characterize the microstructures of the pyrolysis intermediates in the Si-B-C-N ceramics derived from boron-modified polysilazanes and polysilylcarbodiimide precursors. The structural changes of the compositions at different tetrahedral sites (SiC_xN_{4-x} units) in the Si-C-N matrix of the amorphous intermediates are followed by ^{29}Si MAS NMR signals as function of the ceramic composition and the thermolysis temperature. ^{13}C MAS NMR is the standard method to probe sp^2- and sp^3- carbon in amorphous ceramics. However, for the pyrolysis intermediates above 1400 °C, ^{13}C NMR signals are usually not observable due to long spin-lattice relaxation time. ^{15}N NMR experiments were obtained only for the amorphous ceramics, which are derived from the ^{15}N enriched precursors.

It is suspected that the addition of boron retards the nucleation of SiC and Si_3N_4 nanocrystallites, by reducing the carbon and nitrogen activities (via formation of a BNC_x matrix) [38, 61]. In other words, the BNC_x phase plays an important role for the unusual high temperature stability of these materials. However, a satisfactory and complete picture about the structural composition of the BNC_x phase is still missing. There is still lack of evidence that the three elements are in a honeycomb network rather than mechanical mixtures of graphite and hexagonal boron nitride, both turbostratically disordered. Therefore, in this work, - particular emphasis is given to the structural composition of the BNC_x phase. For this purpose, double

resonance experiments such as $^{11}B\{^{15}N\}$ REDOR, $^{11}B\{^{15}N\}$ SEDOR and ^{11}B spin echo are applied, which allow the measurement of the dipolar coupling between like and unlike spins, being directly related to the internuclear distance. From the REDOR and SEDOR experiments, the dipolar coupling between boron and nitrogen nuclei can be obtained. The ^{11}B spin echo technique provides the ^{11}B second moment in the amorphous ceramics. The experimental double resonance and spin echo curves are simulated using hexagonal BN (h-BN) as model system, whose internuclear distances are known from X-ray diffraction [62].

It should be mentioned that similar REDOR experiments were performed earlier by Jansen *et al.* earlier on another Si-B-C-N ceramic system, for which only a single ^{13}C, ^{29}Si and ^{15}N enriched sample, heat-treated at one particular temperature, was available [63–67]. However, in the present study a series of samples, pretreated at different temperatures, is available which allows a systematic study of the whole pyrolysis process.

In addition, $^{11}B\{^{14}N\}$ REAPDOR experiments, which are suitable for spin systems where two quadrupolar nuclei are involved, are performed. Although this technique gives the same information as the REDOR experiment, it does not require ^{15}N isotopic enrichment. So far, there was no application of this technique for multi spin systems, where the spins are strongly coupled.

Chapter 2

Non oxide precursor-derived (Si)-B-C-N ceramic

In general, the procedure for the preparation of ceramics from organo-element compounds consists of four steps (see Figure 2.1):

i Synthesis of pre-ceramic oligomers or polymers from monomer units. The obtained precursors contain structural units of the final ceramic materials.

ii Crosslinking of the polymer to form a two- or tree-dimensional pre-ceramic network, while the organic groups are removed by thermolysis.

iii Pyrolysis of the preceramic network to get amorphous covalent ceramics.

iv Crystallization of the amorphous solids into thermodynamically stable phases.

So far, the transition process from the amorphous to the crystalline state has attracted a lot of interest in the structural characterization of precursor-derived ceramics. Apart from the silicon based ceramics (Si-B-C-N) the silicon free B-C-N ceramic materials have been studied.

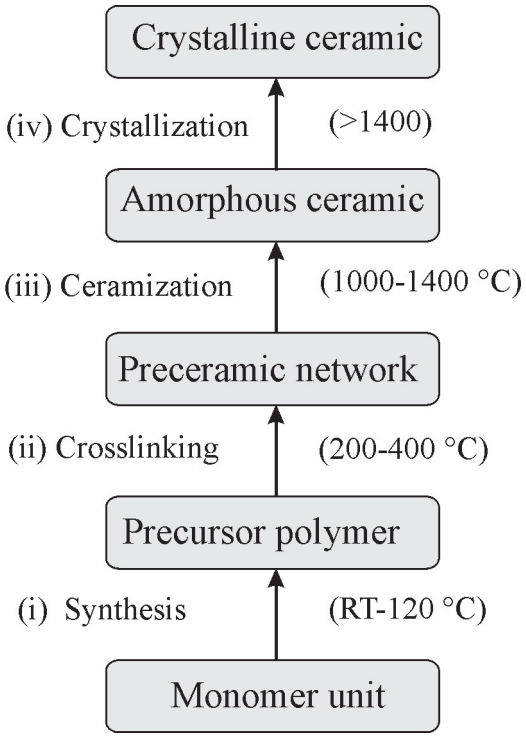

Figure 2.1. Process of precursor-derived Si-B-C-N ceramics.

Thermolysis of organometallic polymers in controlled atmosphere and heat treatment conditions is a comparatively simple and inexpensive process for producing both oxide and non-oxide ceramics. It provides a means of controlling and adjusting the microstructure design and the shape of ceramic components, which often cannot be achieved using classical techniques such as melting, sintering or chemical deposition. PDCs possess several advantages, as compared to ceramics obtained by conventional methods. They possess a high chemical purity, much better homogeneity, low processing temperatures and have versatile fabrication manner. In contrast to traditional ceramic methods, their fabrication does not require sinter additives.

2.1 Precursors

In the present work, the thermal evolution of quaternary Si-B-C-N and ternary B-C-N systems derived from boron-modified polysilazanes (**1** to **6**), polysilylcarbodiimides (**7**) and poly(borosesquicarbodiimides) (**8**) was studied. The starting polymer precursors and their pyrolysis intermediates at different temperatures were prepared in the group of Prof. F. Aldinger at the Max-Planck-Institut für Metallforschung.

The molecular structures of the precursors **1** to **4** and **5** to **8** are presented in Figures 2.2 and 2.3, respectively, and the compositions are given in Table 2.1. A short description of the synthesis of these precursors is given in Section 2.2. More detailed information about the synthesis as well as the characterization of the obtained polymer precursors can be found in the literatures [24, 68–72].

Table 2.1. Elemental composition of polymer precursors.

precursors	derived formula	precursor formula	Ref
1	$\{B[C_2H_4Si(CH_3)NH]_3\}_n$	$Si_3B_1C_9N_3H_{24}$	[24]
2	$\{B[C_2H_4Si(H)NH]_3\}_n$	$Si_3B_1C_6N_3H_{18}$	[69]
3	$\{B[C_2H_4Si(H)N(CH_3)]_3\}_n$	$Si_3B_1C_9N_3H_{24}$	[73]
4	$\{B[C_3H_6Si(CH_3)NH]_3\}_n$	$Si_3B_1C_{12}N_3H_{30}$	[70]
5	$\{B[C_2H_4SiH(H)C_2H_4Si(H)NH]_3\}_n$	$Si_6B_1C_{12}N_3H_{36}$	[71]
6	$\{B[C_2H_4SiH(CH_3)C_2H_4Si(H)NH]_3\}_n$	$Si_6B_1C_{15}N_3H_{42}$	[71]
7	$\{B[C_2H_4\text{-}SiH_2\text{-}(NCN)_{0.5}]_3\}_n$	$Si_3B_1C_{7.5}N_3H_{18}$	[68]
8	$[B_2(NCN)_3]_n$	$B_2C_9N_3$	[72]

The type of backbone and the side chains of the precursor molecules substantially influence the ceramic yield, chemical composition and microstructure of the derived ceramics. The present polymer precursors for the quaternary ceramics (Si-B-C-N)

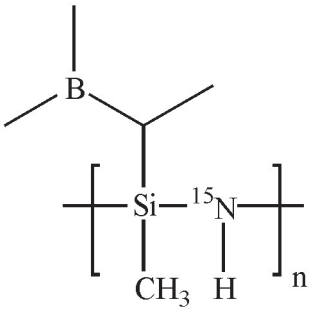

Precursor **1**

^{15}N labeled boron-modified
polymethylvinylsilazane

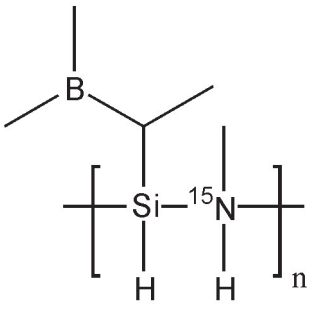

Precursor **2**

^{15}N labeled boron-modified
polyhydridovinylsilazane

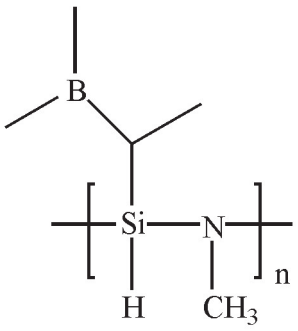

Precursor **3**

Boron-modified
polyhydridomethylaminovinylsilazane

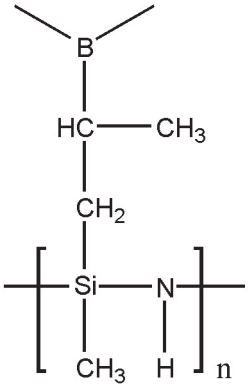

Precursor **4**

Boron-modified
polyallylmethylvinylsilazane

Figure 2.2. The molecular structures of the precursors **1**, **2**, **3** and **4**.

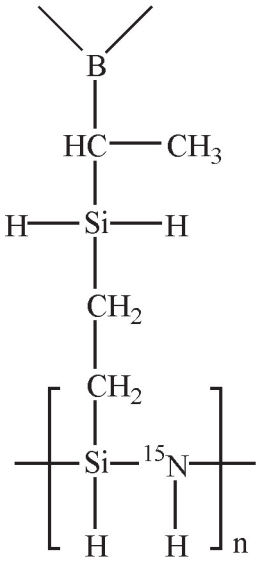

Precursor **5**

Hydrosilylized ^{15}N labeled
boron-modified polyhydridovinylsilazane

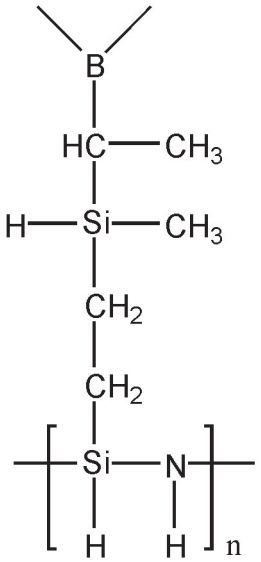

Precursor **6**

Hydrosilylized boron-modified
polyhydridovinylsilazane

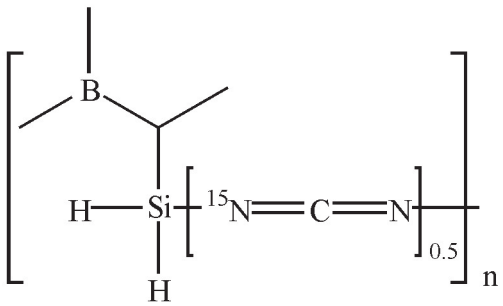

Precursor 7

^{15}N labeled boron-modified
polyhydridovinylsilylcarbodiimide

$[B_2(^{15}NCN)_3]_n$

Precursor **8**

^{15}N labeled
poly(borsesquicarbodiimide)

Figure 2.3. The molecular structures of the precursors **5**, **6**, **7** and **8**.

are characterized by a direct attachment of the silicon atoms to the carbon and nitrogen atoms, and the -C-B-C- linkages. The structure of the precursors firstly differ by the number of silicon and carbon atoms per monomer units, and by the groups (H and CH_3) bonded to silicon and nitrogen. The difference between polysilazanes and polysilylcarbodiimides is the bridging group in the polymer backbone.

For the synthesis of boron-modified polysilazanes **1** to **7**, vinyl- or propenyl-substituted silanes were used as monomeric silicon and carbon source. The vinyl and propenyl groups provide the integration of boron into the polysilazane and polysilylcarbodiimide via hydroboration reaction to yield C-B-C linkages.

In former studies, it has been proven that the hydroboration reaction is not regio-selective [74]. As an example, the mechanism for the hydroboration of vinyl groups is shown in Figure 2.4. The boron atoms can be bonded to the CH or CH_2 moieties, resulting in α- or β- products. The relative amounts of α- and β- products depend on the substitutes on the silicon atoms and affect the yield of the derived ceramic materials [75].

For the $^{11}B\{^{15}N\}$ REDOR studies, ^{15}N isotopic enriched polysilazanes **1**, **2**, **5** (100 %) and polycarbodiimides **7**, **8** (50 %) were synthesized using 100 % of ^{15}N isotopic

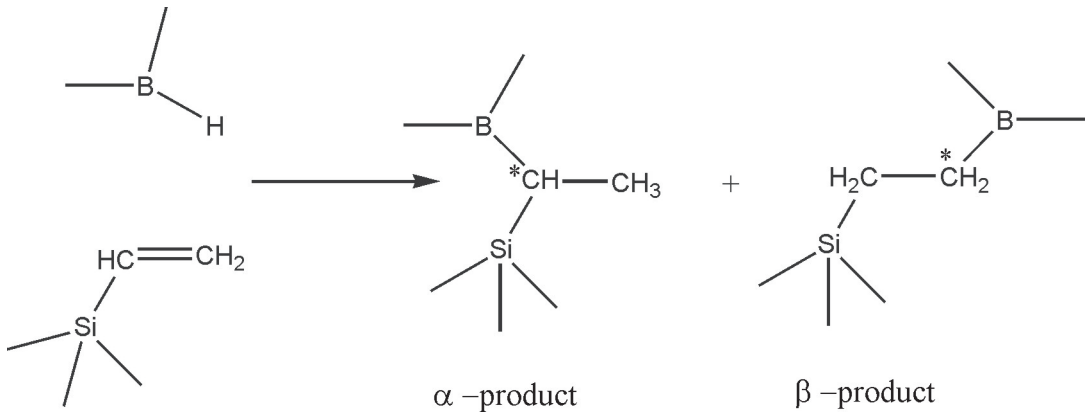

Figure 2.4. Hydroboration reaction of vinyl groups.

enriched ammonia ($^{15}NH_3$) and 50 % of ^{15}N isotopic enriched cyanamide ($H_2{}^{15}NCN$), respectively.

2.2 Precursor synthesis

2.2.1 Boron-modified polyvinylsilazanes 1 and 2

In general, the boron-modified polyvinylsilazanes $\{B[C_2H_4Si(R)NH]_3\}_n$ (R=CH_3; **1** and R=H; **2**) can be synthesized by polymer (P) or monomer (M) routes starting in both cases from simple monomer unit as dichlorovinylsilanes $(CH{=}CH_2)Si(R)Cl_2$ (**a**) [69, 76]. The monomer route shown in Figure 2.5 starts with the incorporation of boron via a hydroboration reaction. In this reaction, the starting compound (**a**) reacts with borane dimethylsulfide ($H_3B{\cdot}SMe_2$) to form tris(chlorosilylethyl)borane $B[C_2H_4Si(R)Cl_2]_3$ (M). In the presence of ammonia (NH_3) the boron containing monomer reacts to give the desired precursors **1** or **2**.

In the polymer route shown in Figure 2.6, the sequence of the reactions is inverted. At first, the ammonolysis reaction of the dichlorovinylsilanes (**a**) to get boron-free polyvinylsilazanes (P) is performed, which is followed by the hydroboration reaction. In the present study, polymer precursors **1** and **2** were prepared by the polymer route. The efficiency of the hydroboration reaction in the case of precursors **1** and

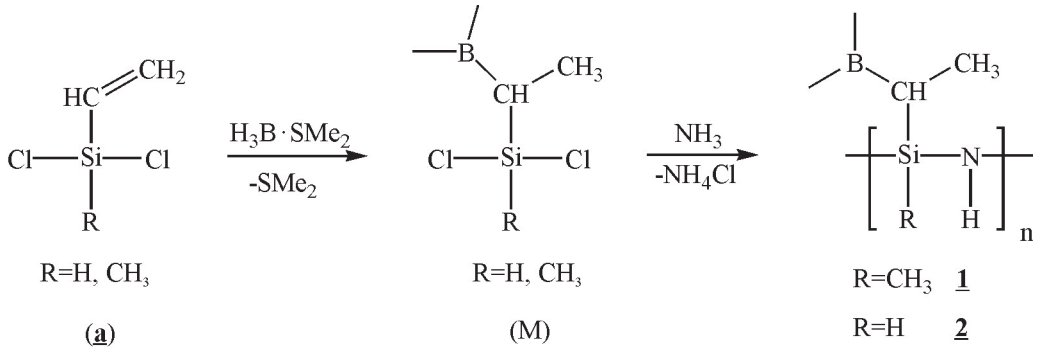

Figure 2.5. Reaction schema for the monomer route.

2 is 100 % and 86 %, respectively [69].

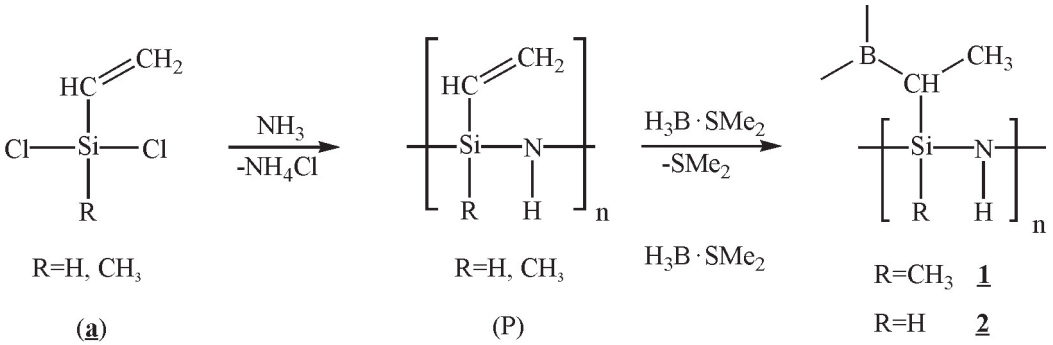

Figure 2.6. Reaction schema for the polymer route.

2.2.2 Tris(hydridosilylethyl)boranes

Tris(hydridosilylethyl)boranes with general type of $B[C_2H_4Si(R^{1,2})_nH_{3-n}]_3$ (n=0, 1 and 2) were used as starting compounds for the preparation of precursors **3**, **5**, **6** and **7**. Tris(hydridosilylethyl)boranes can be synthesized both from tris(chlorosilylethyl)boranes and hydridovinylsilanes [77]. The synthetic pathway used for the preparation of precursors in the present work is shown in Figure 2.7.

Hydridovinylsilanes of the general structure $(H_2C{=}CH)Si(R^{1,2})_nH_{3-n}$ (**b**) are difficult to handle in neat form. They were synthesized from the corresponding

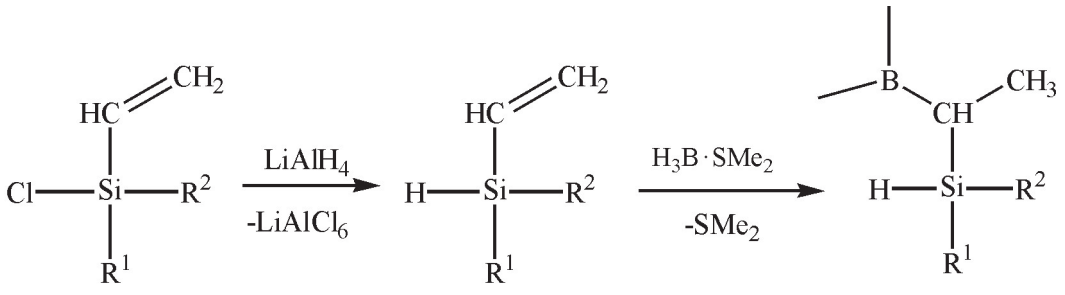

$R^1{=}R^2{=}Cl$ (n=0) $R^1{=}R^2{=}H$ $R^1{=}R^2{=}H$ **3c**, **5c** and **7c**

$R^1{=}Cl$, $R^2{=}CH_3$ (n=1) $R^1{=}H$, $R^2{=}CH_3$ $R^1{=}H$, $R^2{=}CH_3$ **6c**

(a) **(b)**

Figure 2.7. Synthesis of tris(hydridosilylethyl)boranes from hydridovinylsilanes.

chlorovinylsilanes $(H_2C{=}CH)Si(R^{1,2})_nCl_{3-n}$ (**a**) with $LiAlH_4$ in diethyl ether and reacted in situ [77]. Subsequently, the hydroboration reaction of hydridovinylsilanes (**b**) takes place in presence of boranedimethylsulfide ($H_3B{\cdot}SMe_2$) to form tris(hydridosilylethyl)boranes (**3c**, **5c**, **6c** and **7c**).

2.2.3 Boron-modified polyhydridomethyl-aminovinylsilazane 3 by a dehydrocoupling

Synthesis of polymer precursor **3**, boron-modified polyhydridomethylaminovinyl-silazane $\{B[C_2H_4Si(H)N(CH_3)]_3\}_n$ is shown in Figure 2.8. Precursor **3** was obtained by a dehydrocoupling reaction of tris(hydridosilylethyl)boranes $B[C_2H_4SiH_3]_3$ **3c** with methylamine NH_2CH_3 [73]. This reaction was performed in tetrahydrofuran solution at 60 °C without adding catalyst (**a.** neat). Aminolysis can also be performed in the presence of catalytic amounts of n-butyl lithium (**b**.cat), which was added to the toluene/tetrahydrofuran solution of starting compound. In both cases the precursors were obtained in high yield, > 90 %. The starting compound tris(hydridosilylethyl)borane (**3c**) itself is synthesized from hydridovinylsilane by reaction pathway as given in Figure 2.7.

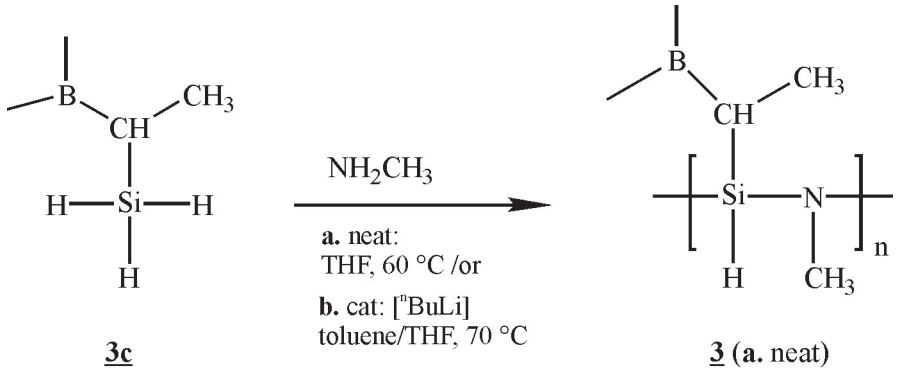

Figure 2.8. Synthesis of boron-modified polyhydridomethylaminovinylsilazane **3** from tris(hydridosilylethyl)borane.

2.2.4 Boron-modified polyallylmethylvinylsilazane 4

Boron-modified polyallylmethylvinylsilazane **4** $\{B[C_3H_6Si(CH_3)NH]_3\}_n$ can be synthesized via both the monomer and the polymer route, starting with allyldichloromethylsilane, $(H_2C{=}CHCH_2)Si(CH_3)Cl_2$, as monomeric silicon/carbon source [70]. Figure 2.9 shows the synthetic pathway of the polymer route used here. In this case, first the ammonolysis of allyldichloromethylsilane (**a**) with ammonia takes place to form boron-free polyallylmethylvinylsilazane (**b**) with an yield of 83 % leaving NH_4Cl as byproduct. Subsequent hydroboration of the vinyl group (**b**) with boranedimethylsulfide provides the desired polymer precursor **4**. In the monomer route, the reaction sequence is inverted.

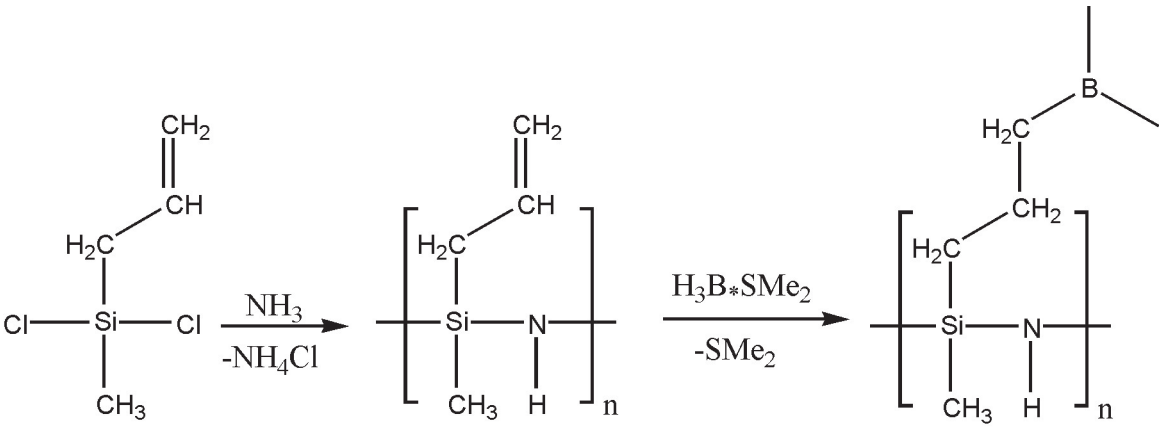

a **b** **4**

Figure 2.9. Synthesis of boron-modified polyallylmethylvinylsilazane **4** by polymer route.

2.2.5 Boron-modified hydrosilylized polyhydridovinylsilazanes 5 and 6

Figure 2.10 shows the synthetic procedure for the preparation of boron-modified hydrosilylized polyhydridovinylsilazanes $\{B[C_2H_4SiH(R^2)C_2H_4Si(H)NH]_3\}_n$ (R^2=H; **5** and R^2=CH_3; **6**). Polymer precursors **5** and **6** are obtained in quantitative

yields by the reaction of oligovinylsilazane $[(H_2C{=}CH)Si(H)NH]_n$ (**P**) with tris(hydridosilylethyl)boranes $B[C_2H_4Si(R^2)H_2]_n$ (R^2=H; **5c** and R^2=CH_3; **6c**) in a thermally induced hydrosilylation reaction without the use of solvents and catalysts, and without the formation of byproducts [71, 78].

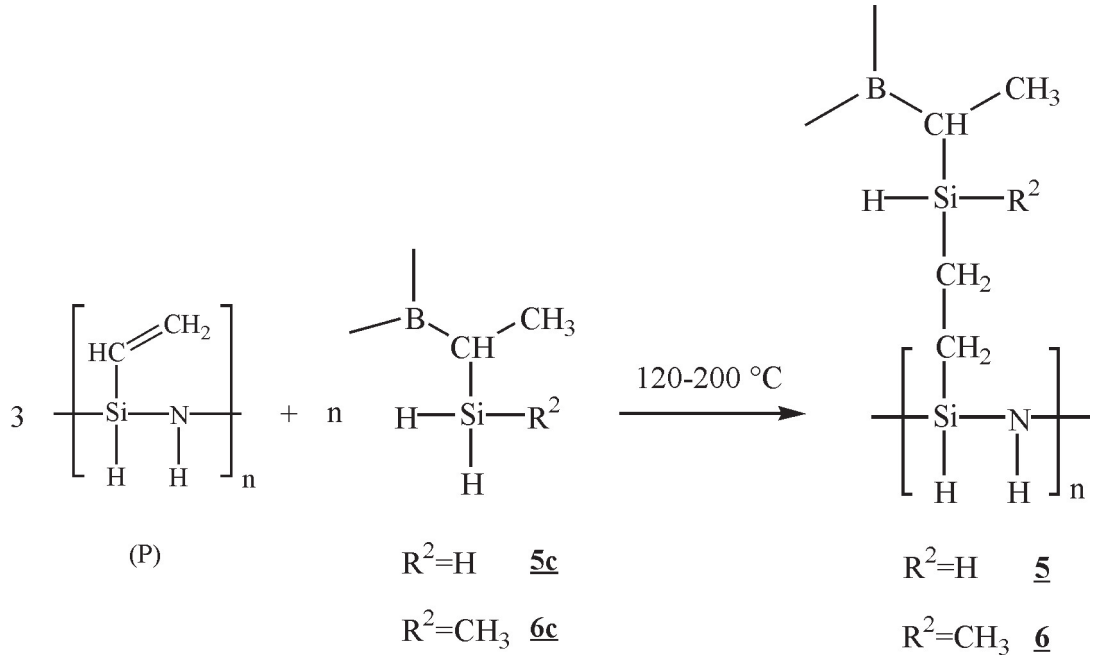

Figure 2.10. Synthesis of boron-modified hydrosilylized polyhydridovinylsilazanes **5** and **6** from tris(hydridosilylethyl)boranes.

The starting compounds tris(hydridosilylethyl)boranes (**5c** and **6c**) and polyvinylsilazane (**P**) were also synthesized from the chlorovinylsilane. As the polyvinylsilazane is the fist product of the polymer route given in Figure 2.6, it can be obtained by aminolysis of chlorovinylsilane with ammonia. The synthetic pathway of the tris(hydridosilylethyl)boranes (**5c** and **6c**) from chlorovinylsilane is also given in Figure 2.8 [53, 79].

2.2.6 Boron-modified polysilylcarbodiimide 7

According to the reaction given in Figure 2.11, boron-modified polysilylcarbodiimide $\{B[C_2H_4\text{-}SiH_2\text{-}(NCN)_{0.5}]_3\}_n$ was obtained by a dehydrocoupling reaction of

tris(hydridosilylethyl)borane $B[(C_2H_4)SiH_3]_3$ (**7c**) with cyanamide $H_2N\text{-}C{\equiv}N$ as described in [68]. This synthetic pathway gives the opportunity to adjust the nitrogen amount, varying the molar ratio between the starting compound (**7c**) and cyanamide. This is particularly important because it is supposed that the extraordinary thermal stability of this type of ceramics strongly depends on the S:B:N ratio. In the current precursor the molar ratio starting compound (**7c**) and cyanamide is chosen 1:1.5, resulting in a Si:B:N ratio of 1:1:3.

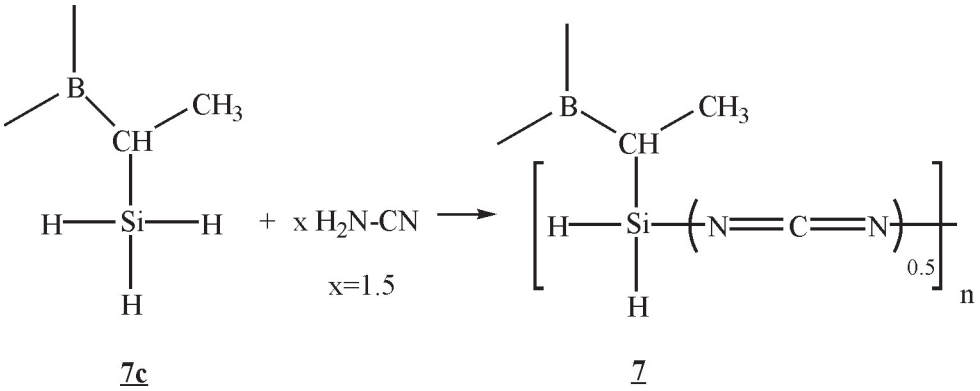

7c **7**

Figure 2.11. Synthesis of boron-modified polysilylcarbodiimide **7** from tris(hydridosilylethyl)boranes.

2.2.7 ^{15}N labeled poly(borosesquicarbodiimide) 8

^{15}N labeled poly(borosesquicarbodiimide) $[B_2(^{15}NCN)_3]_n$ was synthesized in two steps [80]. In the first step, $H_2{}^{15}NCN$ labeled cyanamide was synthesized by reaction of ^{15}N labeled ammonia ($^{15}NH_3$) with bromocyanide (BrCN) in high yield (see Figure 2.12). In the second step, ^{15}N labeled cyanamide ($H_2{}^{15}NCN$) reacts with triethylaminoborane in tetrahydofuran solution (see Figure 2.13). To avoid oxygen contamination, the as-prepared precursor polymer was directly thermolyzed at 1100 °C in an argon atmosphere without further processing steps.

$$^{15}NH_3 + BrCN \longrightarrow H_2{}^{15}NCN + {}^{15}NH_4Br$$

Figure 2.12. Synthesis of ^{15}N labeled cyanamide.

$$BH_3{*}N(C_2H_5)_3 + H_2{}^{15}NCN \longrightarrow \underline{\mathbf{8}}\ [B_2(^{15}NCN)_3]_n$$

Figure 2.13. Synthesis of ^{15}N labeled poly(borosesquicarbodiimides) **8**.

2.3 Crosslinking and ceramization

All the precursors are transformed into to the amorphous ceramics by thermolysis under inert gas atmosphere. This thermal conversion is accompanied by the formation of gaseous byproducts like H_2, NH_3 and CH_4, and therefore, mass loss occurs during the polymer-to-ceramic conversion. According to the DTA analysis, the mass loss takes mainly place in the range between 180 and 700 °C.

The ceramic yield derived from the DTA analysis of precursor systems **1** to **7** are summarized in Table 2.2. The ceramic yield depends significantly on the crosslinking of the preceramic polymer. It has been demonstrated by Aldinger and co-workers that the low weight substitute (H) at silicon is responsible for a higher degree of crosslinking. This avoids depolymerization of the precursors during thermolysis and consequently, inhibits polymer skeleton degradation and volatilization of low molecular mass species [69]. It can be seen that precursors **1** and **4**, in which proton atoms are replaced by CH_3, result in a lower ceramic yield. Particularly, in case of precursor **4**, the very poor ceramic yield (21.6 %) is due to the depolymerization and volatilization of smaller molecules. In the case of precursors **5** and **6**, the alkyl moieties causes only small loss during the heat treatments and they split off in radical reactions as alkanes or alkenes.

Table 2.2. The ceramic yield and compositions after pyrolysis at about 1400 °C.

	Derived formula	Ceramic yield	Ceramic compositions	Ref
1	$\{B[C_2H_4Si(\underline{CH_3})NH]_3\}_n$	56.0 %	$Si_3B_{1.0}C_{4.3}N_2$	[24]
2	$\{B[C_2H_4Si(\underline{H})NH]_3\}_n$	86.5 %	$Si_3B_{1.1}C_{5.3}N_3$	[69]
4	$\{B[C_3H_6Si(\underline{CH_3})NH]_3\}_n$	21.6 %	$Si_3B_{1.0}C_{5.6}N_{2.8}$	[70]
5	$\{B[C_2H_4SiH(\underline{H})C_2H_4Si(\underline{H})NH]_3\}_n$	83.0 %	$Si_6B_{1.1}C_{10.0}N_{3.4}$	[71]
6	$\{B[C_2H_4SiH(CH_3)C_2H_4Si(\underline{H})NH]_3\}_n$	82.0 %	$Si_6B_{1.2}C_{11.5}N_{3.4}$	[71]

2.4 Crystallization

After pyrolysis at high temperature, the precursor-derived amorphous materials yield thermodynamically metastable or stable crystalline phases. It is known that the quaternary Si-B-C-N ceramics obtained by the above mentioned precursors exhibit exceptional high-temperature stability as the crystallization of Si_3N_4 and SiC occurs at higher temperature as compared to the boron free ternary Si-C-N ceramics (see Table 2.3). X-ray diffraction and NMR studies reveal that Si_3N_4 and SiC crystallites form at different temperature depending on the ceramic compositions. However, the mechanisms of the amorphous into the crystalline state and the reason for high-temperature stability of amorphous state are not yet clear.

On the basis of the elemental analysis, the stable phase compositions BN, Si_3N_4,

Table 2.3. The crystallization and decomposition temperatures of Si-B-C-N ceramics derived from the boron modified polysilazanes and polysilylcarbodiimide.

Starting precursors	Crystallization Temperature [°C]	Crystalline	Decomposition temperature [°C]	Ref
1	1850	Si_3N_4/SiC (nano)	2050	[69]
2	1750	β-$Si_3N_4/\alpha, \beta$-SiC	1980	[81]
4	1800	Si_3N_4/SiC (nano)	2000	[70]
5	1550	β-Si_3N_4/α -SiC	1850	[71]
6	1550	β-$Si_3N_4/\alpha, \beta$-SiC	2000	[71]
7	1800	Si_3N_4/SiC (nano)	2000	-

SiC and graphite in the Si-B-C-N ceramics can be calculated thermodynamically using the CALPHAD (CaALulation of PHAse Diagram) approach [82, 83]. The phase fractions (below 1484 °C, 1 bar N_2) derived from CALPHAD calculations for precursor systems **2**, **4** and **5** are given in Table 2.4. At 1484 °C, Si_3N_4 should react

Table 2.4. The predicted crystalline phase fractions derived from the CALPHAD calculation.

precursor system	BN	Si_3N_4	SiC	C	Ref
2	16.0%	28.0 %	24.0 %	32.0 %	[69, 84]
4	15.8%	26.8 %	25.4 %	32.0 %	[70]
5	10.8%	19.9 %	41.3 %	28.0 %	[71]

with graphite to form silicon carbide:

$$Si_3N_4 + 3C \rightarrow 3SiC + 2N_2 \uparrow \tag{2.1}$$

Accordingly, the total mass of the composite should decrease due to the loss of gaseous nitrogen. However, according to the high-temperature TGA investigations for ceramics **1** to **7**, the thermodynamically expected decomposition reaction did not take place.

The thermally induced degradation of Si-N based ceramics is usually due to evaporation of N_2 generated by the decomposition of silicon nitride. According to the thermodynamic calculations, the decomposition of Si_3N_4 into the elements should start at around 1840 °C at 1 atm N_2 (see Eq.(2.2)).

$$Si_3N_4 \rightarrow 3Si + 2N_2 \uparrow \tag{2.2}$$

Chapter 3

Solid State NMR spectroscopy

^{29}Si, ^{13}C and ^{15}N multinuclear NMR, ^{11}B spin echo as well as double resonance experiments such as ^{11}B{^{15}N} REDOR and ^{11}B{^{14}N} REAPDOR were employed to understand the structure of the amorphous Si-B-C-N and B-C-N ceramics. The NMR properties of the nuclei investigated in the present work are summarized in Table 3.1.

Table 3.1. NMR-properties of nuclei investigated in the present work.

Stable nuclear isotopes	Nuclear spin	Natural abundance [%]	Gyromagnetic ratio [10^7rad/sT]	Quadrupole moment [$Q/10^{-30}m^2$]
^{29}Si	1/2	4.7	-5.319	-
^{13}C	1/2	1.1	6.728	-
^{15}N	1/2	0.4	-2.712	-
^{11}B	3/2	80.4	2.874	4.06
^{14}N	1	99.6	1.934	2.01

3.1 The Hamiltonian of spin interactions

NMR spectroscopy exploits the fact that nuclei with an odd number of protons, neutrons or both have an intrinsic non-zero spin angular momentum, I (nuclear spin). Both the magnitude and the orientation of the nuclear spin are quantized in the presence of an external magnetic field. The state of the nucleus i-terms of the nuclear spin wavefunction is described by the quantum numbers I and m, and is usually given by $|I, m\rangle$ in Dirac bra and ket notation. m is the magnetic quantum number ($m = -I, -I+1, , I-1, I$). The basic eigen equations for the nuclei are given by [85, 86]

$$\hat{\vec{I}}^2|I, m\rangle = I(I+1)|I, m\rangle \tag{3.1a}$$

$$\hat{I}_z|I, m\rangle = m|I, m\rangle \tag{3.1b}$$

where $\hat{\vec{I}}$ and $\hat{I}_z$ are the vector operators of the nuclear spin and its z component, respectively. The operators $\hat{I}^2$ and $\hat{I}_z$ commute, since they have identical eigenfunctions. The matrix elements of $\hat{I}_x$ and $\hat{I}_y$ are evaluated using the raising and lowering operators, which are defined as

$$\hat{I}_+ = I_x + iI_y \tag{3.2a}$$

$$\hat{I}_- = I_x - iI_y \tag{3.2b}$$

The properties of the raising ($\hat{I}_+$) and lowering ($\hat{I}_-$) operators can be written by

$$\hat{I}_+|I, m\rangle = \sqrt{I(I+1) - m(m+1)}|I, m+1\rangle \tag{3.3a}$$

$$\hat{I}_-|I, m\rangle = \sqrt{I(I+1) - m(m-1)}|I, m-1\rangle \tag{3.3b}$$

The nuclei with a spin possess a magnetic moment $\hat{\mu}$, which interacts with its surroundings. The magnetic moment is related to the spin angular momentum via

$$\hat{\mu} = \gamma\hbar\hat{I} \text{ and } |\hat{\mu}| = |\gamma|\hbar\sqrt{I(I+1)} \tag{3.4}$$

Here the *gyromagnetic ratio*, γ, is a constant specific for the nucleus under consideration. The energy operator for the spin system is called Hamiltonian $\hat{H}$. The Hamiltonian varies from system to system depending on the interactions in the spin system. In NMR different nuclear spin interactions are considered, which are grouped in external or internal contributions. Therefore, the Hamiltonian of the nuclear spin interactions can be written as [87, 88]

$$\hat{H} = \hat{H}_{ext} + \hat{H}_{int} \tag{3.5}$$

The NMR spectrometer supplies two kinds of external magnetic fields [89, 90]: a very strong static field, $\vec{\mathrm{B}}_0$, usually called the operating magnetic field (a few Tesla, in which field ^{1}H resonate at a few hundred MHz), and a much smaller pulsed oscillating radio-frequency (rf) field, $\vec{\mathrm{B}}_{rf}$. Figure 3.1 shows the external magnetic field in the laboratory (LAB) frame, (x, y, z). $\vec{\mathrm{B}}_0$ is along the z-axis, and $\vec{\mathrm{B}}_{rf}$ is perpendicular to $\vec{\mathrm{B}}_0$. $\hat{H}_{ext}$ is the sum of interactions of the nuclear spin with the external magnetic fields $\vec{\mathrm{B}}_0$ (Zeeman interaction, $\hat{H}_z$) and $\vec{\mathrm{B}}_{rf}$ ($\hat{H}_{rf}$)

$$\hat{H}_{ext} = \hat{H}_z + \hat{H}_{rf} \tag{3.6}$$

The nuclei experience magnetic and electric fields originating from the sample itself. These interactions are included in the internal spin Hamiltonian $\hat{H}_{int}$. In the solid state, three principal internal interaction mechanisms must be considered [91, 92]:

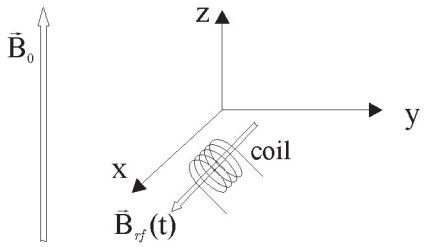

Figure 3.1. External magnetic fields in the laboratory frame (x,y,z). $\vec{B}_0$ is the applied static magnetic field along the z-axis. $\vec{B}_{rf}$ is pulsed oscillating radio-frequency field perpendicular to B_0 (in the present case it is along the x-axis). It is generated by the rf-coil.

- $\hat{H}_{CS}$, magnetic interaction of the nuclei with the surrounding electrons (*chemical shielding*)
- $\hat{H}_D$, dipolar interaction induced by the coupling with other nuclei
- $\hat{H}_Q$, interactions between the electric nuclear quadrupole moment of the I>1/2 - nuclei and the local electric field gradient surrounding these nuclei (*electric nuclear quadrupolar coupling*)

$\hat{H}_{int}$ can be written as sum of these interactions

$$\hat{H}_{int} = \hat{H}_{CS} + \hat{H}_D + \hat{H}_Q \tag{3.7}$$

The effect of these interactions on the energy level can be calculated using standard perturbation theory, i.e., they result in small perturbations of the energy levels arising from application of $\hat{H}_z$.

3.1.1 The Zeeman interaction

The interaction of the nuclear magnetic moment $\vec{\mu}$ with the static magnetic field $\vec{B}_0$ is called Zeeman interaction and is described as

$$\hat{H}_z = -\hat{\mu}\vec{B}_0 = -\gamma\hbar B_0\hat{I}_z \tag{3.8}$$

with eigenvalues

$$E_m = -\gamma\hbar m B_0 \tag{3.9}$$

The Zeeman interaction causes an energy splitting between the various nuclear spin states. In the simplest case of nuclei with I=1/2, two distinct eigenstates ($m = \pm 1/2$) exist. This interaction forces the nuclei to precess around the static magnetic field direction with the angular Larmor frequency ω_0. For an applied magnetic field, the Larmor frequency is a constant characteristic of the nucleus under consideration

$$\omega_0 = \gamma B_0 \tag{3.10}$$

The Zeeman interaction can be rewritten as

$$\hat{H}_z = -|\hbar\omega_0|\hat{I}_z \tag{3.11}$$

for positive γ. The opposite sign on the term $\hbar\omega_0$ would hold for negative γ.

When a group of spins is exposed to a magnetic field, the number of spins in the lower energy level, n_+ ($m = +1/2$), and the number in the upper energy level, n_- ($m = -1/2$), follow the Boltzmann statistics, as given by

$$\frac{n_-}{n_+} = \exp\left(\frac{-\gamma\hbar B_0}{kT}\right) \tag{3.12}$$

where k is Boltzmann constant and T is the temperature in Kelvin. Since $\gamma\hbar B_0 \ll kT$, Eq.(3.12) can be rewritten as

$$\frac{n_-}{n_+} \approx 1 - \frac{\gamma\hbar B_0}{kT} \tag{3.13}$$

The population difference between spin states is very small, since the $\frac{\gamma\hbar B_0}{kT}$ value is very low. For example, the population difference between the two states of the proton spins at 9.4 T and at room temperature is only 0.0032.

3.1.2 Interaction with the radio-frequency fields

The signal in NMR spectroscopy is proportional to the population difference between the states, as described by Eq.(3.12). In order to change the population of the spin states an radio-frequency field $\mathrm{B}_{rf}(t) = B_1 \cos(\omega t)$ is applied along the x-axis perpendicular to the static magnetic field in the laboratory frame (see Figure 3.1). The interaction of a nuclear spin with this field can be expressed by the Hamiltonian

$$\hat{H}_{rf} = -\gamma\hbar B_1 \cos(\omega t + \varphi)\hat{I}_x \tag{3.14}$$

where ω is the career frequency and φ is a phase. When the rf field oscillates close to the resonance frequency ω_0, which corresponds to the Zeeman energy splitting, transitions between the spin states will occur.

The introduction of the rf pulse complicates the motion of the spin in the magnetic field. On the one hand, the spin precesses around the B_0 field with the Larmor frequency, while on the other hand, it nutates due to the action of the rf field. The description of the spin is facilitated after introduction of the "rotating frame", which rotates with frequency ω around the z-axis of the applied static magnetic field. In this rotating frame, the rf Hamiltonian is time-independent. At the same

time, transformation into the rotating frame introduces a fictitious magnetic field $\vec{B}_f$, giving

$$\vec{B}_f = -\omega/\gamma \tag{3.15}$$

which is opposite to the direction of the static magnetic field $\vec{B}_0$. The effective Hamiltonian in the rotating frame becomes

$$\hat{H}_{eff} = -\gamma\hbar(\vec{B}_0 - \vec{B}_f)\hat{I}_z + \gamma\hbar\vec{B}_1\hat{I}_x = (\omega_0 - \omega)\hbar\hat{I}_z - \omega_1\hbar\hat{I}_x \tag{3.16}$$

where $(\omega_0 - \omega)$ is the so-called resonance offset. When $\omega_0 = \omega$, the irradiation is said to be on-resonance.

An on-resonance pulse of θ_φ ($\varphi = \pm$x, $\pm$y) with different phase φ can be obtained by adjusting the duration of the irradiation of the pulse, t_{pulse}, to satisfy the following condition

$$\theta = \gamma B_1 t_{pulse} = \omega_1 t_{pulse} \tag{3.17}$$

For instance, a 90°_x pulse applied along the x-axis in the rotating frame rotates the magnetization vector by 90° from the +z direction into the -y axis in terms of a right-handed rotation.

3.1.3 The chemical-shift interaction

The chemical shift or shielding interaction originates from the effect of B_0 on the electrons around a nucleus. When the electrons with the magnetic moments precess about the external magnetic field, additional small magnetic fields are induced. This induced magnetic field $\vec{B}_{ind}$ is directly proportional to the applied magnetic field $\vec{B}_0$ and is written by

$$\vec{B}_{ind} = \tilde{\sigma}\vec{B}_0 \tag{3.18}$$

where $\tilde{\sigma}$ is a 3×3 matrix, called the chemical shielding anisotropy (CSA) tensor [89, 93]. $\tilde{\sigma}$ is very sensitive to the chemical environment, e.g. electro-negativity, hybridization, hydrogen bonding of a given nuclei, as well as to the relative orientation of the molecule with respect to the external magnetic field. As a result, the local magnetic field $\vec{\mathrm{B}}_{loc}$, felt by each nucleus, is

$$\vec{\mathrm{B}}_{loc} = \vec{\mathrm{B}}_0 - \vec{\mathrm{B}}_{ind} = (1 - \tilde{\sigma})\vec{\mathrm{B}}_0 \tag{3.19}$$

The Hamiltonian of the chemical shielding interaction is

$$\hat{\mathrm{H}}_{CS} = -\hbar\gamma\vec{\mathrm{B}}_{ind}\hat{\vec{\mathrm{I}}} = -\hbar\gamma\vec{\mathrm{B}}_0\tilde{\sigma}\hat{\vec{\mathrm{I}}} \tag{3.20}$$

$\vec{\mathrm{B}}_{ind}$ is much smaller than $\vec{\mathrm{B}}_0$, and therefore the chemical shift Hamiltonian, $\hat{\mathrm{H}}_{CS}$, can be treated as a perturbation with respect to $\hat{\mathrm{H}}_0 = \omega_0\hat{I}_z$. Thus, if only the secular part of the Hamiltonian (i.e. part which commutes with I_z) is considered, then Eq.(3.20) in the laboratory (LAB) frame is given by [94]

$$\hat{\mathrm{H}}_{CS} = -\hbar\gamma B_0\sigma_{zz}^{LAB}\hat{I}_z = -\hbar\omega_0\sigma_{zz}^{LAB}\hat{I}_z \tag{3.21}$$

In the principal axis system (PAS), the shielding tensor, $\tilde{\sigma}$, is diagonal with principal components σ_{11}, σ_{22} and σ_{33} ($\sigma_{11} \leq \sigma_{22} \leq \sigma_{33}$). Figure 3.2 shows the relative orientation of the principal axis system of chemical shielding tensor with respect to the external magnetic field B_0. The component σ_{zz}, which is parallel to B_0, can be expressed by the tensor components in the PAS

$$\sigma_{zz} = \sigma_{11}\sin^2\phi\cos^2\theta + \sigma_{22}\sin^2\phi\cos^2\theta + \sigma_{33}\cos^2\phi \tag{3.22}$$

Here the angles ϕ and θ describe the orientation of the chemical shift tensor with respect to B_0. The trace of the shielding tensor, isotropic shielding constant, is

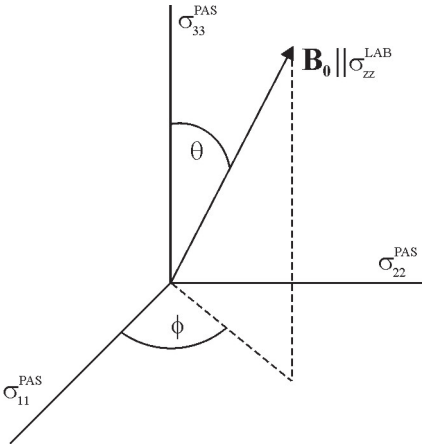

Figure 3.2. The relative orientation of principal axis system of chemical shielding tensor with respect to the external magnetic field B_0.

defined by

$$\sigma_{iso} = \tfrac{1}{3} Tr\tilde{\sigma} = \tfrac{1}{3}(\sigma_{11} + \sigma_{22} + \sigma_{33}) \tag{3.23}$$

By introducing the the asymmetry of the shielding (η_{CS}) and the chemical shift anisotropy ($\Delta\sigma$) parameters

$$\Delta\sigma = \sigma_{33} - \sigma_{iso} \tag{3.24a}$$

$$\eta_{CS} = \frac{\sigma_{22} - \sigma_{11}}{\sigma_{33} - \sigma_{iso}} \tag{3.24b}$$

Eq.(3.22) can be rearranged to give

$$\sigma_{zz} = \sigma_{iso} + \frac{1}{2}\Delta\sigma \left[\left(3\cos^2\theta - 1\right) + \eta_{CS}\sin^2\theta\cos\phi\right] \tag{3.25}$$

The chemical shift Hamiltonian and the resonance frequency are given by

$$\hat{\mathrm{H}}_{CS} = \hbar\omega_0 \left\{-\sigma_{iso} - \tfrac{1}{2}\Delta\sigma \left[(3\cos^2\theta - 1) - \eta_{CS}\sin^2\theta\cos(2\phi)\right]\right\} \hat{I}_z \tag{3.26}$$

$$\omega_{CS} = -\omega_0\sigma_{iso} - \tfrac{1}{2}\omega_0\Delta\sigma \left[\left(3\cos^2\theta - 1\right) - \eta_{CS}\sin^2\theta\cos(2\phi)\right] \tag{3.27}$$

The first term in Eq.(3.27) gives the isotropic chemical shift frequency, ω_{iso}, relative

to ω_0 and the second term describes the effect of molecular orientation on the chemical shift. For a nucleus with a spherical symmetry of the electronic charge ($\eta_{CS} = \Delta\sigma = 0$), only the isotropic shielding component remains and the spectrum consists of a narrow line. For an axially symmetric CSA tensor (η_{CS}=0), ω_{CS} is given by

$$\omega_{CS} = -\omega_0\sigma_{iso} - \tfrac{1}{2}\omega_0\Delta\sigma\left(3\cos^2\theta - 1\right) \tag{3.28}$$

The values of the shielding components are absolute values with respect to the bare nucleus. In NMR, it is common to observe signals with respect to a reference, where the difference between the sample and reference signals is called chemical shift, symbolized by δ, and expressed in units of parts of per million [ppm]

$$\delta = \frac{\omega_{sample} - \omega_{ref}}{\omega_0} 10^6 \simeq (\sigma_{ref} - \sigma_{sample}) \tag{3.29}$$

where ω_{ref} is the reference frequency.

3.1.4 Dipolar interaction

The dipolar interaction presents the magnetic interactions between nuclear magnetic moments. The classical interaction energy U between two magnetic moment vectors $\hat{\vec{\mu}}_1$ and $\hat{\vec{\mu}}_2$ is [94]

$$U = \frac{\mu_0}{4\pi}\left[\frac{\hat{\vec{\mu}}_1\hat{\vec{\mu}}_2}{r^3} - \frac{3(\hat{\vec{\mu}}_1\cdot\vec{r})(\hat{\vec{\mu}}_2\cdot\vec{r})}{r^5}\right] \tag{3.30}$$

where $\vec{r}$ is the vector between $\vec{\mu}_1$ and $\vec{\mu}_2$. The dipolar Hamiltonian of two coupled spins I_1 and I_2 can be derived by substitution of $\hat{\vec{\mu}}_1 = \gamma_1\hbar\hat{I}_1$ and $\hat{\vec{\mu}}_2 = \gamma_2\hbar\hat{\vec{I}}_2$.

$$\hat{H}_D = \frac{\mu_0}{4\pi}\frac{\gamma_1\gamma_2\hbar^2}{r^3}\left[\hat{\vec{I}}_1\cdot\hat{\vec{I}}_2 - \frac{3(\hat{\vec{I}}_1\cdot\vec{r})(\hat{\vec{I}}_2\cdot\vec{r})}{r^2}\right] \tag{3.31}$$

where

$$\hat{\vec{I}} \cdot \vec{r} = \hat{I}_x x + \hat{I}_y y + \hat{I}_z z \tag{3.32a}$$

$$x = r\sin\theta\cos\phi,\ y = r\sin\theta\sin\phi,\ z = r\cos\theta \tag{3.32b}$$

By using the raising and lowering operators $\hat{I}_+$ and $\hat{I}_-$, given in Eq.(3.2), and transforming the Cartesian coordinates (x, y, z) to the corresponding spherical coordinates (r, θ, ϕ) (see Figure 3.3), the dipolar Hamiltonian can be written in terms of a convenient "dipolar alphabet" as [85]

$$\hat{H}_D = -\frac{\mu_0}{4\pi}\frac{\gamma_1\gamma_2\hbar^2}{r^3}\left[A + B + C + D + E + F\right] \tag{3.33}$$

where the terms A-F are given by

$$\begin{aligned} A &= \hat{I}_{1z}\hat{I}_{2z}(3\cos^2\theta - 1) \\ B &= -\tfrac{1}{4}(\hat{I}_{1+}\hat{I}_{2-} + \hat{I}_{1-}\hat{I}_{2+})(3\cos^2\theta - 1) \\ C &= \tfrac{3}{2}(\hat{I}_{1z}\hat{I}_{2+} + \hat{I}_{1+}\hat{I}_{2z})\sin\theta\cos\theta\exp(-i\phi) = D^* \\ E &= \tfrac{3}{4}\hat{I}_{1+}\hat{I}_{2+}\sin^2\theta\exp(-2i\phi) = F^* \end{aligned} \tag{3.34}$$

Only terms A and B commute with I_z and are independent of time. The

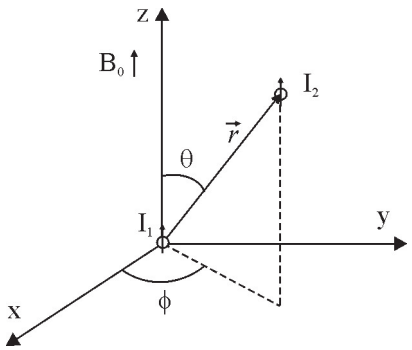

Figure 3.3. Internuclear vector $\vec{r}$ in laboratory frame (x, y, z).

Hamiltonian due to the first-order perturbations A and B is called the secular part

of the dipolar Hamiltonian, $\hat{H}_{D,sec}$, and is given by

$$\hat{H}_{D,sec} = -\frac{\mu_0}{4\pi}\frac{\gamma_1\gamma_2\hbar^2}{r^3}\left[\hat{I}_{1z}\hat{I}_{2z} - \frac{1}{4}(\hat{I}_{1+}\hat{I}_{2-} + \hat{I}_{1-}\hat{I}_{2+})\right](3\cos^2\theta - 1) \tag{3.35}$$

Using $\hat{I}_{1+}\hat{I}_{2-} + \hat{I}_{1-}\hat{I}_{2+} = 2\hat{I}_1 \cdot \hat{I}_2 - 2\hat{I}_{1z}\hat{I}_{2z}$, Eq.(3.35) can be rewritten as

$$\hat{H}_{D,sec} = -\frac{D}{2}\hbar\left[3\hat{I}_{1z}\hat{I}_{1z} - \hat{I}_1\hat{I}_2\right](3\cos^2\theta - 1) \tag{3.36}$$

where D denotes the dipolar coupling constant (in unit of rad/s), given by

$$D = \frac{\mu_0}{4\pi}\frac{\gamma_1\gamma_2\hbar}{r^3} \tag{3.37}$$

It is important to distinguish between homonuclear and heteronuclear dipolar couplings. The spin part in term B is called flip-flop operator. It causes transitions between different spin states of two coupled spins. The secular dipolar Hamiltonian for like-spins I_i and I_j (homonuclear coupling, $\gamma_i = \gamma_j = \gamma_I$ and $D_{ij} = \frac{\mu_0}{4\pi}\frac{\gamma_I^2\hbar}{r_{ij}^3}$) becomes

$$\hat{H}_{D,homo} = -\frac{D_{ij}}{2}\hbar\left[3\hat{I}_{iz}\hat{I}_{jz} - \hat{I}_i\hat{I}_j\right](3\cos^2\theta_{ij} - 1) \tag{3.38}$$

In case of dipolar interaction between unlike spins I and S due to different Larmor frequencies (heteronuclear coupling, $\gamma_I \neq \gamma_S$ and $D_{IS} = \frac{\mu_0}{4\pi}\frac{\gamma_I\gamma_S\hbar}{r_{IS}^3}$), the spin flip-flop process is no longer energy-conserving. Hence, the term B also acts as second-order perturbation, and the first-order secular part is only determined by the term A

$$\hat{H}_{D,hetero} = -D_{IS}\hbar\hat{I}_z\hat{S}_z(3\cos^2\theta_{IS} - 1) \tag{3.39}$$

Both the homonuclear and heteronuclear dipolar couplings are independent of the static magnetic field strength B_0, and depend on the orientation of the internuclear vector and the inverse cube of the distance. The term $(3\cos^2\theta - 1)$ describes the

anisotropy of the dipolar interaction. The dipolar frequencies are given by

$$\omega_{D,homo} = \pm\frac{3}{4}D_{ij}(3\cos^2\theta_{ij} - 1) \tag{3.40}$$

$$\omega_{D,hetero} = \pm\frac{1}{2}D_{IS}(3\cos^2\theta_{IS} - 1) \tag{3.41}$$

Dipolar coupling leads to a line broadening of the NMR spectrum. Figure 3.4 shows homonuclear and heteronuclear dipolar powder pattern for two isolated spin pairs with the same dipolar coupling constant ($D_{ij} = D_{IS}$). The dipolar

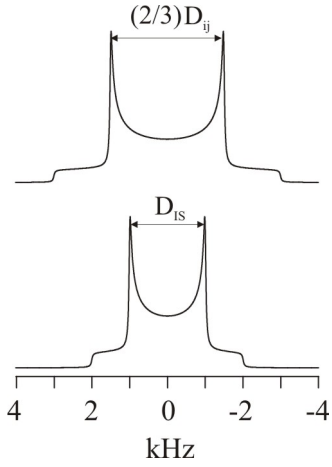

Figure 3.4. Pake powder pattern for homonuclear (top) and heteronuclear (bottom) two isolated spin pairs with the dipolar coupling constant of $D_{ij} = D_{IS} = 2$ kHz.

interaction is very important in NMR, since by measuring the magnitude of the dipolar interaction between the nuclei, the distance between these nuclei can be determined. However, in solids the dipolar interaction often acts between many abundant spins, which produces overlapping powder patterns and broad featureless lines. However, structural information can be obtained by the calculation of the second moment of the dipolar interactions. Homonuclear dipolar interactions are essentially eliminated if the nucleus of interest is "dilute" in the system being studied. The homo and heteronuclear dipolar couplings can be experimentally observed for abundant nuclei. In the present work, the ^{11}B-^{11}B homonuclear dipolar coupling is measured by the spin echo pulse sequence, while the ^{11}B - ^{15}N and ^{11}B - ^{14}N heteronuclear dipolar couplings are measured by REDOR/SEDOR and REAPDOR

techniques, respectively. However, the natural abundance of the ^{15}N nucleus is very small, the REDOR and SEDOR experiments are performed, therefore, on ^{15}N isotopic enriched samples.

3.1.5 The quadrupolar interaction

Nuclei with spin $I > 1/2$ possess a nuclear quadrupole moment, Q, because the nuclear charge distribution is non-spherical (see Figure 3.5). If the shape of the charge distribution, $\rho(\vec{r})$, is that of a prolate spheroid, Q is positive; if it is oblate, Q becomes negative. Q is constant for a given nuclei and does not change with the chemical environment of the nucleus. For example, for ^{11}B ($I = 3/2$) and ^{14}N ($I = 1$) nuclei, Q equals to $4.06{\cdot}10^{-30}$ and $2.04{\cdot}10^{-30}$ m^2, respectively. The energy

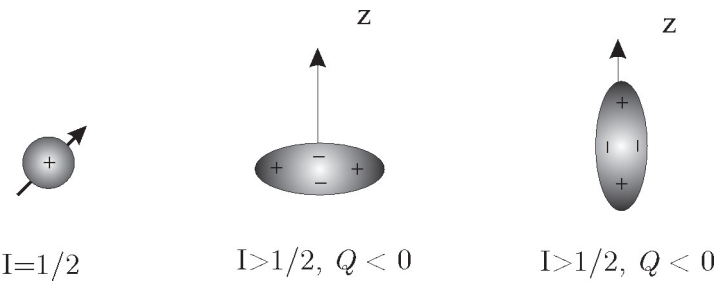

Figure 3.5. The shape of the nuclear charge distribution. z is the nuclear spin axis.

of the charge distribution in an electrostatic potential $V(r)$ is

$$E = \int \rho(\vec{r}) V(\vec{r}) d^3r \tag{3.42}$$

The electrostatic potential can be expanded as a Taylor series

$$V(\vec{r}) = V(0) + \sum_{\alpha=1}^{3} x_\alpha \left.\frac{\partial V}{\partial x_\alpha}\right|_{r=0} + \frac{1}{2!} \sum_{\alpha,\beta=1}^{3} x_\alpha x_\beta \left.\frac{\partial^2 V}{\partial x_\alpha \partial x_\beta}\right|_{r=0} + \cdots \tag{3.43}$$

where x_α ($\alpha = 1, 2, 3$) stands for x, y, z. Defining

$$V_\alpha = \left.\frac{\partial V}{\partial x_\alpha}\right|_{r=0}, V_{\alpha\beta} = \left.\frac{\partial^2 V}{\partial x_\alpha \partial x_\beta}\right|_{r=0} \tag{3.44}$$

Eq.(3.42) is rewritten as

$$E = V(0)\int \rho(\vec{r})d^3r + \sum_{\alpha=1}^{3} V_\alpha \int x_\alpha \rho(\vec{r})d^3r + \frac{1}{2!}\sum_{\alpha,\beta=1}^{3} V_{\alpha\beta}\int x_\alpha x_\beta \rho(\vec{r})d^3r + \cdots \tag{3.45}$$

The integrals in the first and second terms are identified as the overall charge distribution and the components of the electric dipole moment of the charge distribution, respectively. The third term is the electrical quadrupole term. The quadrupole moment can be described as a deviation from spherical symmetry

$$Q_{\alpha\beta} = \int (3x_\alpha x_\beta - \delta_{\alpha\beta} r^2)\rho(\vec{r})d^3r \tag{3.46}$$

Using this equation, the quadrupole energy E_Q in Eq.(3.45) in terms of $Q_{\alpha\beta}$ can be rewritten by

$$E_Q = \frac{1}{6}\sum_{\alpha,\beta=1}^{3}\left[V_{\alpha\beta}Q_{\alpha\beta} + V_{\alpha\beta}\delta_{\alpha\beta}\int r^2\rho(\vec{r})d^3r\right] \tag{3.47}$$

where $V_{\alpha\beta}$ is the electric field gradient (EFG). The electric field gradient tensor is symmetric, i.e. $V_{xy} = V_{yx}$ and traceless, i.e. $V_{xx} + V_{yy} + V_{zz}$=0 (the Laplace equation). Therefore, the second part in Eq.(3.47) does not contribute to the sum, leaving

$$E_Q = \frac{1}{6}\sum_{\alpha,\beta=1}^{3} Q_{\alpha\beta}V_{\alpha\beta} \tag{3.48}$$

Accordingly, the quadrupolar coupling Hamiltonian is

$$\hat{H}_Q = \frac{1}{6}\sum_{\alpha,\beta=1}^{3} \hat{Q}_{\alpha\beta}V_{\alpha\beta} \tag{3.49}$$

where $\hat{Q}_{\alpha\beta}$ is a quantum-mechanical operator with

$$\hat{Q}_{\alpha\beta} = e\sum_{k}(3x_{\alpha k}x_{\beta k} - \delta_{\alpha\beta}r_k^2) \tag{3.50}$$

Here, the sum is taken over k protons, since the neutrons in the nucleus are uncharged. By substituting the special component in Eq.(3.50) by the spin operators using the Wigner-Eckart theorem, the quadrupolar Hamiltonian in Cartesian coordinate frame can be written by [89, 93]

$$\hat{H}_Q = \frac{eQ}{6I(2I-1)}\sum_{\alpha,\beta=1}^{3} V_{\alpha\beta}\left[\tfrac{3}{2}(\hat{I}_\alpha\hat{I}_\beta + \hat{I}_\beta\hat{I}_\alpha) - \delta_{\alpha\beta}\hat{I}^2\right] \tag{3.51}$$

where α, β refer to the frame of reference of the spin operators.

In the principal axis system (PAS), only the diagonal elements ($|V_{xx}| \geq |V_{yy}| \geq |V_{zz}| = eq$) are nonzero. The quadrupole coupling constant, C_{qcc}, and the asymmetry parameter, η_Q, are defined from the principal values

$$C_{qcc} = \frac{eQV_{zz}}{h} = \frac{e^2qQ}{h} \tag{3.52a}$$

$$\eta_Q = \frac{V_{xx} - V_{yy}}{V_{zz}} \ (0 \leq \eta_Q \geq 1) \tag{3.52b}$$

C_{qcc} measures the strength of the quadrupolar interaction, while η_Q measures the departure of the EFG from axial symmetry. In quite the same way, the quadrupolar frequency ν_Q (in Hz) or ω_Q (in rad/s) is defined by

$$\nu_Q = \frac{\omega_Q}{2\pi} = \frac{3e^2qQ}{2I(2I-1)h} = \frac{3C_{qcc}}{2I(2I-1)} \tag{3.53}$$

A higher spin quantum number is therefore accompanied by a lower quadrupolar frequency, i.e. for spin $I = 1$, $I = 3/2$ and $I = 5/2$ nuclei ν_Q is $1/2C_{qcc}$, $2/3C_{qcc}$ and $3/20C_{qcc}$, respectively.

In the PAS, the Cartesian tensor representation of the quadrupolar Hamiltonian (Eq.3.51) takes form

$$\hat{H}_Q^{PAS} = \frac{eQ}{4I(2I-1)\hbar}\left[V_{zz}(3\hat{I}_z^2 - \hat{I}^2) + (V_{xx} - V_{yy})(\hat{I}_x^2 - \hat{I}_y^2)\right] = \tag{3.54a}$$

$$= \frac{\omega_Q}{6}\left[3\hat{I}_z^2 - \hat{I}^2 + \eta_Q(I_x^2 - I_y^2)\right] \tag{3.54b}$$

Since the raising and lowering spin operators provide appropriate selection rules, the Hamiltonian in terms of $\hat{I}_-$, $\hat{I}_+$ and $\hat{I}_z$ can be rewritten as

$$\hat{H}_Q^{PAS} = \frac{\omega_Q}{6}\left[3\hat{I}_z^2 - \hat{I}^2 + \tfrac{1}{2}\eta_Q(I_+^2 - I_-^2)\right] \tag{3.55}$$

The transformation from the PAS to the LAB frame (Zeeman coordinate system) is more conveniently realized, if the quadrupolar interaction is expressed as scalar product of two irreducible tensors of second-rank, the spherical tensor operator (T_q, spin term) and the electric field gradient tensor (V_q) [95–97]

$$\hat{H}_Q = \frac{eQ}{2I(2I-1)\hbar}\sum_{q=-2}^{+2}(-1)^q T_q V_q \tag{3.56}$$

V_q are written in terms of V_q^{PAS} using the Wigner rotation matrix elements $D_{n,q}^{(2)}$ [98]

$$V_q = \sum_{n=-2}^{2} D_{n,q}^{(2)}(\phi,\theta,\psi)V_q^{PAS} \tag{3.57}$$

were ϕ, θ and ψ are the Euler angles defining the orientation of the principal axis system of the EFG tensor in the laboratory frame. V_q^{PAS} and T_q can be related to the Cartesian components to the following equations [99]

$$\mathrm{V}_0^{PAS} = \sqrt{\tfrac{3}{2}}eq = \sqrt{\tfrac{3}{2}}V_{zz} \quad \mathrm{V}_{\pm1}^{PAS} = 0 \quad \mathrm{V}_{\pm2}^{PAS} = \tfrac{1}{2}eq\eta_Q \tag{3.58}$$

$$\mathrm{T}_0 = \sqrt{\tfrac{1}{6}}(3\hat{I}_z^2 - \hat{I}^2) \quad \mathrm{T}_{\pm 1} = -\tfrac{1}{2}\hat{I}_{\pm}(2I_z \pm 1) \quad \mathrm{T}_{\pm 2} = \tfrac{1}{2}\hat{I}_{\pm}^2 \tag{3.59}$$

The spherical tensor representation of the quadrupolar interaction in the LAB frame becomes [98]

$$\hat{H}_Q = \frac{eQ}{4I(2I-1)\hbar}\left[\sqrt{\tfrac{1}{6}}(3\hat{I}_z^2 - \hat{I}^2)V_0 - \tfrac{1}{2}\{\hat{I}_-(2\hat{I}_z - 1)V_1 + \hat{I}_+(\hat{I}_z + 1)V_{-1} + \hat{I}_-^2 V_{+2} + \hat{I}_+^2 V_{-2}\}\right] \tag{3.60}$$

In the high field limit, where $H_Q \ll H_z$, the terms of Hamiltonian which commute with I_z lead to perturbations of first-order, $H_Q^{(1)}$, and second-order, $H_Q^{(2)}$, [96, 98]

$$\hat{H}_Q^{(1)} = \frac{eQ}{4I(2I-1)\hbar}\sqrt{\tfrac{1}{6}}(3\hat{I}_z^2 - \hat{I}^2)V_0 \tag{3.61}$$

$$\hat{H}_Q^{(2)} = -\frac{1}{\omega_0}\left(\frac{eQ}{4I(2I-1)\hbar}\right)^2\left[(4\hat{I}^2 - 8\hat{I}_z^2 - 1)V_{-1}V_1 + (2\hat{I}^2 - 2\hat{I}_z^2 - 1)V_{-2}V_2\right]\hat{I}_z \tag{3.62}$$

with the tensor elements V_q given by Eq.(3.63) in footnote [1]. The first-order term, $\hat{H}_Q^{(1)}$, is independent of ω_0 and is an even function of $\hat{I}_z$. In contrast, the second-order integration $\hat{H}_Q^{(2)}$ is inverse proportional to ω_0 and is an odd function of $\hat{I}_z$. The first-order quadrupolar Hamiltonian and perturbation energy $E_m^{(1)}$ are given by

$$\hat{H}_Q^{(1)} = \frac{\omega_Q^{(1)}}{2}\left[3\hat{I}_z^2 - \hat{I}^2\right] \tag{3.64}$$

$$E_m^{(1)} = \omega_Q^{(1)}\left[3m^2 - I(I+1)\right] \tag{3.65}$$

[1]

$$\begin{aligned}
V_0 =& \sqrt{\tfrac{3}{2}}eq\left[\tfrac{1}{2}(3\cos^2\theta - 1) + \tfrac{1}{2}\eta_Q\sin^2\theta\cos 2\phi\right] \\
2V_1V_{-1} =& -\tfrac{3}{2}e^2q^2\left[(-\tfrac{1}{3}\eta_Q^2\cos^2 2\phi + 2\eta_Q\cos 2\phi - 3)\cos^4\theta\right. \\
&\left. + (\tfrac{2}{3}\eta_Q^2\cos 2\phi^2 - 2\eta_Q\cos 2\phi - \tfrac{1}{3}\eta_Q^2 + 3)\cos^2\theta + \tfrac{1}{3}\eta_Q^2(1 - \cos^2 2\phi)\right] \\
V_2V_{-2} =& \tfrac{3}{2}e^2q^2\left[(\tfrac{1}{24}\eta_Q^2\cos 2\phi^2 - \tfrac{1}{4}\eta_Q\cos 2\phi + \tfrac{3}{8})\cos^4\theta\right. \\
&\left. + (-\tfrac{1}{12}\eta_Q^2\cos 2\phi^2 + \tfrac{1}{6}\eta_Q^2 - \tfrac{3}{4})\cos^2\theta + \tfrac{1}{24}\eta_Q^2\cos 2\phi^2 + \tfrac{1}{4}\eta_Q\cos 2\phi + \tfrac{3}{8}\right]
\end{aligned} \tag{3.63}$$

with

$$\omega_Q^{(1)} = \omega_Q \tfrac{1}{2} \left\{ (3\cos^2\theta - 1) + \eta_Q \sin^2\theta \cos 2\phi \right\} \tag{3.66}$$

The frequency shift of the $m-1 \rightarrow m$ transition with respect to the Larmor frequency ω_0 is

$$\omega_{m-1,m}^{(1)} = \omega_Q^{(1)}(1-2m) \tag{3.67}$$

The magnitude of the first-order quadrupolar splitting $\omega_Q^{(1)}$ is proportional to C_{qcc} and independent on the applied magnetic field. Figure 3.6 shows the energy level diagrams for spin half integer ($I = 3/2$) and integer ($I = 1$) nuclei, respectively. For an $I = 3/2$ spin system, the first-order quadrupole splitting produces two satellite transitions (ST) $\pm 1/2 \leftrightarrow \pm 3/2$, which are shifted by the $\pm 2\omega_Q^{(1)}$. The central transition (CT) $-1/2 \leftrightarrow 1/2$ is not affected in first-order. For an $I = 1$ nuclei the single-quantum transitions $-1 \rightarrow 0$ and $0 \rightarrow 1$ are shifted by $\omega_Q^{(1)}$ and $-\omega_Q^{(1)}$ due to first-order quadrupolar splitting, respectively.

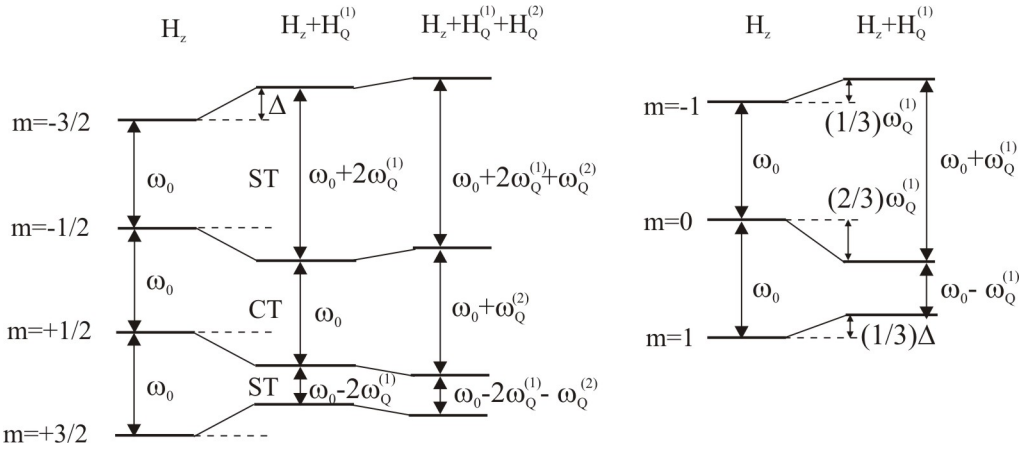

Figure 3.6. Energy levels diagrams for spins $I = 3/2$ (left) and $I = 1$ (right).

The second-order frequency for the $m-1 \rightarrow m$ transition with respect to ω_0 can be

also obtained by means of Eq.(3.62) and is given by

$$\omega_Q^{(2)} = \omega_{m-1,m}^{(2)} = -\frac{2}{\omega_0}\left(\frac{eQ}{4I(2I-1)\hbar}\right)^2 \times$$
$$\times \left[(24m(m-1) - 4I(I+1) + 9)V_{-1}V_1 + \tfrac{1}{2}(12m(m-1) - 4I(I+1) + 6)V_{-2}V_2\right] \tag{3.68}$$

The second-order quadrupolar shift is much smaller than the first-order quadrupolar shift, as it is inverse proportional to the Larmor frequency ω_0. In other words, the magnitude of the quadrupolar splitting decreases with increasing external magnetic field B_0. The second-order quadrupolar shift of the central transition, using Eq.(3.68) and (3.63), can be written as [97]

$$\omega_{-1/2,1/2}^{(2)} = -\frac{\omega_Q^2}{6\omega_0}\left[I(I+1) - \tfrac{3}{4}\right](A\cos^4\theta - B\cos^2\theta + C) \tag{3.69}$$

$$A = -\tfrac{27}{8} - \tfrac{9}{4}\eta_Q\cos 2\phi - \tfrac{3}{8}(\eta_Q\cos 2\phi)^2$$
$$B = +\tfrac{30}{8} - \tfrac{1}{2}\eta_Q^2 + 2\eta_Q\cos 2\phi - \tfrac{3}{4}(\eta_Q\cos 2\phi)^2$$
$$C = -\tfrac{3}{8} + \tfrac{1}{3}\eta_Q^2 - \tfrac{1}{4}\eta_Q\cos 2\phi - \tfrac{3}{8}(\eta_Q\cos 2\phi)^2$$

When the EFG has axial symmetry ($\eta_Q = 0$), Eq.(3.69) becomes simply

$$\omega_{-1/2,1/2}^{(2)} = -\frac{\omega_Q^2}{16\omega_0}\left[I(I+1) - \tfrac{3}{4}\right](1-\cos^2\theta)(9\cos^2\theta - 1) \tag{3.70}$$

The quadrupolar parameters can be measured by simulation of the lineshape. Figure 3.7 shows simulated first and second-order quadrupolar powder pattern for ^{11}B and ^{14}N nuclei with various asymmetry parameters η_Q. The first-order powder pattern is observable only for small quadrupole coupling constant, C_{qcc}, up to a few hundred kHz. The first order lineshape is symmetric. From Eq.(3.66) it can be easily seen that, the value of the first-order quadrupolar splitting of the symmetric transitions for ^{11}B nuclei is twice that for ^{14}N nuclei, although the same quadrupolar frequency

(4.35 kHz) was used for simulations.

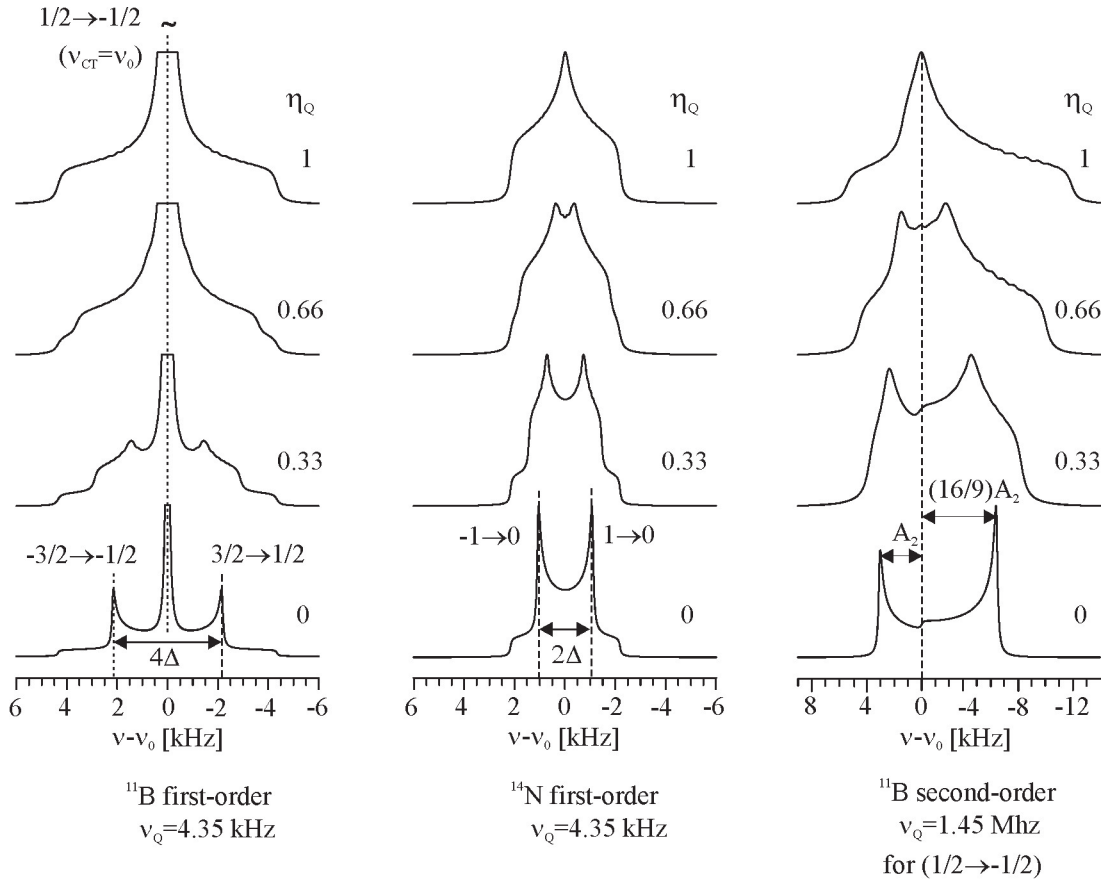

Figure 3.7. Simulated first and second-order quadrupolar powder pattern for ^{11}B ($I = 3/2$) and ^{14}N ($I = 1$) nuclei with different asymmetry parameters η_Q.

For larger C_{qcc} values, the satellite transitions are spread over a large frequency range and are usually not observable. When C_{qcc} is in the order of a few MHz, a second-order lineshape of the central transition can be observed, and the centre of gravity is shifted with respect to the isotropic chemical shift value. In case of an axially symmetric EFG, the two singularities are shifted by A_2 and $(16/9)A_2$ from the ν_0. For $I = 3/2$ spin system A_2 is $9\nu_Q^2/48\nu_0$.

3.2 Magic angle spinning

Magic angle spinning (MAS) is probably the most widely used technique to enhance spectral resolution in solid-state NMR. If the solid sample, loaded into a cylindrical container (called the rotor), spins rapidly about its symmetry axis (spinning axis), which is inclined at a fixed angle θ_m to the applied magnetic field (see Figure 3.8), the average of the second-order Legendre polynomial in the spin Hamiltonian becomes

$$\left\langle (3\cos^2\theta - 1) \right\rangle = \tfrac{1}{2}(3\cos^2\theta_m - 1)(3\cos^2\beta - 1) \tag{3.71}$$

where θ is the angle between the applied magnetic field and the principal z-axis of the spin interaction tensor, and β is the angle between the principal z-axis of the spin interaction tensor and the spinning axis. If θ_m is set to 54.7° (called magic angle), then $(3\cos^2\theta_m - 1) = 0$.

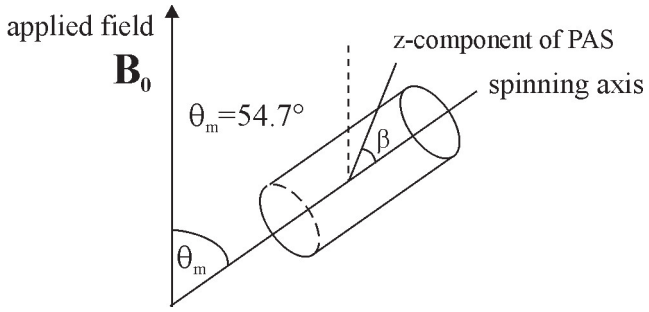

Figure 3.8. Magic angle spinning in the LAB frame. The sample is spun in a cylindrical rotor about a spinning axis ($\theta_m = 54.7°$) with respect to the applied magnetic field $\mathbf{B}_0$.

If a NMR signal is broadened by inhomogeneous interactions, such as the heteronuclear dipolar interaction, chemical shift anisotropy and first-order quadrupolar interactions, which contain a $(3\cos^2\theta_m - 1)$ term, MAS leads to a MAS NMR signal consisting of a narrow central line at center of gravity, ω_{iso}, of the signal and spinning sidebands spaced at intervals of the spinning frequency ω_r,

at frequency [90]

$$\omega_k = \omega_{iso} \pm k\omega_r \tag{3.72}$$

where $k = 1, 2,...n$ denotes the order of spinning sidebands.

Under sample spinning the chemical shift Hamiltonian becomes time dependent and is expressed by

$$\hat{H}_{CS}(t) = \hbar\omega_0\hat{I}_z\sigma_{iso} + \frac{1}{2}(\sigma_{zz} - \sigma_{iso})(3\cos^2\theta_m - 1)(3\cos^2\beta - 1)\hbar\omega_0\hat{I}_z + \xi(t)\hbar\omega_0\hat{I}_z \tag{3.73}$$

with

$$\xi(t) = C_1\cos(\omega_r t) + S_1\sin(\omega_r t) + C_2\cos(2\omega_1 t) + S_2\sin(\omega_r t)$$

where C_1, C_2, S_1 and S_2 are functions of the Euler angles involved in the coordinate transformation. The first term (isotropic part) in Eq.(3.73) is invariant under sample rotation. The second term reflects the averaged anisotropy of the chemical shift tensor which depends on the angle between spinner axis and external magnetic field B_0. When $\theta_m = 54.7°$, the second term is zero and the shift anisotropy is removed from the MAS spectrum. If the angle θ_m deviates from the magic angle, a scaled anisotropy is observed. The last term in Eq.(3.73) gives rise to spinning sidebands.

Under MAS, the time dependent dipolar Hamiltonian is given by

$$\hat{H}_{D,sec}(t) = -\frac{1}{2}D(3\hat{I}_{1z}\hat{I}_{2z} - \hat{I}_1\hat{I}_2)\left[G_0 + G_1\cos(\omega_r t + \phi) + G_1\cos(2\omega_r t + 2\phi)\right] \tag{3.74}$$

with

$$G_0 = \tfrac{1}{2}(3cos^2\beta - 1)(3\cos^2\theta_m - 1)$$
$$G_1 = \tfrac{3}{4}\sin 2\theta_m \sin 2\theta$$
$$G_2 = -\tfrac{3}{4}\sin^2\theta_m \sin^2\theta$$

As the first term G_0 is averaged out to zero under MAS, the dipolar frequency is modulated by the spinning frequency. The time dependent Hamiltonian of first-order

quadrupolar interaction can be expressed in the same way as the dipolar interaction. Unlike the first-order interactions, the second-order term is not a second-rank tensor, and is not averaged to zero by fast spinning and only reduces in width by factor of about 3.6. Therefore, the resolution of the spectra of quadrupole nuclei is usually limited by the second-order quadrupolar line-broadening effect. The resolution can be improved by increasing the external magnetic field B_0. If ω_r is large compared to the static linewidth (fast spinning limit), the first-order correction terms of the anisotropic interactions, such as chemical shift anisotropy, dipolar and quadrupolar interactions are completely averaged out.

Under MAS, the PAS of quadrupolar spin has to first transformed into the rotor frame with the Wigner matrix $D(\phi, \beta, \gamma)$ [100]. The angles (ϕ, β, γ) describe the location of the rotor axis in the PAS of the EFG. Only then the transformation into the LAB frame is performed using $D(\omega_r t, \theta, 0)$. Thus Eq.(3.62) describes the MAS average Hamiltonian for quadrupolar nucleus with a new definition of the term V_q, which is given by [101, 102]

$$V_q = \sum_{m=-2}^{2} D^{(2)}_{m,q}(\omega_r t, \theta_m, 0) \sum_{n=-2}^{2} D^{(2)}_{n,q}(\phi, \theta, \gamma) V_q^{PAS} \tag{3.75}$$

Hence, in the fast spinning limit, the spatial part of the second-order quadrupolar Hamiltonian becomes a sum of Legendre polynomials with ranks 0, 2 and 4 (the terms with ranks 1 and 3 vanishes due to symmetry) [103]

$$\langle \omega_Q^{(2)} \rangle_{rot} = A_0 P_0(\cos\beta) + A_2 P_2(\cos\beta) + A_4 P_4(\cos\beta) \tag{3.76}$$

$$\begin{aligned} P_0(\cos\theta) &= 1 \\ P_2(\cos\theta) &= (3\cos^2\theta - 1) \\ P_4(\cos\theta) &= (35\cos^4\theta - 30\cos^2\theta + 3) \end{aligned}$$

where A_2 and A_4 are function of ω_Q, ω_0, η_Q and relative orientation of quadrupolar

tensor and rotor axis. β is the angle between the rotor axis and the static magnetic field B_0. A_0 is the second-order quadrupolar shift, ω_{Qiso}, and is given by

$$A_0 = \omega^{(2)}_{Qiso} = -\frac{\omega^{(2)}_Q}{30\omega_0}(1 + \tfrac{1}{3}\eta_Q^2)\left[I(I+1) - \frac{3}{4}\right] \tag{3.77}$$

The shift in units of ppm, $\delta^{(2)}_{Qiso}$, can be calculated by $\delta^{(2)}_{Qiso} = 10^6 \times \omega^{(2)}_{Qiso}/\omega_0$. The observed chemical shift (the centre of gravity, δ_{CG}) of the NMR signal of quadrupole nuclei is shifted from the isotropic chemical shift value, δ_{CS}, and is given by [104]

$$\delta_{CG} = \delta_{CS} + \delta^{(2)}_{Qiso} \tag{3.78}$$

The position of the signal (center of gravity) is the same as in the static experiment. Figure 3.9 shows calculated static and MAS spectra for the central transition of a spin-3/2 nucleus. The quadrupolar shift coupled with the orientation-dependent line broadening of the central transition can make it difficult to determine the true chemical shift accurately.

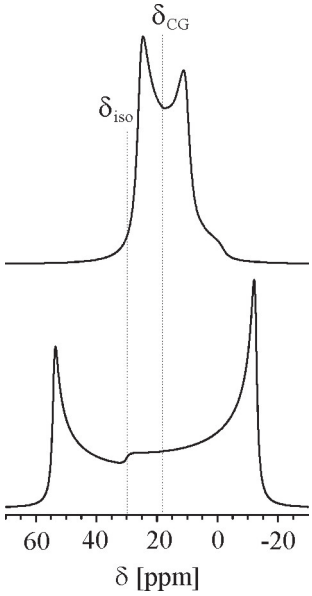

Figure 3.9. Simulated static (bottom) and MAS (top) ^{11}B NMR spectra for the central transition. (Isotropic chemical shift σ_{iso} = 30 ppm, quadrupolar coupling constant C_{qcc}=2.9 MHz, and asymmetry parameter $\eta_Q = 0$.)

3.3 NMR experiments

3.3.1 Single pulse and cross-polarization NMR

^{13}C, ^{29}Si, ^{15}N, ^{14}N and ^{11}B NMR spectra are obtained by single pulse (SP) experiments, as shown in Figure 3.10 (left). A single radio frequency pulse with amplitude B_1, applied on the I-spins, turns the magnetization from its equilibrium position, around B_1 by an angle θ, which is defined by Eq.(3.17). After the direct excitation of the nuclear magnetization, the free induction decay (FID) of the nuclear magnetization can be observed. The excited magnetization relaxes back to equilibrium. There are two characteristic relaxation times: longitudinal or spin-lattice relaxation time T_1 and transverse or spin-spin relaxation time T_2. T_1 characterizes the relaxation of magnetization parallel to $\vec{B}_0$, while the T_2 characterizes the relaxation in the plane perpendicular to the $\vec{B}_0$ [105].

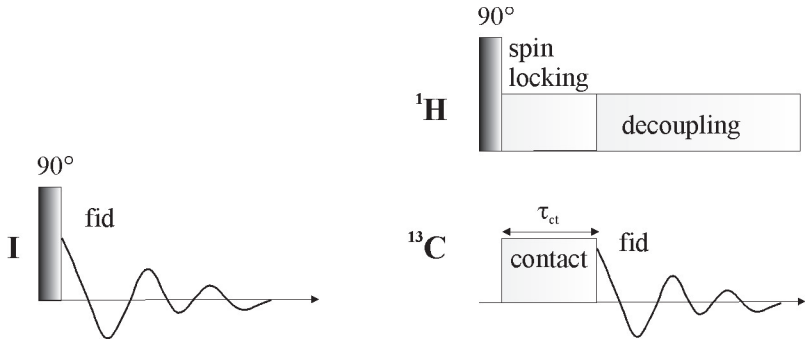

Figure 3.10. Pulse sequences for single pulse (left) and cross-polarization (right) NMR experiments.

For I=1/2 nuclei, a maximum signal can be obtained by using a 90° pulse, which turns the magnetization of the I- spins into the x-y plane. The delay between the experiments depends on T_1. For quantitative work, the pulse delay should be at least five times T_1. As the flip angle decreases, less time is required to establish equilibrium along the B_0 axis. The optimum flip angle for the fixed pulse delay, τ_d is called the *Ernst angle*, $\alpha_e = exp(-\frac{\tau_d}{T_1})$ [106]. For instance, the delay should be T_1

with a pulse angle of 68°.

In case of nuclei with a low natural abundance, a low gyromagnetic ratio or long T_1, the single pulse experiment can be time consuming. In this case, cross-polarization (CP) [107–109] can be employed to enhance the sensitivity of the observed nuclei. This technique relies on the polarization transfer from ^{1}H or other abundance nuclei to the observed nuclei. Figure 3.10 (right) shows the pulse sequence of the CP experiment. After the rotation of the proton magnetization by a 90° pulse, spin locking pulses are applied on the ^{1}H and ^{13}C spins. The radio frequency spin lock fields $B_{1(^1H)}$ and $B_{1(^{13}C)}$ are adjusted experimentally in order to match the "Hartmann-Hahn condition" [110]

$$\gamma_{^1H} B_{1(^1H)} = \omega_{1(^1H)} = \omega_{1(^{13}C)} = \gamma_{^{13}C} B_{1(^{13}C)} \tag{3.79}$$

where $\omega_{1(^1H)}$ and $\omega_{1(^{13}C)}$ are the precession frequencies of ^{1}H and ^{13}C, respectively. Now, the ^{1}H and the ^{13}C spins precess with the same frequency, both spin reservoirs are coupled through internuclear dipole-dipole interactions. Therefore, during the contact pulses polarization transfer can take place, which leads to a sensitivity enhancement by a factor of about $\gamma_{^1H}/\gamma_{^{13}C}$=4. After the magnetization of the observed nucleus has been built up, the FID can be detected in the presence of ^{1}H decoupling. ^{1}H decoupling is used to remove the dipole-dipole interaction between ^{1}H and ^{13}C. Another advantage of using CP is that the relevant relaxation time T_1 of the proton is usually much shorter than that of the ^{13}C nuclei thus allowing for a shorter recycle delay between the scans.

The obtained ^{13}C CP NMR spectra provide only qualitative results, since the efficiency of cross polarization depends on the dipolar coupling between ^{13}C and ^{1}H, which is inverse proportional to r^3_{C-H}. It means that the signal enhancement for the protonated carbon is more efficient than that for non-protonated carbon atoms.

3.3.1.1 ^{13}C, ^{29}Si and ^{15}N NMR spectra

^{13}C, ^{29}Si, ^{15}N nuclei have a spin I=1/2 and the spin Hamiltonian terms are therefore the same. The spin Hamiltonian terms consist of contributions from chemical shift anisotropy, homo and heteronuclear dipolar interactions. However, under MAS (combined with high-power proton decoupling, if necessary) the first-order anisotropic contributions of the chemical shift and dipolar interaction (see Chapter 3), which are scaled by the factor $3cos^2\theta - 1$, can be eliminated. As an example, in Figure 3.11 the influence of the spinning rate on the ^{13}C NMR spectra of Si-B-C-N ceramics pyrolized at 1050 and 1400 °C is shown. For spectra obtained using a spinning rate of 5 kHz, there are spinning sidebands from sp^2-carbon signal due to residual chemical shift anisotropy. Increasing the spinning rate, the chemical shift anisotropy is completely averaged out to enhance the intensity of the central band.

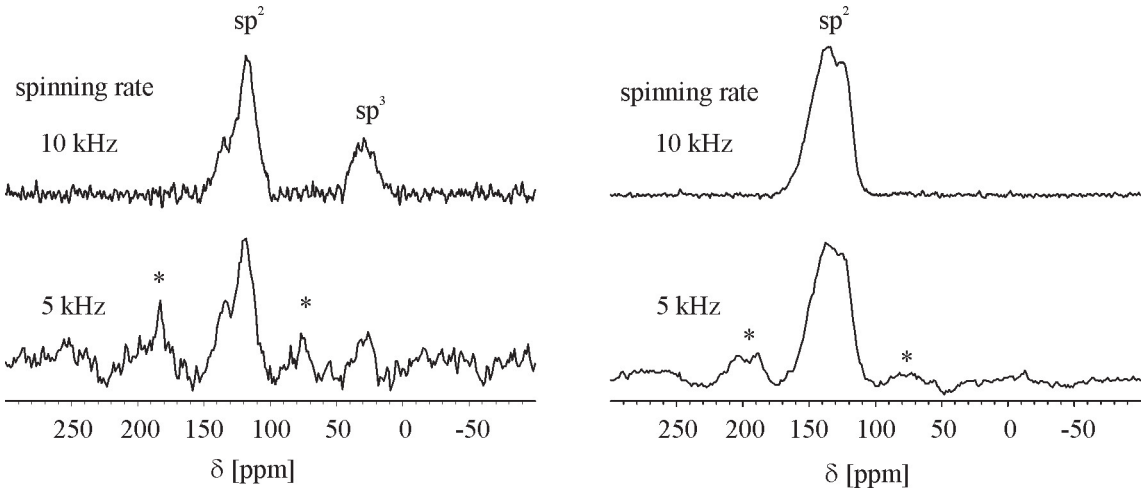

Figure 3.11. The influence of the spinning rate on the ^{13}C NMR spectra of Si-B-C-N ceramics pyrolized at 1050 (left) and 1400 °C (right).

3.3.1.2 ^{11}B NMR spectra

In general, the ^{11}B nucleus possess high sensitivity, as its natural abundance is 80 %. However, the ^{11}B nucleus has a spin I=3/2, thus the spin Hamiltonian term

contains first and second-order quadrupolar interactions. The quadrupolar coupling constant, C_{qcc} of the tri-coordinated ^{11}B nuclei is usually larger (a few MHz) than for tetra-coordinated ^{11}B sites. For instance, in case of hexagonal (h-BN) and cubic (c-BN) boron nitride, the quadrupolar coupling constant C_{qcc} are 2.9 MHz and nearly zero, respectively. However, in case of quadrupolar interactions larger than the radio frequency ($\omega_{rf} \ll \omega_Q$), the $1/2 \rightarrow -1/2$ central transitions, which is affected only by the second-order quadrupolar contribution, can be observed selectively [111, 112].

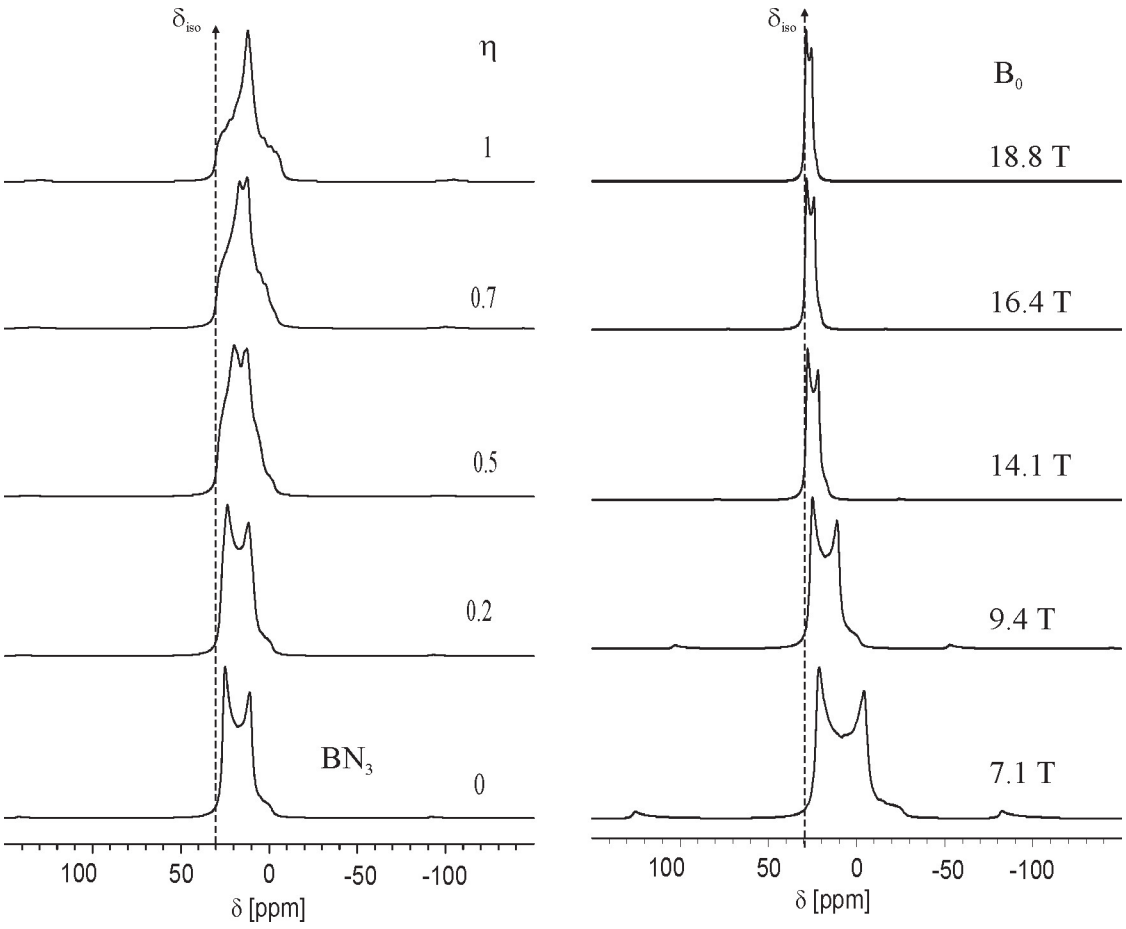

Figure 3.12. Simulated ^{11}B MAS spectra for second-order quadrupolar line broadening (ν_r=15 kHz, C_{qcc}=2.9 MHz and δ_{iso}=30 ppm). Effect of the asymmetry parameter, η (B_0=9.4 T) (left). Effect of operating magnetic field strength, B_0 ($\eta_Q = 0$, h-BN) (right).

Figure 3.12 (left) shows that the residual anisotropic lineshapes of the ^{11}B MAS spectra depend on the asymmetry parameter η_Q ($0 < \eta_Q < 1$). In case of the

h-BN (η_Q=0), the ^{11}B lineshape shows two main singularities. The strength of the second-order quadrupolar line broadening depends not only on C_{qcc}, but also on the external static magnetic field strength (see Eq.(3.83)). Figure 3.12 (right) shows the second-order quadrupolar broadening of the h-BN line as a function of the operating magnetic field strength B_0. It should be noted that as B_0 decreases, the ^{11}B NMR spectrum not only increases in linewidth, but also shifts with respect to the isotropic value (δ_{iso}=30 ppm) due to second-order quadrupolar shift.

The boron chemical shift ranges from 100 to -10 ppm for tri-coordinated boron atoms and from 0 to -130 ppm for tetra-coordinated boron [113]. The isotropic chemical shifts for the tri- and tetra-coordinated boron sites in B-C-N units are summarized in Table 3.2. The chemical shift difference between BC_xN_{x-3} (x=0, 1, 2) sites is 5-10 ppm. Therefore, in case of low operating magnetic fields these boron sites usually suffer from a lack of resolution. It should be noted that in the present work all ^{11}B NMR spectra were recorded at an operating magnetic field of 9.4 T (400 MHz proton resonance frequency), in which tri and tetra-coordinated boron sites can be distinguished. In case of h-BN the quadrupolar coupling constant of ^{11}B is large (2.9 MHz). Therefore, it is difficult to excite the satellite transitions experimentally.

Table 3.2. ^{11}B isotropic chemical shift value for tri- and four-coordinated boron sites.

^{11}B sites	δ_{iso} **[ppm]**
BC_3	85-65
BC_2N	40-50
BCN_2	30-35
BHN_2	31
BN_3	25-30
BN_4	0
$BNC_3(sp^3)$	-10

3.3.1.3 ^{14}N NMR spectra

There are two NMR effective nitrogen isotopes: ^{14}N ($I = 1$) and ^{15}N ($I = 1/2$) with abundances of 99.63 % and 0.37 %, respectively. Both have rather low gyromagnetic ratios (γ), and so rather low NMR sensitivity. ^{14}N has quadrupolar coupling constants from hundreds kHz to a few MHz. Therefore, both the first-order quadrupolar interaction and low resonance frequency makes the observation of ^{14}N extremely difficult.

C_{qcc} of ^{14}N for h-BN is about 144 kHz. In this case, ^{14}N MAS NMR spectrum of the h-BN, shown in section 5.1, is dominated by the first-order quadrupolar interaction, which is partially averaged out by MAS, resulting in spinning sidebands.

3.3.2 ^{11}B spin echo

The homonuclear second moment, $M_{2(homo)}$, characterizing the homonuclear dipole-dipole coupling among ^{11}B spins, can be measured by the spin echo pulse sequence [114, 115] ($90° - \tau - 180° - \tau$) illustrated in Figure 3.13. Following an initial 90° preparation pulse, the transverse magnetization decays during the first half of the evolution period (τ) due to the combined effect of dipolar interactions and chemical shift dispersion. However, the application of a 180° pulse after τ reverses the part of the decay due to the chemical shift and heteronuclear dipole-dipole couplings contributions, resulting in a spin echo signal at the time 2τ, ($I(2\tau)$). Thus, the intensity of the spin echo is attenuated only by the homonuclear dipolar coupling during the dipolar evolution time 2τ.

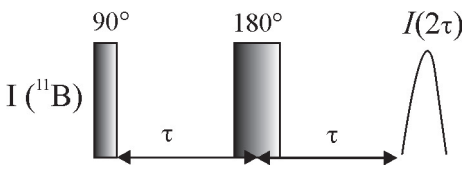

Figure 3.13. Spin echo pulse sequence.

Experimentally, for short evolution periods and multispin couplings, the normalized echo intensity, $I(2\tau)/I_0$, can be described by a Gaussian function

$$\frac{I(2\tau)}{I_0} = exp\left[-(2\tau)^2 \frac{M_{2(homo)}}{2}\right] \tag{3.80}$$

where $M_{2(homo)}$ is the second moment of the spin echo decay arising from homonuclear dipole-dipole coupling and 2τ is the evolution period of the spin echo pulse sequence.

Serious complication arises, however, if the spins are subject to strong nuclear electric quadrupolar interactions, which alter the echo amplitudes. In such cases, it is still possible to extract dipole-dipole coupling information from echo decay spectroscopy, if the 180° pulse is applied selectively to the central transition ($|1/2\rangle \leftrightarrow |-1/2\rangle$) [116–119]. In case of spin-3/2 nuclei the homonuclear second moment associated with a selective excited central transition can be approximately calculated by [116, 120]

$$M_{2(homo)} = 0.9562 \left(\frac{\mu_0}{4\pi}\right)^2 \gamma^4 \hbar^2 \sum_j \left(\frac{1}{r_{ij}^6}\right) \tag{3.81}$$

where r_{ij} are the internuclear distances, and the other symbols denote universal constants. Eq.(3.81) is fulfilled under the following approximations: (a) the quadrupolar satellite transitions are shifted far off-resonance, (b) the resonance frequency differences of most of the interacting spin pairs are smaller than the strength of the dipolar couplings, and (c) heteronuclear dipolar couplings are negligible on the time scale of the experiment. These conditions are satisfied if the analysis is restricted to the initial segment ($0 < 2\tau < 200$ μs) of the spin echo decay curve [121, 122]. In addition, if $M_{2(hetero)}$ is larger than $M_{2(homo)}$, the heteronuclear coupling causes a drastic decrease of the spin echo decay curves.

3.3.3 ^{11}B{^{15}N} and ^{11}B{^{14}N} double resonance NMR

3.3.3.1 ^{11}B{^{15}N} SEDOR

According to the van Vleck theory [123], the contribution to the heteronuclear second moment $M_{2(hetero)}$, for a nucleus (I) dipolarly coupled to surrounding heteronuclei (S), can be calculated directly from internuclear distance distributions [124, 125]

$$M_{2(hetero)} = \frac{4}{15}\left(\frac{\mu_0}{4\pi}\right)^2 \hbar^2\gamma_I^2\gamma_S^2 S(S+1)N_I^{-1}\sum_S \frac{1}{r_{IS}^6} \tag{3.82}$$

where γ is gyromagnetic ratio and S is 1/2 for ^{15}N.

$M_{2(hetero)}$ can be measured by the spin echo double resonance (SEDOR) experiment [126–131], which is carried out under static conditions. Therefore, the heteronuclear dipolar frequency ω_D is given by

$$\omega_D(\theta) = \pm\pi D(3\cos^2\theta - 1) \tag{3.83}$$

where θ is the angle between the internuclear vector and the external magnetic field, and D is the dipolar coupling constant, which defines the internuclear distance r_{IS} between the coupled I and S spins

$$D = \frac{\mu_0}{4\pi}\frac{\hbar\gamma_i\gamma_S}{r_{IS}^3} \tag{3.84}$$

The pulse sequence of the SEDOR experiment is shown in Figure 3.14. The Hahn echo ($90^\circ - \tau - 180^\circ - \tau$) sequence applied to the I-spins refocuses the heteronuclear dipole coupling and the chemical shift anisotropy producing an echo at 2τ. The full echo amplitude, $S_0(2\tau)$, is

$$S_0(2\tau) = S_i e^{-2\tau/T_2} \tag{3.85}$$

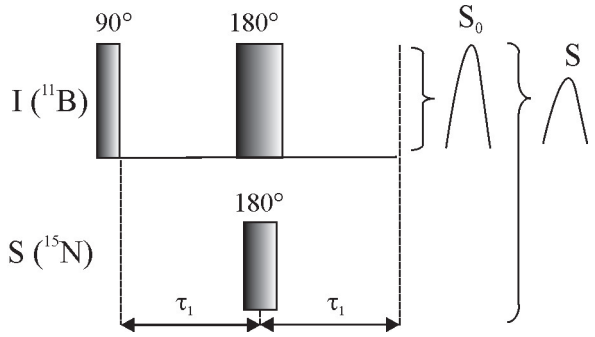

Figure 3.14. SEDOR pulse sequence.

where T_2 is the spin-spin relaxation time and S_i is the I-spin signal intensity following the 90° pulse. However, if a 180° pulse is applied to the S-spin system, it will invert the sign of any I-S dipole coupling. Consequently, I-S dipolar coupling does not refocus and the spin echo amplitude is attenuated, which gives a reduced echo signal, $S(2\tau)$

$$S(2\tau) = S_i e^{-2\tau/T_2} \cos(\Phi) \tag{3.86}$$

where $\Phi = 2\tau\omega_D$ is the phase angle during an evolution time τ. By taking the ratio of the two signal amplitudes $S_0(2\tau)$ and $S(2\tau)$, T_2 can be eliminated

$$S(2\tau)/S_0(2\tau) = \cos(2\tau\omega_D) \tag{3.87}$$

Thus, the ratio is independent of relaxation effects and chemical shift anisotropy, and only depends on the I-S dipolar interactions, which can be measured as function of the revolution time. For a multi-spin system, the normalized decay $S(2\tau)/S_0(2\tau)$ of the spin echo amplitude is typically observed to be Gaussian, and $M_{2(hetero)}$ can be calculated according to the simple expression [132]

$$S(2\tau)/S_0(2\tau) = e^{-(2\tau)^2 \frac{M_{2(hetero)}}{2}} \tag{3.88}$$

However, since the SEDOR technique is carried out under static conditions (without

MAS), the SEDOR measurements only yield average values for the internuclear distance if the sample contains two or more different types of I-S-spin pairs with different internuclear distances, r_{IS}. Combinations of the heteronuclear spin echo technique with application of MAS are referred to as REDOR, TEDOR and REAPDOR techniques.

3.3.3.2 ^{11}B{^{15}N} REDOR

The Rotational Echo Double Resonance (REDOR) method has proven to be very useful for the accurate measurement of internuclear distances between unlike nuclei. REDOR reintroduces the heteronuclear dipolar interaction between two nuclear species S and I under MAS [127, 133, 134]. The dipolar transition frequency in MAS NMR experiments is given by

$$\omega_D = \pm\frac{1}{2}D\left\{\sin^2\beta\cos 2(\phi+\omega_r t) - \sqrt{2}\sin 2\beta\cos(\phi+\omega_r t)\right\} \tag{3.89}$$

where D is the dipolar coupling constant given by Eq.(3.84), ω_r is the sample spinning rate, and ϕ and β are the azimuthal and polar angles of the internuclear vector with respect to spinning axis.

Figure 3.15 shows the REDOR pulse sequence. The REDOR experiment consists of two parts: the first experiment, a rotor - synchronized spin echo (90° - τ - 180° - τ) on resonance I-spin, serves as "*reference*" experiment. τ is a multiple of the rotor period T_r. In this experiment, the average value of ω_D over each rotor cycle is zero. The intensity of full echo signal $S_0(\tau)$ is given by Eq.(3.85).

In the second part, a term of 180° pulses is applied to the S-spin, which is coupled to the I-spin, for every half rotor period. The S-spin 180° pulse inverts the precession direction of the magnetization of the observed I nucleus. Therefore, the average

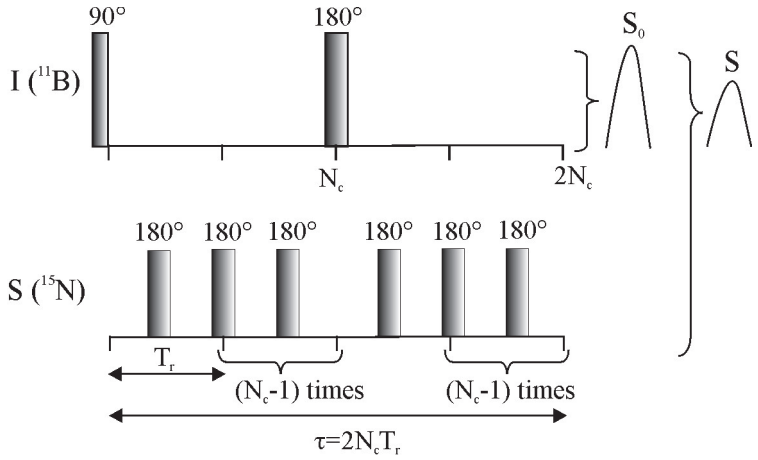

Figure 3.15. REDOR pulse sequence. T_r is the rotor period and N_c is the rotor cycle.

heteronuclear dipolar frequency over one rotor period is not zero and is given by

$$\overline{\omega_D} = \pm\frac{1}{T_r}\left[\int_0^{T_r/2}\omega_D dt - \int_{T_r/2}^{T_r}\omega_D dt\right] = \pm\frac{D}{\pi}\sqrt{2}\sin 2\beta\sin\phi \tag{3.90}$$

where D is the dipolar coupling constant given in Eq.(3.84). The negative sign in front of the second term in Eq.(3.90) arises from the 180° pulse of the S-spin. Therefore, the phase angle Φ, for the $2N_c$ rotor cycle can be given by

$$\Phi = \overline{\omega_D} 2N_c T_r = \frac{2N_c T_r D}{\pi}\sqrt{2}\sin 2\beta\sin\phi \tag{3.91}$$

where T_r is the rotor period. The reduced REDOR signal is

$$S = S_i e^{-2\tau}\cos(\Phi) = S_i e^{-2N_c T_r/T_2}\cos(\Phi) \tag{3.92}$$

and the ratio of the reduced and full signal is

$$S/S_0(\tau) = \cos(\Phi) \tag{3.93}$$

For a powder sample, the normalized echo amplitude can be obtained by averaging

over each orientation, as given by

$$\Delta S/S_0 = 1 - S/S_0 = 1 - \frac{1}{2\pi}\int_{\phi}\int_{\beta}\cos(\Phi)\sin\beta d\phi d\beta \tag{3.94}$$

where $\sin\beta$ is the geometrical weighting factor. This relation depends not only on the I-S dipolar coupling but also on k, the number of the S_k-spins coupled to the I-spin and the angle S_1-I_1-S_2. Experimental $\Delta S/S_0$ fractions as function of the evolution time τ can be simulated to derive the dipolar coupling constant. The internuclear distance between coupled spins I and S can be calculated by Eq.(3.83). Figure 3.16 shows the simulated $^{11}B\{^{15}N\}$ REDOR decay curves for BN, BN_2 and BN_3 spin systems.

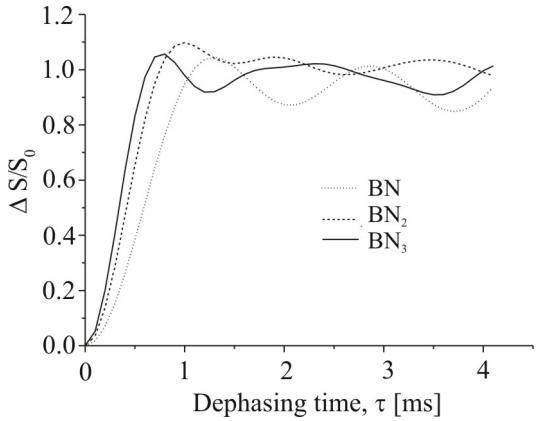

Figure 3.16. $^{11}B\{^{15}N\}$ REDOR simulated curve for BN, BN_2 and BN_3 spin system. B-N distance is 1.44 Å. N-B-N angle is 120°.

For short evolution times, the geometry dependence of the dephasing curve is negligible, and the REDOR dephasing curves can be approximated by a simple analytical equation [135, 136]

$$\frac{\Delta S}{S_0} = \frac{1}{3\pi^2 S(S+1)}(2N_c T_r)^2 M_{2(hetero)} \tag{3.95}$$

3.3.3.3 $^{11}B\{^{14}N\}$ REAPDOR

The rotational echo adiabatic passage double resonance (REAPDOR) experiment is designed to recover the heteronuclear dipolar coupling between spin-1/2 and quadrupolar nuclei [137–141]. The $^{11}B\{^{14}N\}$ REAPDOR pulse sequence is shown in Figure 3.17. Like the REDOR technique, the REAPDOR relies on two experiments, i.e. one experiment to measure the full spectrum (S_0) and a second one to get the reduced spectrum (S).

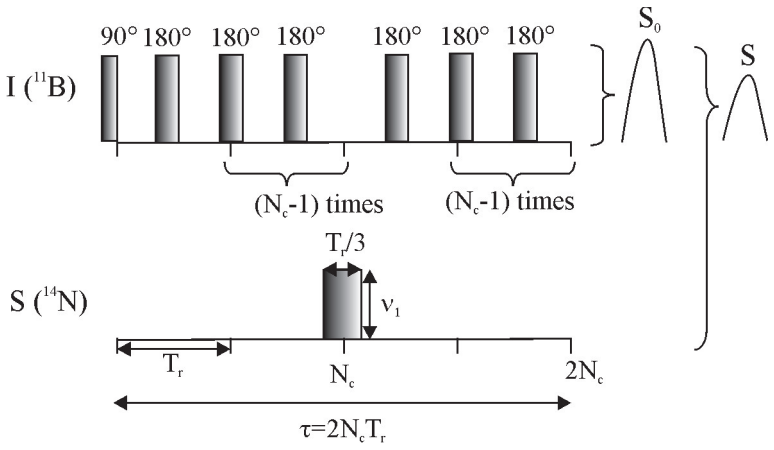

Figure 3.17. $^{11}B\{^{14}N\}$ REAPDOR pulse sequence.

In both experiments, 180° pulses are applied to the observed nuclei (^{11}B) every half rotor period, except at the midpoint of the experiment. In this way, the chemical shift anisotropy is refocused at the beginning of data acquisition. This 180° pulse train causes dipolar dephasing of the ^{11}B spins coupled to ^{14}N spins. This occurs during the first half of the evolution period. In the first experiment, the average dipolar dephasing of the two half of the dipolar evolution period are opposite in sign, and the dipolar interaction is refocused. This produces the full signal (S_0), which accounts for the T_2 decay.

In the second experiment, the dipolar dephasing between ^{11}B and ^{14}N can be reintroduced by a single radio-frequency pulse. This should be done on the quadrupolar nuclei (^{14}N) in the middle of the dipolar evolution period. This results

in a reduced signal, (S). However, the quadrupolar interaction for ^{14}N nuclei is usually so large that simple short radio frequency pulses, such as 180° pulses causes only a small fraction of quadrupolar spins to change state. Effective irradiation of the ^{14}N nuclei can only occur if an adiabatic-passage pulse is used. Under MAS, the quadrupolar splitting ($Q_{(t)}$), is time dependent and changes its sign two or four times per rotor period, depending on the orientation of the quadrupolar tensor with respect to the rotor. When $Q_{(t)}$ passes through zero, there is a short period during which the states are mixed. If $Q_{(t)}$ passes slowly through the zero crossings, the passage is said to be adiabatic. This results into a change of the spin states. The adiabatic condition is satisfied when [142]

$$\alpha = \nu_1^2/\nu_Q\nu_R > 1, \tag{3.96}$$

where ν_1, ν_R and ν_Q are the nutation frequency, the rotor and quadrupolar frequency, respectively. If the passage is fast, the system will be unaffected by the zero crossings and spin states remain unchanged.

Gullion and coworkers have numerically calculated the fraction of spins, which make zero crossings during the adiabatic-passage pulse, in a powder sample. Their studies have shown that for very short ^{14}N radio frequency irradiation times, only the fraction of spins making single zero crossings is significant. The fraction of double, triple and quadruple zero crossings increases only at longer irradiation times. The fraction of spins making a single zero crossings during the adiabatic-passage reaches the maximum of 0.7 at one third of rotor period ($T_r/3$) [143]. This alters the dipolar dephasing of ^{11}B spins in the first and second half evolution periods, resulting into dephased signal, S. In the specific case of ^{11}B$\{^{14}$N$\}$ REAPDOR experiments performed on Si-B-C-N ceramics, we used radio frequency field of ν_1=70 kHz and a rotor speed of ν_r=10 kHz. Therefore, under the condition of ν_Q<490 kHz there

is still adiabacity as α<1. For h-BN, the ^{14}N quadrupolar frequency is reported to 210 kHz.

The normalized difference signals between the two experiments, i.e. $(S_0\text{-}S)/S_0$, recorded as function of an evolution period gives the REAPDOR curve, from which the heteronuclear dipolar interactions can be determined. In case of two isolated spins, the universal REAPDOR dipolar dephasing curves can be obtained. The universal curve depends only on the dipolar coupling constant D, and can be fitted by a simple equation, given by [144]

$$\Delta S/S = 0.61 - exp[-(1.47D\tau)^2] \tag{3.97}$$

However, in our case, as we have a multispin system, the analysis of the REAPDOR curve, unlike the REDOR curve, depends not only on the dipolar interaction, but also on the quadrupolar coupling constant of dephasing ^{14}N nuclei as well as the relative orientation of the dipolar and quadrupolar tensors. Therefore, simulations of the REAPDOR curves were performed taking into account the aforementioned magnetic parameters. Simulation curves were done using the NMR simulation package SIMPSON [145] with a BN_3 spin system (using h-BN as model compound). The SIMPSON input file used for the REAPDOR simulation of h-BN is given in the appendix. The N-B-N angle is 120°. The dipolar coupling constant between ^{11}B and ^{14}N is 930 kHz, which corresponds to a r_{BN} of 1.44 $\mathring{A}$ and quadrupolar frequency of ^{14}N is 144 kHz. The experimental parameters used for the simulations were the following: rotor period of 10 kHz, and the radio frequency of ^{11}B and ^{14}N are 192 and 70 kHz, respectively. The effect of the relative orientation of the dipolar and quadrupolar tensors are given in Figure 3.18.

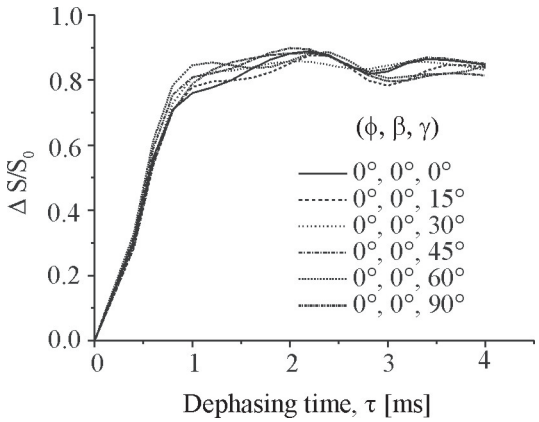

Figure 3.18. ^{11}B{^{14}N} REAPDOR simulation for BN_3 system: D=930 Hz (r_{BN} = 1.44 Å), η=0.

Chapter 4

Experimental section

All solid state ^{13}C, ^{29}Si and ^{15}N NMR spectra were recorded at room temperature under MAS conditions.

4.1 Single pulse and cross-polarization NMR measurements

In the present work, ^{13}C, ^{29}Si, ^{15}N single pulse (SP) and ^{13}C cross-polarization (CP) MAS NMR experiments were carried out in order to characterize Si-B-C-N and B-C-N ceramic materials. $^{13}C\{^{1}H\}$ cross-polarization NMR experiment were performed on samples pyrolized up to 600 or 1050 °C. At higher pyrolysis temperatures, the proton amount is too low to perform CP NMR experiments. ^{13}C, ^{29}Si and ^{15}N nuclei are stable isotopes with natural abundance of 1.1, 4.7 and 0.4 %, respectively. The experimental NMR signal to noise ratio depends on the natural abundance of the observed nuclei. Although the natural abundance of ^{13}C and ^{29}Si nuclei is very low, NMR spectra can be still observed without isotopic enrichment. Conversely, the natural abundance of ^{15}N is too low and the NMR spectra can be

observed only for ^{15}N isotopic enriched samples. Therefore, ^{15}N NMR spectra were acquired only for ceramics **1**, **2**, **5** and **7**, **8**, which are 99 % and 50 % ^{15}N isotopic enriched, respectively.

^{13}C NMR experiments were performed on a Bruker CXP 300 spectrometer operating at a static magnetic field of 7 T using a Bruker MAS probe. The resonance frequency is 79 MHz. All ^{13}C MAS NMR experiments were done at a sample spinning rate of 10 kHz applying either single pulse or cross-polarization excitation. For single pulse MAS NMR experiments, the 90° pulse width was 4 μs and recycle delay was 15 s. For cross-polarization MAS NMR experiments, the 90° pulse width was 4 μs, contact time was 5 ms and recycle delays of 5 s. ^{13}C chemical shifts were determined relative to the external standard adamantane (δ=58.36 ppm)

^{29}Si and ^{15}N single pulse MAS NMR experiments were performed on a Varian InfinityPlus 400 spectrometer operating at a static magnetic field of 9.4 T using 4 mm triple resonance HXY probe. The resonance frequencies for ^{29}Si and ^{15}N nuclei were 79.41 and 40.5 MHz, respectively. The ^{29}Si MAS NMR spectra were recorded under MAS condition (sample rotation frequency: 5 kHz) by direct excitation applying 45° pulses of 2.3 μs in width, and recycle delays of 45 s. Chemical shift were determined relative to the external standard Q_8M_8, the trimethylsilylester of octametric silicate (δ=11 ppm).

^{15}N MAS NMR spectra were recorded under MAS conditions (sample rotation frequency: 10 kHz) by direct excitation, applying 90° pulses of 3.5 μs, and recycle delays of 15 s. ^{15}N chemical shifts were referenced to external standard glycine (100% ^{15}N-enriched)(δ=-345 ppm).

The solid state ^{11}B NMR experiments were performed at room temperature on a Varian InfinityPlus 400 spectrometer operating at a static magnetic field of 9.4 MHz using 4 mm triple resonance HXY probe. The resonance frequency was 128.26 MHz.

^{11}B NMR spectra were recorded by direct excitation applying 90° pulse of 1.1 μs, and recycle delays between 2 and 64 s. Chemical shift were determined relative to the external standard $B(OH)_3$ (δ=18.3 ppm). In case of the ^{11}B MAS NMR spectra, sample rotation frequency was 10 kHz.

The solid state ^{14}N MAS NMR experiments were performed at room temperature on a Varian InfinityPlus 400 spectrometer, at frequency of 28 MHz using a Varian 4 mm triple resonance MAS probe with the low gamma box. Solid samples were spun at 10 kHz, using 4 mm ZrO_2 rotors. The ^{29}Si MAS NMR spectra were recorded with a single pulse of 90° (3.5 μs) and a recycle delay between the experiments of 300 s.

4.2 ^{11}B spin echo experiments

^{11}B spin echo experiments were performed at room temperature on a Varian InfinityPlus-400 spectrometer operating at a static magnetic field of 9.4 T using 4 mm triple resonance HXY probe. The ^{11}B{^{15}N} SEDOR spectra were recorded under a static conditions with the same pulse width and recycle delays as for the REDOR experiments. During the ^{11}B NMR the number of scans varied between 64 and 256 depending on the actual signal to noise ratio of the samples.

4.3 ^{11}B{^{15}N} SEDOR measurements

^{11}B{^{15}N} SEDOR experiments were performed at room temperature on a Varian InfinityPlus 400 spectrometer operating at a static magnetic field of 9.4 T using 4 mm triple resonance HXY probe. The ^{11}B{^{15}N} SEDOR spectra were recorded under static conditions with the same pulse width and recycle delays as for REDOR

experiments. The number of scans varied between 64 and 256 depending on the actual signal-to-noise ratio of the samples.

4.4 ^{11}B{^{15}N} REDOR measurements

^{11}B{^{15}N} REDOR experiments were performed at room temperature on a Varian InfinityPlus-400 spectrometer operating at a static magnetic field of 9.4 MHz using 4 mm triple resonance HXY probe. ^{11}B{^{15}N} REDOR spectra were recorded with sample spinning frequency of 10 kHz, recycle delays between 2 and 64 s depending on the ^{11}B spin-lattice relaxation time. ^{11}B 90° and 180° pulse widths were 1 and 1.95 μs, respectively, while the ^{15}N dephasing 180° pulse width was 7 μs.

4.5 ^{11}B{^{14}N} REAPDOR measurements

^{11}B{^{14}N} REAPDOR experiments were performed at room temperature on a Varian InfinityPlus-400 spectrometer operating at a static magnetic field of 9.4 MHz using 4 mm triple resonance HXY probe. To reach the ^{14}N resonance frequency, the low gamma box was used. ^{11}B{^{15}N} REAPDOR spectra were recorded with sample spinning frequency of 10 kHz recycle delays between 2 and 64 s depending on the ^{11}B spin-lattice relaxation time. ^{11}B pulse widths were the same as for the REDOR experiments, while the ^{14}N adiabatic pulse was 33.33 μs.

4.6 Simulation of REDOR curves

Numerical simulations were done with laboratory written MATLAB routines and SIMPSON program package [145], employing the direct method in conjunction with the REPULSION set of 100 angle [146], to test whether the ^{11}B-^{11}B dipolar

couplings influence the $^{11}B\{^{15}N\}$ REDOR signals. They showed that the effect of the homonuclear couplings on the dephasing of ^{11}B-nucleus is negligible in our experiments. The final REDOR curves were therefore done with a home written MATLAB routine which uses purely heteronuclear ^{11}B-^{15}N couplings, based on the equations described in Ref. [147]. The program variables are the number of coupled spins, the bond orientations and bond lengths. In addition, a scaling factor was introduced with accounts for the fact that the experimental REDOR curves do not reach the full attenuation level, $\Delta S/S_0=1$. Representative model calculations have shown that the MATLAB routines and the SIMPSON program provide identical results.

4.7 Simulation of REAPDOR curves

Numerical simulations of the REAPDOR curves were done with SIMPSON program package [145]. The SIMPSON input file of $^{11}B\{^{14}N\}$ PEAPDOR simulation curves for h-BN is given in an appendix.

Chapter 5

Results and discussion

5.1 Hexagonal boron nitride

Crystalline hexagonal boron nitride (h-BN) was used as model compound for the analysis of ^{11}B spin echo, ^{11}B{^{15}N} REDOR and ^{11}B{^{14}N} REAPDOR experiments on Si-B-C-N and B-C-N precursor-derived ceramics. As the h-BN in the present study is non-labeled, only ^{11}B spin echo and ^{11}B{^{14}N} REAPDOR curves can be obtained experimentally, while for ^{11}B{^{15}N} REDOR experiments only theoretical data are discussed.

The molecular structure of h-BN is given in Figure 5.1. The hexagonal boron nitride is composed of layers of hexagonal sheets in which boron is bonded to 3 nitrogen atoms, in close analogy to the graphite structure. The difference between the graphite and h-BN lies in the nature of the layer packing. In h-BN, the hexagonal rings of atoms are packed directly on top of each other, whereas in graphite a form of close packing exists, in which the atoms lie between the centres of the hexagonal rings of the adjacent layers. Unlike the C-C bond, the B-N bond has an electrical dipole moment. The different packing may be due to the interaction of these dipoles.

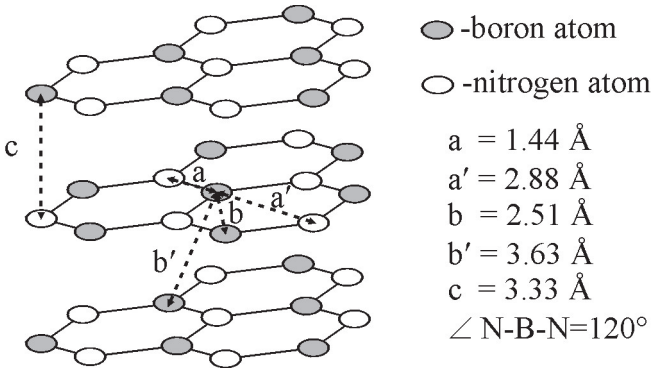

Figure 5.1. Molecular structure of h-BN.

Each boron atom is surrounded by three bonded N atoms at a distance of a=1.44 $\mathring{A}$ and three non-bonded N atoms at a′=2.88 $\mathring{A}$ and six neighbor boron atoms at b=2.51 $\mathring{A}$ within one layer, and six neighbor boron atoms at b′=3.63 $\mathring{A}$ in the adjusting layers [62]. The interlayer spacing is c=3.33 $\mathring{A}$ and the N-B-N bond angle is 120°. Using the internuclear distances of h-BN, the homonuclear (B-B) and heteronuclear (B-N) second moments, M_2, are calculated theoretically (see Table 5.1). The M_2 contributions from the second neighbor atoms at the longer distances are very small, since the dipolar second moment is inversely proportional to the cube of the internuclear distance, and can be therefore ignored.

In case of non-labeled h-BN, each boron is coupled to 4.8 ^{11}B and 3 ^{14}N at shorter

Table 5.1. Homonuclear and heteronuclear second moment (M_2) calculated for h-BN.

	spin system	**Internuclear distances**	M_2 $[10^6 rad^2/s^2]$
1^{st} neighbors	^{11}B - ^{11}B	2.51 Å	23
	^{11}B - ^{14}N	1.44 Å	18.3
	^{11}B - ^{15}N	1.44 Å	13.5
2^{nd} neighbors	^{11}B - ^{11}B	3.63 Å	2.5
	^{11}B - ^{14}N	2.88 Å	0.3
	^{11}B - ^{15}N	2.88 Å	0.2

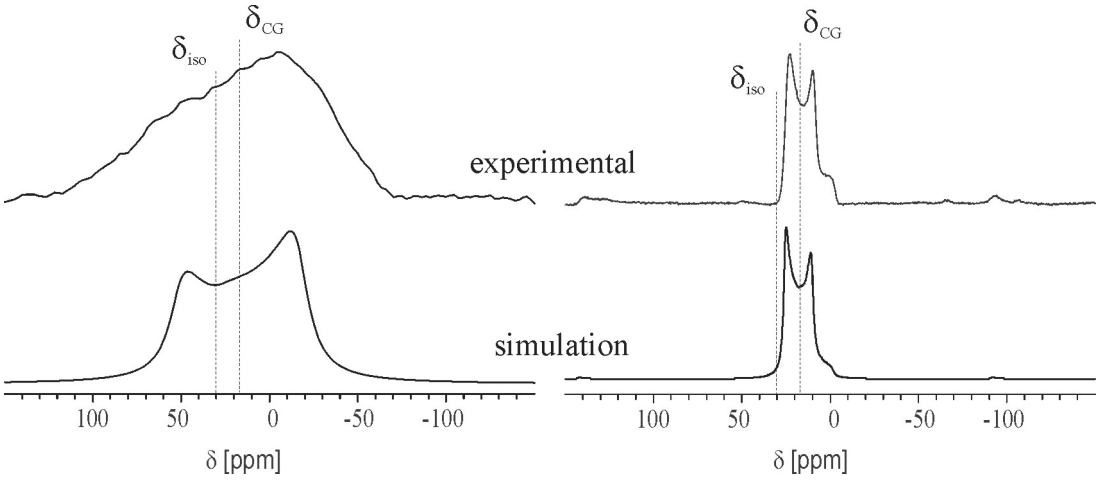

Figure 5.2. Static (left) and MAS (ν_r=10 kHz) (right) ^{11}B single pulse NMR spectra of h-BN obtained on operating magnetic field of 9.4 T. The parameters used for simulations: C_{qcc}=2.9 MHz, $\eta = 0$ and $\delta_{iso} = 30$ ppm.

distances, as the natural abundance of ^{11}B and ^{14}N are 80 and 99.63 %, respectively. Therefore, the total homonuclear and heteronuclear second moments of ^{11}B coupled to ^{11}B and ^{14}N are $111{\cdot}10^6$ and $55{\cdot}10^6 rad^2/s^2$, respectively.

^{11}B and ^{14}N NMR study

Figure 5.2 (top) shows static and MAS ^{11}B single pulse NMR spectra of h-BN. The spectra are characteristic for central transition lineshapes broadened by second-order quadrupolar interaction. Both spectra are simulated with the Simpson package taking into account only the second-order quadrupolar interaction with a quadrupolar coupling constant C_{qcc}=2.9 MHz, an asymmetry parameter η_Q=0 and an isotropic chemical shift δ_{iso}=30 ppm [148].

It can be seen that the static ^{11}B NMR spectrum is additionally broadened by homonuclear and heteronuclear dipolar interactions besides the second-order quadrupolar interaction. In the MAS spectrum, the dipolar interactions are completely averaged by sample spinning, while the second-order quadrupole effects are only partially averaged out, resulting in a residual anisotropic lineshape.

In both the static and MAS spectra the centre of gravity, δ_{CG}, is shifted from the

isotropic chemical shift δ_{iso} value by about 13 ppm. The MAS spectrum of h-BN exhibits two main singularities, which are shifted with respect to δ_{iso} by -5.5 and -19 ppm.

In Figure 5.3.a the ^{14}N MAS NMR spectrum of hexagonal boron nitride is shown. The pulse cycling was 3600 s, since ^{14}N T_1 of the h-BN is very long due to its crystalline structure. The broad spectrum with spinning sidebands is due to first-order quadrupolar interaction and chemical shift anisotropy. The fitting parameters of the simulated spectrum (see Figure 5.3.b) are consistent with literature data [149, 150].

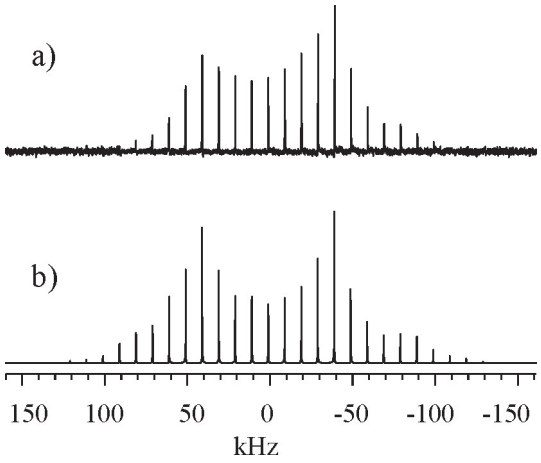

Figure 5.3. ^{14}N MAS NMR spectrum of h-BN. a) Experimental spectra: Pulse cycling is 3600 s, number of repetition is 26 and sample spinning rate of 10 kHz. b) Simulated spectra: δ_{iso}=63 ppm, chemical shift anisotropy is 160 ppm, η_{CS}=0, C_{qcc}=144 kHz and η_Q=0.

^{11}B{^{15}N} REDOR study

The REDOR technique relies on the dephasing of abundant I-1/2 nuclei or quadrupole nuclei with a low quadrupolar coupling constant. Therefore, both ^{11}B{^{15}N} REDOR and ^{11}B{^{14}N} REDOR experiment cannot be obtained for non-labeled h-BN, as the ^{15}N natural abundance is nearly to zero and the ^{14}N NMR spectrum of h-BN too broad to be inverted by a 180° pulse.

In Figure 5.4 ^{11}B{^{15}N} REDOR simulations with different B-N distances (1.48, 1.55

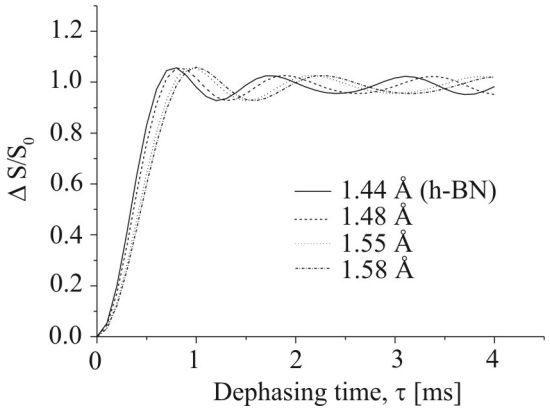

Figure 5.4. Theoretical $^{11}B\{^{15}N\}$ REDOR curves for BN_3-spin system with different B-N distances. N-B-N bond angle is 120°.

and 1.58 Å) are shown. It can be seen that the initial slope of the REDOR curve depends on the B-N bond distance while the plateau of the curve is modulated by the geometry of the system.

$^{11}B\{^{14}N\}$ REAPDOR study

In order to have a reference for the $^{11}B\{^{14}N\}$ REAPDOR experiment, h-BN sample with a known crystalline structure was examined. The experimental REAPDOR spectra of h-BN, recorded for different evolution periods, are presented in Figure 5.5. It can be seen that there are distortions of the lineshape during the evolution period. Particularly, they occur at long evolution periods as the number of 180° pulses increases. This is probably due to the very long ^{11}B T_1 relaxation times in h-BN. However, due to the lineshape distortion, a quantitative analysis of the REAPDOR data is difficult in case of h-BN.

Figure 5.6 shows experimental REAPDOR curves, obtained from analyzing the peak area of the whole spectra (left) and the peak intensity at 20 ppm (right). Both curves are compared with the theoretical REAPDOR curve (solid lines). It is clear that the second analytical approach provides a better agreement with the theoretical curve. Therefore, in the present work, all experimental REAPDOR curves were obtained using the peak intensities.

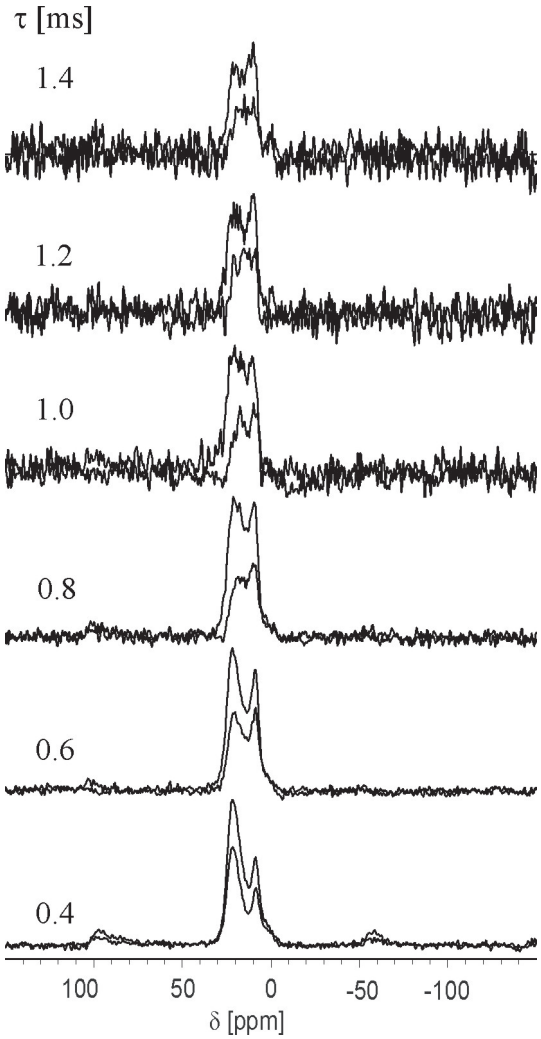

Figure 5.5. $^{11}B\{^{14}N\}$ REAPDOR spectra of h-BN obtained at different evolution times, τ.

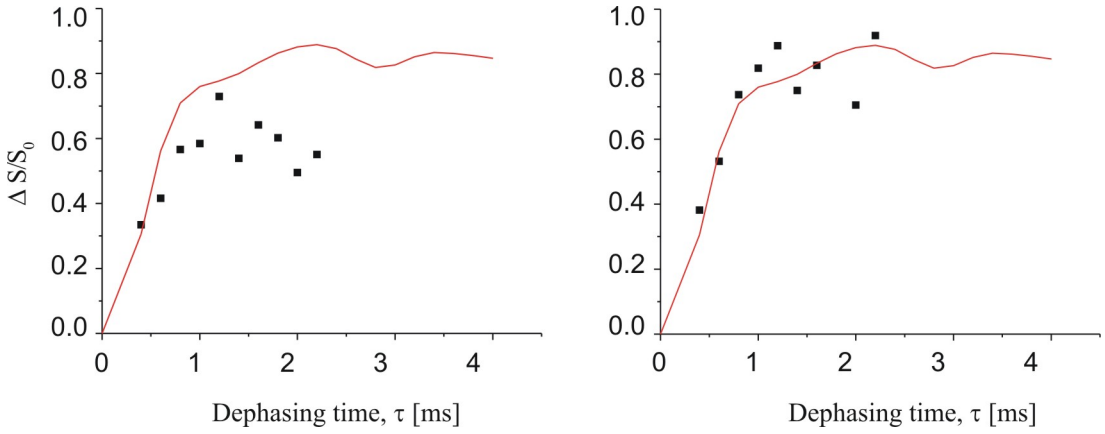

Figure 5.6. Experimental REAPDOR curves (solid square) for h-BN obtained by analyzing the peak area (left) and intensity of the singularity at 20 ppm (right). The solid lines correspond to the theoretical REAPDOR curves.

The optimization of the REAPDOR experiment with h-BN was difficult due to long ^{11}B T_1 relaxation time. Therefore, for optimization of the 180° pulse train samples of the Si-B-C-N ceramic were used, which have a shorter spin-lattice relaxation time T_1.

^{11}B spin echo study

The experimental ^{11}B spin echo decay curve of h-BN is displayed in Figure 5.7 (open circles). The initial part of the experimental ^{11}B spin echo decay curve ($2\tau < 0.1$ ms) can be fitted by the Gaussian function given in Eq. 3.80. The obtained homonuclear second moment ($M_{2(homo)}$) of $107.5{\cdot}10^6 rad^2/s^2$ and the corresponding B-B distance of 2.52 $\AA$ are in good agreement with the theoretical values (see Table 5.1).

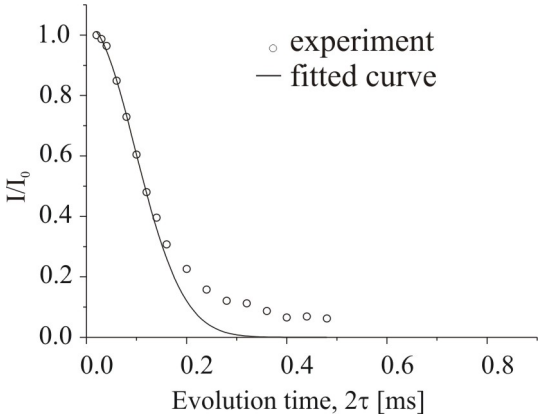

Figure 5.7. The experimental ^{11}B spin echo decay for h-BN (open circles). The solid line corresponds to Gaussian line fitting with $2\tau < 0.1$ ms.

5.1.1 Conclusion

The ^{11}B static as well as MAS NMR, and ^{14}N MAS NMR were performed on h-BN. The experimental ^{11}B and ^{14}N MAS NMR spectra were simulated with SIMPSON package. The quadrupolar coupling constants, asymmetry parameters, isotropic and anisotropic chemical shift values obtained from the simulations are consistent with those reported in [148–150].

Furthermore, ^{11}B spin echo and ^{11}B{^{14}N} REAPDOR experiments were applied for h-BN for the first time. The obtained B-B (2.51 $\mathring{A}$) and B-N distances (1.44 $\mathring{A}$) are in good agreement with those derived from X-ray diffraction [62].

5.2 Polysilazane and polysilylcarbodiimide derived Si-B-C-N ceramics

5.2.1 ^{15}N labeled boron-modified polymethylvinylsilazane 1

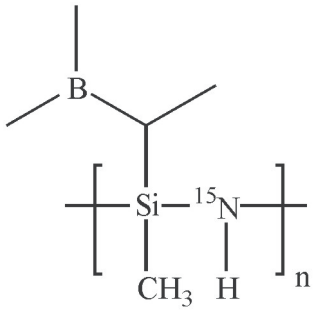

Precursor 1

^{13}C NMR studies

Figure 5.8 shows the cross-polarization (CP) and single pulse (SP) ^{13}C MAS/NMR spectra of precursor system **1** after pyrolysis at 600, 800, 1050 and 1400 °C, while the corresponding chemical shift assignments are given in Table 5.2.

The amount of protons in the intermediates pyrolized above 600 °C is not sufficient to perform cross-polarization experiments. Therefore, the ^{13}C-{^{1}H} CP experiment is only performed for the sample pyrolized at **600 °C** (see Figure 5.8). The CP spectrum exhibits two broad signals attributed to sp^2- and sp^3- carbon atoms. The peak centered at 136 ppm is associated with sp^2-carbons and indicates that the amorphous (graphite-like) carbons start to grow at this temperature. The broad peak in the range of 50 to -10 ppm refers to sp^3-carbons bonded to silicon atoms in different tetrahedral sites reflecting CH$_3$Si, CH$_2$Si$_2$, CHSi$_3$ and CSi$_4$ groups.

For the pyrolysis intermediates above 400 °C, it is assumed that crosslinking reactions occur between CH$_3$ and NH groups, according to the schema given in Figure 5.9 [74]. The reaction forms an amorphous Si-C-N matrix and CH$_4$ as gaseous byproduct, resulting in a decrease of the CH$_3$Si sites. By further increasing the pyrolysis temperature, the sp^2-carbon phase and the CSi$_4$ sites should evolve as a result of the formation of new C-Si bonds as well as of the breaking of the C-B

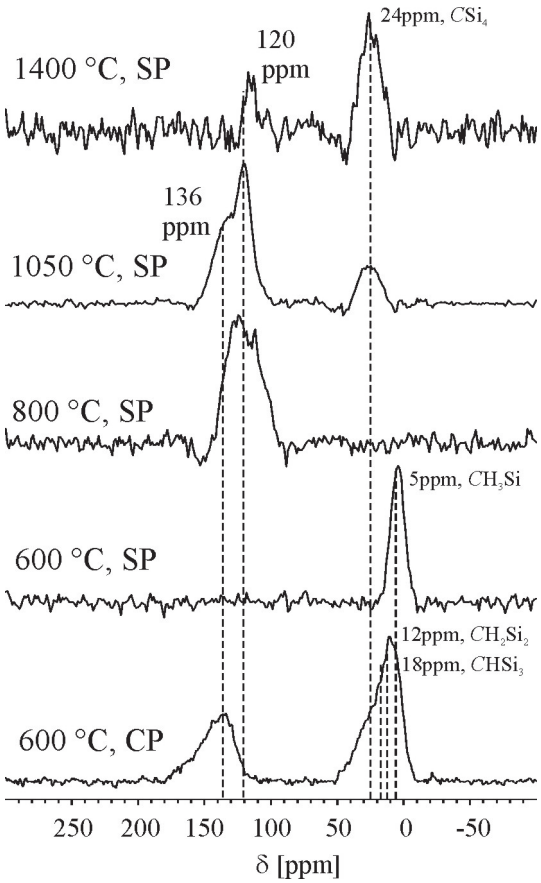

Figure 5.8. Cross-polarization (CP) and single pulse (SP) ^{13}C MAS NMR spectra of precursor system **1**.

bonds (see ^{29}Si and ^{11}B NMR results).

The single pulse ^{13}C NMR spectrum of the **600 °C** sample (see Figure 5.8) exhibits only a single signal at 5 ppm due to the CH_3Si sites. The ^{13}C resonances, which are present in the CP spectrum, i.e. the sp^2-carbon and sp^3-carbon bonded to more than one silicon atoms, are not detected in the SP experiment, because in the CP experiment the delay between acquisitions depends on the proton spin-lattice relaxation times, which are shorter than those of ^{13}C. The absence of those resonances indicates that their ^{13}C spin-lattice relaxation times is longer than for the CH_3 units, as the methyl group carbon relaxes faster due to its mobility.

In the SP spectrum of the **800 °C** sample only the signal from sp^2-carbon at about 120 ppm is registered. The peak at 5 ppm (CH_3Si sites) vanishes, indicating that

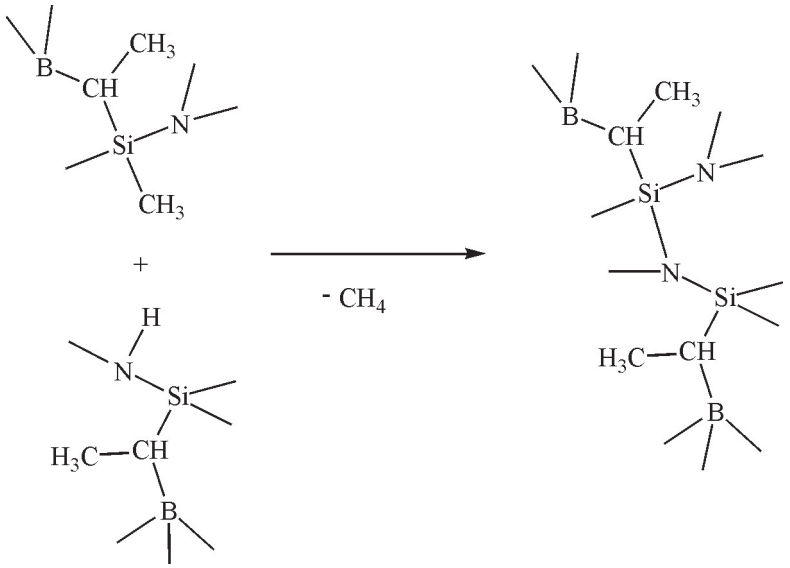

Figure 5.9. Crosslinking reaction between CH_3 and NH groups.

the aforementioned crosslinking reaction is complete at this temperature. However, the resonance from CSi_4 sites are missing.

In the spectrum of the **1050 °C** sample both sp^2- and sp^3-carbon resonances are registered. The sp^3-carbon signal at about 24 ppm, related to the ^{13}C resonance in silicon carbide, only appears at this stage. The sp^2-carbon resonance consists of partially resolved signals at 136 and 120 ppm. It should be noted that there is a significant increase in S/N ratio for this sample. ^{13}C T_1 determined by the inversion recovery experiment (the results are not presented here) was about 5 s. For the other samples considerably longer ^{13}C spin-lattice relaxation times, T_1, were found.

Table 5.2. ^{13}C chemical shift assignments.

Precursor system 1		$\delta_{(^{13}C)}$ [ppm]					
		sp^2-carbon		sp^3-carbon			
		graphite-like carbon		CSi_4	$CHSi_3$	CHi_2Si_2	CH_3Si
1400 °C	(SP)	-	120	24	-	-	-
1050 °C	(SP)	136	120	24	-	-	-
800 °C	(SP)	-	120	-	-	-	-
600 °C	(SP)	-	-	-	-	-	5
600 °C	(CP)	136	-	24	18	12	5

The increase of the S/N ratio for the sample annealed at 1050 °C is therefore due to the decrease of T_1, since the same recycle time of 15 s was used for all ^{13}C NMR spectra.

The shorter T_1 for the 1050 °C sample can be explained by the results of the EPR analysis for this precursor system **1** [74]. It has been reported that this sample contains highly concentrated unpaired electrons attributed to carbon-centered free radicals. Such paramagnetic centers may result in a decrease of ^{13}C T_1.

In the spectrum of the **1400 °C** sample, peaks at 120 (sp^2-carbon) and 24 ppm (sp^3-carbon) are observed, while the peak at 138 ppm associated with sp^2-carbon vanishes. A significant decrease of the S/N ratio indicates the absence of paramagnetic defects. The decrease of the sp^2-carbon signal intensity, as compared to the sp^3-carbon signal indicates that the sp^2-carbon atoms carry the aforementioned free radicals in the intermediate at 1050 °C.

^{29}Si NMR studies

Figure 5.10 shows single pulse ^{29}Si MAS NMR spectra of precursor **1** annealed between 600 and 1400 °C. All spectra exhibit broad resonances, as expected for the amorphous structure, in which usually a distribution of bond lengths and angles should exist. In this case, the ^{29}Si NMR spectra are attributed to different silicon sites in the amorphous Si-C-N network. Gaussian line fittings of the experimental spectra for different SiC_xN_{4-x} (x=0, 1, 2, 3 and 4) units were performed taking into account the literature values for these units. The chemical shift values and relative intensities of the deconvoluted peaks as well as the corresponding literature references used for assignment are given in Table 5.3.

The ^{29}Si NMR spectrum of the **600 °C** sample is deconvoluted into two peaks at -7 and -22 ppm. Both peaks are assigned to silicon atoms bonded to two nitrogen and two carbon atoms in sp^2 or sp^3 configurations (see Table 5.3). Upon increasing

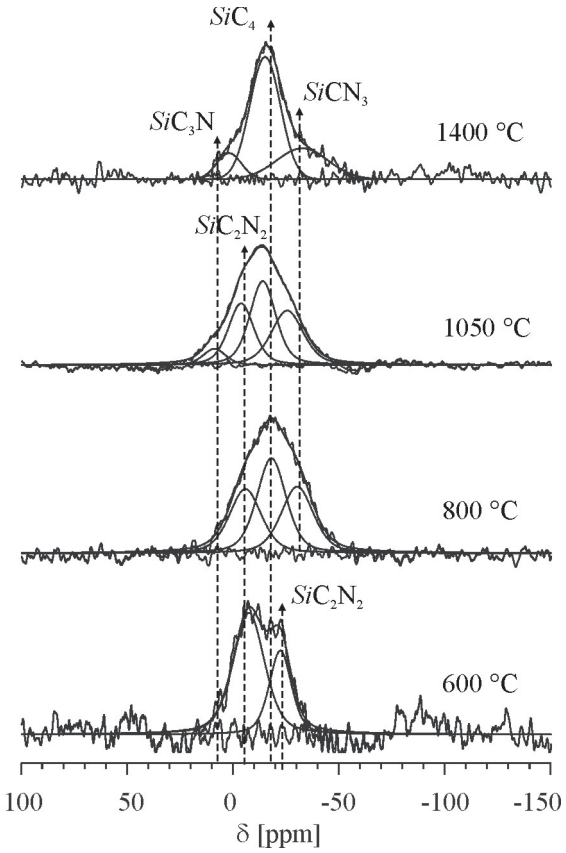

Figure 5.10. Single pulse ^{29}Si MAS NMR spectra of precursor system **1**.

the annealing temperature, the $SiC_2(sp^3)N_2$ units continuously decrease in intensity (from 67 to 27 %) and finally disappear after pyrolysis at 1400 °C, while the signal of the $SiC(sp^3)C(sp^2)N_2$ units disappears after pyrolysis at 800 °C.

The deconvolution of the spectrum of the **800 °C** sample reveals the presence of two new silicon sites with chemical shifts of -18 ppm and -30 ppm. These signals are related to SiC_4 and $SiCN_3$ units, respectively. The conversion of SiC_2N_2 units into SiC_4 takes place following the scheme shown in Figure 5.11. The conversion of BC_3 to BN_3 units (see ^{11}B NMR part) also follows this scheme.

The spectrum of the **1050 °C** sample does not show any significant difference from that at 800 °C, except for some changes of the chemical shift values. However, the S/N ratio of the ^{29}Si NMR spectra exhibits the same trend as in the ^{13}C NMR spectra. At 1050 °C, the S/N ratio therefore increases significantly, which can be

Table 5.3. ^{29}Si NMR data derived from Gaussian line fitting.

Prec.	$\delta_{(^{29}Si)}$ [ppm]					
sys. 1	$SiC_3(sp^3)N$	$SiC_2(sp^3)N_2$	SiC_4	$SiC(sp^3)C(sp^2)N_2$	$SiCN_3$	Si_3N_4
1400 °C	2	-	-15	-	-32	-
1050 °C	9	-4	-14	-	-25	-
800 °C	-	-6	-18	-	-30	-
600 °C	-	-7	-	-22	-	-
(Ref)	0.5/7	-5	-18.5	-	-24/-34	-48/-50
	[151]	[152, 153]	[154, 155]	[74]	[152, 156]	[157, 158]
	Relative intensity [%]					
1400 °C	11	-	63	-	26	-
1050 °C	6	27	37	-	30	-
800 °C	-	29	40	-	31	-
600 °C	-	67	-	33	-	-

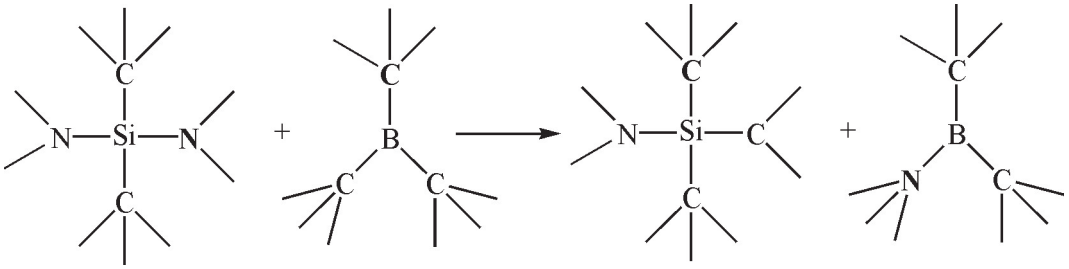

Figure 5.11. Reaction scheme between the SiC_2N_2 and BC_3 units.

again traced back to the presence of carbon paramagnetic centers in the sample (see ^{13}C NMR part).

After pyrolysis of precursor **1** at **1400 °C** there is no evidence of $SiC_2(sp^3)N_2$ units. Consequently, the intensity of the SiC_4 units increases from 37 to 63 %. At this temperature the ceramic material is characterized by the carbon enriched (SiC_3N and SiC_4 units) and nitrogen enriched ($SiCN_3$ units) silicon sites. The silicon signal is, however, still broad indicating that the ceramic is still amorphous. This is in agreement with the X-ray data, which show that crystalline phases of SiC and Si_3N_4 are formed only after annealing up to 1750 °C [24]. The growth of the Si_3N_4 crystalline phase is slower in the Si-B-C-N ceramic as compared to boron free Si-C-N ceramic materials.

^{15}N NMR studies

Figure 5.12 shows single pulse ^{15}N MAS NMR spectra of precursor **1** pyrolized at 800, 1050 and 1400 °C. All spectra exhibit a very broad resonance in the chemical shift range of tri-coordinated nitrogen with different atomic environments. These broad spectra are deconvoluted by Gaussian line fitting using three peaks. The results of the deconvolutions (chemical shift values, line width and relative intensities) are summarized in Table 5.4. Based on the literature data (also given in Table 5.4) the deconvoluted peaks are assigned to NHB_2, NB_3/ NHBSi and NSi_3 units.

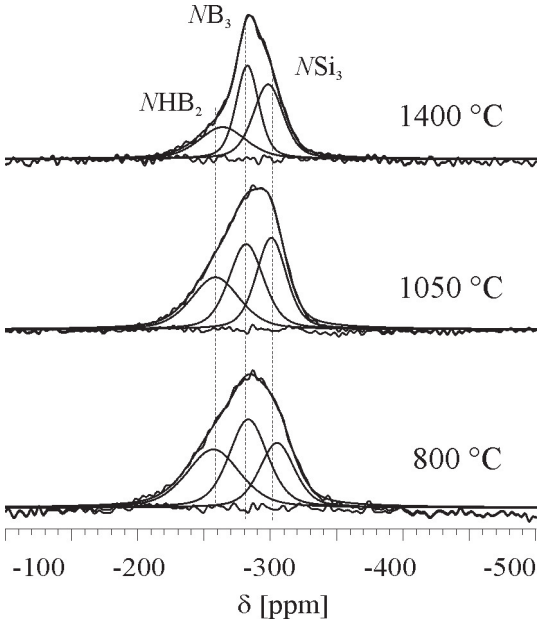

Figure 5.12. Single pulse ^{15}N MAS NMR spectra of precursor system **1**.

Table 5.4. ^{15}N NMR data derived from Gaussian line fitting.

Prec.	$\delta_{(^{15}N)}$ [ppm]			**Line width** [Hz]			**Relative intensity** [%]		
sys. 1	NHB_2	NB_3/ NHBSi	NSi_3	NHB_2	NB_3/ NHBSi	NSi_3	NHB_2	NB_3/ NHBSi	NSi_3
1400 °C	-264	-282	-298	1700	820	1090	25	37	38
1050 °C	-258	-281	-300	1730	1250	1090	30	36	34
800 °C	-253	-283	-305	1920	1390	1270	35	39	26
(Ref)	-266, -275	-282	-309						

In the spectrum of the **800 °C** sample the peaks at -253 and -305 ppm are attributed

to NHB_2 [159, 160] and NSi_3 units [157, 161], respectively. The peak at about -282 ppm most probably is a superposition of NB_3 and NHBSi units, since these units appear in the same chemical shift range [157, 161]. The $NHSi_2$ units, which are characteristic for the starting precursor polymer, are expected to resonate in the range of -332 to -351 ppm [162]. This signal, however, is not observed after annealing above 800 °C.

The ^{15}N NMR spectra at **1050** and **1400 °C** resemble that for the sample from 800 °C. Upon increasing the annealing temperature, NHB_2 units decrease in intensity from 25 to 35 %, while for the NSi_3 units an increase in intensity from 26 to 38 % is observed. This observations confirm that the peak at about -281 ppm is attributed not only to NB_3 but also to NHSiB units. After pyrolysis at 1400 °C the peak at -281 ppm reduces in linewidth from 1250 to 820 Hz. This reflects the absence of NHSiB units at this temperature.

The presence of the NHB_2 units indicates that the derived ceramic contains residual protons even after pyrolysis at 1400 °C. It should be noted that the highest amount of the NHB_2 units is found in the present system (see ^{15}N labeled precursor systems **2**, **5** and **7**). A further discussion of this peak will be made in the chapter dealing with precursor system **2**. It is expected that at higher annealing temperature NB_3 and NSi_3 units remain, resulting in the formation of the crystalline hexagonal boron nitride and silicon nitride domains.

^{11}B NMR studies

The ^{11}B MAS NMR spectra of precursor system **1** after thermal annealing at temperatures between 200 °C and 1400 °C are presented in Figure 5.13. For comparison, the ^{11}B NMR spectrum of h-BN is also shown. As presented in Section 5.1, tri-coordinated boron nuclei (BX_3 sites) usually possess large quadrupolar coupling constants. In this case, the central transition 1/2↔-1/2 (CT), whose

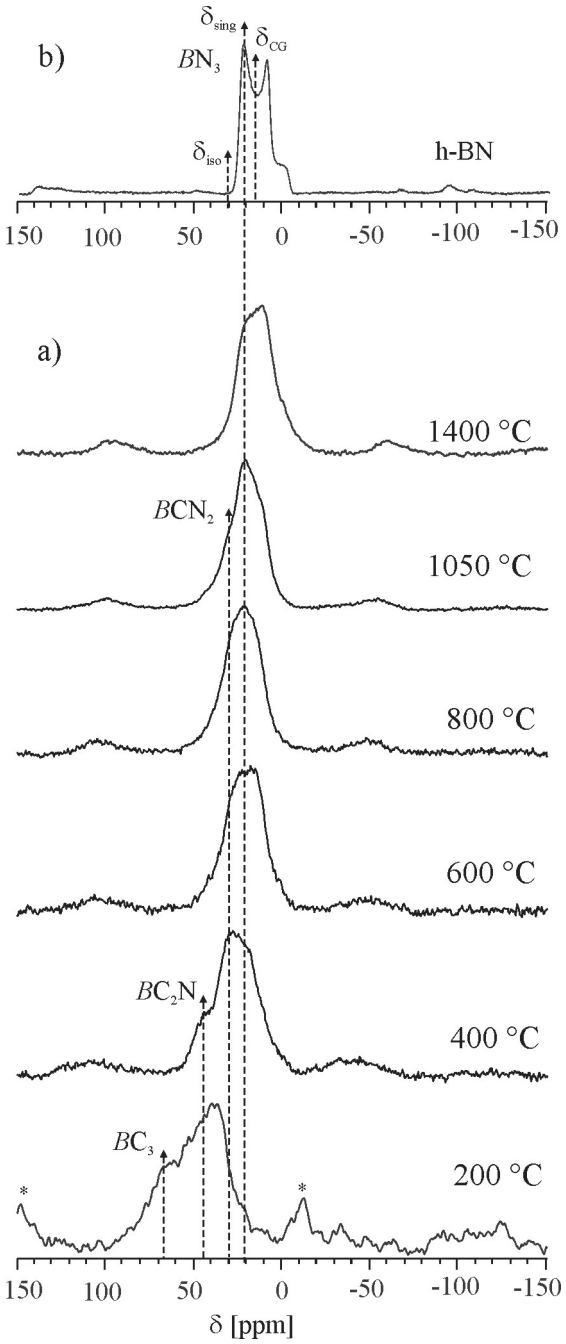

Figure 5.13. Single pulse ^{11}B MAS NMR spectra of a) precursor system **1** and b) pure h-BN. The dotted lines correspond to position of the low field singularity for tri-coordinated boron sites, δ_{sing}.

resonance is shifted and broadened by the second-order quadrupolar interactions, can be observed selectively. The ^{11}B NMR line shape of h-BN (see Figure 5.13.b) is characteristic for a second-order quadrupolar interaction with a quadrupolar coupling constant C_{qcc}=2.9 MHz, an asymmetry parameter η=0 and an isotropic chemical shift δ_{iso}=30 ppm. (see Section 5.1)

The ^{11}B isotropic chemical shift values (δ_{iso}) for BC_xN_{3-x} (x=0, 1, 2, 3) units from liquid state NMR studies on various reference compounds are summarized in Table 5.5. The ^{11}B NMR spectra of precursor system **1** are characterized by tri-coordinated boron atoms within BC_xN_{3-x} units. The deconvolution of these broad spectra into different quadrupolar powder patterns is impossible, at least at the employed magnetic field of 9.4 T. In case of an axially symmetric quadrupole coupling tensor the ^{11}B MAS NMR line shape of the central transition exhibits two singularities (see section 3.1.5). The position of the singularity at low field, which has a high intensity, is taken as δ_{sing}. For h-BN, the δ_{sing} is observed at about 20 ppm and is shifted from δ_{iso} by -10 ppm, while the center of gravity (δ_{CG}) is shifted from δ_{iso} by -13 ppm. Therefore, according to the ^{11}B NMR spectra of tri-coordinated boron sites, the low field shoulders observed in the ^{11}B NMR spectra of 1400, 1050, 400 and 200 °C samples are taken as the δ_{sing} values for BN_3, BCN_2, BC_2N and BC_3 units, respectively. The corresponding δ_{sing} values are marked by dotted lines in the ^{11}B NMR spectra and are given in Table 5.5. It can be seen that the centre of gravity of the ^{11}B NMR spectra as well as δ_{sing} are shifted with respect to δ_{iso} due to second-order quadrupolar shift (see section 3.1.5).

The ^{11}B NMR spectrum of the **200 °C** sample shows resonances due to the carbon enriched BC_3 (68 ppm) and BC_2N (45 ppm) units. This indicates that the decomposition of the B-C bonds at this temperature is not complete. For the **400 °C** sample, the BC_3 units completely vanish, while the intensity of the BC_2N units decreases, giving rise to new resonances. They are attributed to BCN_2 (30

Table 5.5. ^{11}B chemical shift values for tri- coordinated BC_xN_{3-x} units. δ_{sing} are chemical shift values for precursor system **1** and h-BN; δ_{iso} are the isotropic chemical shift values reported in the liquid state on various reference compounds.

Boron sites	$\boldsymbol{\delta_{sing}}$ [ppm]	$\boldsymbol{\delta_{iso}}$ [ppm]
BN_3		24-35 [163, 164]
h-BN	22	30 [165]
BCN_2	30	33-46 [163]
BC_2N	45	51-60 [162, 164]
BC_3	68	86 [164]

ppm) and BN_3 (22 ppm) units.

After annealing above **600 °C**, the ^{11}B NMR spectra are dominated by the signal characteristic of BN_3 units. Therefore, the transformation of the BC_3 units into the BN_3 units occurs mainly between 200 and 600 °C through the reaction shown in Figure 5.11. The signal from the BCN_2 units most likely exists up to **1050 °C**. It is difficult to quantify the amount of BCN_2 units in the present spectra. However, they are supposed to lose in intensity with increasing annealing temperature. After annealed at **1400 °C**, the boron atoms are trigonally coordinated by three nitrogen atoms.

^{11}B{^{15}N} REDOR and SEDOR studies

^{11}B{^{15}N} REDOR experiments were performed for all pyrolysis intermediates. However, the **200 °C** annealed sample will be not discussed, as the reference and dephased spectra are found to be identical. This indicates that the amount of B-N bonds is too low at this temperature.

Figure 5.14 shows representative ^{11}B{^{15}N} REDOR spectra for precursor system **1** after an evolution period τ of 1.0 ms. Reference, dephased and difference spectra are denoted as S_0, S and $\Delta S = S_0 - S$, respectively (see Section 3.3.3.2). Due to lack of resolution of the different boron units (BC_2N, BCN_2 and BN_3) in the ^{11}B NMR

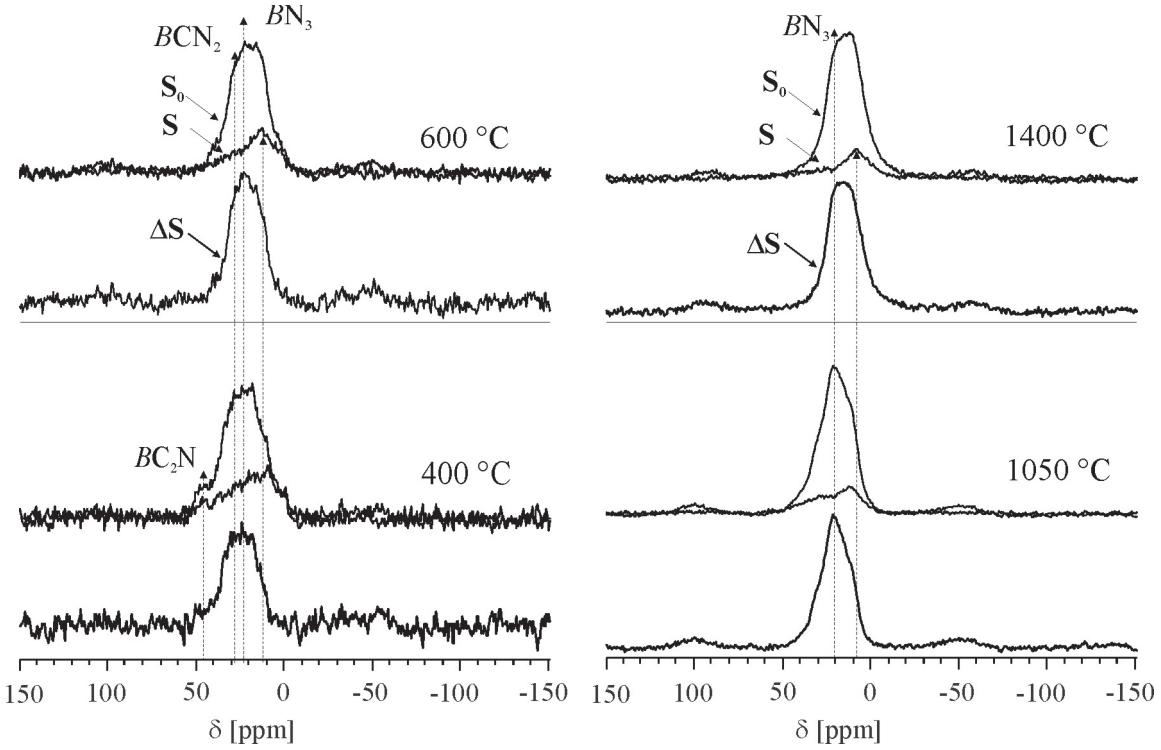

Figure 5.14. $^{11}B\{^{15}N\}$ REDOR spectra of precursor system **1** after an evolution time of τ=1 ms (ν_r=10 kHz). S_0, S and $\Delta S=S_0$-S are reference, dephased and deference spectra, respectively.

spectra, it is impossible to get REDOR curves for each unit. However, it is seen that the intensity of the dephased spectra decreases as the annealing temperature increases, indicating an increase of the dipolar interaction between boron and nitrogen nuclei. This is obviously due to the decrease of the BCN_2 units. Moreover, from the dephased spectra it can be seen that the signal at about 10 ppm does not experience any dephasing. This signal might be associated with boron sites, which are not bonded to nitrogen.

Figure 5.15 shows the experimental REDOR data and numerical calculations for various dipolar evolution times for precursor system **1**. The experimental REDOR data for the BN_3 units were obtained using the intensities at the chemical shift position, which corresponds to the maximum intensity in the ΔS spectra. This approach was used to minimize the contribution from other ^{11}B sites, hence the

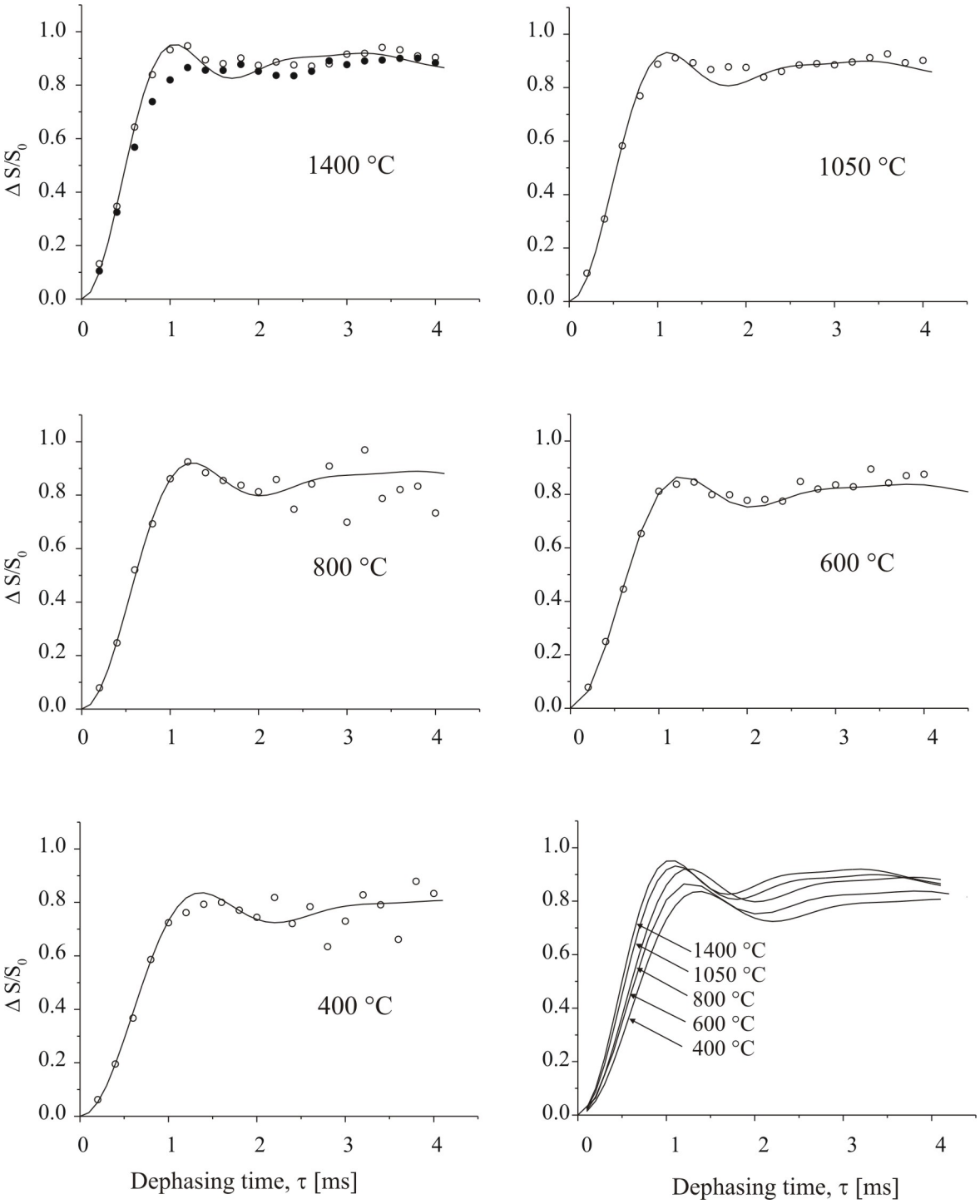

Figure 5.15. $^{11}B\{^{15}N\}$ REDOR curves for precursor system **1**. Open circles refer to the experimental data. The solid lines correspond to theoretical curves for a BN_3 spin system with the parameters given in Table 5.6.

dipolar coupling between ^{11}B and ^{15}N nuclei is the strongest for BN_3 units. The maximum intensity in the ΔS spectra usually occurs between 20 and 22 ppm for most of the samples. Simulation of the experimental data were performed assuming a BN_3 spin system with planar structure like in h-BN (see Section 5.1). In addition, *a scaling factor* was introduced which accounts for the fact that the experimental REDOR data do not reach the full attenuation level of ΔS=1. The good agreement of the experimental and the theoretical REDOR curves confirms that the BN_3 units in the precursor system **1** exhibit a planar geometry, with a B-N-B angle of 120°.

The dipolar coupling constant and scaling factor derived from the simulations are summarized in Table 5.6. The B-N distances were calculated from the dipolar coupling constant according to Eq.(3.37). The dipolar coupling constant increases from 730 to 950 Hz with increasing annealing temperature, and the corresponding B-N distances from 1.75 to 1.6 $\mathring{A}$ are found to be larger than that in h-BN (1.44 Å). The increase in dipolar coupling constant is most likely due to a decrease of the BCN_2 units. The scaling factor shows the same trend as dipolar coupling constant, confirming a decrease of the BCN_2 units as the annealing temperature increases.

In addition, REDOR curves were obtained from analyzing the peak area, whose results for the 1400 °C sample are depicted in Figure 5.15 (filled circles). The lower values for the REDOR fractions from the peak integrals (open circles) as compared to that from the peak intensity analysis are caused by the above mentioned ^{11}B resonance at about 10 ppm, which overlaps with the resonance from the BN_3 units. It should be noted that the same behavior was observed for all pyrolysis intermediates (the results are not presented here).

The experimental SEDOR data and the Gaussian fitting of the initial part ($2\tau < 0.1$ ms) of the experimental decays for precursor system **1** are displayed in Figure 5.16. The heteronuclear second moment, $M_{2(hetero)}$, values derived from these fittings, given in Table 5.6, contain a contribution of different BC_xN_{3-x}units rather than

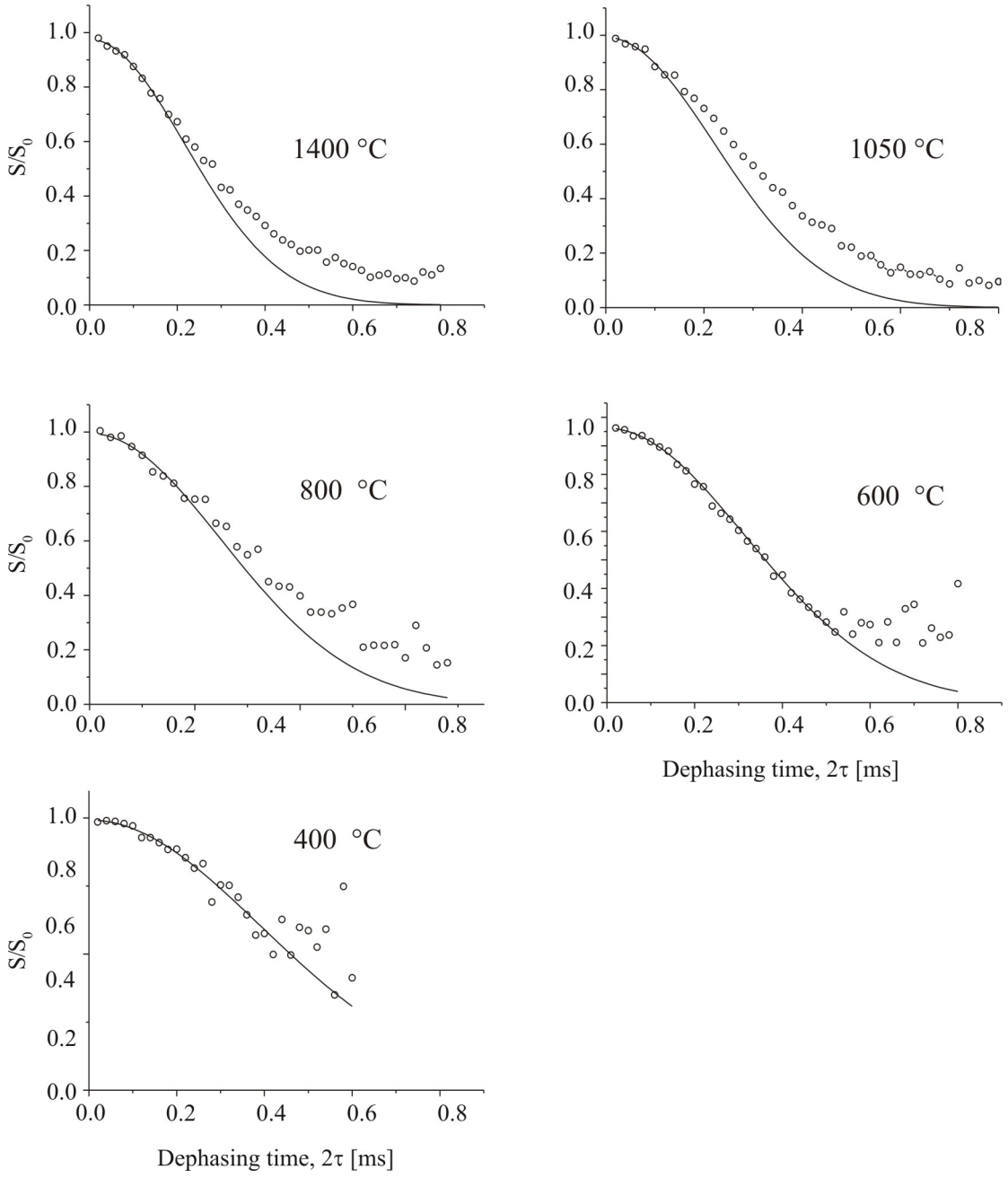

Figure 5.16. $^{11}B\{^{15}N\}$ SEDOR curves for precursor system **1**. Open circles refer to the experimental data. The solid lines are theoretical curves with the $M_{2(hetero)}$ values given in Table 5.6.

Table 5.6. $^{11}B\{^{15}N\}$ SEDOR and REDOR data for precursor system **1**.

Annealing temperature	REDOR			SEDOR	
	Dipolar coupling constant [Hz]	**Scaling factor**	**B-N distance**	$\mathbf{M_{2(hetero)}}$ $[10^6 rad^2/s^2]$	**B-N distance**
1400 °C	950	90	1.60 Å	21.3	1.60 Å
1050 °C	900	88	1.63 Å	20.4	1.61 Å
800 °C	800	87	1.70 Å	18.7	1.64 Å
600 °C	790	82	1.70 Å	11.0	(1.79 Å)
400 °C	730	79	1.75 Å	3.7	(2.15 Å)

pure BN_3 units, as the static ^{11}B NMR spectra are very broad. Figure 5.17 (left) shows the experimental $M_{2(hetero)}$ values against annealing temperature.

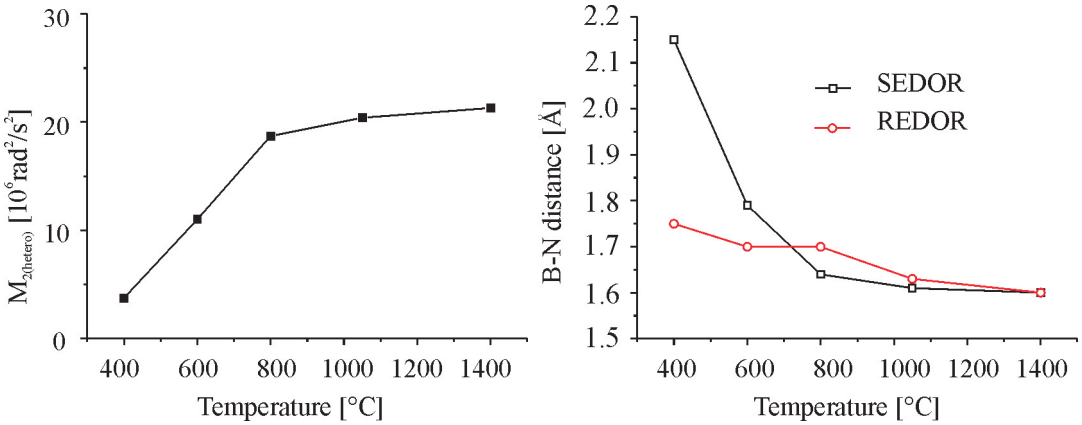

Figure 5.17. Heteronuclear second moment (left) and the B-N distances (right) against annealing temperature for precursor system **1**.

For the sample pyrolized at 400 °C, the low value of $M_{2(hetero)}$ of $3.7{\cdot}10^6 rad^2/s^2$, is due to the presence of the BC_2N units. The most dramatic changes in the $M_{2(hetero)}$ values occur between 400 and 800 °C due to the transformation of BC_2N and BCN_2 units into the BN_3 units, resulting in an increase of $M_{2(hetero)}$ from $3.7{\cdot}10^6$ to $18.7{\cdot}10^6 rad^2/s^2$.

Boron-nitrogen distances (r_{BN}) can be calculated from $M_{2(hetero)}$ by Eq.(3.82) for the BN_3 units. The obtained r_{BN} values from the SEDOR experiment are compared with those from the REDOR experiment (see Table 5.6 and Figure 5.17 (right)).

It can be seen that the r_{BN} values are almost identical for both experiments above 600 °C. The results confirm that above this annealing temperature, the precursor system **1** is mainly dominated by BN_3 units.

^{11}B spin echo studies

For short evolution times the spin echo decay (I/I_0) can be fitted by a Gaussian function (see Eq.(3.80)) to obtain the homonuclear second moment, $M_{2(homo)}$. For longer evolution times the experimental decay diverges from the Gaussian function and is modulated by other interactions such as quadrupolar and heteronuclear interactions. The boron-boron distance can be computed from $M_{2(homo)}$ using Eq.(3.81).

Figure 5.18 shows the experimental ^{11}B spin echo decay of precursor system **1** and Gaussian fitting of the initial part ($2\tau < 0.1$ ms) of the experimental decays. The $M_{2(homo)}$ values derived from the curve fittings are given in Table 5.7. $M_{2(homo)}$ of the samples below 1050 °C are found to be higher than those of the samples annealed at 1050 and 1400 °C. However, upon increasing the annealing temperature, $M_{2(homo)}$ increases as a result of a increase of the BN-layer. The ^{11}B resonance frequency difference from different boron sites in the samples pyrolized at lower temperatures might cause a faster decay. In that case, the ^{11}B spin echo decay can not be analyzed in terms of a $M_{2(homo)}$ contribution.

In addition, the obtained B-B distances for the precursor-derived ceramic at 1050 and 1400 °C are found to be longer than that in h-BN (2.51 Å) (see Table 5.7). This probably indicates that the BN-layers in precursor-derived ceramics do not possess a long-range order.

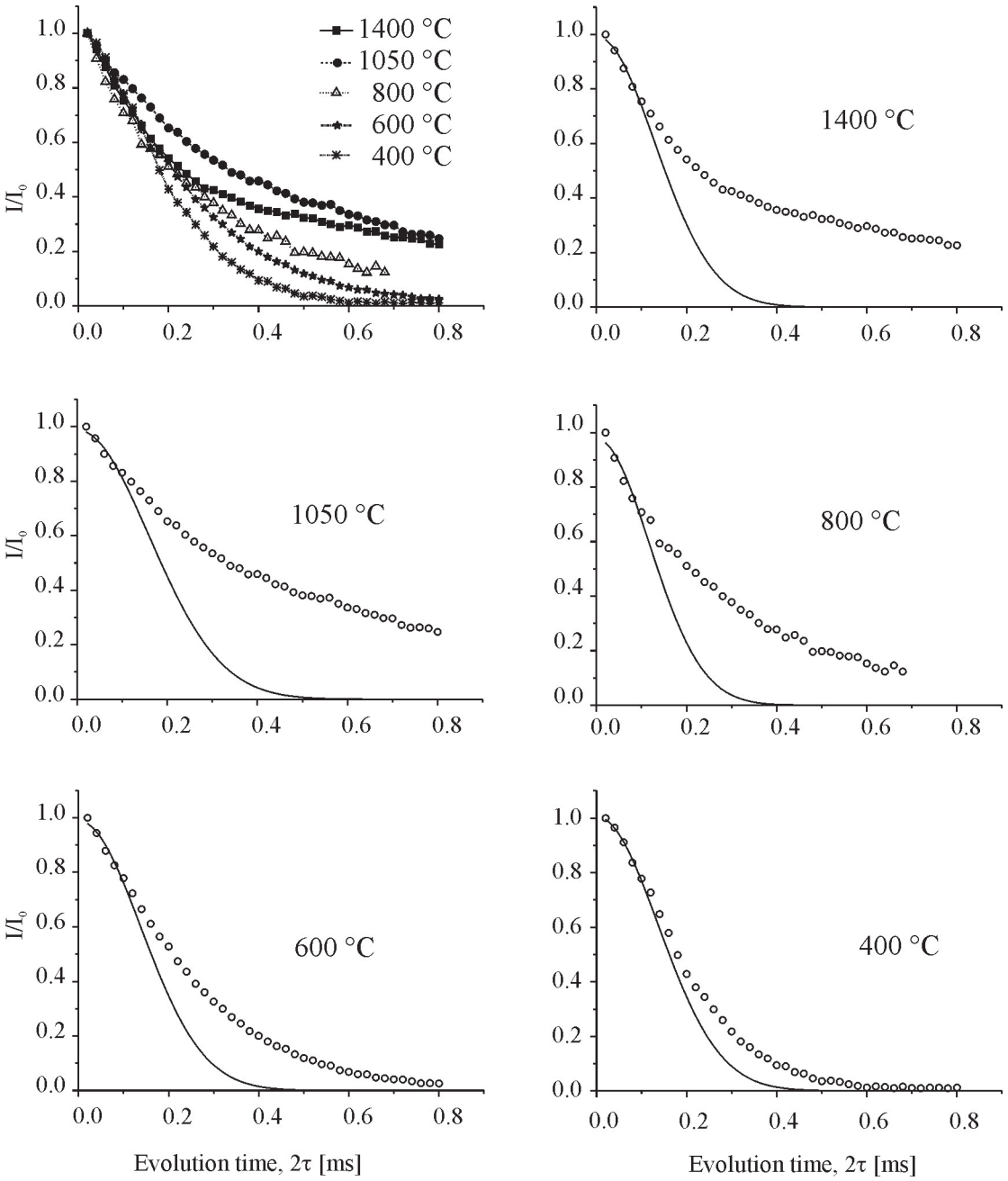

Figure 5.18. ^{11}B spin echo decay curves for precursor system **1**. The symbols refer to the experimental data. The solid lines are theoretical curves with the $M_{2(homo)}$ values given in Table 5.7.

Table 5.7. ^{11}B spin echo data for precursor system **1**.

Annealing temperature	$\mathbf{M_{2(homo)}}[10^6 rad^2/s^2]$	**B-B distance** [Å]
1400 °C	59	2.78
1050 °C	39	2.98
800 °C	73	-
600 °C	52	-
400 °C	54	-
h-BN	110	2.51

5.2.2 ^{15}N labeled boron-modified Polyhydridovinylsilazane 2

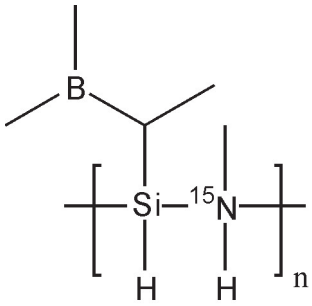

Precursor 2

The structure of polymer precursor **2** differs from that of precursor **1** only by the groups bonded to the silicon atom, i.e. silicon is bonded to H, while in precursor **1** silicon is bonded to CH_3 groups. It is known that the substitution of a silicon-bonded CH_3 group by H leads to an efficient cross-linking during the pyrolysis, resulting in a high ceramic yield [69]. The ceramic compositions of these precursors after annealing at about 1400 °C are compared in Table 5.8.

Table 5.8. Ceramic compositions of **1** and **2**.

Ceramics	Ceramic composition
precursor **1**	$Si_3B_{1.0}C_{4.3}N_2$ [24]
precursor **2**	$Si_3B_{1.1}C_{5.3}N_3$ [69]

^{13}C and ^{29}Si NMR studies

Representative ^{13}C and ^{29}Si NMR spectra of the pyrolysis intermediates derived from precursors **1** and **2** after annealing at 1400 °C are shown in Figure 5.19 (left) and (right), respectively. The ^{13}C NMR spectra of both samples exhibit sp^2- (110 ppm) and sp^3- (30 ppm) carbons attributed to a graphite-like phase and the CSi_4 units, respectively. It can be seen that the sp^2-carbon signal in precursor **2** is slightly higher as compared to that in precursor **1**. This observation is consistent with fact that the amount of carbon atoms in intermediate **2** is higher than in intermediate **1**.

The respective ^{29}Si NMR spectra show different line shapes reflecting different

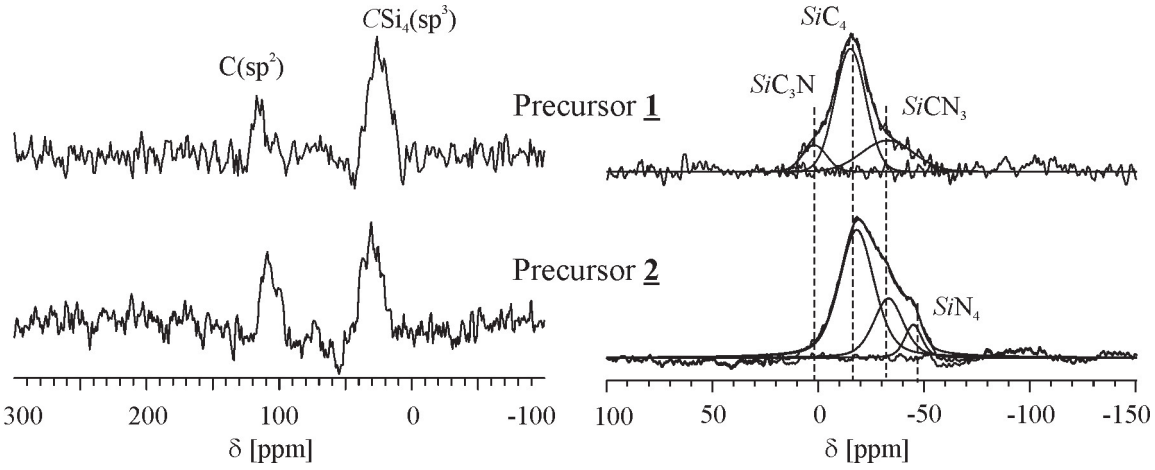

Figure 5.19. Single pulse ^{13}C (left) and ^{29}Si (right) MAS NMR spectra of precursors **1** and **2** pyrolized at 1400 °C.

tetrahedral silicon sites. From the results of the line fitting for SiC_xN_{4-x} units it can be seen that the pyrolysis intermediate **2** exhibits a higher amount of N enriched silicon sites ($SiCN_3$ and SiN_4 units) as compared to intermediate **1**. This finding is consistent with the composition of these ceramics, i.e. the amount of nitrogen in ceramic **2** is higher than in ceramic **1** (see Table 5.8).

In contrast to the boron free ceramic (Si-C-N), the nitrogen atoms in the Si-B-C-N ceramic are involved in the formation of Si_3N_4 and BN crystalline domains. Therefore, the structure of the Si-C-N matrix in the quaternary ceramics depend on the Si:B:N atomic ratio. In other words, a higher amount of N to Si and B should result in an increase of N enriched silicon sites. In the present case, the Si:B atomic ratio of 3:1 is the same for both ceramics. Therefore, the higher amount of nitrogen in intermediate **2** is responsible for the higher amount of N enriched silicon sites as observed in the ^{29}Si NMR spectra. Accordingly, the lower amount of the C enriched silicon sites in intermediate **2** might be also responsible for the higher amount of the free carbon atoms, i.e. the sp^2- carbon signal observed in the ^{13}C NMR spectra.

^{15}N NMR studies

The ^{15}N NMR spectra of precursors **1** and **2** obtained after annealing at 1400 °C are

compared in Figure 5.20. The ^{15}N NMR data, derived from Gaussian line fittings, are summarized in Table 5.9.

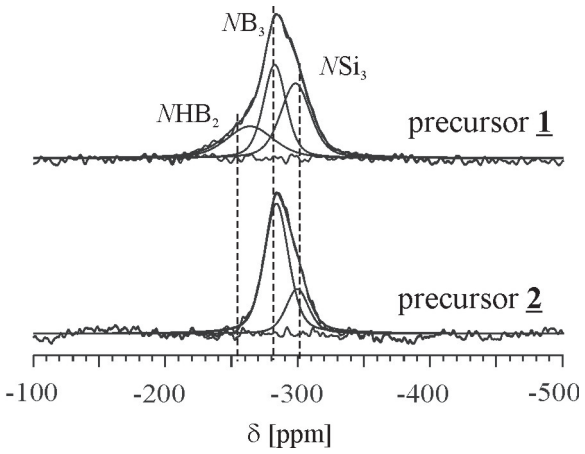

Figure 5.20. Single pulse ^{15}N MAS NMR spectra of precursors **1** and **2** pyrolized at 1400 °C.

Table 5.9. ^{15}N NMR data derived from Gaussian line fitting.

1400 °C	$\delta_{(^{15}N)}$ [ppm]			**Line width** [Hz]			**Relative intensity** [%]		
	NHB_2	NB_3	NSi_3	NHB_2	NB_3	NSi_3	NHB_2	NB_3	NSi_3
precursor **1**	-264	-282	-298	1700	820	1090	25	37	38
precursor **2**	-	-283	-299	-	880	820	-	75	25

The ^{15}N NMR spectrum of precursor **1** was found to consist of three structural units (NHB_2, NB_3 and NSi_3), while the present precursor **2** exhibits only NB_3 and NSi_3 units. The relative intensity of the BN_3 units (75 %) in the precursor **2** is found to be higher than in precursor **1** (37 %) due to the presence of NHB_2 units in precursor **1**. This confirms that the Si-H group in precursor **2** leads to higher degree of cross-linking as compared to the Si-CH_3 group in precursor **1**.

^{11}B{^{15}N} REDOR studies

^{11}B{^{15}N} REDOR measurements were performed on precursor **2** pyrolized at temperatures between 400 and 1400 °C. Figure 5.21 shows representative ^{11}B NMR

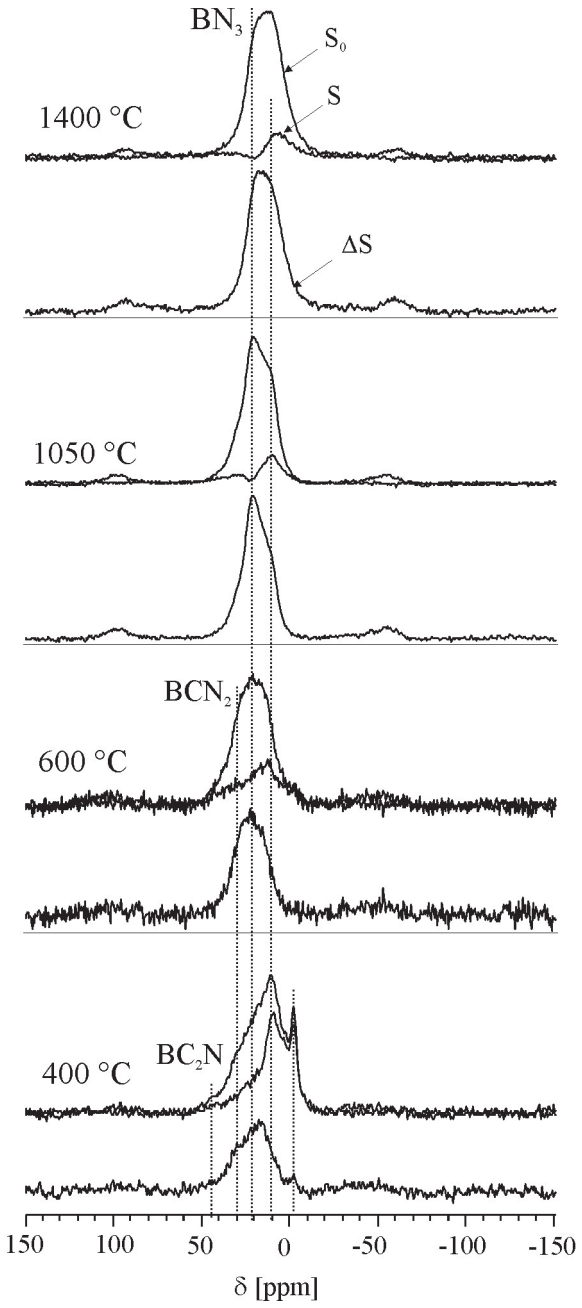

Figure 5.21. $^{11}B\{^{15}N\}$ REDOR spectra of precursor system **2** after an evolution time of τ=0.8 ms (ν_r=10 kHz). S_0, S and $\Delta S=S_0$-S refer to reference, dephased and difference spectra, respectively.

spectra denoted as reference (S_0), dephased (S) and difference ($\Delta S = S_0 - S$) spectra after an evolution period of 0.8 ms (8 rotor periods).

The reference spectrum of the pyrolysis intermediate at **400 °C** shows resonances of tri- and four-coordinated boron sites. The broad signal is attributed to BCN_2 and BN_3 units, while the sharp peak at -1.2 ppm is assigned to four-coordinated boron sites, BC_4 units. In the dephased spectrum, the dipolar dephasing of ^{11}B coupled to ^{15}N occurs due to BCN_2 and BN_3 units, while the BC_4 units do not experience any dephasing.

At temperatures above **400 °C**, the ^{11}B REDOR reference spectra are similar to those of precursor **1**. However, the intensities of the dephased spectra show stronger dipolar dephasing with respect to the previous system. Figure 5.22 shows experimental and simulated REDOR curves for the BN_3 units. Experimental REDOR curves were obtained using the peak intensities in the same way as described for precursor system **1**. The results of the simulation and the derived B-N distances (r_{BN}) are summarized in Table 5.10.

The REDOR results of the present system are compared with those of system **1**. Figure 5.23 shows the scaling factors (left) and the obtained B-N distances (right) against annealing temperature. The boron-nitrogen distance, r_{BN}, in both systems decreases as the annealing temperature increases. Moreover, both systems show the same correlation of the scaling factors and internuclear distances, i.e. r_{BN}

Table 5.10. $^{11}B\{^{15}N\}$ REDOR data for precursor system **2**.

Annealing temperature	**Dipolar coupling constant** [Hz]	**Scaling factor**	**B-N distance** [Å]
1400 °C	1040	1.00	1.55
1050 °C	1040	1.00	1.55
600 °C	830	0.92	1.68
400 °C	830	0.78	1.68

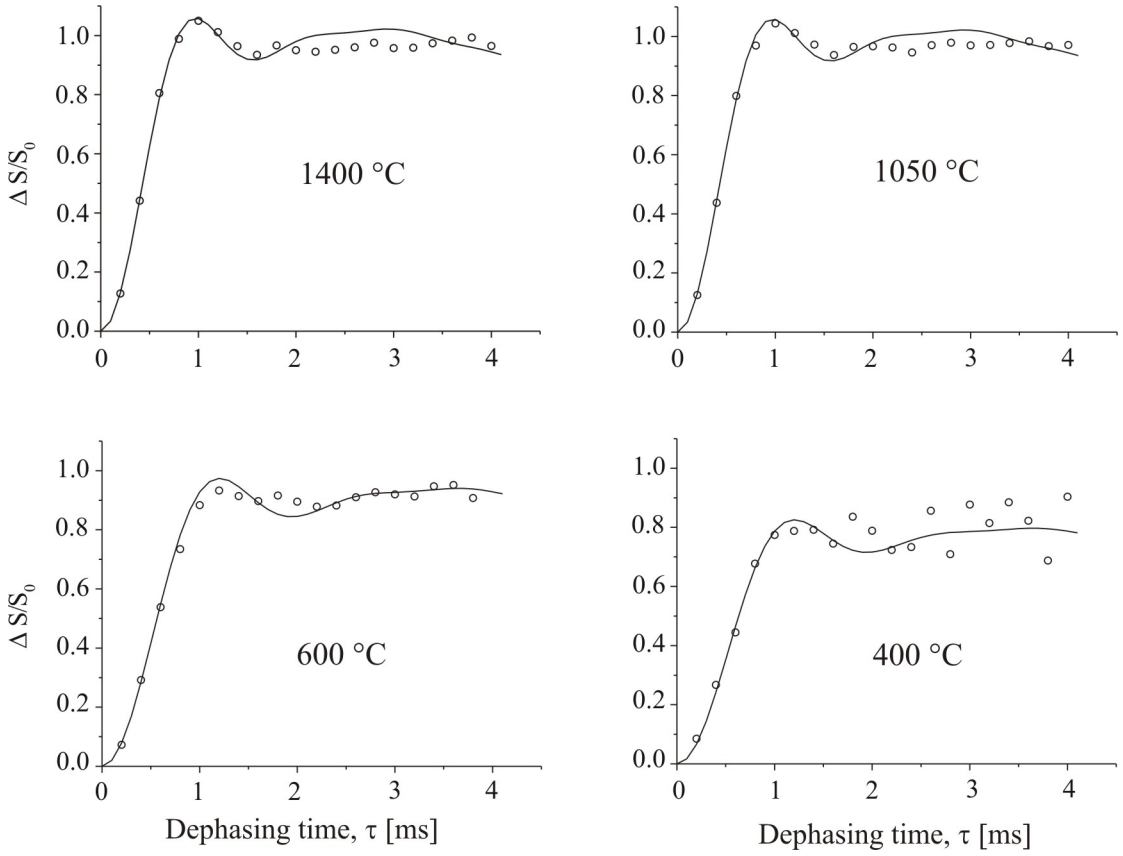

Figure 5.22. $^{11}B\{^{15}N\}$ REDOR curves for precursor system **2**. Open circles refer to the experimental data. The solid lines are theoretical curves for a BN_3 spin system with B-N distances given in Table 5.10.

decreases with increasing scaling factors. As mentioned earlier during the discussion of precursor system **1**, the scaling factor most likely reflects the amount of the structural unit BCN_2. In other words, the higher scaling factor corresponds to a lower amount of BCN_2 units. Consequently, B-N distances in precursor system **2** are found to be smaller. In the pyrolysis intermediates **2** at **1050** and **1400 °C**, the maxima of dipolar dephasing reaches 1, and r_{BN} is found to be shorter. However, the value of r_{BN} 1.55 $\mathring{A}$ is 0.11 $\mathring{A}$ larger than in h-BN.

^{11}B spin echo studies

^{11}B spin echo decay curves, i.e. the normalized intensity I/I_0 as a function of the evolution time, of precursors **1** and **2** pyrolized at 1050 °C are depicted in Figure

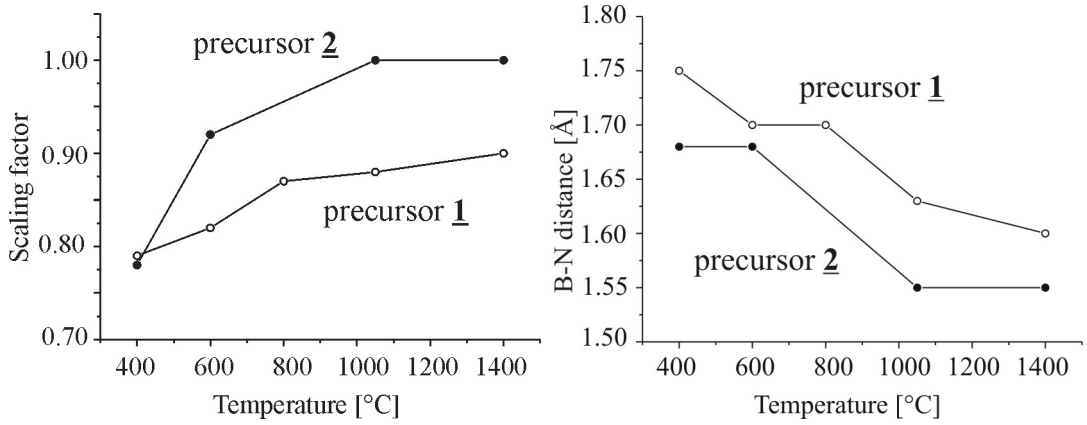

Figure 5.23. Scaling factors (left) and the B-N distances (right) against annealing temperature.

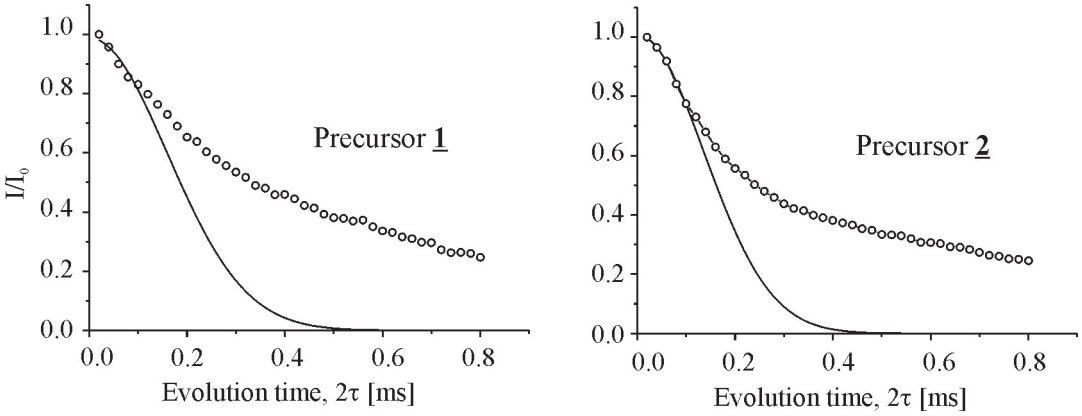

Figure 5.24. ^{11}B spin echo decay curves for precursors **1** and **2** pyrolized at 1050 °C. Open circles refer to the experimental data. The solid lines are theoretical curves with the $M_{2(homo)}$ values of $39.3{\cdot}10^6$ (left) and $53.7{\cdot}10^6 rad^2/s^2$ (right).

5.24. The homonuclear second moment values ($M_{2(homo)}$) for precursor **1** and **2** obtained by fitting the initial part ($2\tau < 0.1$ ms) of the decay curves are $39.3{\cdot}10^6$ and $53.7{\cdot}10^6 rad^2/s^2$, respectively. An increase of the ^{11}B second moment is expected for precursor **2** as a result of formation of the BN layer structure, where boron atoms are surrounded by the maximum number of boron atoms. Therefore, the smaller value of $M_{2(homo)}$ in precursor **1** can be explained by the presence of the NB_2H units and the relatively higher amount of BN_2C units, which result in a distortion of the BN layers. The B-B distance calculated from the $M_{2(homo)}$ for precursor **2**, assuming a BN layer structure, is 2.78 $\AA$, which is about 9 % longer than in h-BN.

5.2.3 Boron-modified polyhydridomethylaminovinylsilazane 3

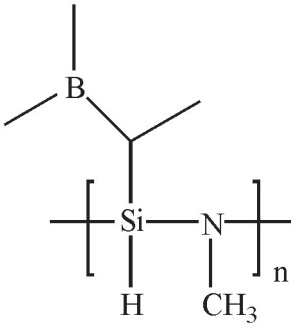

Precursor 3

The molecular structure of the starting polymer precursor **3** differs from the other polysilizanes discussed in this thesis by the CH_3 substitution at the nitrogen atom.

^{13}C NMR studies

^{13}C NMR spectra of precursor **3** pyrolized at 800, 1050 and 1400 °C are depicted in Figure 5.25 while the chemical shift assignments are given in Table 5.11. The spectrum of the **800 °C** sample exhibits the same resonance as the intermediate **1** at the same temperature. The peak centered at 120 ppm is attributed to sp^2-carbon (graphite-like carbon).

For the pyrolysis intermediate at **1050 °C** two peaks at about 120 and 138 ppm due to sp^2-carbon can be identified. The sp^3-carbon signal attributed to the CSi_4 units is not detected. The ^{13}C CP/MAS spectrum of this sample shows only a sp^3-carbon signal from $CHSi_3$ units. It is important to underline that after pyrolysis at 1050 °C, all Si-B-C-N ceramic systems studied in the present work show the same sp^2-carbon resonances at 120 and 138 ppm. However, in contrast to the other precursor systems the intensity of the peak at 138 ppm in precursor **3** is higher than that at 120 ppm.

For the samples annealed at **1400 °C** both sp^2- and sp^3-carbon signals are observed. It should be noted that the sp^2-carbon signal at 138 ppm can be still seen, in contrast to the previous precursors (**1** and **2**) pyrolized at the same temperature, where only the peak at 120 ppm is observed. Moreover, the S/N ratio for the pyrolysis intermediates at 1050 and 1400 °C is higher as compared to the previous systems.

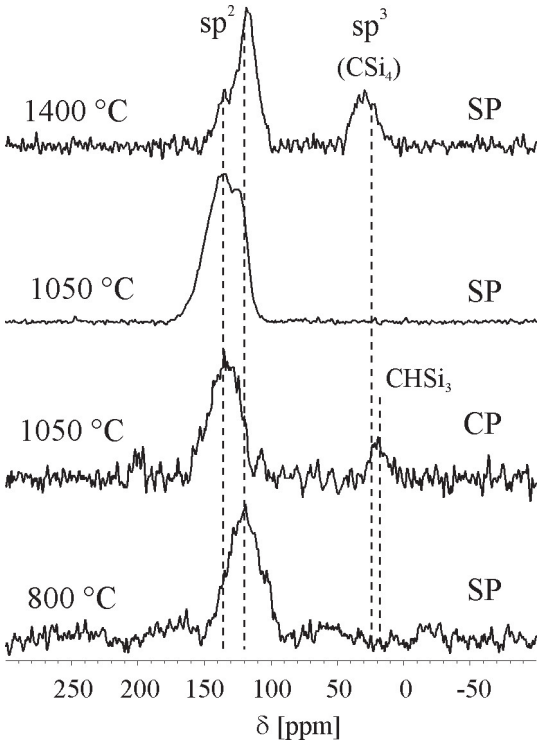

Figure 5.25. Cross-polarization (CP) and single pulse (SP) ^{13}C MAS NMR spectra of precursor system **3**.

This indicates that the carbon atoms associated with the resonance at 138 ppm carry the carbon centered paramagnetic defects, which is discussed in Section 5.2.1.

Table 5.11. ^{13}C chemical shift assignments.

Precursor system 3		$\delta_{(^{13}C)}$ [ppm]			
		sp^2-carbon		sp^3-carbon	
				CSi_4	$CHSi_3$
1400 °C	(SP)	136	120	30	-
1050 °C	(SP)	136	-	-	-
1050 °C	(CP)	136	-	-	20
800 °C	(SP)	-	120	-	-

However, the nature of different sp^2-carbon signals is not clear. According to the literature, the low-field resonance (140-160 ppm) reflects sp^2-carbon bonded to heteroatoms, while the high-field resonance (120-100 ppm) arises from sp^2-graphite like carbon. For example, as a result of the theoretical calculation of the ^{13}C chemical

shift value for the graphitic C_3N_4 phase, the (sp^2)C-N resonance is predicted at 144 ppm [166, 167]. It is interesting to note that the same relationship between the S/N ratio and sp^2 carbon resonance has been observed for the C-N ceramic materials, which contains also paramagnetic defects [166]. In other words, the S/N ratio of the ^{13}C spectra increases as the (sp^2)C-N resonance increases in intensity. If we assume that the peak at 138 ppm is from sp^2-carbon bonded to heteroatoms, it might be due to carbon atoms, which are incorporated into B-C-N or Si-C-N amorphous network. Such a deformation in the sp^2 graphite-like structure could cause the above mentioned paramagnetic defects.

In addition, a higher intensity of the sp^2-carbon as compared to that in the previous intermediates **1** and **2** (see section 5.2.2) is observed. This finding can be again explained by a higher amount of nitrogen bonded silicon sites in intermediate **3** (see ^{29}Si NMR).

^{29}Si NMR studies

Representative ^{29}Si NMR spectra of the pyrolysis intermediates at 1050 and 1400 °C are depicted in Figure 5.26. The corresponding chemical values and relative intensities derived from the Gaussian line fittings are summarized in Table 5.12. For comparison the ^{29}Si NMR data of precursor system **1** are also given.

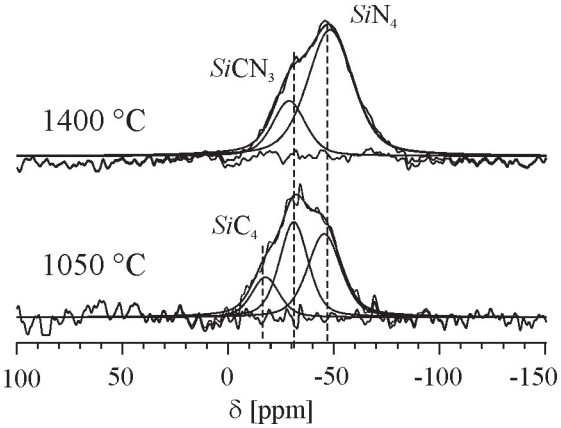

Figure 5.26. Single pulse ^{29}Si MAS NMR spectra of precursor system **3**.

Table 5.12. ^{29}Si NMR data derived from Gaussian line fitting.

Precursor system	$\delta_{(^{29}Si)}$ [ppm]				
	SiC_3N	SiC_2N_2	SiC_4	$SiCN_3$	Si_3N_4
1400 °C (**3**)	-	-	-	-29	-48
1400 °C (**1**)	2	-	-15	-32	-
1050 °C (**3**)	-	-	-18	-31	-45
1050 °C (**1**)	9	-4	-14	-25	-
	Relative intensity [%]				
1400 °C (**3**)	-	-	-	24	76
1400 °C (**1**)	11	-	63	26	-
1050 °C (**3**)	-	-	17	41	42
1050 °C (**1**)	6	27	37	30	-

The spectrum of the pyrolysis intermediate at **1050 °C** shows an amorphous Si-C-N network consisting of SiC_4, $SiCN_3$ and Si_3N_4 sites with relative intensities of 17 %, 41 % and 42 % (see Table 5.12), respectively. It can be seen that the amount of N enriched silicon sites ($SiCN_3$ and Si_3N_4) is much higher as compared to that in intermediate **1**.

Upon heating at **1400 °C**, the signal of the SiC_4 sites increases in intensity from 37 to 63 % for precursor **1**, while for precursor **3** the Si_3N_4 site signal increases from 42 to 76 %. Thus, the formation or cleavage of the Si-C bonds is assumed to result in a decrease or increase of the amount of sp^2-carbon, respectively, which is also confirmed by the ^{13}C NMR data.

The aforementioned structural compositions of amorphous intermediates can be traced back to the molecular structures of the starting precursor polymers. Until now we compared the structural compositions of three systems (**1**, **2** and **3**). It has been demonstrated that N enriched silicon sites increase in the order of **1** < **2** ≪ **3** and that the increase leads to an increase of the sp^2-carbon. On the other hand, the molecular structures of the starting polymers differ only by the groups bonded to Si and N atoms. Moreover, it is known that the groups bonded

to Si and N atoms play an important role for the crosslinking reactions during the pyrolysis. As already mentioned (see section 5.2.2) in case of precursor systems **1** and **2** (derived from the polysilazanes), the structural difference of ceramic compositions are due to the groups bonded to Si atoms, since both precursors contain N-H groups. The most significant structural difference in an amorphous Si-C-N network as well in the graphite-like carbon resonance occurs in precursor system **3** (derived from polyaminosilizane) due to substitution of H by CH_3 at the nitrogen atoms.

^{11}B NMR studies

Figure 5.27 compares the ^{11}B NMR spectra of the pyrolysis intermediates **3** at 1050 and 1400 °C (solid lines) with h-BN (dotted lines). It should be emphasized that ceramic **3** shows the best agreement between the ^{11}B NMR lineshapes the model compound, h-BN. This might indicate a higher ordering of boron nitride layers in precursor system **3** as compared to the other Si-B-C-N ceramic systems.

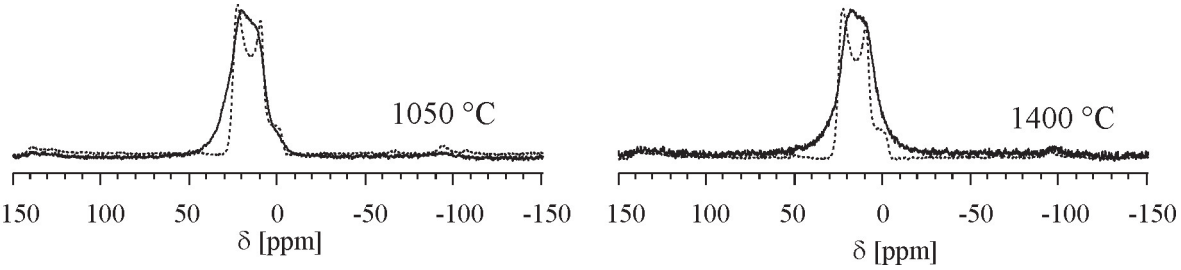

Figure 5.27. Single pulse ^{11}B MAS NMR spectra of precursor system **3** (solid lines) and h-BN (doted lines).

^{11}B{^{14}N} REAPDOR studies

The REAPDOR technique is designed for recoupling of the heteronuclear dipolar interaction, where the dipolar dephasing nuclei possess a large quadrupolar coupling constant (see Section 3.3.3.3). In the case of h-BN, the ^{14}N quadrupolar coupling constant is 140 kHz and the overall width of ^{14}N spectrum is about 100 kHz (see Section 5.1). An attempt to record ^{14}N NMR spectra of the present samples failed. This is fully understandable as the ^{14}N NMR resonance in Si-B-C-N ceramics is

expected to be broader than in h-BN due to the presence of the NB_3 and NSi_3 units in an amorphous network.

Figure 5.28 shows representative $^{11}B\{^{14}N\}$ REAPDOR spectra of the pyrolysis intermediates **3** at 1050 and 1400 °C after an evolution period of 1.0 ms. The intensity of the dephased spectra (S) decreases as the annealing temperature increases, resulting in an increase of dipolar dephasing of ^{11}B coupled to ^{14}N nuclei. From the comparison of the reference and dephased spectra a peak at about 10 ppm can be identified, which obviously does not experience any dephasing. It has been already mentioned (in section 5.2.1) that this peak is also observed in the REDOR experiments for the other precursor systems.

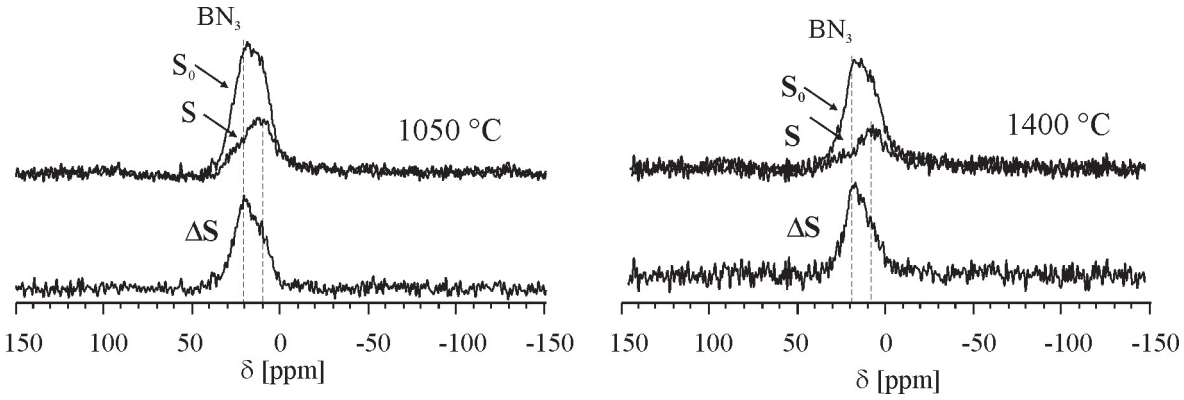

Figure 5.28. ^{11}B $\{^{14}N\}$ REAPDOR spectra of precursor system **3** after an evolution time of 1.0 ms (ν_r=10 kHz). S_0, S, $\Delta S=S_0-S$ refer to reference, dephased and difference spectra, respectively.

The experimental curves for the pyrolysis intermediates at 1050 and 1400 °C are shown in Figure 5.29. The REAPDOR curve was obtained using the peak intensities of reference and dephased spectra. A more detailed description of the REAPDOR analysis is given in Section 5.1. The solid and dashed lines in Figure 5.29 correspond to the numerical simulation of the REAPDOR curve with B-N distances of 1.44 and 1.55 $\mathring{A}$ assuming a BN_3 spin system as in hexagonal BN. The B-N distances for these intermediates are obviously the same as in h-BN (1.44 Å), and a good agreement between experimental and simulated curves is found.

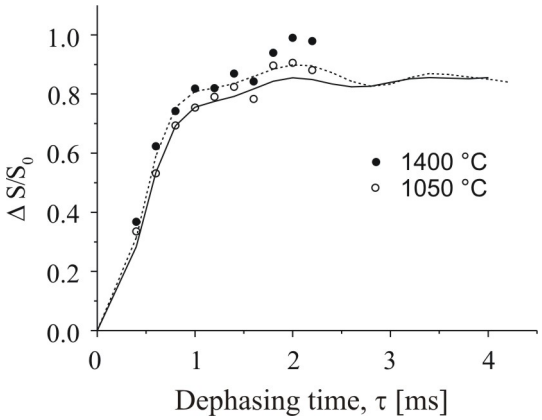

Figure 5.29. $^{11}B\{^{14}N\}$ REAPDOR curves for precursor **3**. Open and filled circles refer to the experimental data. The solid and dashed lines are theoretical curves for a BN_3 spin system with B-N distances of 1.44 and 1.55 Å, respectively.

^{11}B spin echo studies

Figure 5.30 shows the ^{11}B spin echo decay curves, i.e. the normalized intensity I/I_0 as a function of evolution time, of the pyrolysis intermediates **3** at 1050 and 1400 °C (open circles) and the curves from Gaussian fitting (solid lines). The homonuclear second moment, $M_{2(homo)}$, obtained by Gaussian fitting the initial part of the decay curves and the corresponding B-B distances (r_{BB}), and are given in Table 5.13.

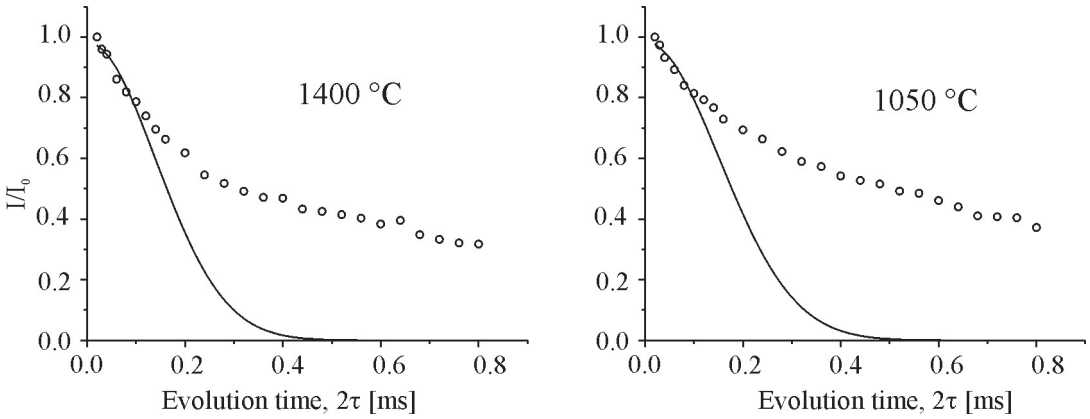

Figure 5.30. ^{11}B spin echo decay curves for precursor **3**. Open circles refer to the experimental data. Solid lines are theoretical curves with the $M_{2(homo)}$ values given in Table 5.13.

The values of $M_{2(homo)}$ are similar to those found in the intermediates **1** at the same temperatures. The corresponding boron-boron distances, r_{BB} are longer than for

Table 5.13. ^{11}B spin echo data for precursor system **3**.

Annealing temperature	$\mathbf{M_{2(homo)}}[10^6 rad^2/s^2]$	**B-B distance** [Å]
1400 °C	50.93	2.85
1050 °C	43.00	2.93

h-BN, although the B-N distances were found to be identical. $M_{2(homo)}$ most likely reflects the distortion in the BN layers, which is supposed to decrease with increasing annealing temperature as a result of the crystallization of the BN domains.

5.2.4 Boron-modified polyallylmethylvinylsilazane 4

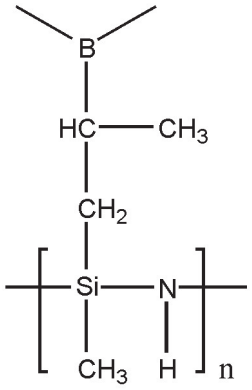

Precursor 4

The molecular structure of precursor **4** differs from previous systems **1** to **3** by the allyl group and, consequently, it contains a higher amount of carbon. The other groups bonded to silicon (CH_3) and nitrogen atoms (H) are the same as in precursor **1**. The composition in at.% of the derived ceramic is 41.7(Si), 5.5(B), 33.3(C) and 19.5(N), and the corresponding empirical formula is $Si_3B_1C_{5.6}N_{2.8}$. In the following ^{13}C and ^{14}N NMR, $^{11}B\{^{14}N\}$ REAPDOR and ^{11}B spin echo NMR results for samples pyrolized at temperatures between 1050 and 2000 °C are presented.

^{13}C NMR studies

Figure 5.31 shows SP ^{13}C NMR spectra of precursor **4** pyrolized at 1050 and 1400 °C. For the 800 °C sample a ^{13}C NMR spectrum was not detectable.

For the **1050 °C** sample, peaks at 136 and 120 ppm, attributed to sp^2-carbon, and a signal at 30 ppm from the CSi_4 units are observed. The relative intensity ratio of sp^2- and sp^3-carbon signals are almost identical to those of precursor system **1**.

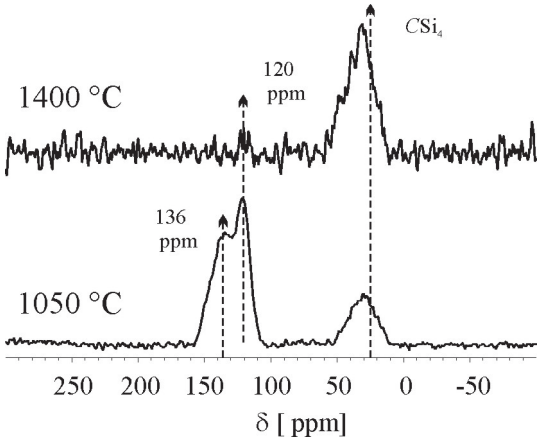

Figure 5.31. Single pulse ^{13}C MAS NMR spectra of precursor system **4**.

For the **1400 °C** sample, the sp^2-carbon signal nearly disappears. Its intensity is found to be much smaller than that of precursor systems **1** and **2**, although the amount of carbon if compared with precursor systems **1** and **2**, is not smaller. It should be noted that previous precursors (**1**-**3**) consists of polysilazanes crosslinked via C-B-C, while in polymer precursor **4** polysilazanes are crosslinked via C_2-B-C_2. It indicates that the ceramic structure not only depends on the ceramic compositions but also on the molecular structure of the polymer precursors.

In addition, the ^{29}Si NMR results of precursor system **4**, which have been reported previously in [168], were similar to those of precursor system **2**, i.e. both ceramics contain N enriched silicon sites (see Section 5.2.2). This is consistent with the fact that the ceramic compositions of **2** ($Si_3B_{1.1}C_{5.3}N_3$) and **4** ($Si_3B_1C_{5.6}N_{2.8}$) are comparable.

^{14}N NMR studies

An ^{14}N NMR signal is only observed for the sample annealed at 1800 °C (see Figure 5.32). The broad resonance, which is partially averaged by MAS into spinning sidebands, is due to the first-order quadrupolar interactions. (see section 3.1.5). The obtained spectrum is associated with the crystal ordering of nitrogen containing phases. It should be noted that an attempt to record ^{14}N NMR spectra of samples annealed below this temperature failed, as the ^{14}N resonance of the amorphous intermediates might be much broader as in a crystalline structure. In general, such a broad spectrum is not as informative as the ^{15}N NMR spectra. From the ^{15}N NMR we know that nitrogen atoms are trigonally coordinated by silicon and boron atoms in an amorphous Si-B-C-N ceramics.

^{11}B NMR studies

The ^{11}B NMR spectra of the pyrolysis intermediates between 1050 and 2000 °C are depicted in Figure 5.33 (solid lines), and are compared to that of h-BN (dashed

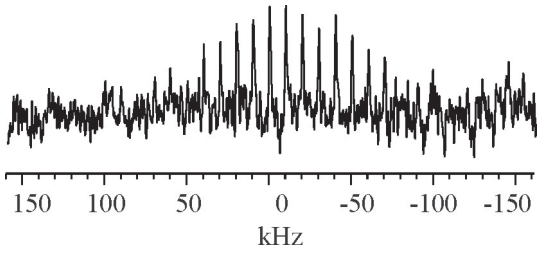

Figure 5.32. Single pulse ^{14}N MAS NMR spectra of precursor **4** pyrolized at 1800 °C; ν_r=10 kHz, na=160, rd= 160 s.

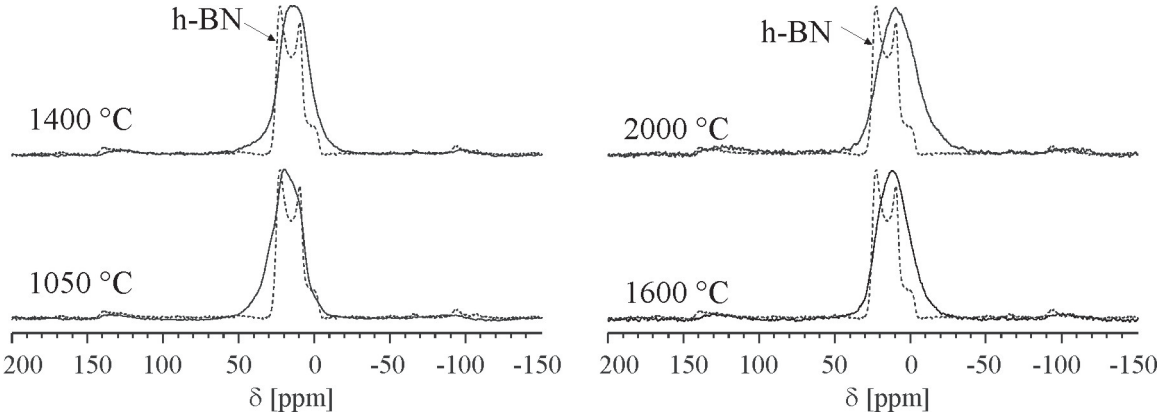

Figure 5.33. Single pulse ^{11}B MAS NMR spectra of precursor system **4** (solid lines) and of h-BN (doted lines).

lines). For the 1050 °C sample, the resonance is dominated by the boron sites bonded to three nitrogen atoms, the small shoulder at about 35 ppm is attributed to BCN_2 units. Upon increasing the annealing temperature, there is no evidence of trigonally coordinated boron sites bonded to carbon. Moreover, a broadening of the ^{11}B resonance is observed with increasing annealing temperature.

^{11}B{^{14}N} REAPDOR studies

Figure 5.34 (left) shows representative ^{11}B NMR spectra obtained from REAPDOR experiments. From the dephased spectra it can be seen that the resonance at about 20 ppm, attributed to BN_3 units, reduces in intensity faster than the resonance at about 10 ppm. The overlap of these resonances makes the analysis of the REAPDOR data difficult. Therefore, the ratio $\Delta S/S$ for BN_3 units was calculated using the peak intensities at 20 ppm. The experimental REAPDOR curves are depicted in Figure

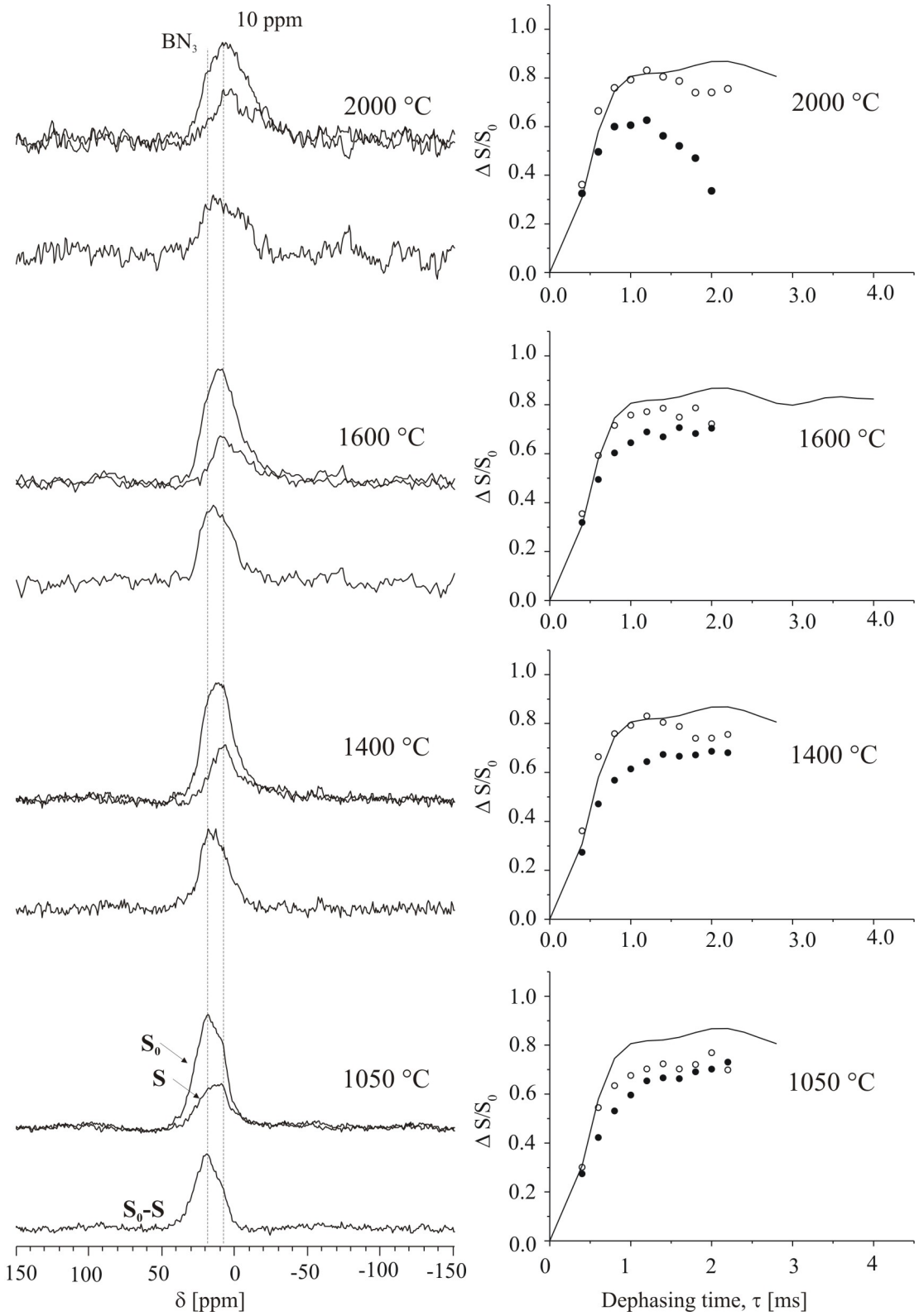

Figure 5.34. $^{11}B\{^{14}N\}$ REAPDOR spectra (left) of precursor system **4** after an evolution time of 1.0 ms (ν_r=10 kHz). $^{11}B\{^{14}N\}$ REAPDOR curves (right): Open and filled circles refer to the experimental data obtained by peak area and the peak intensity at 20 ppm, respectively. The solid lines are theoretical curves for a BN_3 spin system with B-N distances of 1.44 Å.

5.34 (right). The solid lines correspond to the simulation of BN_3 spin system with N-B-N angles of 120° and a B-N distance of 1.44 Å. For the pyrolysis intermediates above 1400 °C, REAPDOR curves calculated using the peak intensity is in good agreement with the simulation. Only for the 1050 °C sample, the experimental REAPDOR curve does not reach the maxima of the simulated curve. This confirms the presence of BCN_2 units, whose resonance obviously overlaps with the resonance from the BN_3 units. REAPDOR curves derived from the peak area do not reach the theoretical plateau value, which can be attributed to the aforementioned ^{11}B resonance at about 10 ppm.

^{11}B spin echo studies

Experimental ^{11}B spin echo decay curves for the pyrolysis intermediates above 1050 °C are presented in Figure 5.35. The solid lines correspond to Gaussian fitting of the initial part of the decay curves ($2\tau < 0.1$ ms). The obtained homonuclear second moment, $M_{2(homo)}$, and the corresponding B-B distances, r_{BB}, are summarized in Table 5.14 and are plotted in Figure 5.36. Upon increasing the annealing temperatures, the experimental spin echo curves decay faster and the Gaussian fit reproduces the experimental data for longer evolution times. However, this deviation is still larger as compared to h-BN. The obtained $M_{2(homo)}$ increases with increasing temperatures, resulting in a decrease of the B-B distances. It indicates that the crystal ordering in the BN domains continuously increases with increasing pyrolysis temperature. Finally, at 2000 °C the obtained B-B distance of 2.53 $\AA$ is very close to that of h-BN (2.51 Å).

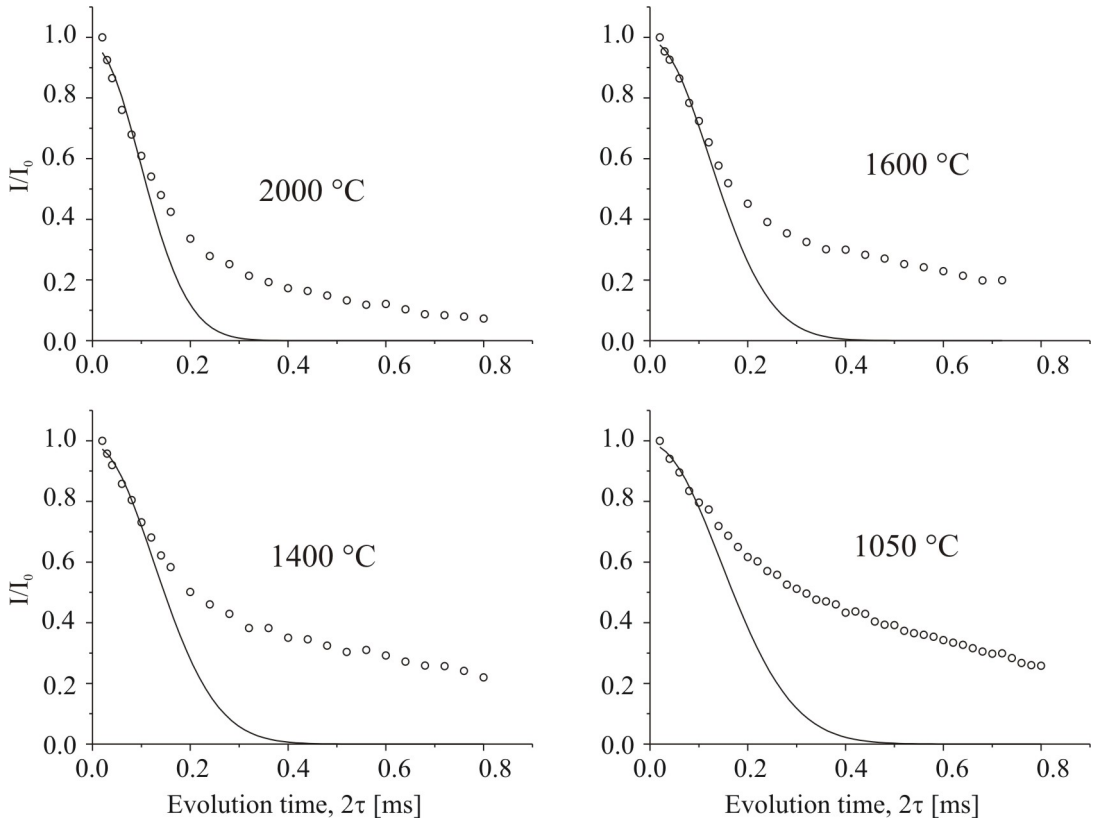

Figure 5.35. ^{11}B spin echo decay curves for precursor system **4**. Open circles refer to the experimental data. The solid lines are theoretical curves with the $M_{2(homo)}$ values given in Table 5.14.

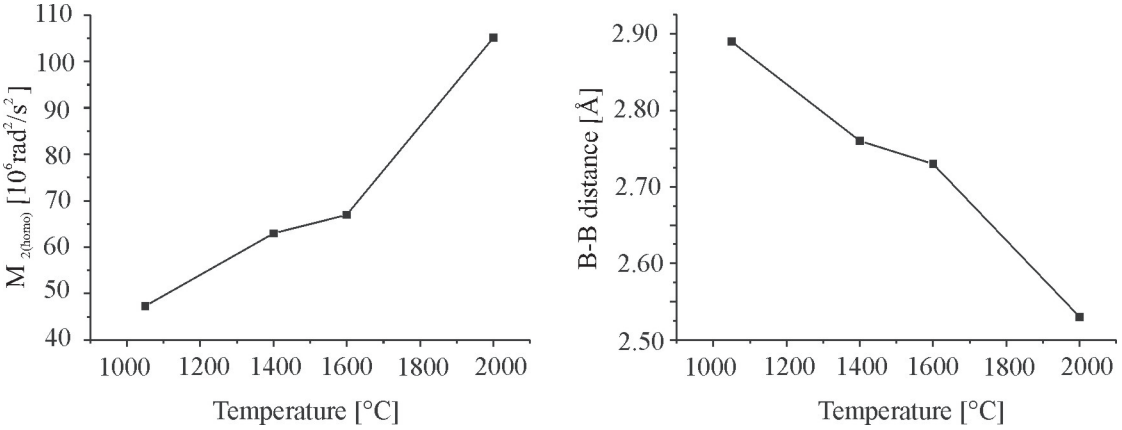

Figure 5.36. Homonuclear second moments (left) and the B-B distances (right) against annealing temperature for precursor system **4**.

Table 5.14. ^{11}B spin echo data for precursor system **4**.

Annealing temperature	$\mathbf{M_{2(homo)}}[10^6 rad^2/s^2]$	**B-B distance**
2000 °C	105	2.53 Å
1600 °C	67	2.73 Å
1400 °C	63	2.76 Å
1050 °C	47	2.89 Å

5.2.5 ^{15}N labeled boron-modified hydrosilylized polyhydridovinylsilazane 5

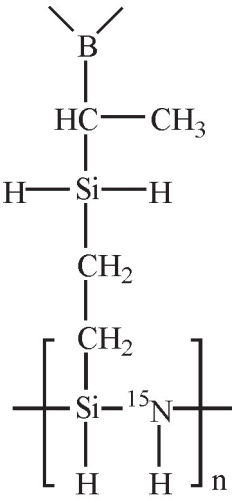

Precursor 5

The composition in at.% of the ceramic derived from precursor 5 is 48.3 (Si), 3.5 (B), 34.5 (C), 13.7 (N) and the corresponding empirical formula is $Si_6B_{1.1}C_{10}N_{3.4}$ [68]. In the obtained ceramic material the amount of Si and C is almost twice the values of the ceramics derived from precursors 1 to 4.

^{13}C NMR studies

^{13}C NMR spectra of precursor 5 pyrolized at 1050 and 1400 °C are depicted in Figure 5.37. The spectrum of the **1050 °C** sample exhibits resonances from sp^2- and sp^3-carbons. The relative intensity of the sp^3-carbon signal is higher as compared to precursor systems 1 to 4. This finding can be explained by the higher amounts of Si per N and B atoms, which leads to an increase of CSi_4 units in SiC and a reduction of sp^2-carbon. The higher amount of SiC is supported by the ^{29}Si NMR results. Upon heating to **1400 °C**, the ^{13}C NMR spectrum shows only the resonance of sp^3-carbons.

^{29}Si NMR studies

The ^{29}Si NMR spectra of precursor 5, pyrolized at temperature between 1050 and 1800 °C, are depicted in Figure 5.37. The results derived from Gaussian line fitting of the ^{29}Si NMR spectra are summarized in Table 5.37. At **1050 °C** the broad spectrum is attributed to SiC_3N, SiC_4 and $SiCN_3$ units with relative intensities of 24, 51 and 7 %, respectively. The observation of a high intensity for the SiC_4 units is consistent with the discussed ^{13}C NMR data.

Upon pyrolysis at **1400 °C**, the decrease in intensity of the SiC_2N_2 units is

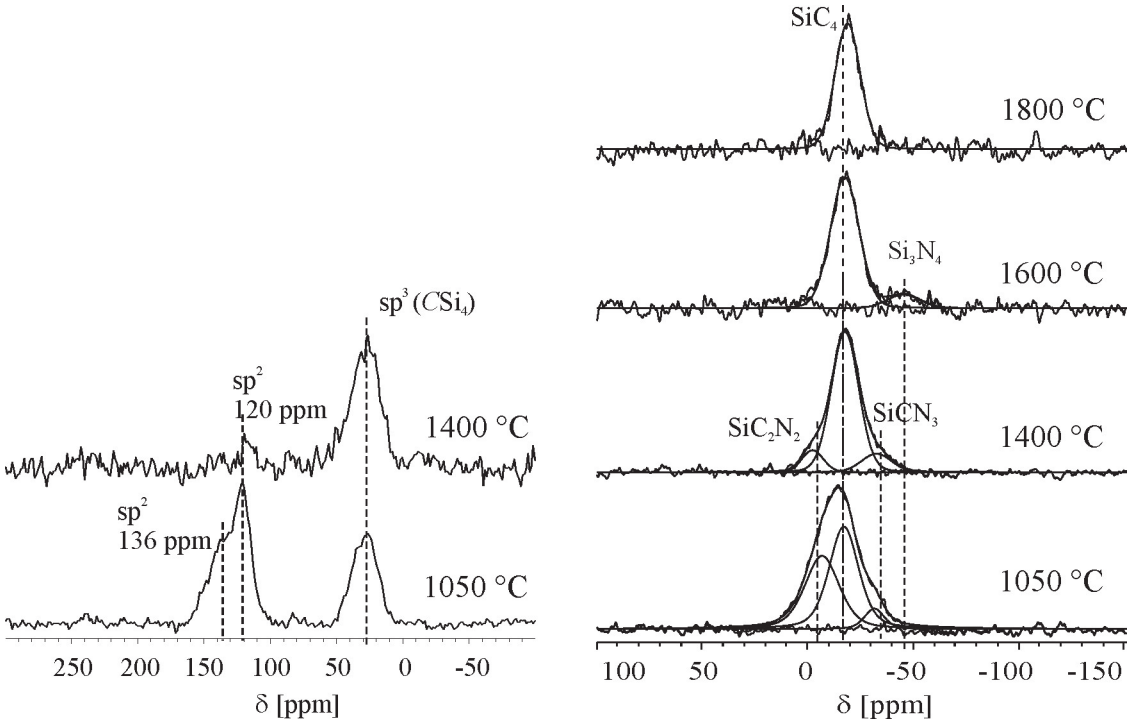

Figure 5.37. Single pulse ^{13}C (left) and ^{29}Si (right) MAS NMR spectra of precursor system **5**.

accompanied by an intensity increase of the SiC_4 units, while the signal from $SiCN_3$ units remains almost unchanged. After annealing at **1600 °C**, the ^{29}Si NMR spectrum shows separation of the crystalline SiC and Si_3N_4 phases. However, the intensity of Si_3N_4 is very low and the peak disappears completely after pyrolysis at 1800 °C, because of the decomposition of the Si_3N_4 crystalline phase. These results are in full agreement with the X-ray analysis presented in a former study [71]. The high temperature stability of the precursor system **5** is low with respect to other systems and it decomposes at 1850 °C. This can be associated with its relatively low content of boron.

^{15}N NMR studies

^{15}N MAS NMR spectra were recorded for the samples pyrolized between 1050 and 1800 °C (see Figure 5.38). At **1050 °C**, the ^{15}N NMR spectrum shows tri-coordinated nitrogen sites, which are assigned to NHB_2, NB_3 and NSi_3 units

Table 5.15. ^{29}Si NMR data derived from Gaussian line fitting.

Precursor	$\delta_{(^{29}Si)}$ [ppm]			
system 5	SiC$_2$(sp^3)N$_2$	SiC$_4$	SiCN$_3$	Si_3N$_4$
1800 °C	-	-18.4	-	-
1600 °C	-	-17.3	-	-44.7
1400 °C	-1.8	-17.2	-32	-
1050 °C	-6.3	-16.6	-31	-
	Relative intensity [%]			
1800 °C	-	100	-	-
1600 °C	-	89	-	11
1400 °C	9	79	12	-
1050 °C	42	51	7	-

with relative intensities of 31, 33 and 36 %, respectively. Moreover, the spectrum exhibits a high signal to noise ratio that significantly reduces after pyrolysis above this temperature. This might be an indication that the carbon centered radicals are located close to the nitrogen atoms.

In the spectrum of the **1400 °C** sample the peak from the BHN_2 units disappears. This indicates the efficiency of the crosslinking in the present precursor system as compared to precursor system **1**. In the present precursor **5**, silicon atoms are bonded to H as in precursor **2**, while in precursor **1** the silicon atoms are bonded to CH_3. As discussed earlier for precursor system **2**, a higher degree of crosslinking is due to the fact that the silicon bonded CH_3 substitution is replaced by H.

For the pyrolysis intermediates above **1400 °C**, the ^{15}N NMR spectra are almost identical. These spectra contain contributions from NB_3 and NSi_3 units. The relative amount of the NB_3 and NSi_3 units is the same as found for the other Si-B-C-N precursor systems. It indicates that nitrogen has a higher affinity to boron rather than to bind silicon, independent of the amount of silicon. However, the overall signal to noise ratio is lower as compared to precursor systems **1** to **4** since the nitrogen content is low.

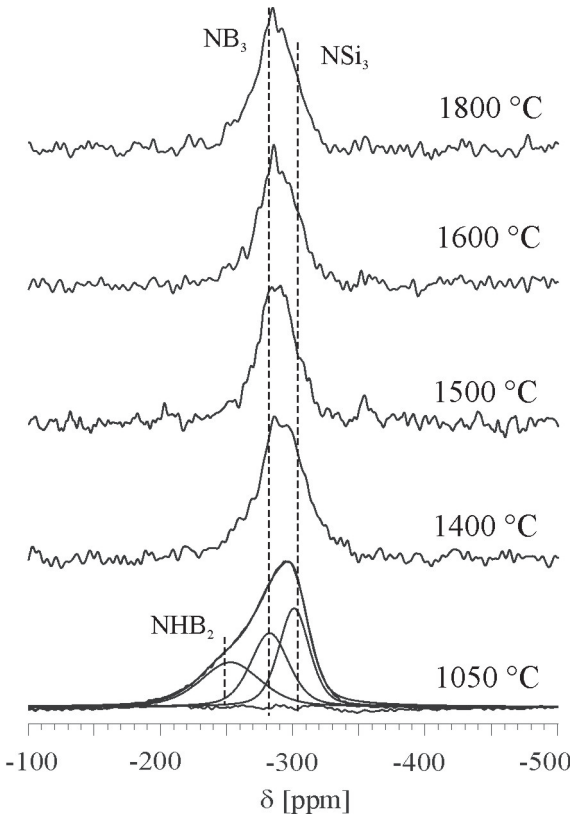

Figure 5.38. Single pulse ^{15}N MAS NMR spectra of precursor system **5**.

The local environment of nitrogen remains the same above this temperature. That is, the thermal reaction (see Figure 5.11), resulting in the breaking of the Si-N bonds to form N-B bonds, are completed at 1400 °C. This finding is confirmed by the ^{11}B{^{15}N} REDOR results (see below).

^{11}B{^{15}N} REDOR and ^{11}B{^{15}N} SEDOR studies

^{11}B{^{15}N} REDOR and SEDOR experiments were performed on precursor **5** pyrolized at temperatures between 1050 and 1900 °C. The ^{11}B NMR spectra obtained from REDOR experiments after a dipolar evolution period of 0.8 ms are presented in Figure 5.39. For the pyrolysis intermediate at **1050 °C**, the line shapes of the full (S_0) and dephased (S) spectra are not identical. The peak at about 20 ppm

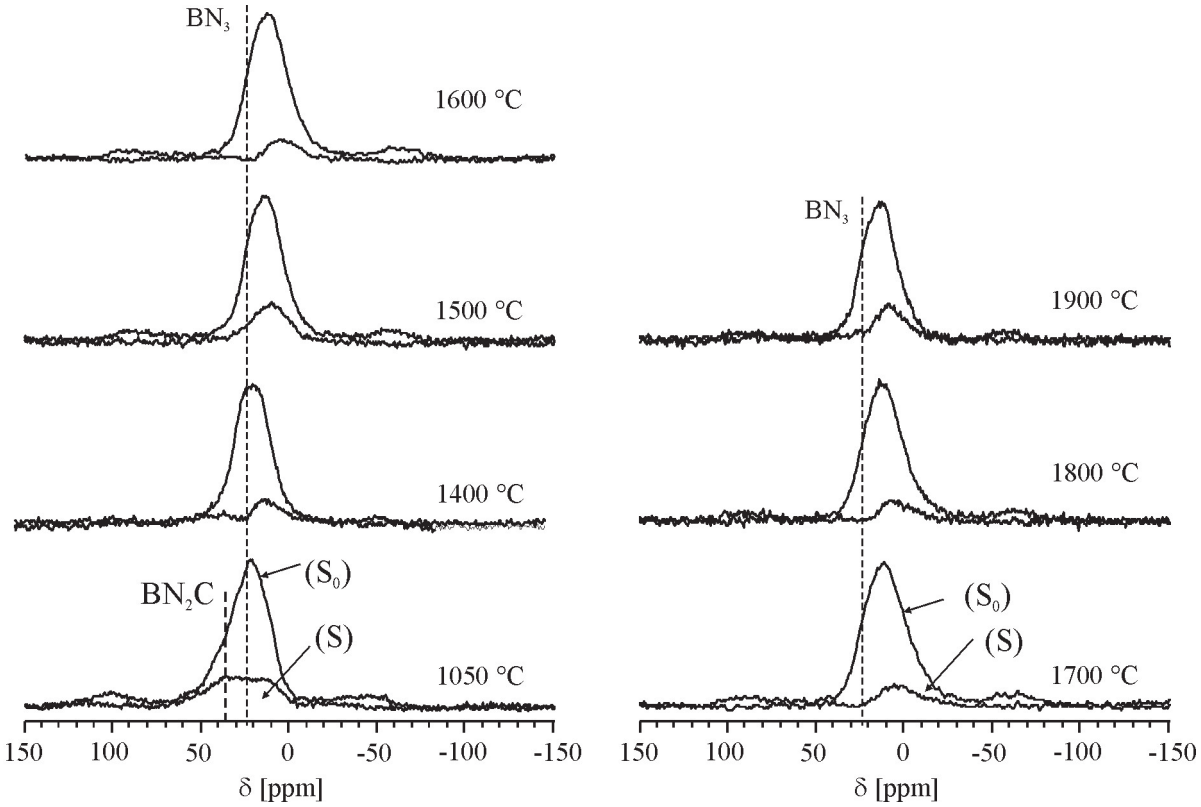

Figure 5.39. $^{11}B\{^{15}N\}$ REDOR spectra of precursor system **5** after an evolution time of τ=0.8 ms (ν_r=10 kHz).

associated to the BN_3 units exhibits a more efficient dephasing. The peak at about 35 ppm is due to BN_2C units. Therefore, it exhibits a weaker dipolar coupling as compared to the BN_3 units.

After pyrolysis above **1400 °C**, the resonance from BN_2C units disappears. Consequently, the dipolar dephasing between boron and nitrogen atoms occurs only due to BN_3 units. Moreover, for all REDOR spectra a resonance at about 10 ppm can be identified, which obviously does not experience any dephasing even at longer dipolar evolution periods.

Figure 5.40 shows representative REDOR and SEDOR data and the corresponding simulations. The parameters derived from the simulations are summarized in Table 5.16 and are plotted in Figure 5.42 against annealing temperature. It can be seen that the B-N distances obtained from REDOR and SEDOR experiments are

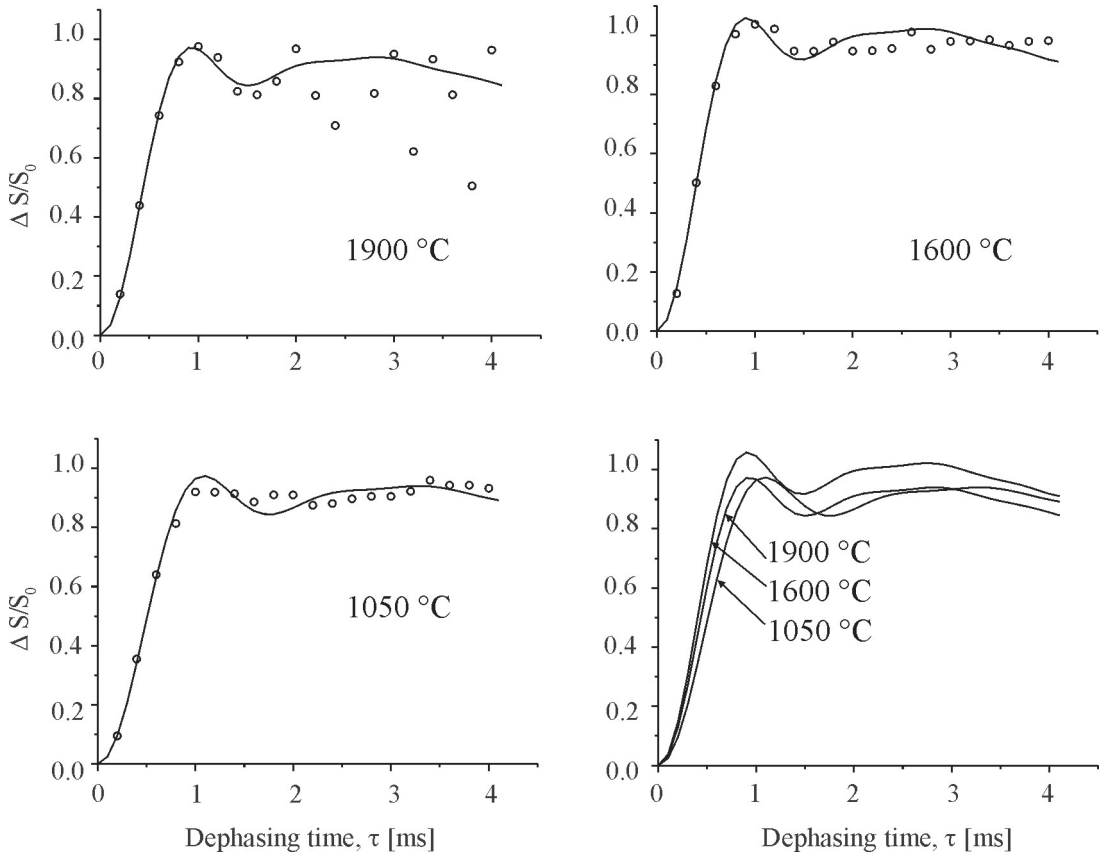

Figure 5.40. $^{11}B\{^{15}N\}$ REDOR curves for precursor system **5**. Open circles refer to the experimental data. The solid lines are theoretical curves for a BN_3 spin system with parameters given in Table 5.16.

comparable. The longest B-N distance (1.62-1.69 Å) as well as the lowest value for the scaling factor (0.92) are found for the intermediate at 1050 °C. This observation is in agreement with the presence of BN_2C units besides BN_3 at this temperature.

For the pyrolysis intermediates between 1400 and 1800 °C, the B-N distances derived from the REDOR experiments are almost identical (1.53 - 1.55 Å) and 7 % longer than in h-BN. The scaling factor increases from 0.97 to 1 with increasing annealing temperature. It should be noted that in general a good match between experimental and theoretical REDOR curves can be achieved. This indicates that the BN_3 units has a planar geometry as in h-BN structure. In addition, the decrease of the scaling factor observed at 1900 °C might be associated with the structural changes in the ceramic is caused by high temperature decomposition at 1850 °C.

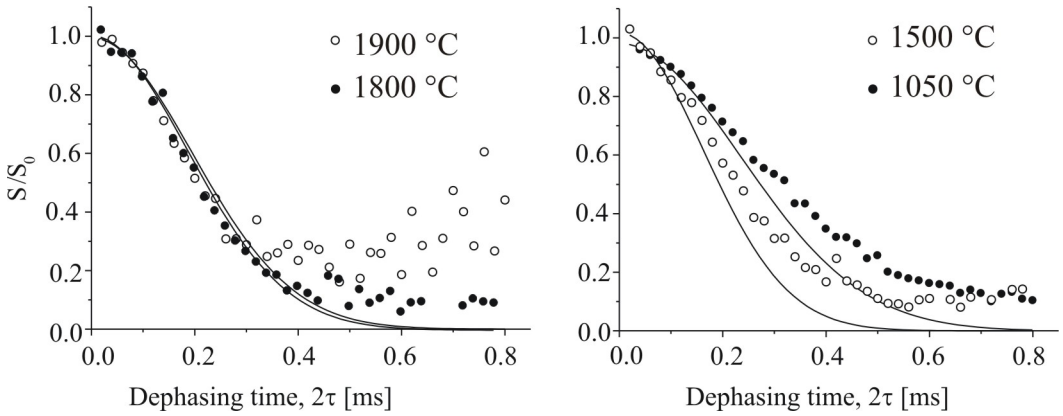

Figure 5.41. $^{11}B\{^{15}N\}$ SEDOR curves for precursor system **5**. Open circles refer to the experimental data. The solid lines are theoretical curves with the $M_{2(hetero)}$ values given in Table 5.16.

Table 5.16. $^{11}B\{^{15}N\}$ REDOR and SEDOR data for precursor system **5**.

Annealing temperature	REDOR			SEDOR	
	Dipolar coupling constant [Hz]	**Scaling factor**	**B-N distance**	$\mathbf{M_{2(hetero)}}$ $[10^6 rad^2/s^2]$	**B-N distance**
1900 °C	1070	0.92	1.54 Å	34.0	1.48 Å
1800 °C	1070	1.00	1.54 Å	30.5	1.51 Å
1700 °C	1070	1.00	1.54 Å	30.1	1.51 Å
1600 °C	1100	1.00	1.53 Å	30.1	1.51 Å
1500 °C	1050	0.98	1.55 Å	27.4	1.54 Å
1400 °C	1050	0.97	1.55 Å	24.3	1.57 Å
1050 °C	920	0.92	1.62 Å	15.6	1.69 Å

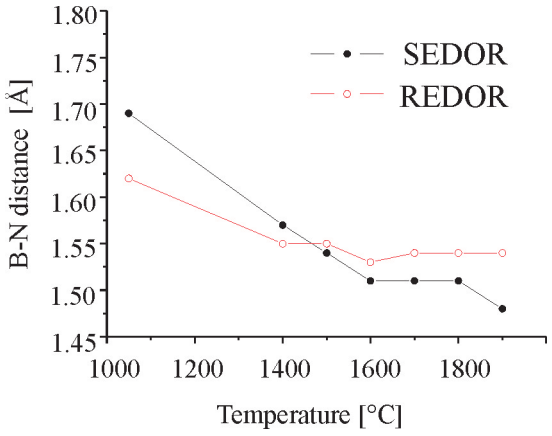

Figure 5.42. The B-N distances against annealing temperature for precursor system **5**.

^{11}B spin echo studies

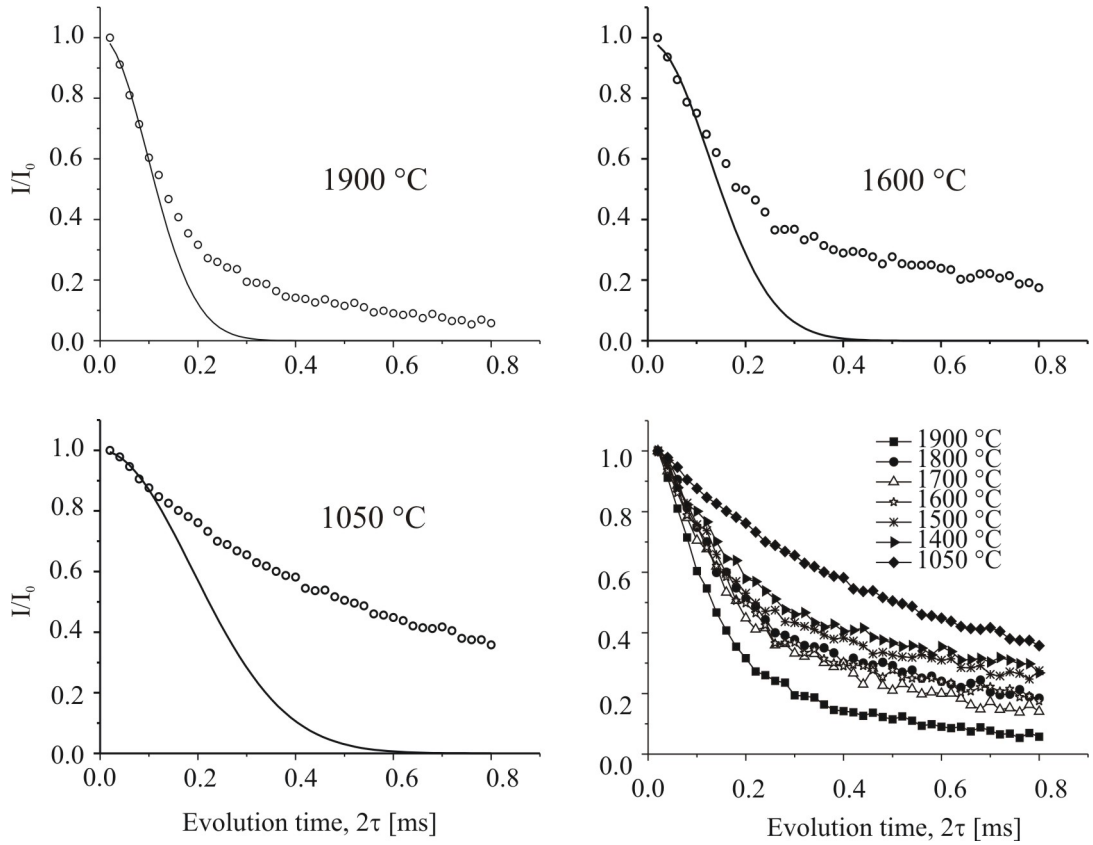

Figure 5.43. ^{11}B spin echo decay curves for precursor system **5**. The symbols refer to the experimental data. The solid lines are theoretical curves with the $M_{2(homo)}$ values given in Table 5.17.

^{11}B spin echo experiments were performed on the pyrolysis intermediates between 1050 and 1960 °C. Figure 5.43 shows representative ^{11}B spin echo experimental decays and Gaussian fit theoretical curves of the initial part of the decays. The homonuclear second moments ($M_{2(homo)}$) derived from the fitting and the obtained B-B distances (r_{BB}) are summarized in Table 5.17 and are plotted in Figure 5.44. The B-B distance is computed assuming that boron is surrounded by 6 boron neighbors as in h-BN.

At **1050 °C**, $M_{2(homo)}$ is $28.06 \cdot 10^6 rad^2/s^2$, while the corresponding B-B distance is 3.07 Å. This value is thus 22 % larger than in pure h-BN (2.51 Å). Therefore, a fully developed BN layer structure does not exist at this temperature. This finding

Table 5.17. ^{11}B spin echo data for precursor system **5**.

Annealing temperature	$\mathbf{M_{2(homo)}}[10^6 rad^2/s^2]$	**B-B distance**
1900 °C	105.13	2.53 Å
1800 °C	63.92	2.75 Å
1700 °C	73.36	2.69 Å
1600 °C	61.87	2.77 Å
1500 °C	57.59	2.80 Å
1400 °C	50.05	2.86 Å
1050 °C	28.06	3.15 Å

is consistent with the ^{11}B and ^{15}N NMR results, which show the presence of BCN_2 and NHB_2 units. However, $M_{2(homo)}$ increases as the annealing temperature increases and finally, at 1960 °C a B-B distance of 2.53 Å, almost the same as in h-BN, is obtained. The B-B distances are temperature dependent, while the B-N distances are found almost identical for the intermediates above 1400 °C.

In this context, the important role of sp^2-carbon for the precursor-derived ceramic stability should be again pointed out. It has been assumed that the extraordinary high temperature stability in Si-B-C-N ceramics is associated with the reduction of carbon activity due to boron addition. On the basis of our studies the incorporation of sp^2-carbon nanodomains in the BN layer can be excluded, which results in interdegitated structures along with bond distortions of the host layers. In this case, additional B-C bonds are expected.

However, separate but intercalated BN and sp^2-carbon (graphite-like) layers might be discussed, which do not require B-C bond formation. In this case, the decrease of the B-B distances can be explained by the structural rearrangements along with a better layer packing, resulting in crystallization of h-BN.

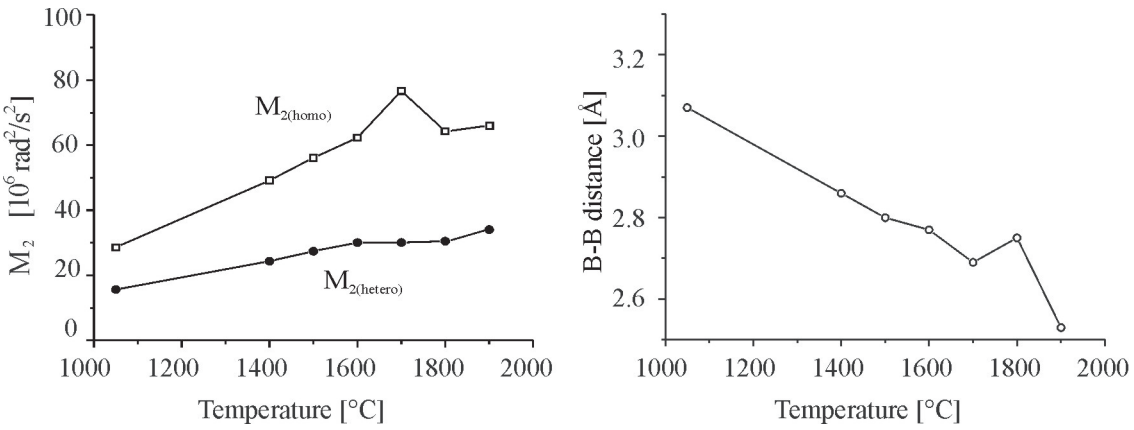

Figure 5.44. Homo- and heteronuclear second moments (left) and B-B distances (right) against annealing temperature for precursor system **5**.

5.2.6 Boron-modified hydridosilylized polyhydridovinylsilazane 6

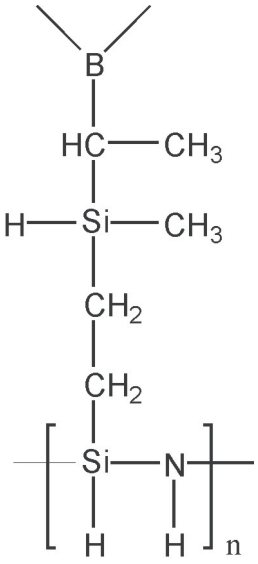

Precursor 6

The molecular structure of precursor **6** is similar to that of precursor **5**, and contains two silicon atoms per monomer units. Therefore, the composition of ceramics derived from these precursors is comparable:

Ceramics	Ceramic composition
precursor **5**	$Si_6B_{1.1}C_{10.0}N_{3.4}$
precursor **6**	$Si_6B_{1.2}C_{11.5}N_{3.4}$

The higher amount of carbon atoms in the obtained ceramic **6** is due to the terminal CH_3 group bonded to the second silicon atom. In the case of precursor **5** that silicon atom is bonded to H.

^{13}C and ^{29}Si NMR studies

^{13}C NMR spectra of precursor **6** pyrolized at temperatures between 600 and 1050 °C are given in Figure 5.45. The spectrum of the **600 °C** sample exhibits a single peak at 2 ppm attributed to the CH_3Si unit. In the spectrum of the **800 °C** sample a broad peak at about 120 ppm attributed sp^2- carbon appears, while the signal from sp^3- carbon is not observed. It should be emphasized that the present sample shows a significantly higher signal to noise ratio as compared to other precursors treated at same temperature. According to the EPR study performed in previous work for precursor system **6**, the highest EPR signal was observed for the 800°C sample, while for other precursor systems, the significant increase in EPR signal has been observed only after pyrolysis at 1050 °C [74]. Therefore, the increase of the S/N ratio for the present sample can be explained by the presence of the higher

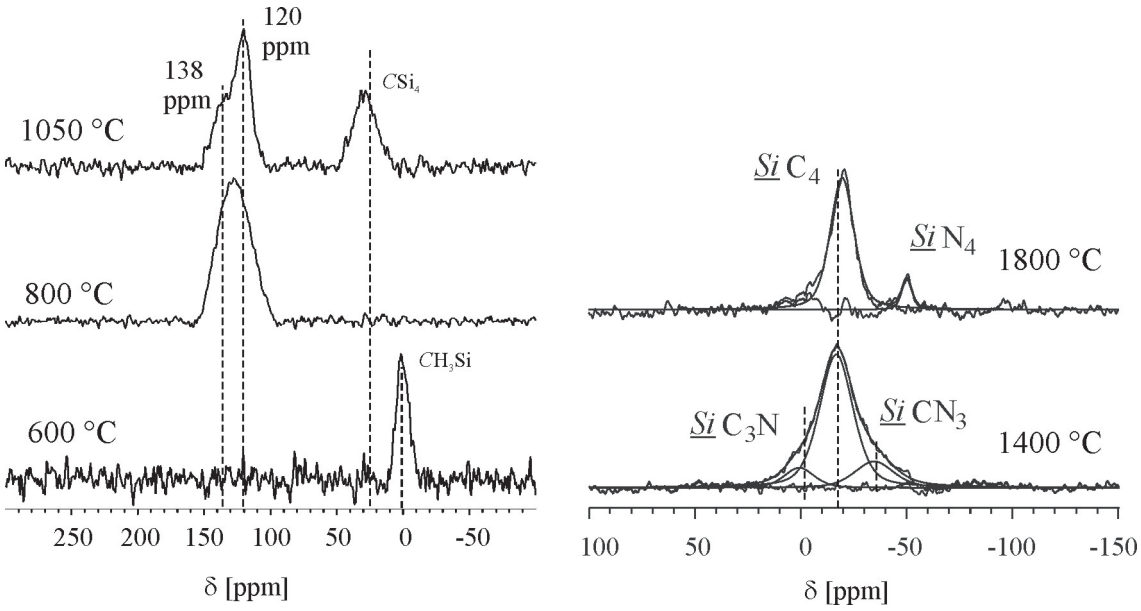

Figure 5.45. Single pulse ^{13}C (left) and ^{29}Si (right) MAS NMR spectra of precursor system **6**.

concentration of paramagnetic defects (see Section 5.2.1).

After annealing at **1050°C**, both sp^2 (graphite-like) and sp^3 (tetrahedral) carbons signals are observed. The relative intensity of the sp^2-carbon signal is higher than that for precursor **5** pyrolized at the same temperature. This observation is consistent with the higher amount of carbon. The ^{13}C NMR spectrum of the **1400 °C** sample, obtained using a recycle time of 15 s, does not show any resonance. It indicates that the crystallization of the amorphous carbon starts at this temperature, resulting in an increase of the ^{13}C spin-lattice relaxation time T_1.

The ^{29}Si NMR spectrum of the 1400 °C sample shows the SiC_3N, SiC_4 and $SiCN_3$ units with relative intensities of 11, 80 and 9 %, respectively. Upon annealing at 1800 °C, an amorphous Si-C-N matrix transforms into crystalline SiC_4 and Si_3N_4 phases with relative intensities of 90 and 9 %, respectively.

^{11}B{^{14}N} REAPDOR studies

^{11}B MAS NMR spectra of precursor **6**, pyrolized between 600 and 1400 °C, and of

h-BN are depicted in Figure 5.46. The ^{11}B NMR spectrum of the **600 °C** sample is broader than that of the samples pyrolized at higher temperature, because of the additional resonances from BNC_2, BN_2C and BC_4 units besides the main resonance from BN_3 units. Due to the second order quadrupolar broadening, the resonances from tri-coordinated boron sites overlap. However, the resonance from BC_4 units can be identified since it has a much smaller quadrupolar coupling constant. The shoulder at about -2 ppm, attributed to BC_4 units, decreases in intensity up to 1050 °C. Below 1400 °C a shoulder at about 30 ppm is visible, which is due to tri-coordinated boron bonded to nitrogen and carbon atoms. The resonance at about 40 ppm stems from BN_2C units, which exists after pyrolysis at 1050 °C. The spectrum of the 1400 °C sample is dominated by BN_3 units.

^{11}B{^{14}N} REAPDOR experiments were performed for these pyrolysis intermediates. ^{11}B{^{14}N} REAPDOR spectra after an evolution time of 1.0 ms (10 rotor periods) are given in Figure 5.46. The intensity at about 20 ppm for the pyrolysis intermediates between 600 and 1050 °C is reduced in the dephased spectra. However, for the 1400 °C sample a significant decrease of that signal is observed due to the absence of the BN_2C units. In addition, the signal from BC_4 units (at about -2 ppm) does not show any dephasing.

The results from the REAPDOR analysis, i.e. $(S_0\text{-}S)/S_0$ ratio as a function of dephasing time obtained by using the peak intensity at about 20 ppm and by signal integration, are depicted in Figure 5.47 (left) and (right), respectively. The solid lines correspond to the simulated curve for BN_3 spin system with a N-B-N angle of 120° and a bond distance of 1.44 $\AA$ as for h-BN. In general, the experimental REAPDOR fractions from the peak intensity show higher values as compared to those from integrations. For the **600°C** sample, the low plateau value of 0.3 is due to BC_4 units, whose amount is higher in the present sample. For samples pyrolized above **800 °C**, the maxima of the dipolar dephasing between ^{11}B and ^{14}N nuclei

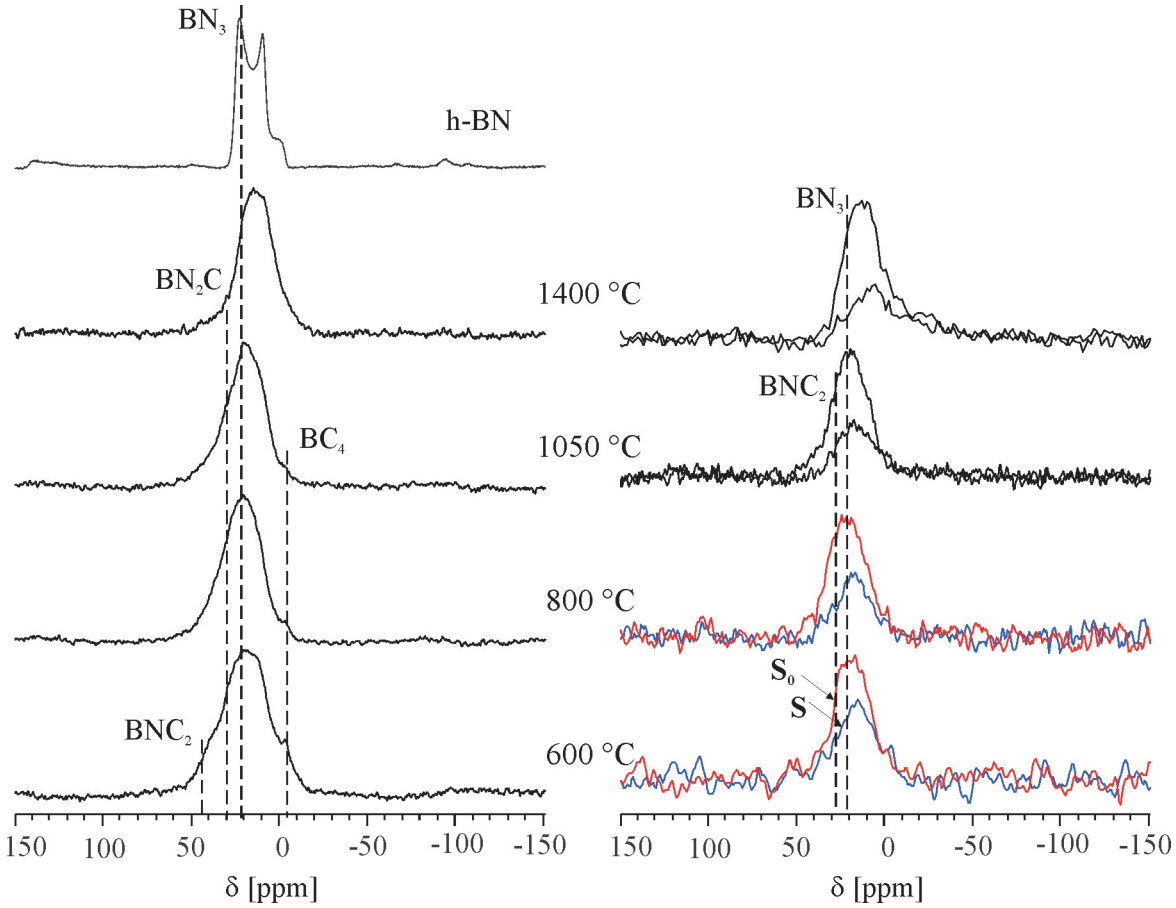

Figure 5.46. Single pulse ^{11}B MAS NMR spectra of precursor system **6** and h-BN (left). ^{11}B{^{14}N} REAPDOR spectra of precursor system **6** (right) after evolution time of τ=1 ms (ν_r=10 kHz).

indicate an increase of the BN_3 units. For the 1400 °C sample, the experimental REAPDOR fraction derived from the peak intensity exhibits good agreement with the simulated curves (solid lines in Figure 5.47), while for the 1050 °C sample the simulated curve is scaled by 0.8 (dashed lines in Figure 5.47).

^{11}B spin echo experiment

The experimental ^{11}B spin echo decay curves for the pyrolysis intermediates between 600 1400 °C are presented in Figure 5.48 (open circles). The solid lines correspond to Gaussian fittings of the initial part of decay curves. The corresponding second moment values are summarized in Table 5.18, which show the same behavior as in previous precursor systems **1**, **3** and **5**, i.e. $M_{2(homo)}$ for the 600 and 800 °C samples

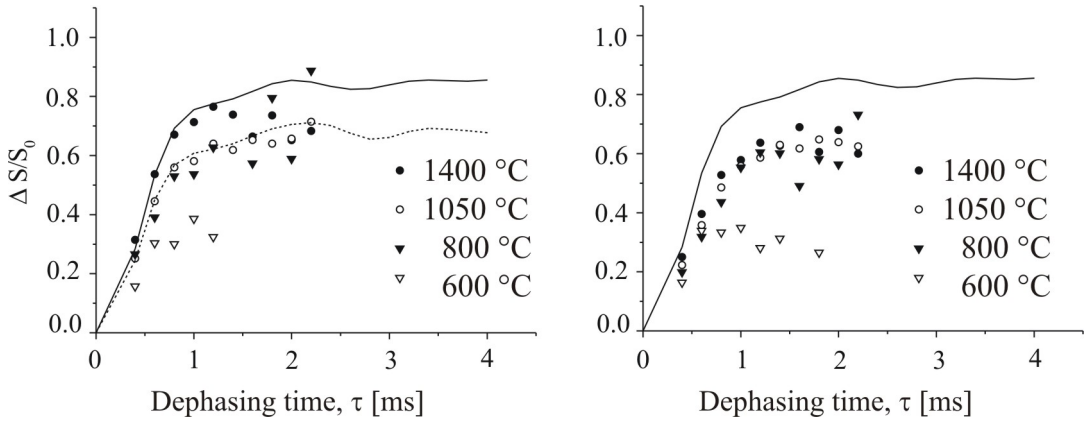

Figure 5.47. $^{11}B\{^{14}N\}$ REAPDOR curves for precursor system **6** (ν_r=10 kHz). The symbols refer to the experimental data obtained from the peak intensity at about 20 ppm (left) and from the total peak area (right). The solid lines are theoretical curves for a BN_3 spin system with B-N distances of 1.44 Å. The dashed lines are theoretical curves scaled by 0.8.

are higher than that for 1050 °C sample. This is in contrast to the expectations. We assume that the faster spin echo decay curves for these samples are due to BN_2C and BN_3 units, which have different resonance frequencies. Therefore, the result cannot be analyzed in terms of pure homonuclear second moment. A more detailed explanation can be found in Section 5.2.1.

The B-B distances obtained for the 1050 and 1400 °C samples are 2.99 and 2.73 Å, respectively. The B-B distance increases with increasing annealing temperature. However, it is still longer than in h-BN.

Table 5.18. ^{11}B spin echo data for precursor system **6**.

Annealing temperature	$\mathbf{M_{2(homo)}}[10^6 rad^2/s^2]$	**B-B distance** [Å]
1400 °C	67.3	2.73
1050 °C	38.5	2.99
800 °C	61.5	-
600 °C	62.6	-

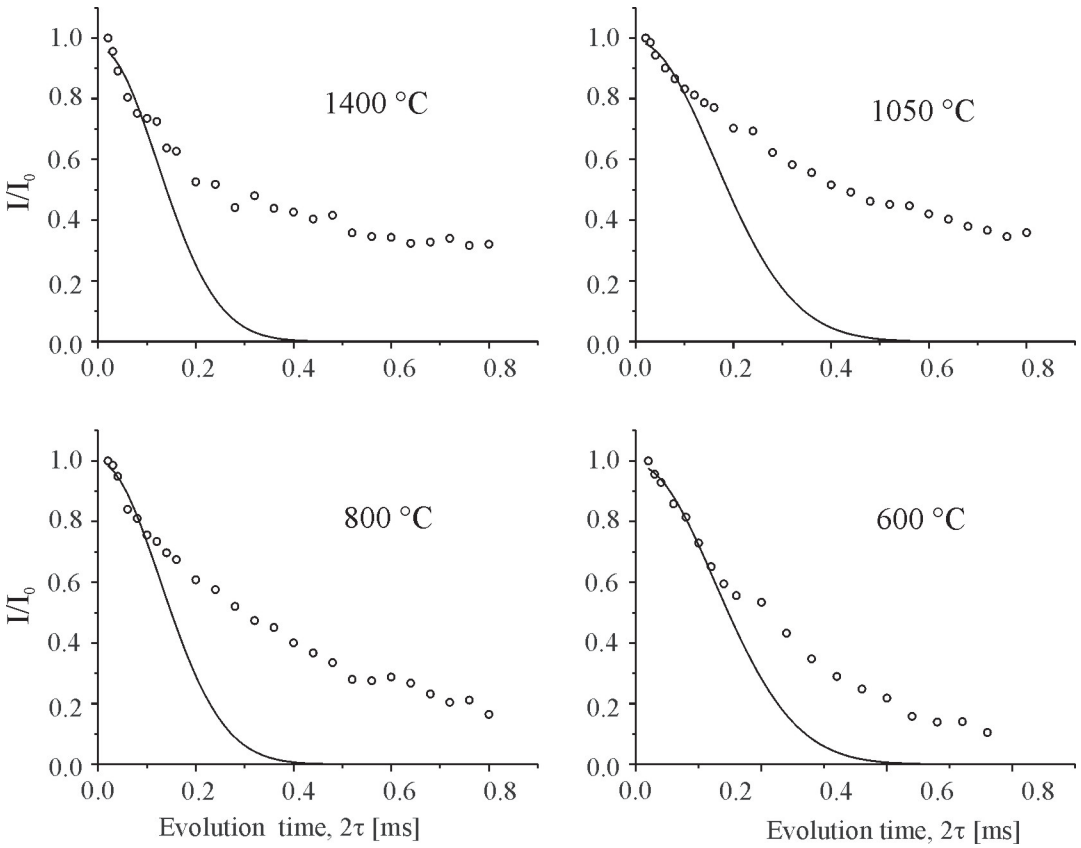

Figure 5.48. ^{11}B spin echo decay curves for precursor system **6**. Open circles refer to the experimental data. The solid lines are theoretical curves with the $M_{2(homo)}$ values given in Table 5.18.

5.2.7 ^{15}N labeled boron-modified polyhydridovinylsilylcarbodiimide 7

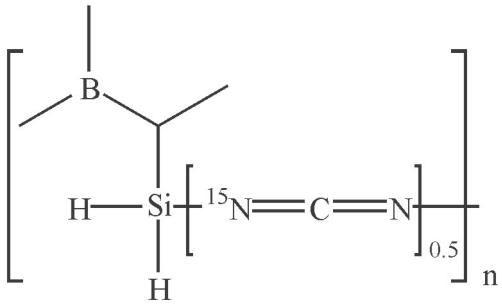

Precursor 7

The molecular structure of precursor **7** differs from previous precursors, as it contains carbodiimide. However, the Si:B:N atomic ratio of 3:1:3 is the same as for previous precursor systems **1** to **4**.

^{13}C and ^{29}Si NMR studies

Figure 5.49 presents ^{13}C CP (left) and SP (right) MAS NMR spectra of precursor **7** pyrolized between 600 and 1400 °C. In the ^{13}C CP/MAS spectrum of the **600 °C** sample two broad signals associated with sp^2- and sp^3-carbons are detected. The resonance from sp^2-carbons centered at 136 ppm is due to graphene-like amorphous carbon, while the sp^3-carbons resonance between 50 and -5 ppm is attributed to the CH_xSi_{3-x} (x=0, 1, 2 and 3) units. The respective ^{13}C SP/MAS NMR spectrum exhibits a single peak at 5 ppm attributed to CH_3Si units. It should be noted that ^{13}C CP and SP NMR spectra are identical to those observed for the pyrolysis intermediate **1** treated at the same temperature (see page 80). Therefore, a more detailed discussion can be found in Section 5.2.1.

The spectrum of the **800 °C** sample shows sp^2 graphite-like carbons. The absence of CH_3Si units indicates a further evolution of the Si-C-N ceramic network. In the SP spectrum of the **1050 °C** sample, resonances from graphite-like carbons and CSi units are detected. A signal from sp^3-carbons bonded to proton is not observed. However, the CP spectrum reveals the presence of CH_xSi_{3-x} units. A significant increase in signal to noise ratio of carbon spectrum is also found. In addition, the relative high intensity of graphite-like carbon with respect to CSi units, can

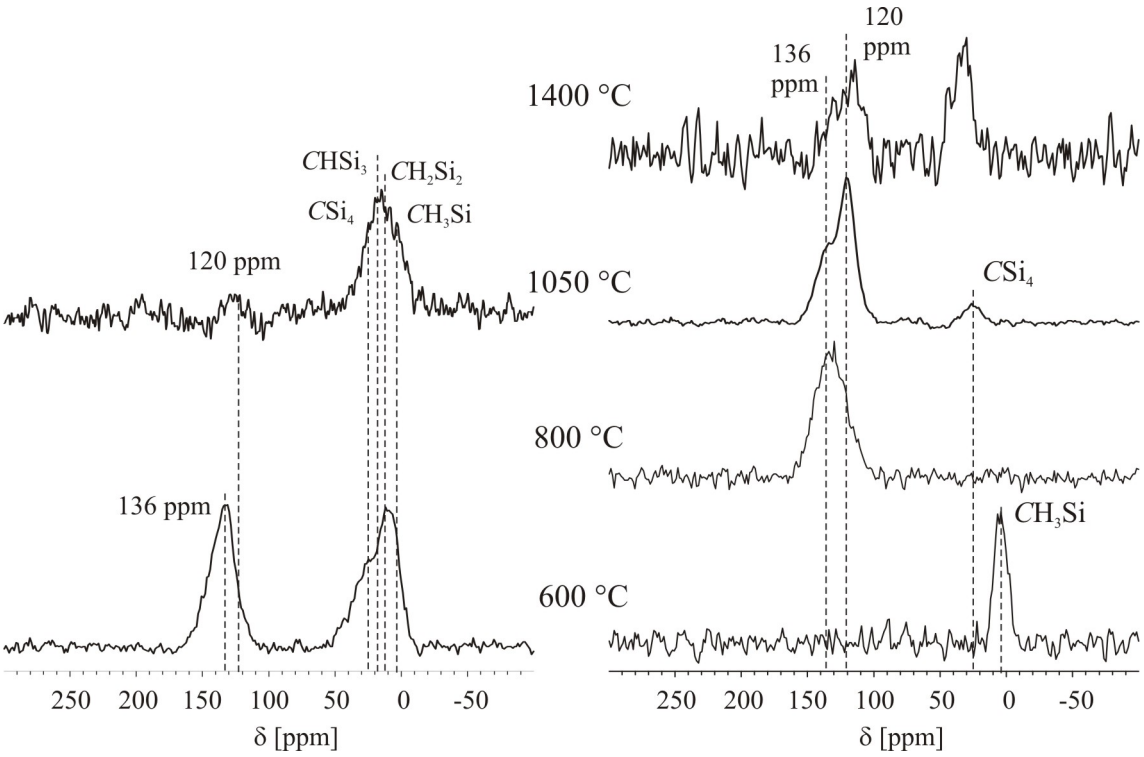

Figure 5.49. CP (left) and single pulse (right) ^{13}C NMR spectra of precursor system **7**.

be explained by the higher amount of nitrogen coordinated silicon (see ^{29}Si NMR). Upon pyrolysis at **1400 °C** the overall signal to noise ratio reduces, most likely due to long T_1 values of the carbon nuclei.

^{29}Si NMR spectra of precursor **7** pyrolized between 1400 and 1900 °C are presented in Figure 5.50. The results from Gaussian line fitting are summarized in Table 5.19. The spectrum of the **1400 °C** sample exhibit resonances from SiC_4, $SiCN_3$ and SiN_4 units with relative intensities of 49, 29 and 22 %, respectively. Upon pyrolysis at **1600 °C**, the signal from $SiCN_3$ units almost disappear, while the SiC_4 and SiN_4 units increase in intensity. In the spectrum of the **1900 °C** sample two signals at about -16.7 and -50.3 ppm with relative intensities of 89 and 11 %, respectively, can be identified. The significant decrease in linewidth of these signals indicate that they are due to the crystalline domains, reflecting SiC and Si_3N_4.

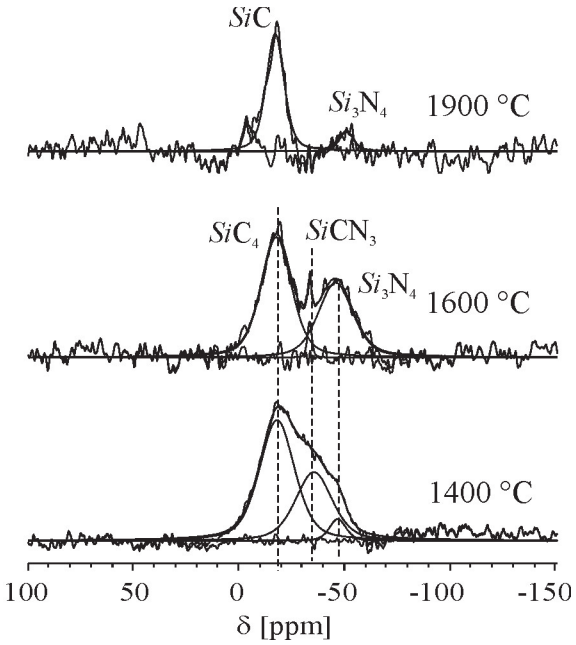

Figure 5.50. Single pulse ^{29}Si MAS NMR spectra of precursor system **7**.

Table 5.19. ^{29}Si NMR data derived from Gaussian line fitting.

Precursor	$\delta_{(^{29}Si)}$ [ppm]			**Line width** [Hz]			**Relative intensity** [%]		
system 7	SiC_4	$SiCN_3$	SiN_4	SiC_4	$SiCN_3$	SiN_4	SiC_4	$SiCN_3$	SiN_4
1900 °C	-16.7	-	-50.3	790	-	630	89	-	11
1600 °C	-17.2	-33.0	-45.2	1340	200	1530	57	3	40
1400 °C	-17.6	-35.0	-46.0	1560	1630	740	49	29	22

^{15}N NMR studies

Figure 5.51 shows ^{15}N MAS NMR spectrum of the pyrolysis intermediate at 1050 °C. The broad resonance is attributed to tri-coordinated nitrogen sites. Gaussian line fitting shows three peaks at about -258, -279 and -298 ppm with relative intensities of 14, 30 and 56 %, respectively. According to the chemical shift values (see Table 5.4) these peaks can be assigned to NHB_2 (14 %), NB_3 (30 %) and NSi_3 (56 %) units. Precursors **1** and **5**, pyrolized at the same temperature, contain the same structural units. However, in the present sample the relative intensity of BHN_2 units is smaller.

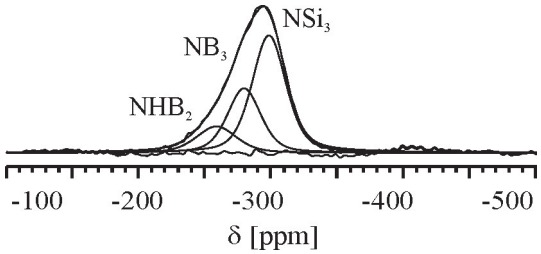

Figure 5.51. Single pulse ^{15}N MAS NMR spectrum of precursor **7** pyrolized at 1050 °C.

^{11}B NMR studies

Figure 5.52 (left) shows ^{11}B MAS NMR spectra of precursor **7** pyrolized between 400 and 1900 °C. For the **400 °C** sample, the broad resonance is due to BN_2C and BN_3 units, while the shoulder at about -2 ppm stems from BC_4 units. The signal from the BC_4 units decreases in intensity after pyrolysis at **600 °C** and disappears at **800 °C**, while the resonance from BCN_2 units remains up to **1050 °C**. The resonance at **1400 °C** is characteristic for BN_3 units in h-BN. Upon further heating, the ^{11}B NMR spectra remain almost unaltered apart from some additional broadening, which increases as the annealing temperature increases.

^{11}B{^{15}N} REDOR studies

^{11}B{^{15}N} REDOR experiment were performed on precursor system **7**, covering the whole temperature range from 400 to 1900 °C. Representative ^{11}B{^{15}N} REDOR spectra, denoted as S_0 (reference spectra) and S (dephased spectra) obtained after 6 rotor periods, are given in Figure 5.52 (right). For the **400 °C** sample, the dephased spectrum is reduced in intensity due to boron sites bonded to nitrogen, and the signal from BC_4 units does not experience any dipolar dephasing. Upon pyrolysis above **800 °C**, the ^{11}B{^{15}N} REDOR spectra alter marginally. In general, the strength of the dipolar dephasing for the present precursor system is found to be less as compared to previous precursor systems, as it is only 50 atom % ^{15}N enriched.

Experimental REDOR curves are given in Figure 5.53 (top). For the pyrolysis

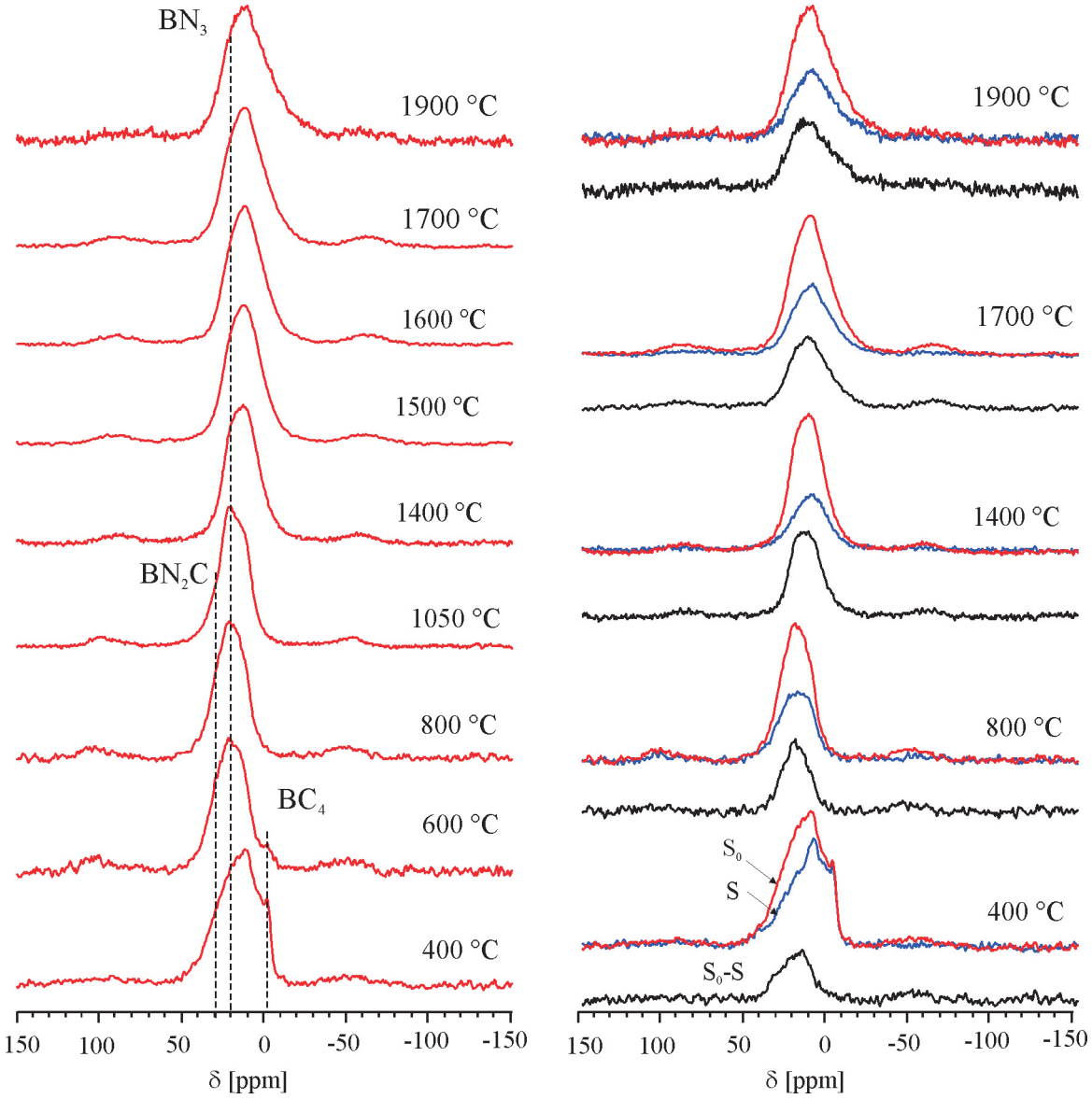

Figure 5.52. Single pulse ^{11}B MAS NMR spectra (left). ^{11}B{^{15}N} REDOR spectra of precursor system **7** after evolution time of τ=0.8 ms (ν_r = 10 kHz) (right).

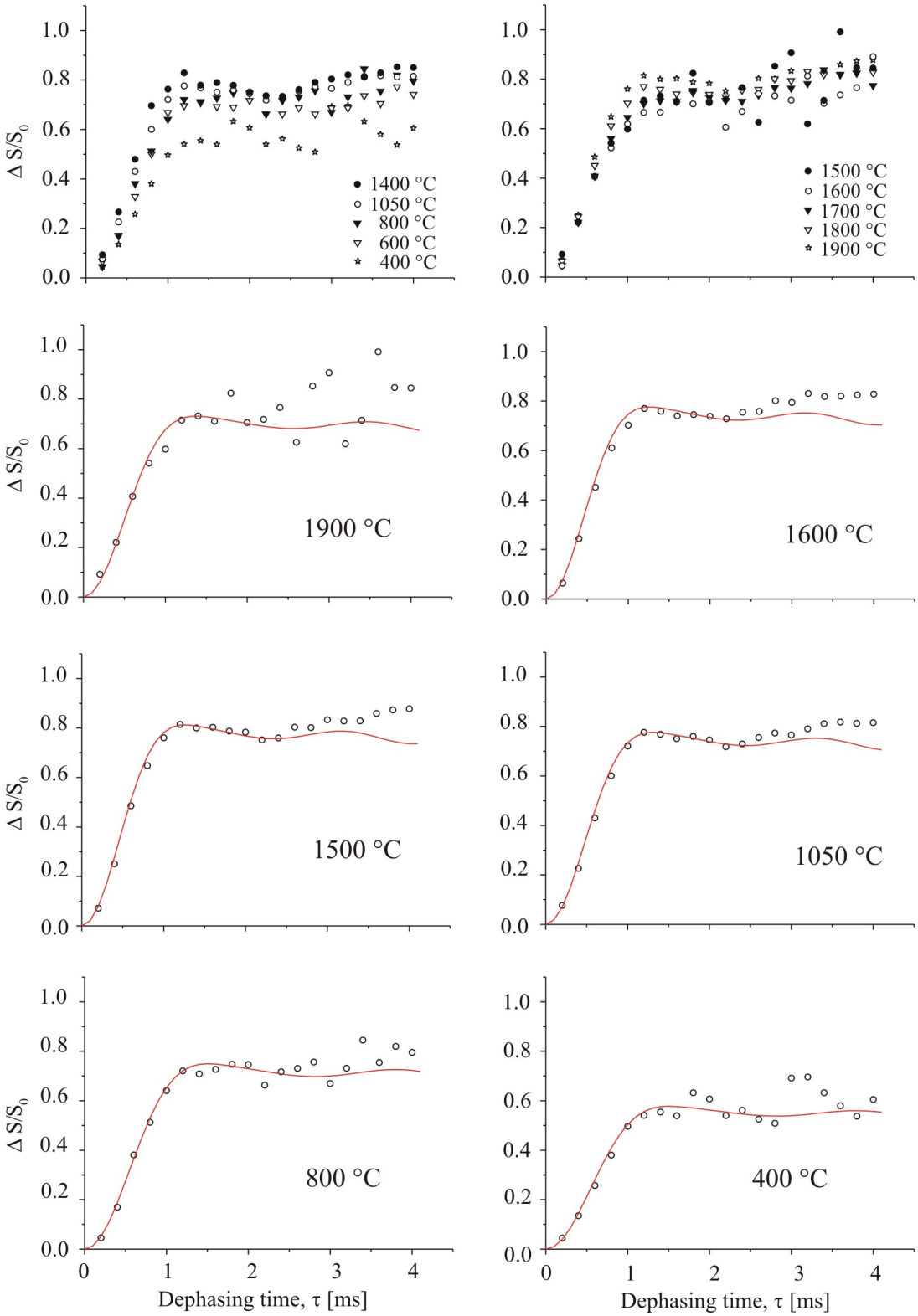

Figure 5.53. $^{11}B\{^{15}N\}$ REDOR curves for precursor system **7**. The symbols refer to the experimental data. The solid lines are to theoretical curves for a BN_3 spin system with parameters given in Table 5.20.

intermediates between 400 and 1400 °C, the REDOR fraction increases significantly with increasing the annealing temperature. Upon increasing the annealing temperatures between 1500 and 1900 °C, the REDOR curves decrease slightly. The obtained experimental REDOR curves were simulated assuming a planar BN_3 structure with identical bond lengths and ideal N-B-N bond angles of 120°. Considering only 50 atom % ^{15}N enrichment for precursor system **7**, the theoretical REDOR curves presented in Figure 5.53 (solid lines) are superpositions of the simulation of the curves from IS_3, IS_2, IS and I spin system (I=^{11}B, S=^{15}N) with statistical weights of 1/8, 3/8, 1/8 and 1/8, respectively. The dipolar coupling constant and scaling factor derived from the simulations and the corresponding B-N distances (r_{BN}) are summarized in Table 5.21. For the 400 °C sample, the lower scaling factor of 0.64 is due to the presence of BC_4 units. Upon further increasing the annealing temperature to 1400 °C, the scaling factor increases up to 0.91. The decrease of the scaling factor for the samples heated above 1400 °C might be due to the additional broadening of the ^{11}B NMR spectra. In general, the r_{BN} values are smaller as compared to previous precursor systems. The B-N distances decreases up to 1600 °C, then increases again which might be due to the aforementioned additional broadening in the ^{11}B NMR spectra.

^{11}B spin echo studies

^{11}B spin echo experiments were performed on precursor system **7**. The normalized spin echo decay curves for the pyrolysis intermediates between 400 and 1900 °C are given in Figure 5.54. The solid lines correspond to the Gaussian fitting of the initial part of the experimental decay curves ($2\tau < 0.1$). The obtained homonuclear second moment $M_{2(homo)}$, derived from the fittings, as well as the corresponding B-B distances, obtained by assuming a BN-layer structure, are summarized in Table 5.21 and are plotted in Figure 5.55. It has been already mentioned that the faster spin echo decay below 800 °C cannot be analyzed on the basis of pure homonuclear

Table 5.20. $^{11}B\{^{15}N\}$ REDOR data for precursor system **7**.

Annealing temperature	**Dipolar coupling constant** [Hz]	**Scaling factor**	**B-N distance**
1900 °C	1100	0.81	1.53 Å
1800 °C	1100	0.79	1.53 Å
1700 °C	1100	0.83	1.53 Å
1600 °C	1200	0.86	1.48 Å
1500 °C	1200	0.90	1.48 Å
1400 °C	1200	0.91	1.48 Å
1050 °C	1150	0.86	1.52 Å
800 °C	1000	0.83	1.58 Å
600 °C	1000	0.80	1.58 Å
400 °C	1000	0.64	1.58 Å

dipolar interaction. It can be seen that for the pyrolysis intermediates between 1050 and 1900 °C, the B-B distance steadily decreases from 3.25 to 2.62 Å. Obviously, the temperature dependence for the boron-boron distance is much more pronounced than for the boron-nitrogen distance. Again, the derived boron-boron distances are larger than the value of 2.51 $\mathring{A}$ from X-ray studies on pure h-BN [165].

Table 5.21. ^{11}B spin echo data for precursor system **7**.

Annealing temperature	$\mathbf{M_{2(homo)}}[10^6 rad^2/s^2]$	**B-B distance**
1900 °C	86.40	2.62 Å
1800 °C	79.00	2.65 Å
1700 °C	76.32	2.67 Å
1600 °C	59.01	2.79 Å
1500 °C	61.64	2.77 Å
1400 °C	53.73	2.83 Å
1050 °C	23.31	3.25 Å
800 °C	72.63	-
600 °C	65.08	-
400 °C	58.65	-

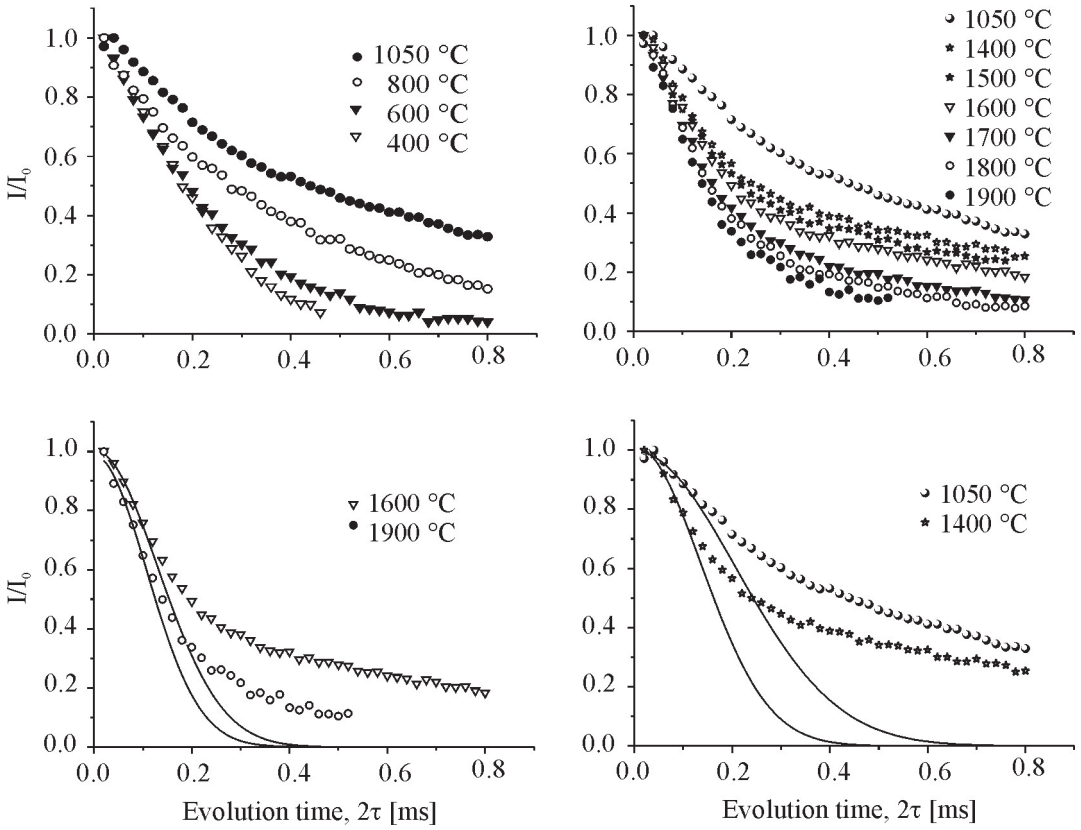

Figure 5.54. ^{11}B spin echo decay curves for precursor system **7**. The symbols refer to the experimental data. The solid lines are to theoretical curves with the $M_{2(homo)}$ values given in Table 5.21.

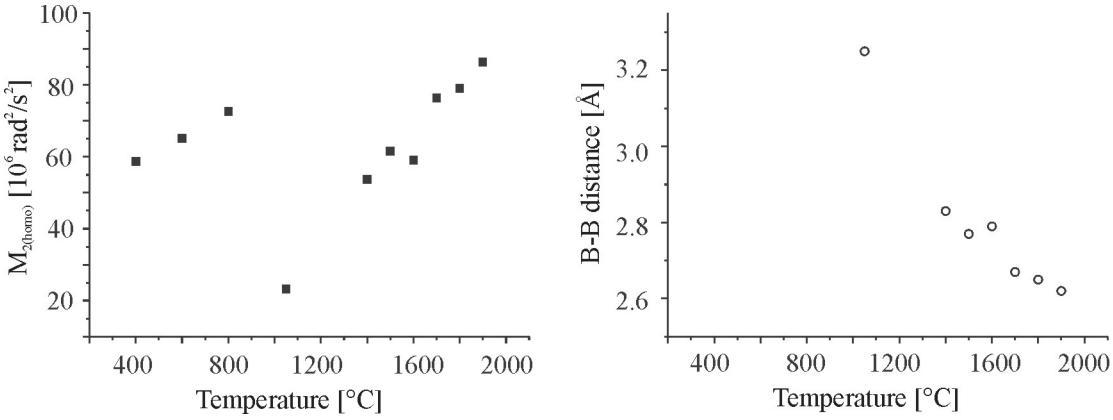

Figure 5.55. Homonuclear second moment (left) and the B-B distances (right) against annealing temperature for precursor system **7**.

5.2.8 Conclusion

In the present work, the thermolysis and crystallization behavior of B-Si-C-N ceramics (**1** to **7**) derived from boron modified polysilazanes and polycarbodiimides were studied by multinuclear ^{13}C, ^{29}Si and ^{15}N MAS NMR, ^{11}B spin echo, $^{11}B\{^{15}N\}$ REDOR and $^{11}B\{^{14}N\}$ REAPDOR techniques.

The thermal behavior of the precursor systems has been investigated by thermogravimetric analysis (TGA) and differential thermal analysis (DTA) [68–71, 73]. A major weight loss occurs up to 600-700 °C due to the organic -to-inorganic conversion. In the temperature range between 700 and 1400 °C, the produced ceramic phase becomes thermally stable showing only a slight weight loss. The high-temperature thermal investigation has shown that the obtained Si-B-C-N ceramics are thermally stable up to 1850-2050 °C [24, 69–71, 73]. Figure 5.56 compares the empirical formula of the starting polymeric precursors and the derived-ceramics. The ceramic yields are given as well. The B:Si atomic ratio of 1:3 for precursors **1**, **2** and **4**, and 1:6 for precursors **5** and **6** remains the same after ceramization, while the amount of carbon atoms reduces significantly due to the decomposition of the organic functional groups as well as crosslinking reactions. A significant loss of carbon occurs for the polysilazanes with R=CH_3 (**1** and **4**) and, consequently, this results in a low ceramic yield. In contrast, the polysilazane-derived ceramics with R=H exhibit higher yield.

X-ray studies show that an amorphous to crystalline transition occurs at about 1750 °C, resulting in the formation of crystalline silicon carbide and silicon nitride phases (see Table 2.2) [24, 70, 71, 73, 169]. In addition, a high-resolution transmission electron microscopy (HR-TEM) investigation has shown the presence of B-C-N layers with a turbostratic structure located along the surface Si_3N_4 and SiC [70, 84].

In a previous work, the pyrolysis intermediates starting from polymer precursor

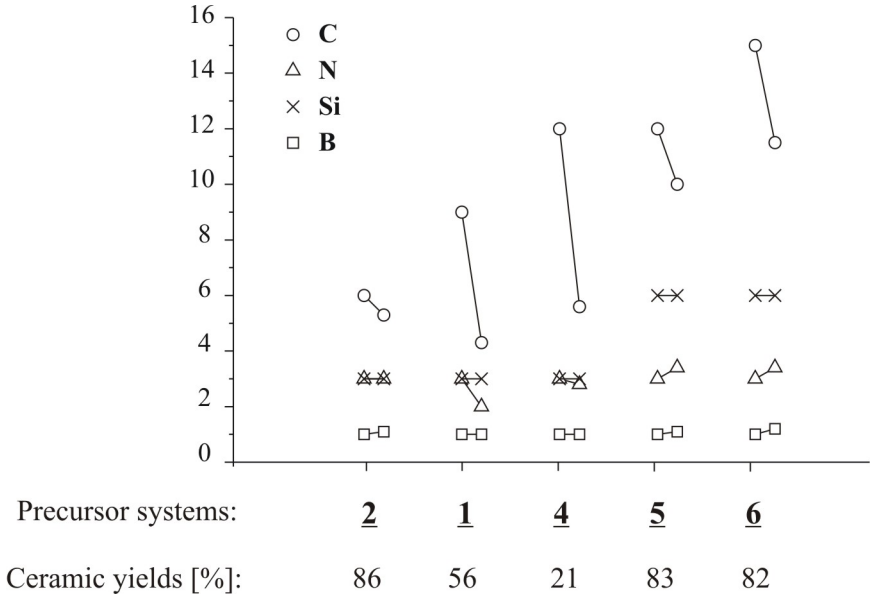

Figure 5.56. Comparison of the number of elements in the empirical formula of the polymer precursors (first symbols) and derived ceramics (second symbols).

have been studied by solid-state NMR spectroscopy [74, 81, 168]. However, the S/N ratio of the ^{13}C NMR spectra for amorphous intermediates above 600 °C was very poor, and above 1050 °C the signals were very weak or completely missing, most probably since only up to 250 scans and too long recycle delays (up to 5 min) were used. In addition, ^{11}B spin echo experiments as well as EPR studies have been performed for the pyrolysis intermediates between 600 and 1400 °C. However, the obtained B-B distances of 4-5 $\mathring{A}$ [74] were much longer as compared to the present results. The EPR study revealed that the 1050 °C samples exhibit a high amount of carbon centered free radicals [74, 168]. It has been assumed that the aliphatic ^{13}C NMR signal loss at this temperature is due to the existence of the radical centers. However, the present study reveals that the pyrolysis intermediates at 1050 °C have a much shorter ^{13}C spin-lattice relaxation time (15 s), most probably due to the presence of carbon-centered radicals.

In the present work, apart from the ^{13}C NMR studies all NMR experiments were performed at a higher operating magnetic field of 9.4 T. Therefore, the obtained

spectra gave better resolution as compared to the previous work. In addition, it should be noted that the second-order quadrupolar broadening in the ^{11}B NMR spectra also strongly depends on the magnetic field strength. ^{11}B NMR studies show that the pyrolysis intermediates at 400 °C contain tri-coordinated (BC_2N, BCN_2, BN_3 units) as well as four-coordinated (BC_4 units) boron sites. The transformation of the BC_3 units into the BN_3 units occurs mainly between 200 and 600 °C due to breaking of the B-C and Si-N bonds. The signal from the BCN_2 units only exists up to 1050 °C. After annealing at 1400 °C, the boron atoms are trigonally coordinated by three nitrogen atoms.

The results of the ^{13}C CP and ^{29}Si single pulse NMR studies show that the microstructure of the Si-B-C-N precursor systems at 600 °C is characterized by sp^2- and sp^3- carbons and an amorphous Si-C-N matrix with $SiC_{4-x}N_x$ (x=0, 1, 2, 3 and 4) structural units. sp^2-carbon is attributed to the graphite-like carbon, while sp^3-carbon signals reflect CSi_4 and CH_xSi_{4-x} (x=1, 2 and 3) units. After annealing at 800 °C, the sp^3-carbon signal cannot be detected. The absence of protonated sp^3- carbon indicates that crosslinking of the residual R and R′ is complete at this temperature. This should result in an increase of the CSi_4 units as well as of graphite-like carbons. The absence of CSi_4 units is attributed to the long spin-lattice relaxation time ^{13}C T_1.

The obtained ^{13}C NMR spectra at 1050 °C show a resonance from the CSi_4 units besides sp^2-carbon peaks at 120 and 138 ppm. The signal at 120 ppm is due to an amorphous carbon phase with graphite-like structure. However, the nature of the sp^2-carbon at 138 ppm observed for all Si-B-C-N ceramics is not yet fully understood. This signal might be due to sp^2-carbon atoms within the BCN network, since the ^{11}B NMR results show that these intermediates also contain BCN_2 units apart from the BN_3 units. Further investigations are necessary to clarify the interconnection between graphite-like carbon and the remaining ceramic network. For the same

reasons, van Wüllen and Jansen *et al.* [170, 171] have used REDOR and REAPDOR experiments on ^{13}C labeled ceramics to obtain the ^{13}C-^{11}B and ^{13}C-^{15}N dipolar couplings. On basis of those former investigations, the sp^2-carbon signal at 141 ppm in the final ceramics $SiBN_3C$ is attributed to carbon atoms bonded to nitrogen. Moreover, this signal also has a substantially stronger ^{13}C-^{11}B dipolar coupling as compared to the additional ^{13}C NMR signal observed at 119 ppm.

Furthermore, the results of our present ^{13}C, ^{29}Si and ^{15}N MAS NMR study show that the structure of the derived amorphous ceramics depends on the elemental compositions as well as on the X, R′ and R functional groups, as they play an important role for crosslinking during pyrolysis. Figures 5.57 and 5.58 compare the ^{29}Si and ^{13}C NMR spectra of the pyrolysis intermediates (1050 and 1400 °C), respectively. Firstly, the precursor systems with X=NCN (**7**) and NCH_3 (**3**) exhibit higher amounts of nitrogen-enriched silicon sites ($SiCN_3$ and SiN_4 units) as compared to the precursor systems with X=NH. Secondly, the precursor systems with R=C_2H_4-SiH(H)C_2H_4 (**5**) and C_2H_4-SiH(CH_3)C_2H_4 (**6**) have a lower amount of nitrogen-enriched silicon sites as they contain the highest amount of silicon and carbon atoms per units. Moreover, the ceramics with a higher amount of nitrogen-enriched silicon sites ($SiCN_3$ and SiN_4 units) contain a higher amount of free carbon than CSi_4 units. This result indicates that the increase of the nitrogen-enriched silicon sites is responsible for a decrease of the Si-C bonds, and consequently the amount of free carbon phase increases.

The NMR investigations further demonstrate that in the temperature range between 1600 and 1800 °C a demixing of the amorphous ceramic sets in, along with the formation of crystalline silicon nitride and silicon carbide phases.

Furthermore, the ^{15}N NMR results show that the Si-B-C-N ceramics obtained at 1050 °C contain tri-coordinated nitrogen sites (NHB_2, NB_3 and NSi_3 units). With increasing annealing temperature, the amount of the NHB_2 units decreases resulting

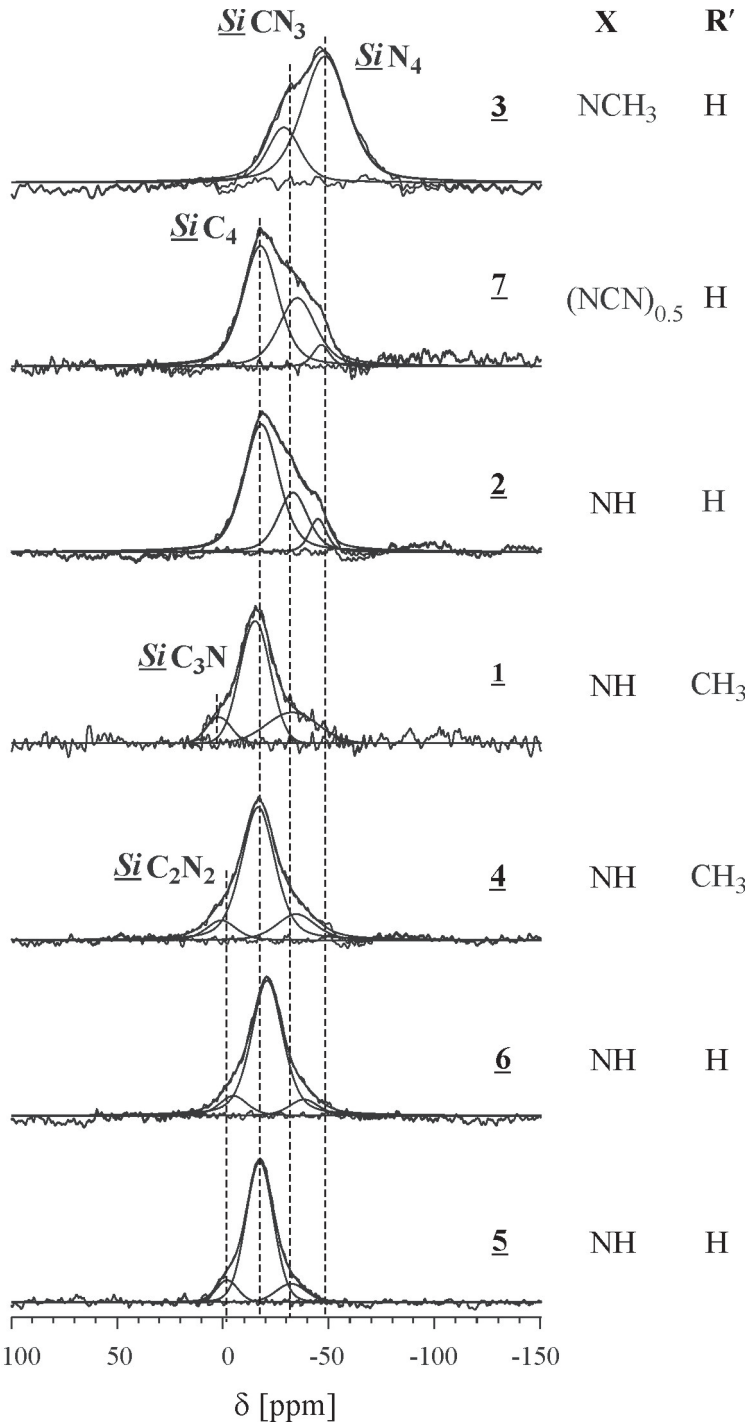

Figure 5.57. Comparison of experimental ^{29}Si MAS NMR spectra of the pyrolysis intermediates at 1400 °C.

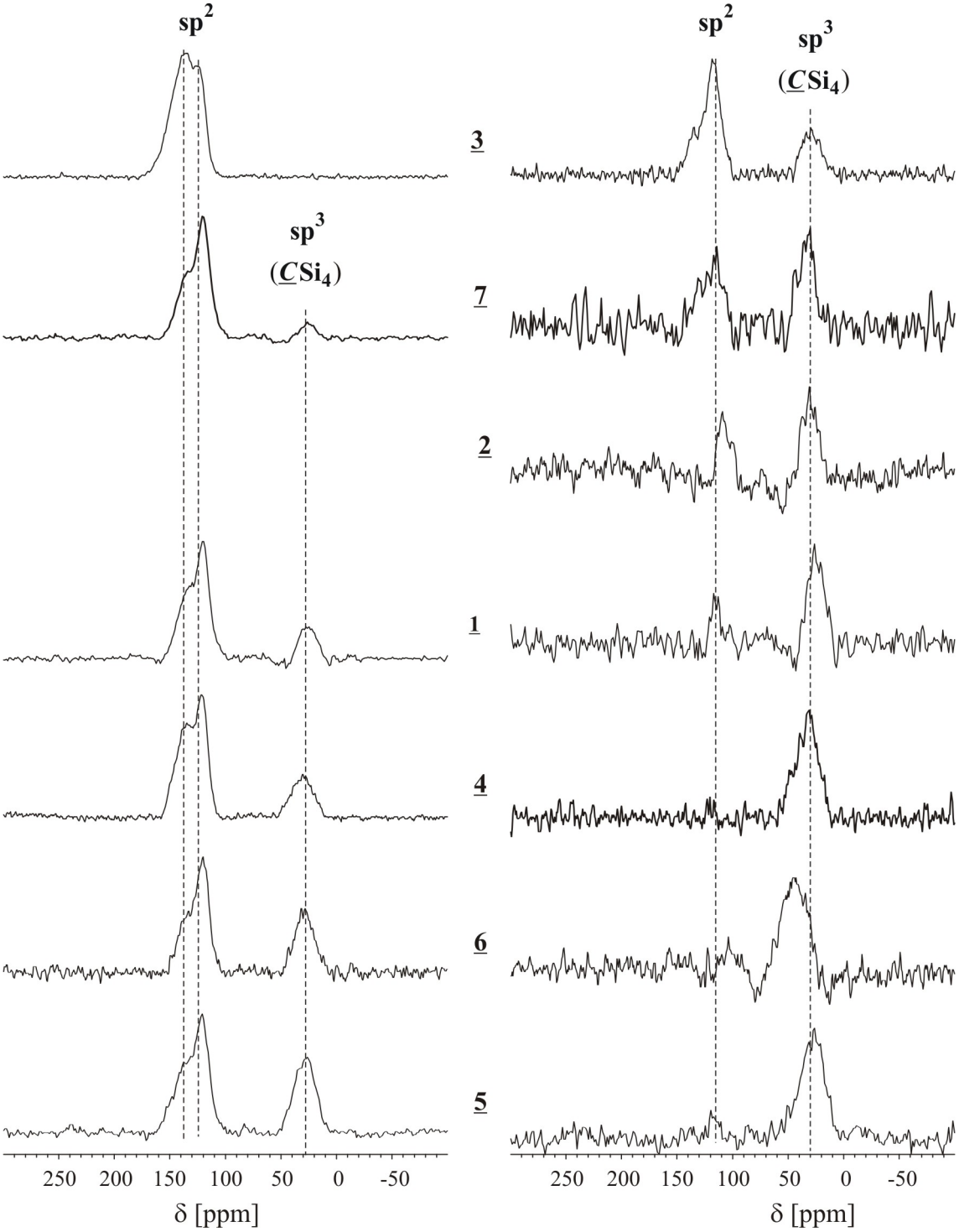

Figure 5.58. Comparison of experimental ^{13}C MAS NMR spectra of the pyrolysis intermediates at 1050 °C (left) and 1400 °C (right).

in an increase of the NB_3 units due to crosslinking. Figure 5.59 compares the ^{15}N NMR spectra of the polysilazane derived ceramics obtained at 1400 °C. The polysilazane **2** with X=NH and R′=H pyrolized at 1400 °C exhibits only NB_3 and NSi_3 units, resulting in a higher degree of crosslinking due to the lower molecular weight of the side-groups. A significantly higher amount of NSi_3 units with respect to NB_3 units was observed for the hydrosilylized polysilazane derived ceramic **5**, as it contains an additional silicon atom per monomer unit.

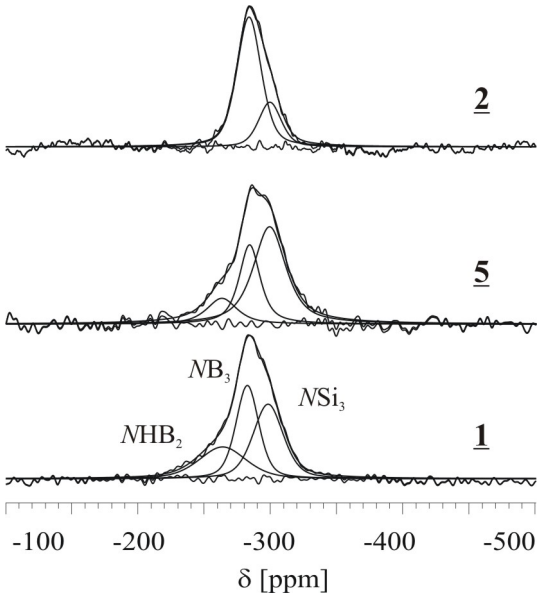

Figure 5.59. ^{15}N NMR spectra of the polysilazane derived ceramics obtained at 1400 °C.

In the present work, double resonance experiments, such as $^{11}B\{^{15}N\}$ REDOR and $^{11}B\{^{14}N\}$ REAPDOR, and ^{11}B spin echo experiments, were performed for the first time on different precursor systems pyrolized in a wide temperature range (400-1900 °C) in order to get internuclear distances. It should be noted that in general a good match between experimental and theoretical REDOR and REAPDOR curves was achieved for all precursor systems. The analysis have proven the presence of the BN_3 units with a planar geometry as in h-BN. The obtained B-N and B-B distances are given in Figure 5.60 as function of the annealing temperature. Both the REDOR

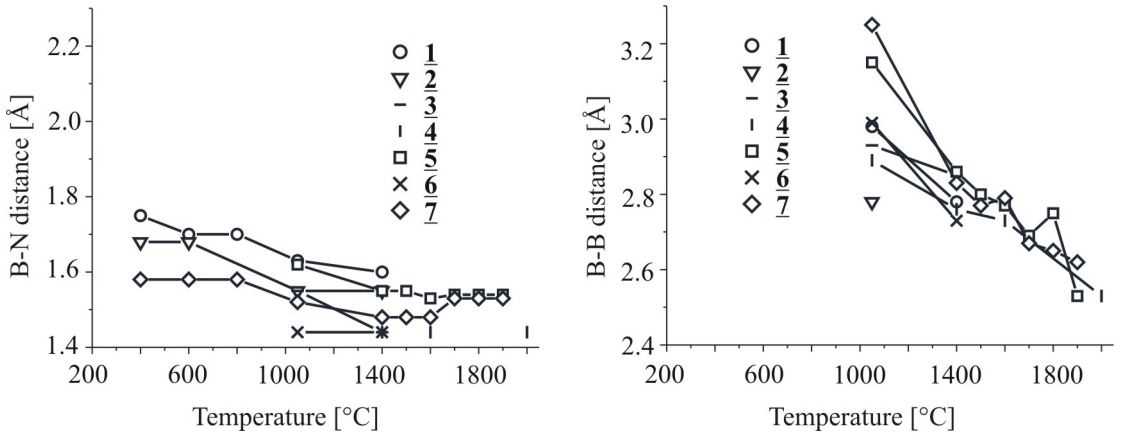

Figure 5.60. B-N and B-B distances derived from the REDOR/REAPDOR and spin echo experiments, respectively.

and the REAPDOR results show that the obtained B-N distances of 1.58-1.71 $\mathring{A}$ are longer than in pure h-BN (1.44 $\mathring{A}$). The most drastic changes occur between 400 and 1400 °C, when the obtained B-N distance decreases continuously with increasing annealing temperature. The longer distances for the samples annealed up to 1050 °C might be due to presence of the BCN_2 units, which lead to some distortion in the BN- layers.

The B-B distances, obtained at 1050 °C for the various precursor systems, are in the range between 2.78 and 3.25 $\mathring{A}$, and are thus longer than in h-BN (2.51 $\mathring{A}$). Therefore, a fully developed BN-layer structure does not exist at this temperature. This result is confirmed by the ^{11}B and ^{15}N NMR studies, which show the presence of BCN_2 and NHB_2 units. For example, the shortest B-B distance is observed for the intermediate derived from polysilazane **2**, which does not contain NHB_2 structural units.

In the temperature range between 1400 and 1900 °C, the temperature dependence of the B-B distances is quite pronounced. The B-B distances decrease from 2.86 to 2.53 $\mathring{A}$, while the B-N distances remain practically unaltered. It was already mentioned that there is no evidence of tri-coordinated boron sites bonded to carbon (e.g. BCN_2 units) for samples annealed above 1400 °C. On the basis of the present

results, it can be concluded that intercalated BN and sp^2-carbon layers most likely constitute the BNC_x phase in this temperature range, where a number of graphite carbon layers sandwiched between BN-layers creating some internal pressure, which in turn is responsible for the observed longer interatomic distances in the BN-layers. However, other scenarios, like the direct incorporation of small sp^2-carbon domains into the BN-sheets, cannot be ruled out.

5.3 Precursor-derived B-C-N ceramics

5.3.1 ^{15}N labeled poly(borsesequicarbodiimide) 8

The synthesis of the ^{15}N labeled poly(borsesequicarbodiimide) $[B_2(^{15}N{=}C{=}N)_3]_2$ **8** and its ceramization (25-1100 °C) to a B-C-N material are reported in reference [80]. The obtained precursor **8** $[B_2(^{15}N{=}C{=}N)_3]_2$ was a colorless solid that is very sensitive against oxygen and moisture. To avoid oxygen contamination, it is directly thermolized at 1100 °C in an argon atmosphere without further processing steps. Annealing of the ceramics at temperatures up to 1700 °C yielded almost the same composition. The chemical compositions of the ceramics after annealing at 1200 and 1600 °C are given in Table 5.22. Upon annealing at temperatures higher than 1700 °C, the samples decomposed predominantly to products of carbon.

Table 5.22. Sample compositions of BCN ceramics.

Annealing temperature	Ceramic composition
1600 °C	$B_1C_{1.5}N_1(O)_{0.1}$
1200 °C	$B_1C_{1.7}N_1(O)_{0.4}$

In the present work, ^{13}C, ^{15}N MAS NMR, ^{11}B{^{15}N} REDOR and ^{11}B spin echo experiments are used to investigate the structural feature of the B-C-N ceramic **8**. It should be noted that X-ray and neutron scattering measurements have been performed on the same samples [72]. These investigations showed that the short-range ordering in the amorphous B-C-N ceramic consists of a honeycomb network (graphite-like structure). However, wide-angle scattering cannot be used to distinguish between a statistical distribution of all three species or a separation of BN and C. Therefore, solid-state NMR studies have been previously employed in order to get more information about the structural features of the B-C-N ceramic [72]. However, the S/N ratio of the ^{13}C NMR spectra was too low to give satisfactory

information. As mentioned earlier during the discussion of the Si-B-C-N ceramics, this is most probably since too long recycle delays of 120 s and only up to 250 scans were used. Moreover, the ^{11}B NMR spectra were broader than those of the present study, since they have been measured at a lower operating magnetic field of 7 T.

^{13}C NMR studies

^{13}C MAS NMR spectra of the ceramics **8** are given in Figure 5.61. The spectrum of the **1200 °C** sample shows two signals centered at 120 and 20 ppm. The signal with the higher intensity is due to the sp^2-carbon attributed to a graphite layer structure. So far, only one ^{13}C NMR study for B-C-N materials was reported which showed broad resonances in the range between 100 and 200 ppm [172]. Moreover, ^{13}C NMR signals for the cubic and hexagonal carbon nitride phases were found at 91 and 144 ppm, respectively [167], while the ^{13}C NMR signals for boron carbide, B_4C occur at 89 and 1 ppm [173]. Likewise, sp^3-carbon in diamond resonates at 40 ppm [174]. Therefore, there is no experimental evidence for the carbon nitride or boron carbide phases in the ^{13}C NMR spectra of the present B-C-N sample. This is consistent with the X-ray diffraction data, which show only distances of graphitic carbon and hexagonal boron nitride. The small signal at 20 ppm, which is in the range of sp^3-carbon, is not clear. A ^{13}C NMR signal at about 15 ppm has been

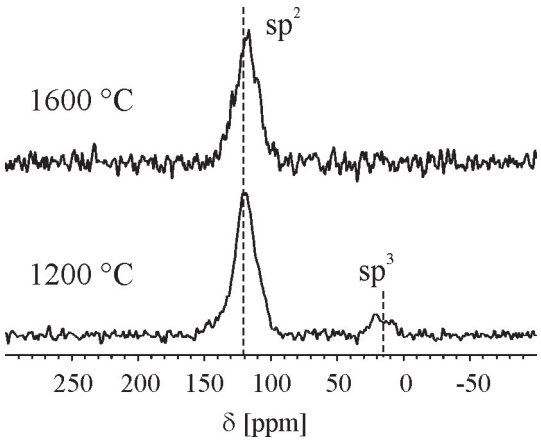

Figure 5.61. Single pulse ^{13}C MAS NMR spectra of precursor system **8**.

observed for amorphous hydrogenated boron carbide with high boron concentration (42 at. % B, 10 at. % C, and 48 at. % H) [175]. Therefore, it can be speculated whether amorphous hydrogenated boron carbide is also responsible for a sp^3 signal in the present sample.

Upon pyrolysis at **1600 °C**, the ^{13}C NMR spectrum exhibits only the sp^2-carbon signal, and the signal to noise ratio is drastically reduced. Since crystalline graphite usually cannot be observed by NMR, the observed sp^2-carbon resonance is attributed to amorphous graphite-like structures.

^{15}N NMR studies

^{15}N NMR spectra of the B-C-N ceramics at 1200 and 1600 °C are given in Figure 5.62. Both spectra show two peaks at -280 and -357 ppm which are due to the sp^2 and sp^3 bonded nitrogen sites, respectively. The small peaks (*) in the spectrum of the 1200 °C sample are spinning sidebands from the peak at -280 ppm. The N(sp^2) signal at -280 ppm is in agreement with the ^{15}N NMR signal reported for h-BN [176–178]. However, the structural composition of the N(sp^3) signal at -357 ppm is not clearly understood. In the previous NMR studies of the present sample, it has been assigned to NB_4 units, since this value is in the range of the computed chemical shielding for cubic boron nitride [177]. However, the present ^{11}B NMR and $^{11}B\{^{15}N\}$ REDOR data rule out this possibility. In fact, the ^{15}N NMR signals reported for the boron-ammonia complexes $Me_{3-x}NH_x{\cdot}BH_3$ ($x = 0, 1, 2, 3$) occur in the same range between -348 and -364 ppm [160]. Therefore, the N(sp^3) signal might be attributed to nitrogen atoms, which are bonded to carbon atoms. Upon annealing at 1600 °C, a decrease of the signal of the NB_3 units is observed which is consistent with the REDOR results reported below.

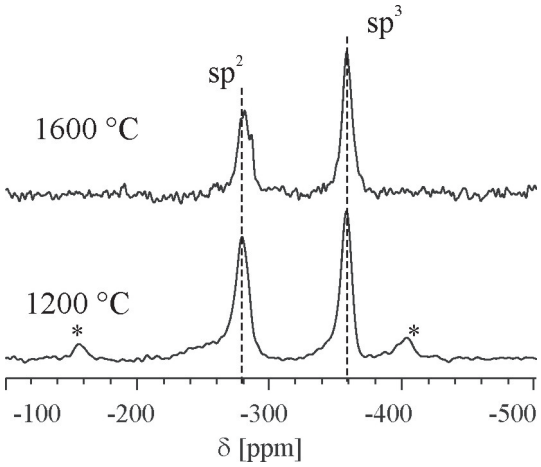

Figure 5.62. Single pulse ^{15}N MAS NMR spectra of precursor system **8**.

^{14}N NMR studies

A ^{14}N MAS NMR spectrum was obtained for the 1700 °C sample, which is not ^{15}N labeled. Figure 5.63 shows the ^{14}N NMR spectrum of this sample together with that for h-BN. It can be seen that the spectrum of the B-C-N ceramic is much broader than that of h-BN due to tri and four-coordinated nitrogen sites (see ^{15}N NMR). The recycle delay used for the ^{14}N NMR spectrum of the B-C-N ceramic was 20 s, while that for the h-BN crystalline sample was 1 hour. Such a shortening of the spin-lattice relaxation time T_1 for the B-C-N sample can be explained by the amorphous character of the ceramic sample.

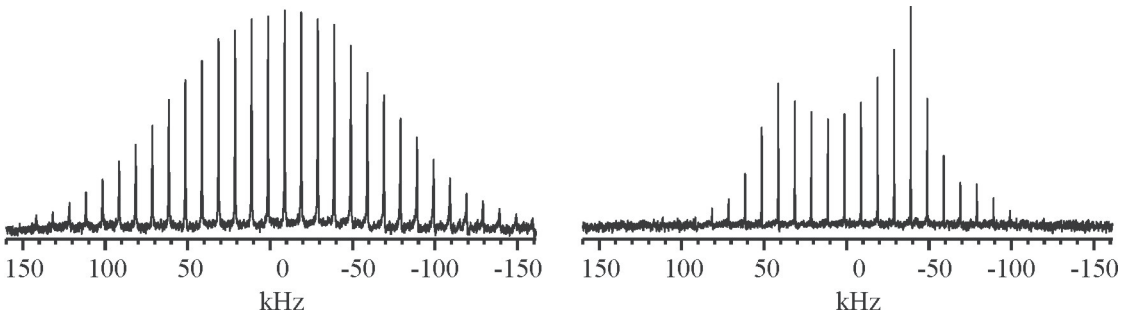

Figure 5.63. Single pulse ^{14}N MAS NMR spectra of precursor **8** pyrolized at 1700 °C (left) and h-BN (right).

^{11}B{^{15}N} REDOR studies

For precursor **8**, pyrolized at 1200 and 1600 °C, $^{11}B\{^{15}N\}$ REDOR experiments were performed on two different spectrometers operating at magnetic field strengths of 9.4 and 14 T. Representative ^{11}B NMR spectra of the B-C-N ceramics, obtained from REDOR experiments, and the simulated spectra for h-BN for the low and high field spectrometers are shown in Figure 5.64 (left) and (right), respectively. The ^{11}B NMR spectrum of the 1200 °C sample obtained at **9.4 T** exhibit a broad resonance centered at about 10 ppm with shoulders at 20 and -2 ppm. After annealing at 1600 °C, the two shoulders slightly decrease in intensity. Moreover, as compared to the ^{11}B NMR spectrum of the h-BN, the spectra of the B-C-N ceramics are broader and their centre of gravity is shifted. Therefore, the ^{11}B NMR spectra of the B-C-N ceramics are attributed to a superposition of three different boron sites.

In the respective ^{11}B NMR spectra obtained at **14 T**, the main peak at 20 ppm is narrowed and is shifted in the direction of the isotropic chemical shift value of h-BN (δ_{iso}=30 ppm), which can be attributed to the larger operating magnetic field. In contrast, the shoulder at -2 ppm does not show any shift and is resolved from the main peak. The main resonance at 20 ppm is characteristic for tri-coordinated boron sites, which usually have a quadrupolar coupling constant, C_{qcc}, of a few MHz. In the case of h-BN with C_{qcc}=2.9 MHz, the spectral linewidth is half of that in the low field spectrum. The REDOR analysis shows that this signal is attributed to two different boron sites with boron atoms bonded to nitrogen and boron atoms without B-N bonds. The small signal at -2 ppm is assigned to four-coordinated boron sites which becomes weaker in intensity after annealing at 1600 °C.

Both REDOR experiments obtained at low and high fields show that the dipolar coupling between the ^{11}B and ^{15}N nuclei occurs only for the tri coordinated boron sites, while the four coordinated boron sites at -2 ppm do not show any REDOR dephasing. Therefore, the four coordinated boron sites are most likely due to BC_4 units and as discussed in the ^{15}N NMR part the presence of the cubic boron nitride

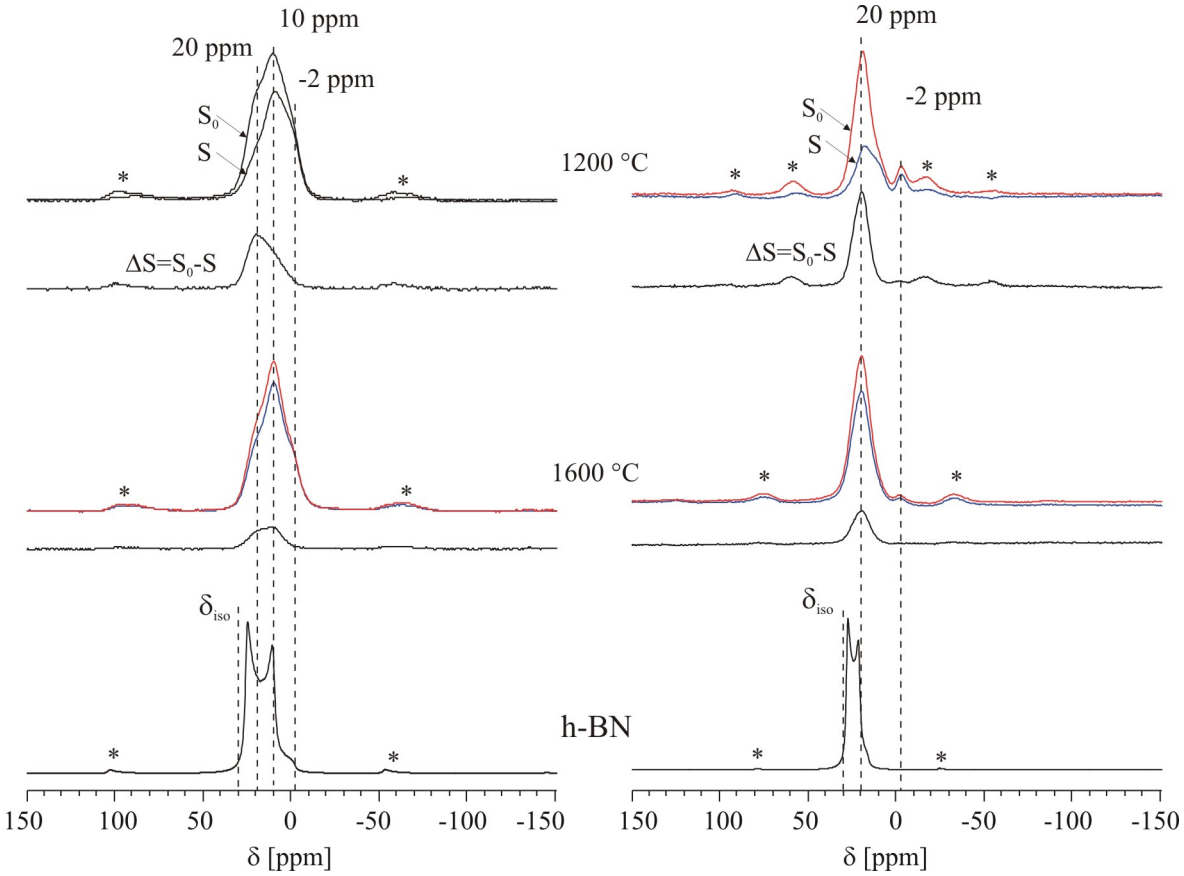

Figure 5.64. $^{11}B\{^{15}N\}$ REDOR spectra of precursor system **8** and simulated ^{11}B NMR spectra for h-BN obtained at the operating magnetic field of 9.4 (left) and 14 T (right). S_0, S and S_0-S refer to reference, dephased and difference spectra, respectively. The sample spinning and dephasing time are 10 kHz and 0.8 ms for the 1600 °C sample recorded at 9.4 and 14 T and 1200 °C sample recorded at 9.4, and are 7 kHz and 0.85 ms for the 1200 °C sample recorded at 14 T, respectively.

phase can be excluded. Moreover, the REDOR spectra show that the strength of the dipolar dephasing is strongly reduced after annealing at 1600 °C.

The experimental $^{11}B\{^{15}N\}$ REDOR curves for the 1200 and 1600 °C samples are given in Figure 5.65 (left) and (right), respectively. In this figure, the dashed line corresponds to the simulated curves for h-BN, while the solid lines correspond to the simulated curves for B-C-N ceramics assuming a BN_3 spin system with planar structure like in h-BN. For the simulation, it has been taken into account that precursor **8** is only 50 atom % ^{15}N enriched. Therefore, the REDOR simulation curves are a superposition of the curves from BN_3, BN_2, BN and B spin systems

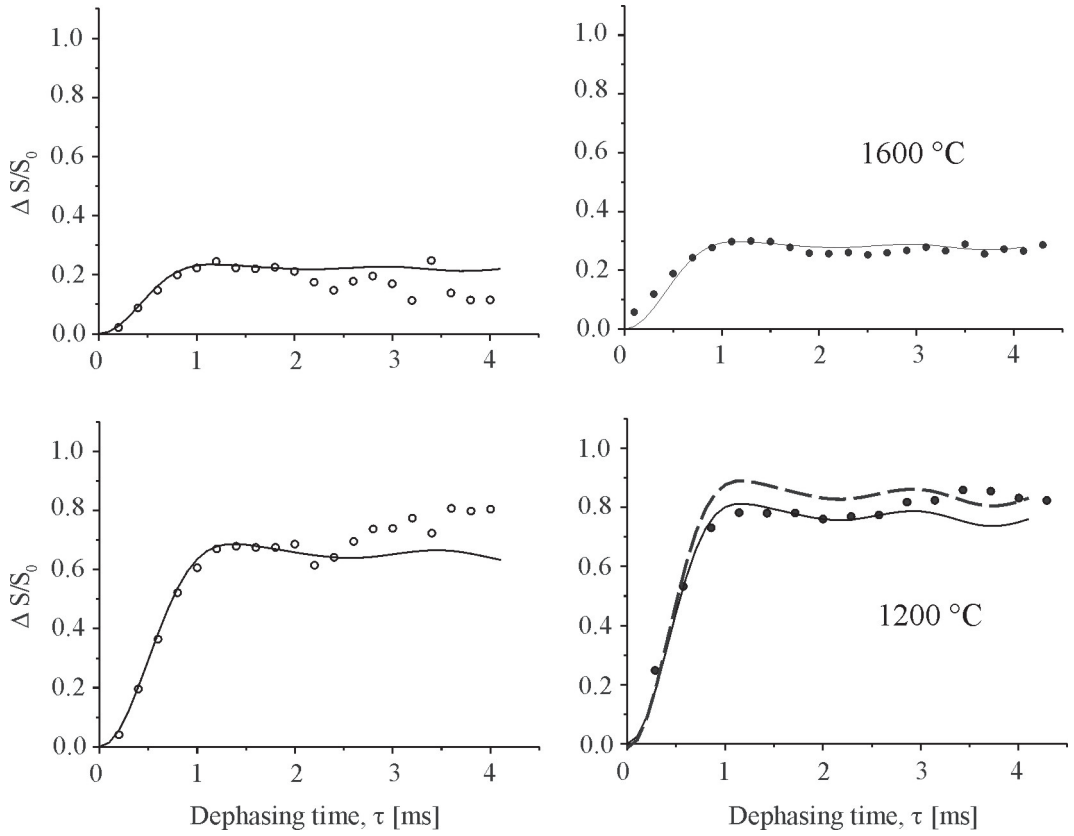

Figure 5.65. $^{11}B\{^{15}N\}$ REDOR curves for precursor system **8**. Open and filled circles refer to the experimental data obtained at 9.4 and 14 T, respectively. The dashed line refers to theoretical curves for a h-BN with 50 at. % in ^{15}N enriched. The solid lines are theoretical curves for BN_3 spin system with parameters given Table 5.23.

with statistical weights of 1/8, 3/8, 3/8 and 1/8, respectively. The B-N distances (r_{BN}) and scaling factors obtained from REDOR curve fitting are summarized in Table 5.23. The scaling factors are normalized to that of h-BN.

For the REDOR experiments obtained at low and high magnetic fields, the derived scaling factors and B-N distances are not identical. Higher scaling factors and shorter distances are found from the experiments at the higher field strength. This might be related to the better spectral resolution which can be achieved as compared to those at lower field. In this case, the obtained B-N distances of 1.44 $\AA$ for the B-C-N ceramics are the same as in h-BN, while the scaling factors are found to be 0.90 and 0.32 for the 1200 and 1600 °C samples, respectively. These results show that the

Table 5.23. $^{11}B\{^{15}N\}$ REDOR data for precursor system **8**.

Annealing temperature	**Dipolar coupling constant** [Hz]	**Scaling factor**	**B-N distance** [Å]
h-BN (sim)	1300	1	1.44
1600 °C (14 T)	1300	0.32	1.44
1200 °C (14 T)	1300	0.90	1.44
1600 °C (9.4 T)	1100	0.27	1.53
1200 °C (9.4 T)	1100	0.76	1.53

1200 °C sample mainly contains BN-domain with hexagonal structure and small fractions of tri and four coordinated boron sites, which are not bonded to nitrogen atoms. After annealing at 1600 °C, the relative amount of the BN-domains decreases in intensity, and consequently the amount of boron sites without nitrogen neighbors increases. The decrease of the BN-domains is also confirmed by the decrease of the NB_3 units observed in the ^{15}N NMR spectrum. It should be mentioned that so far further details about the structure of the boron sites without direct B-N bonds cannot be provided.

^{11}B spin echo studies

^{11}B spin echo experiments were performed on the same samples used for the REDOR experiments. Figure 5.66 shows experimental spin echo decay curves and theoretical curves from Gaussian fitting of the initial part of the decay curves ($2\tau < 0.1$ ms). For the 1200 and 1600 °C samples, the homonuclear second moment $M_{2(homo)}$, obtained from Gaussian fitting, are $115{\cdot}10^6$ and $113{\cdot}10^6 rad^2/s^2$, respectively. These values are bigger than those of pure h-BN ($107{\cdot}10^6 rad^2/s^2$) and of Si-B-C-N ceramics. The larger homonuclear second moment $M_{2(homo)}$ might originate from another boron component besides that in BN-layers. At this stage, without further information about this additional boron component, it is impossible to calculate reliable B-B distance from the M_2 data. It should be noted that the values of $M_{2(homo)}$ for the low and high temperature samples are almost identical, although the relative amount

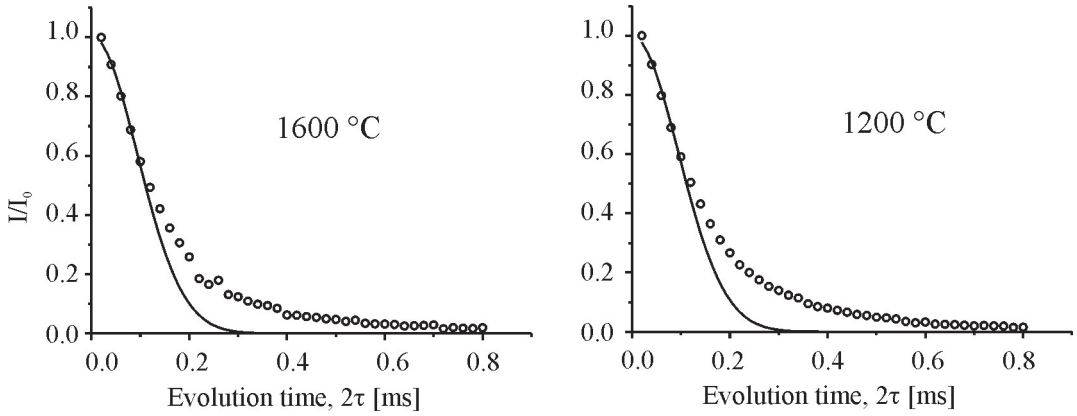

Figure 5.66. ^{11}B spin echo decay curves for precursor system **8**. Open circles refer to the experimental data. Solid lines are theoretical curves with the $M_{2(homo)}$ values of $115 \cdot 10^6 rad^2/s^2$ (1200 °C) and $113 \cdot 10^6 rad^2/s^2$ (1600 °C).

of the BN_3 units reduces from 90 to 32 %, as shown above during the discussion of the REDOR data.

5.3.2 Conclusion

^{13}C and ^{15}N MAS NMR, ^{11}B spin echo and $^{11}B\{^{15}N\}$ REDOR experiments were used to characterize the B-C-N ceramic derived from poly(borsesequicarbodiimide). NMR studies show that the structure of the pyrolysis intermediate at 1200 °C is dominated by amorphous graphite-like carbon and BN-domains with hexagonal structure. Moreover, the present ceramic also contains small amounts of BC_4 units and a $N(sp^3)$ component which most likely consist of nitrogen atoms coordinated with carbon rather than with boron, as independently evidenced by the $^{11}B\{^{15}N\}$ REDOR data. Furthermore, the REDOR analysis reveals that 90 % of the boron atoms belong to BN_3 units in BN-domains with hexagonal structure. The obtained B-N distance of 1.44 $\AA$ from the REDOR experiment are in agreement with that of h-BN. The ^{15}N NMR and REDOR results show that after annealing at 1600 °C, the relative amount of the BN-domains in the B-C-N ceramic significantly decreases. Accordingly, only 33 % of the boron atoms are directly bonded to nitrogen atoms.

The derived values of the ^{11}B homonuclear second moments (from the ^{11}B spin echo experiments) for the 1200 and 1600 °C samples were very similar, but larger than that of h-BN. It indicates that after annealing at 1600 °C, the average B-B distances do not change, although the relative amount of the BN-domains decreases significantly.

Chapter 6

Summary

The precursor-derived Si-B-C-N and B-C-N ceramics are of special interest because of their covalent bonding providing mechanical reliability and high-temperature stability. In general, the precursor-derived ceramics posses several advantages, as compared to the ceramics obtained by conventional method. They exhibit a much better homogeneity on the molecular level. Moreover, the precursor route offers a better flexibility for the design of ceramic tools. More recently, it has been demonstrated that Si-B-C-N ceramics exhibit improved thermal stability up to 2200 °C, while the thermal stability of boron free Si-C-N ceramics is limited to 1485 °C due to reaction of Si_3N_4 with free carbon. The majority of the studies on Si-B-C-N ceramic systems used polysilazanes and polysilylcarbodiimides as precursor polymers, which upon hydroboration and subsequent heat-treatment yield amorphous or crystalline quaternary ceramics. It is anticipated that the thermal stability of Si-B-C-N ceramics primarily relies on their unique structural composition, consisting of nanocrystalline SiC and Si_3N_4 domains as well as of a turbostratic BNC_x phase.

The polymer-to-ceramic conversion involves several amorphous intermediate steps which rules out common techniques, such as X-ray diffraction, for

structural characterization. In this connection, solid-state NMR spectroscopy has demonstrated its particular potential to unravel the structural features of all intermediate steps, also including the amorphous species. NMR spectroscopy probes the molecular environment (short-range order up to a few Å) around selected nuclei, whose magnetic properties strongly depend on the local electronic environment and dipolar interactions with nuclei in the next neighborhood.

In the present contribution, the thermolysis and crystallization behavior of Si-B-C-N and B-C-N ceramic systems are studied by multinuclear (^{13}C, ^{29} Si, ^{15}N and ^{14}N) MAS NMR. Particular emphasis is given to the structural composition of the BNC_x phase. For this purpose, for the first time double resonance experiments such as ^{11}B{^{15}N} REDOR, ^{11}B{^{15}N} SEDOR and ^{11}B{^{14}N} REAPDOR and ^{11}B spin echo were applied, which allow the measurement of the dipolar coupling between like and unlike spins and which is directly related to the internuclear distance. From REDOR and SEDOR experiments, the dipolar coupling between boron and nitrogen nuclei were obtained. ^{11}B spin echo experiments provide the homonuclear second moment in the amorphous ceramics. Also, results from ^{11}B{^{14}N} REAPDOR experiments, which are suitable for spin system where two quadrupolar nuclei are involved, are provided. Although this technique gives the same information as the REDOR experiment, it does not require ^{15}N isotopic enrichment. The experimental double resonance and spin echo curves were simulated using hexagonal BN (h-BN) as model system, whose internuclear distances are known from X-ray diffraction. Therefore, ^{11}B spin echo and ^{11}B{^{14}N} REAPDOR experiments were also performed on h-BN.

The quaternary Si-B-C-N ceramics were prepared by thermolysis of suitable organometallic precursors, such as boron-modified polysilazanes (**1** to **6**) and polycarbodiimides **7** with the general formula $\{B[RSi(R')R''X]_3\}_n$, where the corresponding R, R′, X and R″ groups are defined in Table 6.1. The starting polymeric precursors and their pyrolysis intermediates at different temperatures

were prepared in the group of Prof. F. Aldinger at the Max-Planck-Institut für Metallforschung.

Table 6.1. The investigated boron-modified polysilazanes **1** to **6** and polysilylcarbodiimide **7** with general formula $\{B[RSi(R')R''X]_3\}_n$ and their pyrolysis temperatures.

Precursor system	X	R′	R	R″	^{15}N isotopic enrichment	Pyrolysis temperatures
7	$(NCN)_{0.5}$	H	C_2H_4	H	50 %	400-1900 °C
3	NCH_3	H	C_2H_4	-	-	1050-1400 °C
2	NH	H	C_2H_4	-	100 %	400-1400 °C
1	NH	CH_3	C_2H_4	-	100 %	400-1400 °C
4	NH	CH_3	C_2H_4-CH_2	-	-	600-1400 °C
5	NH	H	C_2H_4-$SiH(H)C_2H_4$	-	100 %	400-2000 °C
6	NH	H	C_2H_4-$SiH(CH_3)C_2H_4$	-	-	1050-1400 °C

The results of the ^{13}C, ^{29}Si and ^{11}B studies show that the Si-B-C-N precursor systems at 600 °C are characterized by (*i*) sp^2- and sp^3- carbons attributed to the graphite-like carbon and $\underline{C}H_{4-x}Si_x$ (x=0, 1, 2 and 3) units, respectively; (*ii*) an amorphous Si-C-N matrix with the $\underline{Si}C_{4-x}N_x$ (x=0, 1, 2, 3 and 4) structural units; and (*iii*) BNC_x.

For all precursor systems pyrolized at 1050 °C, the sp^3-carbon signal is associated with $\underline{C}Si_4$ units, while two sp^2-carbon signals at 120 and 138 ppm can be identified. The signal at 120 ppm is due to an amorphous carbon phase with graphite-like structure. The signal at 138 ppm might be due carbon atoms within the BCN network, since $\underline{B}N_2C$ units most likely exist up to 1050 °C. The ^{15}N NMR spectra for ^{15}N isotopic enriched samples show tri-coordinated nitrogen sites ($\underline{N}HB_2$, $\underline{N}B_3$ and $\underline{N}Si_3$ units). Upon increasing the annealing temperature, the amount of the $\underline{N}HB_2$ units decreases resulting in an increase of the $\underline{N}B_3$ units due to crosslinking. For example, the polysilazane **2** with X=NH and R′=H at 1400 °C exhibits only $\underline{N}B_3$ and $\underline{N}Si_3$ units resulting in a higher degree of crosslinking due to the lower

molecular weight of the side-groups. The highest amount of $\underline{N}Si_3$ units with respect to $\underline{N}B_3$ units was observed for the hydrosilylized polysilazane derived ceramic **5** as it contains one more silicon per monomer unit.

Furthermore, the NMR results reveal that the microstructure of the amorphous ceramics depend on the functional groups X and R, as they play an important role for crosslinking during pyrolysis. The precursor systems with X=NCN and NCH_3 exhibit higher amounts of N-enriched silicon sites ($\underline{Si}CN_3$ and $\underline{Si}N_4$ units) as compared to the precursor systems with X=NH. The precursor systems with R=C_2H_4-SiH(H)C_2H_4 and C_2H_4-SiH(CH_3)C_2H_4 have a lower amount of N-enriched silicon sites as they contain the highest amount of silicon and carbon atoms per monomeric unit. Moreover, the Si-B-C-N ceramics containing a higher amount of C-enriched silicon units show a higher amount of $\underline{C}Si_4$ units as compared to graphite-like carbon.

In general, a good match between experimental and theoretical REDOR and REAPDOR curves were achieved for all precursor systems, indicating that the $\underline{B}N_3$ units have a planar geometry as in h-BN. However, the obtained B-N distances are longer than in pure h-BN (1.44 Å). The most drastic changes occur between 400 and 1400 °C, when the obtained B-N distance of 1.55-1.75 $\mathring{A}$ decreases continuously with increasing annealing temperature. This result can be explained by the decrease of the $\underline{B}N_2C$ units with increasing annealing temperature. For the precursors **5** and **7** annealed at 1400 °C, B-N distances of 1.55 and 1.48 $\mathring{A}$ were found, respectively, and these values do not change significantly upon further increasing the annealing temperature.

The obtained B-B distances for the pyrolysis intermediates at 1050 °C were in the range between 2.78 and 3.25 $\mathring{A}$ and are thus much larger as compared with h-BN. Therefore, a fully developed BN-layer structure does not exist at this temperature. This is confirmed by the ^{11}B and ^{15}N NMR data, which show the presence of the

BCN_2 and NHB_2 units. For example, the shortest B-B distance is observed for the intermediate derived from polysilazane **2**, which does not contain NHB_2 structural units.

After further increasing the annealing temperature, the B-B distances for the various systems are very similar. However, the temperature dependence of B-B distances is quite pronounced, as expressed by the decrease from 2.86 to 2.53 $\mathring{A}$. On the basis of the present results, it can be concluded that intercalated BN and sp^2-carbon domains with hexagonal layer structure most likely constitute the $(BN)C_x$ phase above 1400 °C. The graphite-like carbon layers create some internal pressure which in turn is responsible for the observed interatomic distance increase.

In addition, ternary B-C-N ceramics were investigated by the aforementioned NMR techniques. B-C-N materials are expected to posses a high hardness and a high thermal stability at higher temperature. However, so far the structure of these materials has not been determined in detail. The investigated $B_1C_{1.7}N_1$ ceramic **8** (at 1200 °C) was obtained by pyrolysis of poly(borsesequicarbodiimide) $[B_2(^{15}N{=}C{=}N)_3]_2$. Upon annealing at 1600 °C, the ceramic composition remains almost identical and at 1700 °C, the B-C-N ceramic decomposed to products of carbon.

In the present work, ^{13}C, ^{15}N MAS NMR, $^{11}B\{^{15}N\}$ REDOR and ^{11}B spin echo experiments were used to investigate the structural feature of the pyrolysis intermediates at 1200 and 1600 °C. The NMR results show that the structural composition of the B-C-N ceramics is rather complex. At 1200 °C, B-C-N ceramics mainly contains an amorphous graphite-like carbon and BN-domains with hexagonal structure. $^{11}B\{^{15}N\}$ REDOR studies show that the B-N distances in the BN-domains are the same as in h-BN (1.44 Å). Upon annealing at 1600 °C, the relative amount of the BN_3 units, attributed BN-domains, decreases from 90 to 32 % resulting in an increase of the boron sites without B-N bonds. However, the ^{11}B spin echo

experiments reveal that the ^{11}B homonuclear second moment for the 1200 °C sample ($115{\cdot}10^6 rad^2/s^2$) remains almost the same after annealing at 1600 °C. Furthermore, both pyrolysis intermediates contain the small amount of the BC_4 units and a N(sp^3) component. This latter component is most likely given by nitrogen coordinated by carbon atoms rather than boron atoms, since according to the ^{11}B{^{15}N} REDOR studies, there is no evidence for BN_4 units of a cubic boron nitride phase.

Chapter 7

Zusammenfassung

Ternäre und quaternäre Prekursorkeramiken stehen im Zentrum vielfältiger Forschungsaktivitäten, was u. a. auf die ausgezeichneten mechanischen Eigenschaften und die ungewöhnlichen Hochtemperaturstabilität zurückgeführt werden kann. Im Allgemeinen weisen Prekursorkeramiken gegenüber den auf konventionellem Weg hergestellten Keramiken eine Reihe von Vorteilen auf, die sich z.B. in einer besseren Homogenität in der Elementverteilung und der größeren Flexibilität bei der Werkzeugherstellung niederschlägt. Vor kurzem konnte zudem gezeigt werden, dass Si-B-C-N-Keramiken eine deutlich verbesserte Temperaturstabilität bis zu ca. 2200 °C aufweisen, während Si-C-N-Keramiken sich nur bis ca. 1485 °C einsetzen lassen. Die Mehrzahl der Arbeiten an Si-B-C-N-Keramiken geht von Polysilazanen und Polysilylcarbodiimiden als Precursorpolymere aus, die nach Hydroborierung durch Pyrolyse in die quaternären amorphen bzw. kristallinen Keramiken überführt werden. Die außergewöhnlich gute thermische Stabilität dieser Keramiken wird auf die spezielle strukturelle Zusammensetzung zurückgeführt, was neben nanokristallinen SiC und Si_3N_4-Domänen eine turbostratische BNC_x-Phase einschließt.

Die thermolytische Keramikherstellung, ausgehend von den entsprechenden

Precursorpolymeren, beinhaltet mehrere amorphe Zwischenstufen, für deren strukturelle Charakterisierung konventionelle Verfahren, wie die Röntgendiffraktion, nicht einsetzbar sind. Demgegenüber sind insbesondere aus Festkörper-NMR-Messungen Informationen über den strukturellen Aufbau solcher Materialien zugänglich. Bei der NMR-Spektroskopie wird die Nahordnung (im Bereich von wenigen Å) um die jeweils detektierten Kernspins erfasst, deren magnetische Eigenschaften durch die elektronische Umgebung und durch die dipolaren Wechselwirkungen mit anderen Kernspins entscheidend bestimmt wird.

In dieser Arbeit werden der thermolytische Herstellungsprozess und das Kristallisationsverhalten von Si-B-C-N und B-C-N-Keramiken mittels Multikern-Festkörper -NMR-Spektroskopie (d.h. ^{13}C, ^{29}Si, ^{15}N, ^{11}B und ^{14}N NMR-Messungen) untersucht. Ein Schwerpunkt liegt dabei auf der Bestimmung der strukturellen Zusammensetzung der BNC_x-Phase. In diesem Zusammenhang wurden erstmals eine Reihe von Doppelresonanz-NMR-Messungen, wie ^{11}B{^{15}N}REDOR, ^{11}B{^{15}N}SEDOR, ^{11}B{^{14}N}REAPDOR und ^{11}B Spinecho-Experimente, durchgeführt, woraus sich dipolare Kopplungen und damit internukleare Abstände ermitteln lassen. REDOR und SEDOR-Experimente liefern Abstände zwischen den Bor- und den Stickstoffatomen, während aus ^{11}B Spinecho-Messungen Bor-Bor-Abstände zugäglich sind. ^{11}B{^{14}N}REAPDOR-Messungen liefern grundsätzlich die gleichen Informationen wie die ^{11}B{^{15}N}REDOR-Experimente, d.h. Bor-Stickstoff-Abstände, erfordern jedoch keine zusätzliche ^{15}N-Anreicherung.

Die experimentellen Messkurven der verschiedenen Doppelresonanz- und Spinecho-Messungen wurden unter Annahme einer hexagonalen Bornitrid-Struktur angepasst. Für Referenzzwecke wurden ^{11}B{^{14}N}REAPDOR und ^{11}B Spinecho-Experimente an *h*-BN durchgeführt, für welches die internuklearen Abstände aus Röntgenuntersuchungen bekannt sind.

Table 7.1. Zusammenstellung der untersuchten Proben ausgehend von bormodifizierten Polysilazane (**1**-**6**) und Polycarbodiimide **7** der allgemeinen Formel $\{B[RSi(R')R''X]_3\}_n$.

Prec.	X	R′	R	R″	^{15}N-Anreichungsgrad enrichment	Pyrolyse-temperatur
7	$(NCN)_{0.5}$	H	C_2H_4	H	50 %	400-1900 °C
3	NCH_3	H	C_2H_4	-	-	1050-1400 °C
2	NH	H	C_2H_4	-	100 %	400-1400 °C
1	NH	CH_3	C_2H_4	-	100 %	400-1400 °C
4	NH	CH_3	C_2H_4-CH_2	-	-	600-1400 °C
5	NH	H	C_2H_4-$SiH(H)C_2H_4$	-	100 %	400-1400 °C
6	NH	H	C_2H_4-$SiH(CH_3)C_2H_4$	-	-	1050-2000 °C

Eine Reihe von Si-B-C-N Keramiken wurden durch pyrolytische Umwandlung geeigneter Precursoren, wie bormodifizierte Polysilazane (**1**-**6**) und Polycarbodiimide **7** der allgemeinen Formel $\{B[RSi(R')R''X]_3\}_n$, hergestellt, wobei R, R′, R″ und X in Tabelle 7.1 definiert sind. Die Precursoren und die entsprechenden Intermediate, die bei der Pyrolyse entstehen, wurden in der Gruppe von Prof. F. Aldinger am Max-Planck-Institut für Metallforschung hergestellt.

Die Ergebnisse der ^{13}C, ^{29}Si, ^{15}N und ^{11}B NMR-Messungen zeigen, dass die Proben nach Pyrolyse bei 600 °C sich aus (*i*) sp^2 bzw. sp^3-Kohlenstoff von graphitähnlichen bzw. $CH_{4-x}Si_x$-Einheiten (x = 0, 1, 2, 3), (*ii*) einer amorphen Si-C-N-Matrix mit $SiC_{4-x}N_x$-Einheiten (x = 0, 1, 2 , 3, 4), und (*iii*) einer BNC_x-Matrix zusammensetzen.

Bei den Proben, die bei 1050 °C pyrolysiert wurden, liegt der sp^3-Kohlenstoff nur in Form von CSi_4 vor, während der sp^2-Kohlenstoff zwei Signale bei 120 und 138 ppm aufweist. Das Signal bei 120 ppm kann amorphem Kohlenstoff in graphitähnlichen Strukturen zugewiesen werden, während das Signal bei 138 ppm von Kohlenstoff in der BNC-Matrix herrührt, da bei 1050 °C höchstwahrscheinlich

BN_2C gebildet wird. Die ^{15}N NMR-Spektren der ^{15}N-angereicherten Proben zeigen dreifach koordinierte Stickstoffatome (NHB_2, NB_3 und NSi_3-Einheiten). Mit zunehmender Pyrolysetemperatur nimmt der Anteil der NHB_2-Einheiten ab, während der Anteil der NB_3-Einheiten aufgrund der zunehmenden Vernetzung ansteigt. So weist z.B. das Polysilazan **2**, mit X=NH und R′=H, bei 1400 °C nur noch NB_3 und NSi_3-Einheiten auf, was mit der stärkeren Vernetzung, bedingt durch die stärkere Reaktivität der Si-H-Bindung erklärt werden kann. Den höchsten Anteil an NSi_3-Einheiten im Vergleich zu den NB_3-Gruppen findet man bei den Pyrolyseproben des Precursorsystems **5**, das sich durch einen höheren Siliziumgehalt pro Monomereinheit auszeichnet.

Die NMR-Studien zeigen ferner, dass die strukturelle Zusammensetzung der entsprechenden amorphen Proben stark von den funktionellen Gruppen X und R abhängig ist, da diese für die weitere Vernetzung entscheidend sind. Die Precursorsysteme mit X = NCN und NCH_3 weisen einen höheren Anteil von Stickstoff-reichen Siliziumeinheiten ($SiCN_3$ und SiN_4-Einheiten) auf als die Precursorsysteme mit X = NH. Die Precursorsysteme mit R=C_2H_4-SiH(H)C_2H_4 und C_2H_4-SiH(CH_3)C_2H_4 besitzen einen geringen Anteil an Stickstoff-reichen Siliziumeinheiten, was mit dem höchsten Silizium- und Kohlenstoffgehalt pro Monomereinheit begründet werden kann. Zudem zeigen die Si-B-C-N-Keramiken mit einem höheren Anteil an Kohlenstoff-reichen Siliziumeinheiten mehr CSi_4-Einheiten als graphitähnliche Kohlenstoffkomponenten.

Im Allgemeinen findet man sehr gute Übereinstimmungen zwischen den theoretischen und experimentellen REDOR- und REAPDOR-Kurven aller Precursorsysteme, was auf eine nahezu planare Struktur der BN_3-Einheiten wie in *h*-BN hinweist. Die ermittelten Bor-Stickstoff-Abstände von 1.58 - 1.71 *Å* sind länger als in *h*-BN (1.44 Å), was auf eine Störung der Lagen, bedingt durch die BN_2C-Einheiten, zurückgeführt werden kann. Die stärksten strukturellen

Änderungen findet man zwischen 400 und 1400 °C, wo es zu einer deutlichen Abnahme des Bor-Stickstoff-Abstands mit zunehmender Auslagerungstemperatur kommt.

Der Bor-Bor-Abstand liegt bei den Proben, die bei 1050 °C pyrolysiert wurden, zwischen 2.78 und 3.25 $\mathring{A}$ und ist wiederum größer als in *h*-BN, was ebenfalls eine gestörte *h*-BN-Struktur anzeigt. Dies wird durch die ^{11}B und ^{15}N NMR-Spektren bestätigt, welche BN_2C- und NHB_2-Einheiten zeigen. Den kürzesten Bor-Bor-Abstand findet man beim Polysilazansystem **2**, für das keine NHB_2-Einheiten beobachtet werden.

Die Temperaturabhängigkeit der Bor-Bor-Abstände, die zwischen 1400 und 1900 °C von 2.86 auf 2.53 $\mathring{A}$ abnehmen, ist sehr ausgeprägt, während die Bor-Bor-Abstände innerhalb der verschiedenen Proben nahezu identisch sind. Auf der Basis dieser Ergebnisse kann geschlossen werden, dass die BNC_x-Phase als interkalierte BN und Graphiteinheiten vorliegt. Es wird vermutet, dass die Graphiteinheiten zwischen den BN-Lagen einen internen Druck aufbauen, der letztlich die größeren interatomaren Abstände bedingt. Trotzdem lassen sich andere Modelle, wie die Einbindung von kleinen Graphiteinheiten in die BN-Lagen, insbesondere unterhalb 1050 °C nicht vollständig ausschließen.

Ähnliche Untersuchungen wurden an B-C-N-Keramiken vorgenommen, die eine große Härte und Stabilität bei hohen Temperaturen aufweisen, deren Struktur bisher aber nicht im Detail bekannt ist. Eine ^{15}N-angereicherte Keramik der Zusammensetzung $B_1C_{1.7}N_1$ wurde durch Pyrolyse von Poly(borsesquicarbodiimid), $[B_2(^{15}N{=}C{=}N)_3]_2$, hergestellt. Nach Pyrolyse bei 1600 °C ändert sich die Zusammensetzung nur unwesentlich, während ab 1700 °C Zersetzung eintritt.

In dieser Arbeit wurden ^{13}C, ^{15}N MAS NMR, ^{11}B{^{15}N}REDOR- und ^{11}B Spinecho-Experimente durchgeführt, um die strukturellen Gegebenheiten

der Pyrolsate nach Auslagerung bei 1200 bzw. 1600 °C zu erfassen. Diese NMR-Untersuchungen zeigen, dass der strukturelle Aufbau dieser B-C-N-Keramiken sehr komplex ist. Bei 1200 °C liegen hauptsächlich amorpher, graphitähnlicher Kohlenstoff und Domänen von *h*-BN vor. Die entsprechenden $^{11}B\{^{15}N\}$REDOR-Experimente liefern B-N-Abstände, die mit denen von *h*-BN nahezu übereinstimmen.

Nach Auslagerung bei 1600 °C verringert sich der relative Anteil an BN_3-Einheiten von 90 auf 32 %, was eine deutliche Zunahme von Boratomen ohne direkte B-N-Bindung anzeigt. Aus den ^{11}B Spinecho-Untersuchungen wurden für die Proben, die bei 1200 und 1600 °C ausgelagert wurden, nahezu identische Werte für die zweiten Momente, $M_2\{^{11}B\}$, erhalten. Weiterhin zeigen die Pyrolysate geringe Mengen an BC_4-Einheiten sowie eine N(sp^3)-Komponente. Letztere ist vermutlich aus dreifach, mit Kohlenstoffatomen koordinierten Stickstoffatomen aufgebaut, da die $^{11}B\{^{15}N\}$REDOR-Resultate die Gegenwart von BN_4-Einheiten einer kubischen Bornitrid-Phase ausschließen.

Abbrevations

η	asymmetry parameter
CP	cross-polarization
γ	gyromagnetic ratio
$\mathbf{M}_{2(homo)}$	homonuclear second moment
$\mathbf{M}_{2(hetero)}$	heteronuclear second moment
δ_{iso}	isotropic chemical shift value
LAB	laboratory frame
MAS	magic angle spinning
NMR	nuclear magnetic resonance
$\boldsymbol{I}$	nuclear spin
PDCs	precursor derived ceramics
PAS	principal axis system
C_{qcc}	quadrupolar coupling constant
rf	radio frequency
REAPDOR	rotational echo adiabatic passage double resonance

REDOR rotational echo double resonance

S/N signal to noise

SP single pulse

SEDOR spin echo double resonance

$\mathbf{T}_1$ spin-lattice relaxation time

$\mathbf{B}_0$ static magnetic field

Appendix

^{11}B{^{14}N} REAPDOR simulation pulse program

```
Spinsys {           channels 11B 14N
                    nuclei 11B 14N 14N 14N
                    dipole 1 2 -930 90 0
                    dipole 1 3 -930 0 90 120
                    dipole 1 4 -930 0 90 240
                    quadrupole 2 2 140e3 0 0 90 0
                    quadrupole 3 2 140e3 0 0 90 120
                    quadrupole 4 2 140e3 0 0 90 240 }
par   {  proton_frequency 400e6
                    spin_rate       10000
                    sw              spin_rate*2
                    np              20
                    crystal_file    rep10
                    gamma_angles    5
                    start_operator  I1x
                    detect_operator I1c
                    verbose         1101
                    variable rfx    192000
                    variable rfy    70000 }
proc pulseq {} {  global par
                    maxdt 1.0
                    set t180x [expr 0.5e6/$par(rfx)]
                    set t180y [expr 0.3333e6/$par(spin_rate)]
                    set tr1 [expr 0.5e6/$par(spin_rate)-$t180x]
                    set tr2 [expr 1e6/$par(spin_rate)-$t180y/2-$t180x/2]
                    reset
                      delay $tr1
                      pulse $t180x $par(rfx) x 0 x
```

```
                    delay $tr1
                    pulse $t180x $par(rfx) y 0 x
                  store 1
                  reset
                  acq
                    prop 1
                    delay $tr1
                    pulse $t180x $par(rfx) x 0 x
                    delay $tr2
                    pulse $t180y 0 x $par(rfy) x
                    delay $tr2
                    pulse $t180x $par(rfx) x 0 x
                    delay $tr1
                    pulse $t180x $par(rfx) y 0 x
                    delay $tr1
                  store 2
                    pulse $t180x $par(rfx) x 0 x
                    delay $tr1
                  acq
                  for {set i 2} {$i < $par(np)} {incr i} {
                    reset
                    prop 1
                    prop 2
                    pulse $t180x $par(rfx) x 0 x
                    delay $tr1
                    pulse $t180x $par(rfx) y 0 x
                    delay $tr1
                    store 2
                    pulse $t180x $par(rfx) x 0 x
                    delay $tr1
                  acq  } }
proc main {} {    global par
                  set    f [fsimpson]
                  fsave $f $par(name).fid
                  fzerofill $f 16384
                  faddlb    $f 50 0
                  fft       $f
                  fsave     $f $par(name).spe –binary }
```

List of Figures

List of Tables

Bibliography

[1] Bengisu M., *Engineering ceramics*, Springer, Berlin, 2001.

[2] Rahaman M. N., *Ceramic processing and sintering*, Marcel Dekker, New York, 1995.

[3] Yanagida H.; Komoto K.; Miyayama M., *The chemistry of ceramics*, Wiley, Chichester, 1996.

[4] Lenoe E. M.; Katz R. N.; Burke J. J., *Ceramics for high performance applications III*, Plenum Press, New York, 1983.

[5] Hampshire S., *Non-oxide technical and engineering ceramics*, Proc. Int. Conf (London), Elsevier Applied Science, 1986.

[6] Tanaka H.; Greila P.; Petzowa G., *Int. J. High. Tech. Ceram.* **1** (1985), 107–118.

[7] Weimer A. W., *Carbide, nitride, and boride materials synthesis and processing*, Chapman & Hall, London, 1997.

[8] Segal D., *Chemical synthesis of advanced ceramic materials*, Cambridge University Press, Cambridge, 1989.

[9] Gnesin G. G., *Refract. Ind. Ceram.* **41** (2000), 155.

[10] Rice R. W., *Ceramic fabrication technology*, Marcel Dekker, New York, 2003.

[11] Saito S.; Somiya S., in *International Symposium on Factors in Densification and Sintering of Oxide and Non-oxide Ceramics*, Gakujutsu Bunken Fukyo-kai, Hakone Japan, 1987.

[12] Seyferth D.; Wiseman G. H., *J. Am. Ceram. Soc.* **67** (1984), C132–C133.

[13] Matsumoto R. L. K.; Schwark J. M., *Patent* (1993), US5206327.

[14] Laine R. M.; Sellinger A., *Si-Containing Ceramic Precursors*, in *The chemistry of organic silicon compounds* (Rappoport Z.; Apeloig Y., ed.), John Wiley & Sons, Chichester, 1998, pp. 2245–2315.

[15] Baldus H. P.; Jansen M., *Angew. Chem.* **109** (1997), 338.

[16] Kienzle A.; Bill J.; Aldinger F.; Riedel R., *Nanostruct. Mater.* **6** (1995), 349–52.

[17] Peuckert M.; Vaahs T.; Brck M., *Adv. Mater.* **2** (1990), 398–404.

[18] Bill J.; Aldinger F., *Adv. Mater.* **7** (1995), 775–87.

[19] Galusek D.; Reschke S.; Riedel R.; Dreszler W., *J. Eur. Ceram. Soc.* **19** (1999), 1911.

[20] Friess M.; Bill J.; Aldinger F.; Szabo D. V., *Mech. Corr. Prop.* **A** (1994), 95.

[21] Bill J.; Seitz J.; Thurn G.; Durr J.; Canel J.; Janos B. Z.; Jalowiecki A.; Sauter D.; Schempp S.; Lamparter H. P.; Mayer J.; Aldinger F., *Phys. Status Solidi A* **166** (1998), 269–296.

[22] Iwamoto Y.; Volger W.; Kroke E.; Riedel R.; Saitou T.; Matsunaga K., *J. Am. Ceram. Soc.* **84** (2001), 2170.

[23] Kumar R.; Mager R.; Phillipp F.; Zimmermann A.; Rixecker G., *Int. J. Mater. Res.* **97** (2006), 626–631.

[24] Riedel R.; Kienzle A.; Dressler W.; Ruwisch L.; Bill J.; Aldinger F., *Nature* **382** (1996), 796–798.

[25] Wang Z.-C.; Aldinger F.; Riedel R., *J. Am. Ceram. Soc.* **84** (2001), 2179–2183.

[26] Wang Z.-C.; Gerstel P.; Kaiser G.; Bill J.; Aldinger F., *J. Am. Ceram. Soc.* **88** (2005), 2709.

[27] Takamizawa M., *Patent* (1985), US4505151.

[28] Takamizawa M.; Kobayashi T.; Hayashida A.; Takeda Y., *Patent* (1986), US4604367.

[29] Nghiem Q. D.; Jeon J.-K.; Hong L.-Y.; Kim D.-P., *J. Organomet. Chem.* **688** (2003), 27.

[30] Gerardin C.; Taulelle F.; Bahloul D., *J. Mater. Chem.* **7** (1997), 117–126.

[31] Gervais C.; Babonneau F.; Ruwisch L.; Hauser R.; Riedel R., *Can. J. Chem.* **81** (2003), 1359–1369.

[32] Schmidt W. R.; Narsavage-Heald D. M.; Jones D. M.; Marchetti P. S.; Raker D.; Maciel G. E., *Chem. Mater.* **11** (1999), 1455–1464.

[33] Bernard S.; Weinmann M.; Gerstel P.; Miele P.; Aldinger F., *J. Mater. Chem.* **15** (2005), 289–299.

[34] Wideman T.; Cortez E.; Remsen E. E.; Zank G. A.; Carroll P. J.; Sneddon L. G., *Chem. Mater.* **9** (1997), 2218–2230.

[35] Horz M.; Zern A.; Berger F.; Haug J.; Müller K.; Aldinger F.; Weinmann M., *J. Eur. Ceram. Soc.* **25** (2005), 99–110.

[36] Müller A.; Peng J. Q.; Seifert H. J.; Bill J.; Aldinger F., *Chem. Mater.* **14** (2002), 3406–3412.

[37] Gerstel P.; Müller A.; Bill J.; Aldinger F., *Chem. Mater.* **15** (2003), 4980–4986.

[38] Jalowiecki A.; Bill J.; Aldinger F.; Mayer J., *Composites Part A* **27** (1996), 717.

[39] Zimmermann A.; Bauer A.; Christ M.; Cai Y.; Aldinger F., *Acta Mater.* **50** (2002), 1187–1196.

[40] Franke R.; Bender S.; Arzberger I.; Hormes J.; Jansen M.; Juengermann H.; Loeffelholz J., *Fresenius. J. Anal. Chem.* **354** (1996), 874–8.

[41] Noeth H., *Z. Naturforsch.,* **16B** (1961), 618–20.

[42] Seyferth D.; Plenio H., *J. Am. Ceram. Soc.* **73** (1990), 2131.

[43] Riedel R., *Appl. Organomet. Chem.* (1996), 241.

[44] Bill J.; Kienzle A.; Sasaki M.; Riedel R.; Aldinger F., *Adv. Sci. Technol.* **3B** (1995), 1291–1299.

[45] Baldus H. P.; Passing G.; Sporn D.; Thierauf A., *Ceram. Trans.* **58** (1995), 75.

[46] Baldus H. P.; Jansen M.; Wagner O., *Key Eng. Mater.* **89-91** (1994), 75–9.

[47] Juengermann H.; Jansen M., *Mater. Res. Innovations* **2** (1999), 200.

[48] Jaschke T.; Jansen M., *J. Eur. Ceram. Soc.* **25** (2005), 211–220.

[49] Baldus H.-P.; Jansen M., *Angew. Chem., Int. Ed.* **36** (1997), 328–343.

[50] Jansen M., *Mat. Res.Soc. Symp* (1992), 821.

[51] Jaschke T.; Jansen M., *J. Mater. Chem.* **16** (2006), 2792.

[52] Bernard S.; Weinmann M.; Cornu D.; Miele P.; Aldinger F., *J. Eur. Ceram. Soc.* **25** (2005), 251–256.

[53] Weinmann M.; Haug R.; Bill J.; Aldinger F.; Schuhmacher J.; Müller K., *J. Organomet. Chem.* **541** (1997), 345–353.

[54] Müller A.; Gerstel P.; Weinmann M.; Bill J.; Aldinger F., *Chem. Mater.* **14** (2002), 3398–3405.

[55] Verbeek W., *Patent* (1973), DE2218960.

[56] Ruwisch L., *Ph.D Thesis*, Darmstadt University of Technology, Germany, 1998.

[57] Jansen M.; Jaeschke B.; Jaeschke T., *Struct. Bond.* **101** (2002), 137–191.

[58] Nghiem Q. D.; Kim D.-P., *J. Ind. Eng. Chem.* **12** (2006), 905–910.

[59] Haberecht J.; Nesper R.; Grutzmacher H., *Chem. Mater.* **17** (2005), 2340–2347.

[60] Kienzle A.; Obermeyer A.; Riedel R.; Aldinger F.; Simon A., *Chem. Ber.* **126** (1993), 2569–71.

[61] Jalowiecki A., *Ph.D Thesis*, Max-Planck-Inst. für Metallforschung, Stuttgart, Germany, 1997.

[62] Pease R. S., *Acta Cryst.* **5** (1952), 356–61.

[63] Jeschke G.; Kroschel M.; Jansen M., *J. Non-Cryst. Solids* **260** (1999), 216–227.

[64] Van Wüllen L.; Jansen M., *J. Mater. Chem.* **11** (2001), 223–229.

[65] Van Wüllen L.; MU.; Jansen M., *Chem. Mater.* **12** (2000), 2347–2352.

[66] Sehlleier Y. H.; Verhoeven A.; Jansen M., *Angew. Chem., Int. Ed.* **47** (2008), 3600.

[67] Sehlleier Y.; Verhoeven A.; Jansen M., *J. Mater. Chem.* **17** (2007), 4316.

[68] Weinmann M.; Horz M.; Berger F.; Müller A.; Müller K.; Aldinger F., *J. Organomet. Chem.* **659** (2002), 29–42.

[69] Weinmann M.; Schuhmacher J.; Kummer H.; Prinz S.; Peng J. Q.; Seifert H. J.; Christ M.; Müller K.; Bill J.; Aldinger F., *Chem. Mater.* **12** (2000), 623–632.

[70] Müller A.; Zern A.; Gerstel P.; Bill J.; Aldinger F., *J. Eur. Ceram. Soc.* **22** (2002), 1631–1643.

[71] Weinmann M.; Kamphowe T. W.; Schuhmacher J.; Müller K.; Aldinger F., *Chem. Mater.* **12** (2000), 2112–2122.

[72] Sauter D.; Weinmann M.; Berger F.; Lamparter P.; Müller K.; Aldinger F., *Chem. Mater.* **14** (2002), 2859–2870.

[73] Weinmann M.; Nast S.; Berger F.; Kaiser G.; Müller K.; Aldinger F., *Appl. Organomet. Chem.* **15** (2001), 867–878.

[74] Berger F., *Ph.D Thesis*, University of Stuttgart, Germany, 2003.

[75] Jones P. R.; Myers J. K., *J. Organomet. Chem.* **34** (1972), C9–C11.

[76] Aldinger F.; Weinmann M.; Bill J., *Pure Appl. Chem.* **70** (1998), 439–448.

[77] Weinmann M.; Kamphowe T. W.; Fischer P.; Aldinger F., *J. Organomet. Chem.* **592** (1999), 115–127.

[78] Yive N. S. C. K.; Corriu R.; Leclercq D.; Mutin P. H.; Vioux A., *New J. Chem.* **15** (1991), 85–92.

[79] Weinmann M.; Haug R.; Bill J.; De Guire M.; Aldinger F., *Appl. Organomet. Chem.* **12** (1998), 725–734.

[80] Aldinger F.; Bill J.; Wurm K., Offenlegungsschrift (1998), DE19634777.

[81] Schuhmacher J.; Berger F.; Weinmann M.; Bill J.; Aldinger F.; Müller K., *Appl. Organomet. Chem.* **15** (2001), 809–819.

[82] Seifert H. J.; Aldinger F., *Struct. Bond.* **101** (2002), 1–58.

[83] Kasper B., *Ph.D Thesis*, Universität Stuttgart, Germany, 1996.

[84] Janakiraman N.; Zern A.; Weinmann M.; Aldinger F.; Singh P., *J. Eur. Ceram. Soc.* **25** (2005), 509–520.

[85] MacKenzie K. J. D.; Smith M. E., *Multinuclear Solid-State NMR of Inorganic Materials*, vol. 6, Pergamon, Oxford, 2002.

[86] Levitt M. H., *Spin Dynamics: Basics of Nuclear Magnetic Resonance*, John Wiley & Sons, Chichester, 2002.

[87] Schmidt-Rohr K.; Spiess H. W., *Multidimensional solid-state NMR and polymers*, Academic Press, London, 1994.

[88] Ernst R. R.; Bodenhausen G.; Wokaun A., *Principles of nuclear magnetic resonance in one and two dimensions*, Clarendon, Oxford, 1987.

[89] Abragam A., *The principles of nuclear magnetism*, Clarendon Press, Oxford, 1961.

[90] Mehring M., *Principles of high-resolution NMR in solids*, Springer-Verlag, Berlin, 1983.

[91] Vaughan R. W., Annu. Rev. Phys. Chem. **29** (1978), 397–419.

[92] Cheetham A. K.; Day P., *Solid state chemistry*, Clarendon Press, Oxford, 1992.

[93] Slichter C. P., *Principles of Magnetic Resonance*, Springer, Berlin, 1978.

[94] Duer M. J., *Solid-state NMR spectroscopy: principles and applications*, Blackwell Science, Malden, 2002.

[95] Klinowski J., *Top. Curr. Chem.* **246** (2004), 143.

[96] Freude D., *Quadrupolar nuclei in solid-state nuclear magnetic*, in *Encyclopedia of analytical chemistry: applications, theory, and instrumentation* (Meyers R. A., ed.), Wiley, Chichester, 2000, pp. 12188–12224.

[97] Freude D.; Haase J., *Quadrupole effects in solid-state nuclear magnetic resonance*, in *NMR Basic Principles and Progress.* (Diehl P.;Fluck E.;Gnther H.;Kasfeld R.; Seelig J., ed.), vol. 29, Springer-Verlag, Berlin, 1993, pp. 1–90.

[98] Man P. P., *Quadrupolar interactions*, in *Encyclopedia of nuclear magnetic resonance* (Grant D. M.; Harris R. K., ed.), vol. 6, John Wiley, Chichester, 1996, pp. 3838–3848.

[99] Man P. P., *Phys. Rev. B:* **55** (1997), 8406.

[100] Samoson A.; Kundla E.; Lippmaa E., *J. Magn. Reson.* **49** (1982), 350–357.

[101] Goldbourt A.; Madhu P. K., *Monatsh. Chem.* **133** (2002), 1497–1534.

[102] Wi S.; Ashbrook S. E.; Wimperis S.; Frydman L., *J. Chem. Phys.* **118** (2003), 3131–3140.

[103] Kundla E.; Samoson A.; Lippmaa E., *Chem. Phys. Lett.* **83** (1981), 229–32.

[104] Samoson A., *Chem. Phys. Lett.* **119** (1985), 29–32.

[105] Cowan B. P., *Nuclear magnetic resonance and relaxation*, Cambridge University Press, New York, 1997.

[106] Claridge T. D. W., *High-resolution nmr techniques in organic chemistry*, Pergamon, Amsterdam, 1999.

[107] Pines A.; Gibby M. G.; Waugh J. S., *J. Chem. Phys.* **59** (1973), 569–590.

[108] Gibby M. G.; Pines A.; Waugh J. S., *J. Am. Chem. Soc.* **94** (1972), 6231–6232.

[109] Peersen O. B.; Wu X. L.; Kustanovich I.; Smith S. O., *J. Magn. Reson., Ser A* **104** (1993), 334.

[110] Hartmann S. R.; Hahn E. L., *Phys. Rev.* **128** (1962), 2042–2053.

[111] Samoson A.; Lippmaa E., *J. Magn. Reson. Phys. Rev. Lett.* **79** (1988), 255–68.

[112] Man P. P., *J. Magn. Reson.* **100** (1992), 157–65.

[113] Schurko R. W.; Hung I.; Schauff S.; Macdonald C. L. B.; Cowley A. H., *J. Phys. Chem. A* **106** (2002), 10096–10107.

[114] Han D. Y.; Kessemeier H., *Phys. Rev. Lett.* **67** (1991), 346–9.

[115] Kunwar A. C.; Turner G. L.; Oldfield E., *J. Magn. Reson.* **69** (1986), 124–7.

[116] Haase J.; Oldfield E., *J. Magn. Reson., Ser A* **101** (1993), 30–40.

[117] Flett A. M.; Richard J. C. S., *Proc. Phys. Soc.* **86**, 171–179.

[118] Eckert H.; Elbers S.; Epping J. D.; Janssen M.; Kalwei M.; Strojek W.; Voigt U., *Top. Curr. Chem.* **246** (2005), 195–233.

[119] Man P. P., *Phys. Rev. B:* **52** (1995), 9418–9426.

[120] Gee B.; Eckert H., *Solid State Nucl. Magn. Reson.* **5** (1995), 113–122.

[121] Gee B., *Solid State Nucl. Magn. Reson.* **19** (2001), 73–86.

[122] Van Wüllen L.; Gee B.; Zuechner L.; Bertmer M.; Eckert H., *Ber. Bunsen Ges.* **100** (1996), 1539–1549.

[123] Van Vleck J. H., *Phys. Rev.* **74** (1948), 1168.

[124] Fraissard J. P.; Lapina O. B., *Magnetic resonance in colloid and interface science*, Kluwer Academic Publishers, Dordrecht, 2002.

[125] Van Wüllen L.; Zuechner L.; M-Warmuth W.; Eckert H., *Solid State Nucl. Magn. Reson.* **6** (1996), 203.

[126] Müller K. T., *J. Magn. Reson., Ser A* **113** (1995), 81–93.

[127] Gullion T., *Concepts Magn. Reson.* **10** (1998), 277–289.

[128] Franke D.; Maxwell R.; Lathrop D.; Eckert H., *J. Am. Chem. Soc.* **113** (1991), 4822–4830.

[129] Ueda T.; Tatsumi T.; Eguchi T.; Nakamura N., *J. Phys. Chem. B* **105** (2001), 5391–5396.

[130] Franke D.; Maxwell R.; Lathrop D.; Banks K.; Eckert H., *Phys. Rev. B:* **46** (1992), 8109–18.

[131] Boyce J. B.; Ready S. E., *Phys. Rev. B:* **38** (1988), 11008–18.

[132] Yap A. T. W.; Forster H.; Elliott S. R., *Phys. Rev. Lett.* **75** (1995), 3946–3949.

[133] Gullion T., *Magn. Reson. Rev.* **17** (1997), 83.

[134] Jaroniec C. P.; Tounge B. A.; Rienstra C. M.; Herzfeld J.; Griffin R. G., *J. Magn. Reson.* **146** (2000), 132–139.

[135] Gullion T.; Schaefer J., *J. Magn. Reson.* **81** (1989), 196–200.

[136] Chan J. C. C.; Bertmer M.; Eckert H., *J. Am. Chem. Soc.* **121** (1999), 5238–5248.

[137] Gullion T.; Vega A. J., *Prog. Nucl. Magn. Reson. Spectrosc.* **47** (2005), 123–136.

[138] Kalwei M.; Koller H., *Solid State Nucl. Magn. Reson.* **21** (2002), 145–157.

[139] Hughes E.; Gullion T.; Goldbourt A.; Vega S.; Vega A. J., *J. Magn. Reson.* **156** (2002), 230–241.

[140] Gullion T., *Chem. Phys. Lett.* **246** (1995), 325–30.

[141] Grey C. P.; Veeman W. S.; Vega A. J., *J. Chem. Phys.* **98** (1993), 7711–24.

[142] Grey C. P.; Vega A. J., *J. Am. Chem. Soc.* **117** (1995), 8232–42.

[143] Glaser R. W.; Ulrich A. S., *J. Magn. Reson.* **164** (2003), 104–114.

[144] Goldbourt A.; Vega S.; Gullion T.; Vega A. J., *J. Am. Chem. Soc.* **125** (2003), 11194–11195.

[145] Bak M.; Rasmussen J. T.; Nielsen N. C., *J. Magn. Reson.* **147** (2000), 296–330.

[146] Bak M.; Nielsen N., *J. Magn. Reson.* **125** (1997), 132.

[147] Goetz J. M.; Schaefer J., *J. Magn. Reson.* **127** (1997), 147.

[148] Jeschke G.; Jansen M., *Angew. Chem., Int. Ed.* **37** (1998), 1282–1283.

[149] Jeschke G.; Hoffbauer W.; Jansen M., *Solid State Nucl. Magn. Reson.* **12** (1998), 1–7.

[150] Bastow T. J.; Massiot D.; Coutures J. P., *Solid State Nucl. Magn. Reson.* **10** (1998), 241–245.

[151] Kintzinger J.-P.; Marsmann H., *Oxygen-17 and silicon-29* , Springer-Verlag, Berlin, 1981.

[152] Li Y. L.; Kroke E.; Riedel R.; Fasel C.; Gervais C.; Babonneau F., *Appl. Organomet. Chem.* **15** (2001), 820.

[153] Seitz J.; Bill J.; Egger N.; Aldinger F., *J. Eur. Ceram. Soc.* **16** (1996), 885–891.

[154] Bill J.; Kamphowe T. W.; Müller A.; Wichmann T.; Zern A.; Jalowieki A.; Mayer J.; Weinmann M.; Schuhmacher J.; Müller K.; Peng J.; Seifert H. J.; Aldinger F., *Appl. Organomet. Chem.* **15** (2001), 777–793.

[155] Soraru G. D.; Babonneau F.; Mackenzie J. D., *J. Mater. Sci.* **25** (1990), 3886–93.

[156] Gerardin C., *Ph.D Thesis*, University of Paris VI, 1991.

[157] Harris R. K.; Leach M. J.; Thompson D. P., *Chem. Mater.* **2** (1990), 320–3.

[158] Hatfield G. R.; Carduner K. R., *J. Mater. Sci.* **24** (1989), 4209–19.

[159] Framery E., *Ph.D Thesis*, Universite de Rennes, Rennes, France, 1996.

[160] Gervais C.; Babonneau F.; Maquet J.; Bonhomme C.; Massiot D.; Framery E.; Vaultier M., *Magn. Reson. Chem.* **36** (1998), 407–414.

[161] Brendler E.; Ebrecht E.; Thomas B.; Boden G.; Breuning T., *Fresenius. J. Anal. Chem.* **363** (1999), 185.

[162] Noeth H.; Tinhof W.; Wrackmeyer B., *Chem. Ber.* **107** (1974), 518–28.

[163] Noeth H.; Vahrenkamp H., *Chem. Ber.* **99** (1966), 1049–67.

[164] Noeth H.; Wrackmeyer B., *Chem. Ber.* **107** (1974), 3089–103.

[165] Marchetti P. S.; Kwon D. K.; Schmidt W. R.; Interrante L. V.; Maciel G. E., *Chem. Mater.* **3** (1991), 482–486.

[166] Maya L.; Cole D. R.; Hagaman E. W., *J. Am. Ceram. Soc.* **74** (1991), 1686–1688.

[167] Yoon Y.-G.; Pfrommer B. G.; Mauri F.; Louie S. G., *Phys. Rev. Lett.* **80** (1998), 3388–3390.

[168] Berger F.; Müller A.; Aldinger F.; Müller K., *Z. Anorg. Allg. Chem.* **631** (2005), 355–363.

[169] Janakiraman N.; Weinmann M.; Schuhmacher J.; Müller K.; Bill J.; Aldinger F.; Singh P., *J. Am. Ceram. Soc.* **85** (2002), 1807–1814.

[170] Van Wüllen L.; Roth A.; Jansen M., *Solid State Nucl. Magn. Reson.* **27** (2005), 90–98.

[171] Sehlleier Y. H.; Verhoeven A.; Jansen M., *Angew. Chem.* **120** (2008), 3656.

[172] Andreev Y. G.; Lundstrom T.; Harris R. K.; Oh S. W.; Apperley D. C.; Thompson D. P., *J. Alloys Compd.* **227** (1995), 102.

[173] Harazono T.; Hiroyama Y.; Watanabe T., Bull. Chem. Soc. Jpn. **69** (1996), 2419.

[174] Alam T. M., *Mater. Chem. Phys.* **85** (2004), 310.

[175] Braddock-Wilking J.; Lin S. H.; Feldman B. J., *Solid State Commun.* **119** (2001), 19.

[176] Gastreich M.; Marian C. M., *J. Comput. Chem.* **19** (1998), 716.

[177] Marian C.; Gastreich M., *Solid State Nucl. Magn. Reson.* **19** (2001), 29.

[178] Gervais C.; Babonneau F., *J. Organomet. Chem.* **657** (2002), 75–82.

Publications

Simone Mascotto, **Otgontuul Tsetsgee**, Klaus Mueller, Chiara Maccato, Bernd Smarsly, Doris Brandhuber, Eugenio Tondello and Silvia Gross, *Journal of Materials Chemistry*,**17**, 1-14, 2007

Emmler, T.; **Tsetsgee, O.**; Buntkowsky, G.; Weinmann, M.; Aldinger, F.; Mueller, K., *Soft Materials*, **4**, (2-4), 207-225, 2007

Faccini, F.; Fric, H.; Schubert, U.; Wendel, E.; **Tsetsgee, O.**; Mueller, K.; Bertagnolli, H.; Venzo, A.; Gross, S., *Journal of Materials Chemistry*,**17**, (31), 3297-3307, 2007

Armelao, L.; Gross, S.; Mueller, K.; Pace, G.; Tondello, E.; **Tsetsgee, O.**; Zattin, A., *Chemistry of Materials*,**18**, (25), 6019-6030, 2006

A.S. Ilyushin, N.A. Khatanova, E.A. Rykova, and **Ts. Otgontuul** *Moscow University Physics Bulletin*, **54**, 37-43,1999